The buffer-gas cell and the extraction RFQ for SHIPTRAP

Dissertation der Fakultät für Physik
der
Ludwig-Maximilians-Universität München

vorgelegt von

Jürgen Benno Neumayr
aus Wasserburg am Inn

München, den 28.04.2004

1. Gutachter: Prof. Dr. D. Habs

2. Gutachter: Prof. Dr. G. Graw

Tag der mündlichen Prüfung: 08.07.2004

Summary

SHIPTRAP is a new ion trap system for high-precision mass measurements of transuranium recoil-ions from the SHIP facility at GSI. The system consists of a buffer-gas cell to thermalise the incoming ions, an extraction system to separate the ions from the buffer gas, an RFQ buncher to cool and accumulate the ions and a tandem Penning-trap system for isobaric purification and high-precision mass measurements. The buffer-gas cell and the extraction RFQ were developed, assembled and tested within this thesis at the MLL (Maier-Leibnitz Laboratory) in Garching and at the GSI.

The main requirements given for the gas-cell/extraction-RFQ system are a fast and effective extraction of the stopped recoil ions. Therefore besides the purity of the system preventing recombination and molecule formation, ensured by the use of only non-organic material inside the cell and a highly efficient gas purification, especially the interaction between guiding electric fields and the gas flow inside the system has been optimised. The design optimisation of the different parts of the system was achieved using simulation programs like the VARJET code (gas flow), the SIMION code (ion trajectories in electric fields), a combination of both and the SRIM code (stopping ranges of ions in matter).

In the actual set-up of buffer-gas cell/extraction-RFQ the ions enter the cell through a thin metallic entrance foil (~4 µm thick, Ø 60 mm) and are stopped in the helium buffer gas (~50 – 200 mbar). The thermalised ions are then accelerated by electric fields (~10 V/cm) created by a segmented DC electrode inside the gas cell towards a funnel-shaped ring electrode structure. This funnel guides the ions by the applied RF and DC fields towards the extraction nozzle (Ø 0.6 mm) which acts as an interface between the stopping chamber and the extraction chamber. At the nozzle the buffer gas expands into the extraction chamber ($10^{-1} – 10^{-3}$ mbar) creating a supersonic gas jet and dragging the extracted ions. Inside the extraction-RFQ structure the ions are separated from the buffer gas and are cooled during the transport. In order to guarantee an optimum purity, the set-up is bakeable and a hydrocarbon-free pumping equipment is used.

For characterisation measurements of the set-up both stable and radioactive ions were used.
For off-line measurements stable Er ions were created inside the buffer-gas cell by using a focused pulsed laser beam. These ions were used for field optimisations and the determination of the extraction time of the gas cell. Depending on the field strength mean extraction times of around 5 ms at a He pressure of 50 mbar were achieved.
A completely experimental determination of the overall efficiency of the gas-cell/extraction-RFQ system could be achieved using the characteristic α decay of ^{152}Er ions. This isotope was produced via the reaction ^{121}Sb(^{35}Cl,4n)^{152}Er at the MLL and via ^{116}Sn(^{40}Ar,4n)^{152}Er at GSI. The measurements at the MLL were done in a longitudinal configuration, where the ions entered the gas cell along the extraction

axis. A maximum efficiency, including stopping efficiency and extraction efficiency, of about 8 % could be achieved.

The on-line measurements with stable Ag ions were performed in collaboration with the Gießen group and their Ortho-TOF mass spectrometer. Besides an overall efficiency of the gas-cell/extraction-RFQ system of about 4 %, including the transfer efficiency between the extraction RFQ and the TOF spectrometer, the efficiency dependence on the beam intensity stopped in the cell was studied. Space-charge limitations at intensities beyond $2.5 \cdot 10^8$ ions/s were observed.

The measurements at GSI were performed in the actual SHIPTRAP configuration with an ion injection nearly perpendicular (82.5°) to the cell axis. In addition the measurements were done with and without the SHIPTRAP RFQ buncher coupled to the extraction RFQ. These measurements showed an overall efficiency of the gas-cell/extraction-RFQ system of almost 5 %, while together with the RFQ buncher around 3 % in transmission mode and in bunching mode were achieved.

With this efficiency the SHIPTRAP gas cell ranges amongst the leading facilities for stopping and cooling of radioactive ions world wide, thus enabling the start of the experimental physics program at the SHIPTRAP facility.

Zusammenfassung

SHIPTRAP ist ein neues Ionenfallensystem für hochpräzise Massenmessungen an Transuranen, die am SHIP-Aufbau an der GSI hergestellt werden. Das System besteht aus einer Puffergas-Zelle zur Thermalisierung der erzeugten Ionen, einem Extraktionssystem, um die Ionen vom Puffergas zu separieren, einem RFQ-Buncher zum Kühlen und Akkumulieren der Ionen und einem Tandem-Penning-Fallensystem zur Trennung des isobaren Untergrundes und zur hochpräzisen Massenmessung. Im Rahmen dieser Dissertation wurden die Puffergas-Zelle und der Extraktions-RFQ entwickelt, gebaut und am MLL (Maier-Leibnitz-Laboratorium) in Garching und an der GSI getestet.

Die Hauptanforderung an das System aus Zelle und RFQ ist eine schnelle und effektive Extraktion der gestoppten Ionen. Neben der Reinheit des Systems, die die Vermeidung von Rekombination und Molekülbildung gewährleistet und durch den ausschließlichen Gebrauch von anorganischen Materialien in der Zelle und einer sehr effizienten Gasreinigung erreicht wird, galt es in besonderem Maße das Zusammenspiel zwischen den elektrischen Führungsfeldern und dem Gasfluß im System zu optimieren. Die Optimierung des Designs der verschiedenen Systemteile wurde durch den Einsatz von Simulationsprogrammen erreicht. Dazu gehören VARJET (Gasfluß), SIMION (Ionentrajektorien in elektrischen Feldern), eine Kombination beider und SRIM (Ionenstoppverteilungen).

Beim aktuellen Aufbau von Zelle und RFQ treten die Ionen durch eine dünne metallische Eintrittsfolie (~4 µm Dicke, Ø 60 mm) in die Zelle ein und werden im Helium-Puffergas (~50 – 200 mbar) gestoppt. Die thermalisierten Ionen werden dann durch elektrische Felder (~10 V/cm), die durch eine segmentierte DC-Elektrode innerhalb der Zelle erzeugt werden, auf eine trichterförmige Ringelektrodenstruktur (Funnel) hin beschleunigt. Dieser Funnel führt die Ionen durch die angelegten Gleich- und Wechselspannungsfelder zur Extraktionsdüse (Ø 0.6 mm), die als Verbindung zwischen Zelle und Extraktionskammer dient. An der Düse expandiert das Puffergas in die Extraktionskammer (10^{-1} – 10^{-3} mbar), wobei ein Gasstrahl mit Überschallgeschwindigkeit erzeugt wird, der die Ionen mit sich zieht und extrahiert. Im Extraktions-RFQ werden die Ionen vom Puffergas separiert und während des Transportes gekühlt. Um eine optimale Reinheit zu gewährleisten, ist der Aufbau ausheizbar und das verwendete Vakuumsystem kohlenwasserstofffrei.

Die Messungen zur Charakterisierung des Aufbaus wurden sowohl mit stabilen, als auch mit radioaktiven Ionen durchgeführt.
Für Off-line-Messungen wurden dabei stabile Er-Ionen innerhalb der Zelle mit einem fokussierten und gepulsten Laserstrahl erzeugt. Diese Ionen dienten der Optimierung der Felder und der Ermittlung von Extraktionszeiten aus der Zelle. Je nach Feldstärke wurden so mittlere Extraktionszeiten von etwa 5 ms bei einem Heliumdruck von 50 mbar erreicht.
Eine ausschließlich experimentelle Bestimmung der Gesamteffizienz des Systems Zelle/RFQ konnte mithilfe des charakteristischen Alphazerfalls von ^{152}Er-Ionen erreicht werden. Dieses Isotop wurde mit den Reaktionen ^{121}Sb(^{35}Cl,4n)^{152}Er am MLL

und ^{116}Sn(^{40}Ar,4n)^{152}Er an der GSI erzeugt. Bei den Messungen am MLL wurde eine longitudinale Ausrichtung verwendet, bei der die Ionen entlang der Extraktionsachse in die Zelle eintraten. Für die Effizienz wurde dabei ein Maximum von 8 % ermittelt, wobei dieser Wert die Stop- und die Extraktionseffizienz enthält.

Die On-line-Messungen mit stabilen Silberionen wurden in Zusammenarbeit mit der Giessener Gruppe und ihrem Ortho-TOF-Massenspektrometer durchgeführt. Neben der Bestimmung der Gesamteffizienz für Zelle und RFQ von etwa 4 %, wobei hier die Transfereffizienz zwischen Extraktions-RFQ und dem TOF-Spektrometer beinhaltet ist, wurde die Effizienz in Abhängigkeit von der Intensität des in der Zelle gestoppten Strahles untersucht. Dabei wurden raumladungsbedingte Verluste oberhalb einer Intensität von $2.5 \cdot 10^8$ Teilchen/s beobachtet.

Die Messungen an der GSI wurden in der aktuellen SHIPTRAP-Konfiguration durchgeführt, bei der der Ioneneinschuß nahezu senkrecht zur Extraktionsachse (82.5°) erfolgt. Zusätzlich wurden diese Untersuchungen sowohl ohne, als auch mit dem SHIPTRAP-Buncher gekoppelt an die Extraktionskammer durchgeführt. Diese Untersuchungen zeigten eine Gesamteffizienz von Zelle und RFQ von fast 5 %, während zusammen mit dem Buncher etwa 3 % sowohl im Transmissionsmodus als auch beim Betrieb als Buncher erreicht wurden.

Mit diesen Effizienzen reiht sich die SHIPTRAP Zelle in die weltweit führende Gruppe von Systemen ein, die dem Stoppen und Kühlen von radioaktiven Ionen dienen. Ermöglicht wird damit der Beginn für das experimentelle Programm am SHIPTRAP-Aufbau.

CONTENTS

Chapter 1 Introduction 1

1.1. Production of radioactive ions 1

1.2. The principle of SHIPTRAP 3
1.2.1. The SHIP facility 4
1.2.2. The SHIPTRAP facility 5
1.2.2.1. The RFQ buncher 7
1.2.2.2. The Penning-trap system 8
1.2.3. Physics at SHIPTRAP 10
1.2.4. Existing facilities using buffer-gas cells for stopping and extraction of energetic ions 11

Chapter 2 Behaviour of ions in matter and electric fields 15

2.1. Energy loss of ions in matter 15
2.1.1. Nuclear stopping 16
2.1.2. Electronic stopping 18
2.1.3. Stopping range 20

2.2. Ions in gas 21
2.2.1. Diffusion 21
2.2.2. Ion loss mechanisms 22
2.2.2.1. Neutralisation and charge exchange 22
2.2.2.2. Molecule formation 24
2.2.3. Space-charge and plasma effects 26

2.3. Ions in electric fields 28
2.3.1. Static fields and ion mobility 28
2.3.2. Radiofrequency structures 30
2.3.2.1. Ions in an RFQ 30
2.3.2.2. Ion motion in an RFQ in vacuum 33
2.3.2.3. Ions in a gas-filled RFQ 38
2.3.2.4. Ions in the funnel 40

Chapter 3 The experimental set-up 43

3.1. Overview 44

3.2. Design requirements 44

3.3. The buffer-gas cell 45
3.3.1. The vacuum chamber 45
3.3.2. The entrance window 45
3.3.3. The electrode system 47
3.3.3.1. The DC electrode 47
3.3.3.2. The funnel structure 49
3.3.4. The gas-supply system 52

3.4. The extraction nozzle 54
3.4.1. Gas-dynamical simulations with VARJET 55

3.4.2. Impact-pressure measurements 57

3.5. The extraction system 59

3.6. Realisation of UHV conditions 622
3.6.1. The vacuum system 62
3.6.2. The baking system 66

3.7. The control system 66

Chapter 4 Characterisation of the ion extraction in off-line measurements 69

4.1. The test set-up 69

4.2. Field optimisations 71

4.3. Extraction time measurements 78

Chapter 5 Determination of the extraction efficiency via on-line measurements 83

5.1. On-line measurements at the MLL in Garching 83
5.1.1. Measurements with stable ion beams 83
5.1.2. Direct efficiency measurements using α-emitting reaction products 93
5.1.2.1. Production of α-emitting ions 94
5.1.2.2. The MLL test set-up 95
5.1.2.3. Stopping and extraction efficiency measurements 105

5.2. On-line measurements at GSI 112
5.2.1. Measurements with stable ions 112
5.2.2. Measurements with reaction products 113

5.3. Discussion of the buffer-gas cell performance 123

Chapter 6 Conclusion and outlook 127

6.1. Conclusion 127

6.2. Outlook: Next-generation set-up 128
6.2.1. Improvements of the SHIPTRAP gas cell 129
6.2.2. The new Munich set-up 129
6.2.3. Optimisation program with the new set-up 131
6.2.4. A new extraction structure 131

6.3. Physics program in combination with a Penning-trap system 133
6.3.1. High-precision mass measurements 134
6.3.1.1. Ground-state masses 135
6.3.1.2. Isomer spectroscopy 136
6.3.1.2.1. The α decay of high-spin and K-isomers 137
6.3.1.2.2. The α decay of fission isomeric states 139
6.3.2. In-trap and out-of-trap spectroscopy with Penning traps 140
6.3.2.1. Electron spectroscopy 140
6.3.2.2. Lifetime of 2^+ states in heavy nuclei 141
6.3.2.3. Rare ground-state α decays 142

6.3.3. High-precision *Q* value measurements related to fundamental interactions 142

Appendix 145

1. The control system for gas cell and extraction RFQ 145
1.1. The control of the iseg HV modules 145
1.2. The DS345 function generator control 147
1.3. The control of the baking system 147
1.4. The control of the vacuum and gas-supply system 151

2. The electrical connectors of the gas cell and the extraction RFQ 153

3. The MLL test equipment 154
3.1. The beam-line settings 154
3.2. The data-acquisition system 156

4. Compilation of design and operational parameters 157

5. Possible candidates for mass measurements at the MLL 159

Bibliography 163

Table of figures

Figure 1.1 Schematic view of the ion production using the in-flight method 2
Figure 1.2 Schematic view of the SHIPTRAP principle 3
Figure 1.3 Schematic view of the velocity filter SHIP 4
Figure 1.4 Schematic view of SHIPTRAP 6
Figure 1.5 Photograph of the SHIPTRAP set-up 6
Figure 1.6 Photograph of the SHIPTRAP RFQ buncher 7
Figure 1.7 The principle of the SHIPTRAP RFQ buncher 8
Figure 1.8 Photograph and schematic view of the SHIPTRAP Penning-trap system 9
Figure 1.9 Photograph of the buffer-gas cell actually used in Argonne 11
Figure 1.10 Photographs of the buffer-gas cell/RF carpet actually used at RIKEN ... 12
Figure 2.1 Energy dependence of nuclear and electronic stopping for Kr in C 16
Figure 2.2 TRIM simulation for Ag-ions @ 23 MeV, stopped in Ti/He 21
Figure 2.3 Mass distribution of ions extracted from the Leuven gas cell 25
Figure 2.4 Mass distribution for controlled contaminations of the Leuven gas cell .. 26
Figure 2.5 Schematic view of an RFQ with 4 cylindrical rods 31
Figure 2.6 Schematic view of a hyperbolic Paul trap 31
Figure 2.7 The first stability region in the *a*-*q* plot 35
Figure 2.8 The first stability range with the operating points an RFQ used as a mass filter 36
Figure 2.9 Electric field and simulation for the ion motion in a gas-filled RF funnel. 40
Figure 3.1 Schematic view of the SHIPTRAP buffer-gas cell and extraction RFQ .. 43
Figure 3.2 Picture of the flange containing the entrance window 46
Figure 3.3 The electrode system of the SHIPTRAP buffer-gas cell 47
Figure 3.4 Photograph of the DC electrode system 48
Figure 3.5 Distribution of equi-potential lines (SIMION) for the DC electrode 49
Figure 3.6 Schemativ view of the SHIPTRAP funnel structure 50
Figure 3.7 Photograph of the funnel structure 51
Figure 3.8 Principle of the electrical circuit for the RF funnel 52
Figure 3.9 Schematic view of the gas-supply system 53
Figure 3.10 Technical drawing of the extraction nozzle 54
Figure 3.11 Schematic view of the nozzle flange 55
Figure 3.12 VARJET simulation for the gas velocities inside the gas cell 56
Figure 3.13 Calculated and measured impact pressure values of the gas jet 58
Figure 3.14 Schematic view of the extraction RFQ 59
Figure 3.15 Photograph of the extraction RFQ 60
Figure 3.16 Principle of the electronics circuit of the RFQ 61
Figure 3.17 Schematic view of the vacuum system 62
Figure 3.18 Residual gas inside the buffer-gas chamber at $8{\cdot}10^{-8}$ mbar 64
Figure 3.19 Residual gas inside the buffer-gas chamber after baking at 150 °C 64
Figure 3.20 Residual gas inside the buffer-gas chamber without/with getter pump .. 65
Figure 3.21 Schematic view of the actual PC control system 67
Figure 4.1 Schematic view of the test set-up used for the laser measurements 70
Figure 4.2 Extracted masses from tests with laser-ionised ions using natural Er 71
Figure 4.3 Extraction efficiency as a function of the voltage electrode/funnel 72

Figure 4.4 Extraction efficiency as a function of the RF amplitude at the funnel.....73
Figure 4.5 Extraction efficiency as a function of the RF frequency at the funnel.....74
Figure 4.6 Extraction efficiency as a function of the voltage funnel/nozzle 75
Figure 4.7 Extraction efficiency as a function of the voltage RFQ/ nozzle...............76
Figure 4.8 Plot of a scan for the *q* value of the RFQ 77
Figure 4.9 Time-of-flight spectra for Er^+ ions at a buffer-gas pressure of 40 mbar..79
Figure 4.10 Extraction times as a function of the voltage electrode/funnel 80
Figure 4.11 Extraction times as a function of the buffer-gas pressure/voltages 81
Figure 4.12 Schematic view of the optimum DC potentials for laser-induced ions....82
Figure 5.1 Schematic view of the Gießen Ortho-TOF spectrometer 84
Figure 5.2 Schematic view of the set-up for measurements with stable ions/MLL..85
Figure 5.3 Photograph of the set-up with the Gießen Ortho-TOF spectrometer......86
Figure 5.4 Extracted masses during an on-line test with a ^{107}Ag beam...................87
Figure 5.5 Absolute efficiency as a function of the voltage electrode/funnel 88
Figure 5.6 Absolute efficiency as a function of the DC ramp at the funnel 89
Figure 5.7 Absolute efficiency as a function of the RF amplitude at the funnel 90
Figure 5.8 Absolute efficiency as a function of the RF frequency at the funnel.......91
Figure 5.9 Absolute efficiency as a function of the beam intensity 92
Figure 5.10 Schematic view of the optimum DC potentials for stable ions/MLL........93
Figure 5.11 Part of the nuclear chart in the rare earth region around ^{152}Er 95
Figure 5.12 Schematic view of the set-up for measurements with unstable ions at the MLL 96
Figure 5.13 Photograph of the set-up for measurements with unstable ions at the MLL 97
Figure 5.14 Plot of the Ge-detector photopeak efficiency as a function of the γ energy..98
Figure 5.15 Part of the level scheme of ^{152}Er 99
Figure 5.16 γ-ray energy spectrum following the reaction ^{121}Sb(^{35}Cl,xn)$^{156\text{-}xn}$Er......100
Figure 5.17 Calculated and measured excitation function of ^{121}Sb(^{35}Cl,4n)^{152}Er 101
Figure 5.18 Equilibrium charge distribution for Er @ 0.2 MeV/u after a carbon foil.102
Figure 5.19 Trajectories in the x-z-plane of ^{152}Er in a COSY INFINITY simulation..103
Figure 5.20 Simulated ion trajectories in the x-y-plane at the position of the gas-cell..104
Figure 5.21 α-energy spectrum measured in front of the gas cell (MLL).................106
Figure 5.22 α-energy spectrum measured behind the extraction-RFQ (MLL).........107
Figure 5.23 Absolute efficiencies as a function of the pressure/cell and RF/RFQ...109
Figure 5.24 TRIM simulation for Er-ions @ 29 MeV, stopped in Ti/He....................111
Figure 5.25 Time-of flight spectrum detected behind the RFQ buncher of SHIPTRAP 112
Figure 5.26 Schematic view of the set-up used at GSI 114
Figure 5.27 Schematic view of the set-up including the SHIPTRAP RFQ buncher.114
Figure 5.28 Photograph of the set-up used at GSI including the RFQ buncher 115
Figure 5.29 α-decay energy spectrum measured in front of the gas cell at GSI 116
Figure 5.30 α-decay energy spectrum measured behind the extraction RFQ at GSI..117
Figure 5.31 Absolute efficiency as a function of the degrader thickness at 47 mbar..118

Figure 5.32 Absolute efficiency as a function of the degrader thickness at 62 mbar 119
Figure 5.33 Extraction efficiency as a function of the voltage electrode/funnel 120
Figure 5.34 Extraction efficiency as a function of the voltage funnel/nozzle 121
Figure 5.35 Extraction efficiency as a function of the RF amplitude at the RFQ 122
Figure 6.1 Schematic view of the new Munich gas cell and extraction RFQ set-up 130
Figure 6.2 VARJET simulation for the proposed extraction structure 132
Figure 6.3 Ion-optical simulations (SIMION) for the proposed extraction structure 133
Figure 6.4 Candidates for future precision mass measurements at the MLL 136
Figure 6.5 Overview on the isotopes having isomers with half-lives larger than 1 ms 137
Figure 6.6 Geiger-Nuttal plot for rare earth elements 138
Figure A.1 The control panel for the iseg HV modules 146
Figure A.2 The control panel for the DS345 function generator 147
Figure A.3 Photograph of the modules of the vacuum-chamber baking system 148
Figure A.4 Flow chart of the control system for the baking system 149
Figure A.5 The control panel for the baking system 151
Figure A.6 Schematic view of the planned control system for vacuum and buffer gas supply system 152
Figure A.7 Schematic view of the electrical feedthroughs for the gas cell 153
Figure A.8 Schematic view of the electrical feedthroughs for the extraction chamber 154
Figure A.9 Calibration for the 90° dipole used for the MLL test set-up 155
Figure A.10Control panel for the data acquisition 156

Für Nina und Uschi

Chapter 1

Introduction

One of the most fundamental properties of an atomic nucleus is its mass as it contains information about binding energies and the interactions between nuclear constituents.
For the development of new and the verification of existing nuclear mass theories the experimental determination of the masses with highest precision is inevitable. Presently the masses of more than 2220 nuclides [Wap03] have been determined and measurements are being continued.
A technique for high-precision nuclear mass measurements is provided by Penning traps since singly-charged particles can be stored long enough for accurate analysis. Different set-ups, where Penning traps are coupled to radioactive beam facilities are presently in operation. The most prominent are **I**SOLTRAP at CERN [Bol96], where a precision of the mass measurements up to 10^{-8} is achieved [Her02, Kel02] and the CPT (**C**anadian **P**enning **T**rap) at ANL [Sav01]. Other facilities as LEBIT at MSU [Sch03] and TITAN at TRIUMF [Dil03] are under construction or in the planning phase.

While the mass measurements at ISOLTRAP and CPT are actually focused on the intermediate range of isotope masses, a new facility for heavy radionuclides is in its commissioning phase. The SHIPTRAP set-up [Dil99] is placed behind the SHIP facility [Mün79] at GSI/Darmstadt and is designed especially for mass measurements of transuranium isotopes.

1.1. Production of radioactive ions

The production of radioactive nuclei stands at the beginning of mass measurements of these isotopes in traps. The most common mechanisms for the isotope production are the ISOL method [Pro81], employed e.g. at ISOLDE and the in-flight method, as used e.g. at GSI. Also a special case of the ISOL technique will be discussed, where the target is placed inside a gas cell. This technique is applied e.g. at Jyväskylä [Tas89], Mainz [Sew99] and Leuven[Kud96].

In the ISOL (**I**on **S**eparation **O**n **L**ine) method energetic light ions, preferentially protons, are sent onto a thick target. There the radioactive nuclides are produced by spallation, fragmentation or fission reactions. The reaction products diffuse out of the target and are then ionised and extracted out of the ion source. For the beam transport to the following set-ups the ions are then accelerated to energies of typically some 10 keV.

Besides the advantages of this method, like the excellent beam quality with a well-defined energy and charge state and the possibility to realise low beam energies, there are also disadvantages especially due to the diffusion process. The ionisation efficiency as well as the extraction efficiency depend on the chemical properties of the different elements. In addition due to the time needed by the ions to diffuse out of the target the method is limited to lifetimes typically longer than some 100 ms.

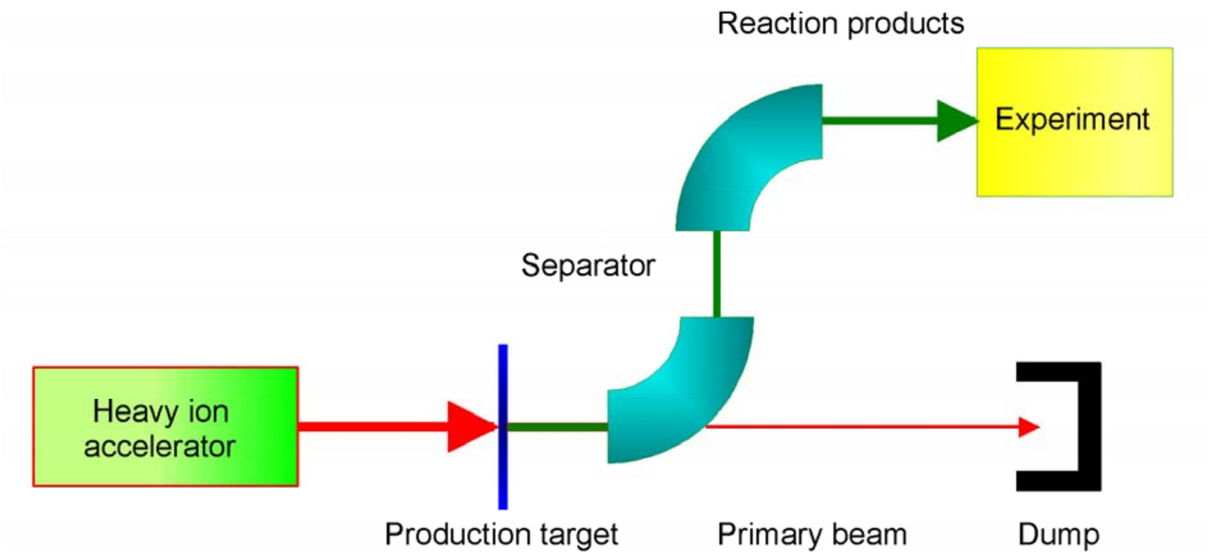

Figure 1.1

The principle of the ion production using the in-flight method. The primary beam (here with energies of typically some MeV/u) hits a production target, where e.g. a fusion reaction is initiated. Then the primary beam is separated from the reaction products and dumped. The produced highly-charged reaction products leave the target with energies in the range of some 10 keV/u to some MeV/u.

In the radioactive isotope production via the in-flight method an ion beam at energies from few MeV/u to GeV/u impinges on a production target but is not stopped in contrast to the ISOL method. Subsequently the nuclides of interest are filtered from the ensemble of reaction products via an electromagnetic separator. The reaction mechanisms in this method (depending on the mass region and incident energy) are transfer reactions, fission, projectile fragmentation, electromagnetic dissociation and fusion reactions.

The advantages of this method are the fast production and separation time and the fact that compared to the on-line facilities a large number of isotopes can be produced simultaneously. One disadvantage with regard to SHIP is the typically lower beam intensity compared to the ISOL method due to the limited cross sections in the thin targets. In terms of mass measurements in traps the main problem is that the produced ions have a broad distribution of charge states and that the ion energy is too high to trap them directly.

In a special version of the ISOL method a thick target is placed in a chamber filled with buffer gas that is used to thermalise the reaction products recoiling out of the target material. The products are then extracted from the cell using the gas flow or a combination of gas flow and guiding electric fields. For the application of electric fields the reaction products have to be ionised. Thus in the case that they are neutralised during the thermalisation they subsequently have to be ionised by natural charge creation mechanisms [Ärj87] or by laser ionisation [Ver94]. The main advantage compared to the 'common' ISOL method is the fast and universal transfer of the ions from the target to the following facilities.

1.2. The principle of SHIPTRAP

SHIPTRAP and similar facilities (e.g. CPT at Argonne [Sav01] and the cell of the Wada group at RIKEN [Wad03]) are based on techniques comparable to both the on-line and the in-flight method to combine the advantages of both of them.

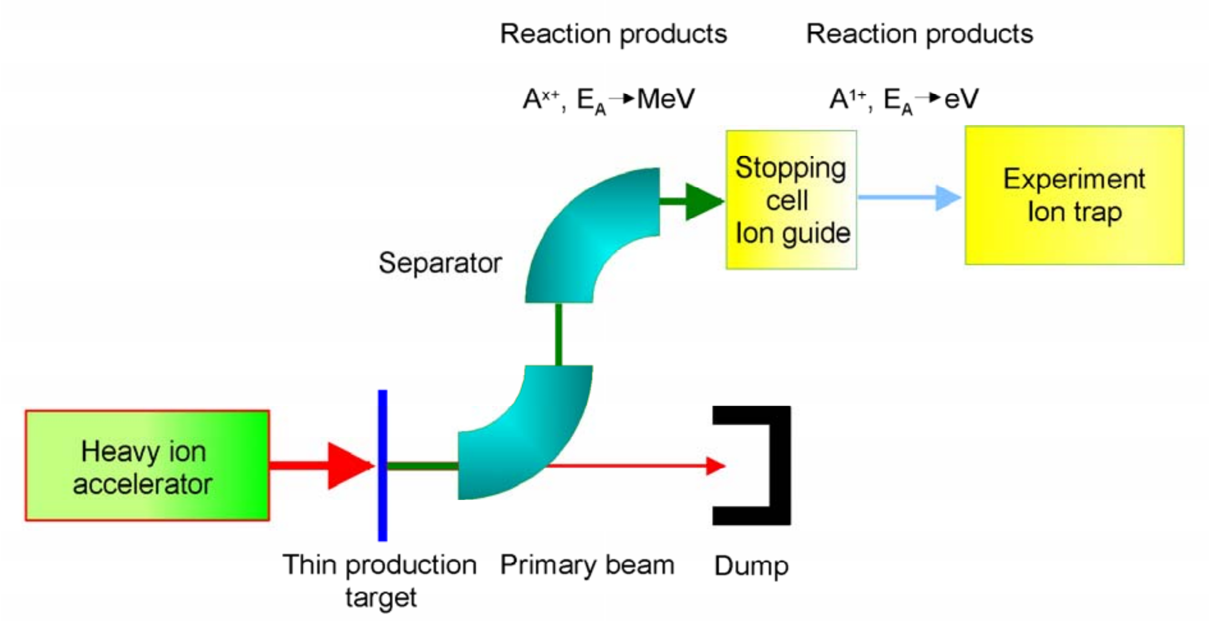
Reaction products
A^{x+}, $E_A \rightarrow$ MeV
Reaction products
A^{1+}, $E_A \rightarrow$ eV
Stopping cell Ion guide
Experiment Ion trap
Separator
Heavy ion accelerator
Thin production target
Primary beam
Dump

Figure 1.2
Schematic view of the SHIPTRAP principle. After the separation from the primary beam the reaction products are thermalised in a buffer-gas stopping cell. After the extraction from the gas cell the ions are guided to the following ion trap or other experiments.

In the case of SHIPTRAP the production of the isotopes takes place by fusion reactions via the in-flight method using thin targets. The fusion reaction products leaving the target with energies of typically several 100 keV/u are then thermalised in a buffer-gas cell, where mainly singly-charged ions remain. After the fast extraction the ions can be reaccelerated or trapped. Thus with this concept it is possible to combine the fast preparation of the transuranium isotopes with the possibility of an efficient trapping for the mass measurements.
Since the thermalised ions have to be transported from the high-pressure region inside the buffer-gas cell to a region of high vacuum inside accelerators or traps, the different parts of a set-up like SHIPTRAP are not only guiding the ions but act in addition as differential pumping stages.

1.2.1. The SHIP facility

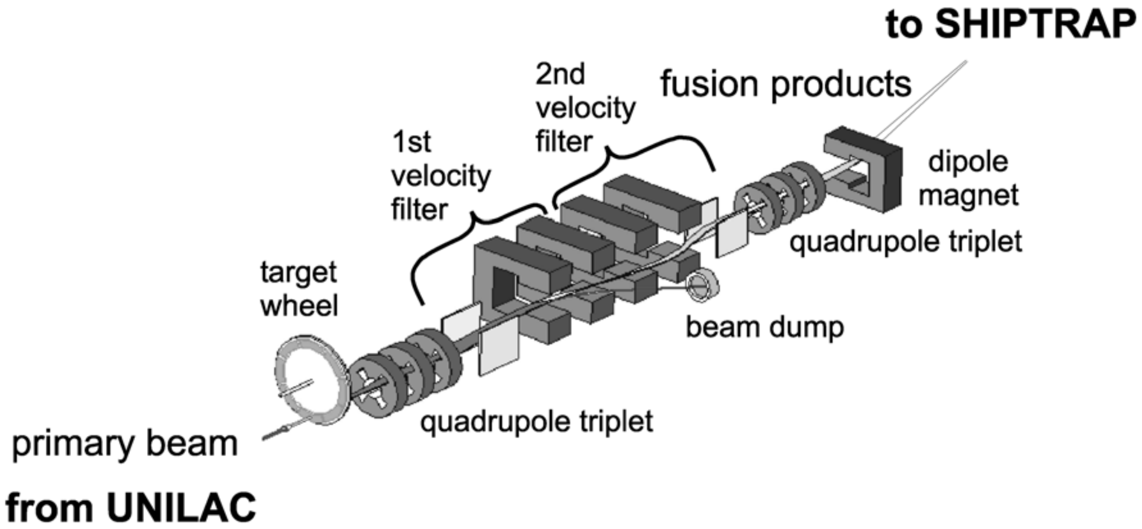

Figure 1.3
Schematic view of the velocity filter SHIP at GSI. The fusion-evaporation products produced at the target recoil into the direction of the primary beam. They are focused into the first velocity filter, where the primary beam is separated and dumped afterwards. The second velocity filter allows for a further purification of the secondary ions, while the following triplet allows for different focusing configurations. The additional 7.5° dipole magnet helps to reduce the background by enabling a detection shifted away from the beam-line direction.

The velocity filter SHIP (**S**eparator for **H**eavy **I**on reaction **P**roducts) [Mün79] is a facility for the production and in-flight separation of heavy ions at GSI/Darmstadt. Figure 1.3 shows a schematic view of SHIP. The reaction products are synthesised when the primary beam, accelerated by the UNILAC (**UNI**versal **L**inear **A**ccelerator), impinges on the target, placed on a rotating target wheel to ensure a better distribution of the energy deposition in the target material. After the first focusing quadrupole triplet two velocity filters are installed, each consisting of two electrostatic plates and two dipole magnets. The first stage is used to separate the reaction products from the primary beam that is dumped after the filter. Together with the two velocity filters the following quadrupole triplet lens allows for different beam focusing configurations. The additional last dipole magnet (7.5°) enables a detection shifted away from the beam-line direction in order to reduce the background.

The ion production is done by fusion-evaporation reactions with projectile energies high enough to exceed the Coulomb barrier of the target nucleus. Depending on the excitation energy the compound nucleus deexcites first by emitting neutrons, protons and α particles prior to the emission of γ rays.

SHIP has been used very successfully for the production of superheavy elements, up to $Z=111$ and $Z=112$, respectively, produced via the fusion reactions

$$^{64}\mathrm{Ni}+{}^{209}\mathrm{Bi}\rightarrow{}^{272}111+1\mathrm{n}$$

and

$$^{70}\mathrm{Zn}+{}^{208}\mathrm{Pb}\rightarrow{}^{277}112+1\mathrm{n}\,.$$

In these cases the identification of the superheavy reaction products was done via α-decay spectroscopy [Hof00]. For this purpose the products were implanted into position-sensitive silicon detectors, where the decay time, position and energy of each decay could be measured. The incident parent nucleus could be identified by detecting the α particles along the correlated decay chain to a known daughter nucleus.

SHIPTRAP has been designed to add the possibility of high-precision mass measurements of transuranium isotopes to the already unique capabilities of the SHIP facility.

1.2.2. The SHIPTRAP facility

The SHIPTRAP facility is shown schematically in Figure 1.4, whereas the whole set-up as installed at GSI can be seen on the photograph of Figure 1.5. SHIPTRAP consists of a gas-filled stopping chamber (1) where the ions, produced and separated at SHIP, are thermalised. After the extraction out of the cell the ions are separated from the buffer gas by an extraction RFQ (**R**adio **F**requency **Q**uadrupole) (2).

After the extraction the ions are injected into the RFQ buncher (3), where they are cooled and accumulated for the transfer into the Penning-trap system consisting of a purification trap (4) and a measurement trap (5).

Due to geometrical restrictions by its position behind the SHIP facility, SHIPTRAP is not in line with the SHIP beam-line direction. Therefore the direction of the separated ions and the longitudinal axis of SHIPTRAP include an angle of 82.5°. This has to be taken into account especially in the design of the buffer-gas cell, as the extraction out of the cell is in parallel to the SHIPTRAP axis. The configuration of the almost perpendicular positioning is visible in Fig. 1.5.

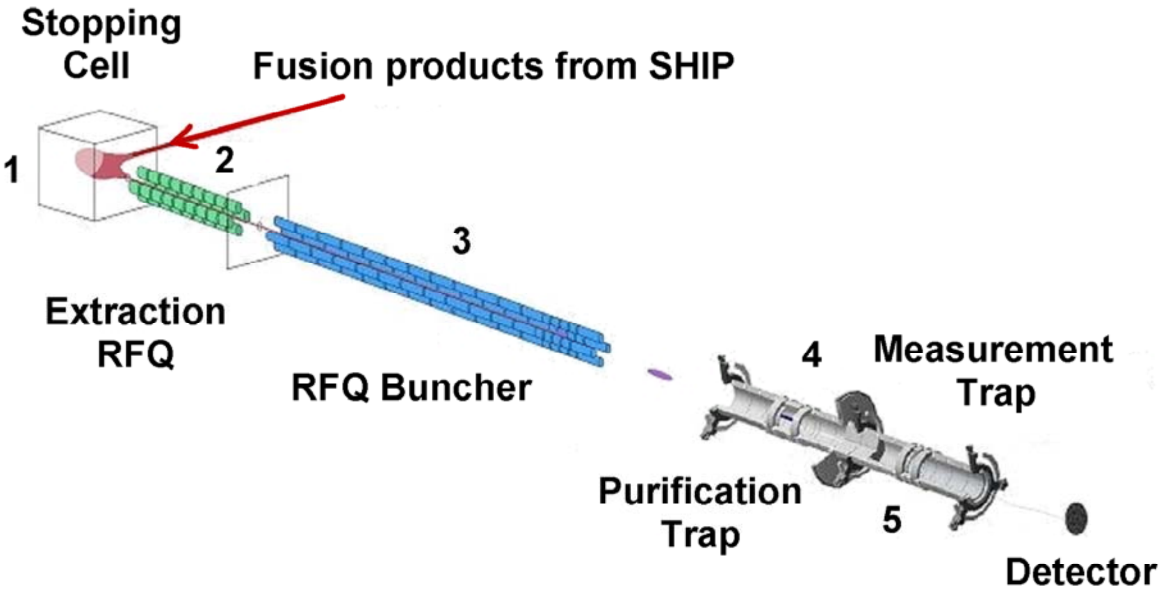
Stopping Cell
Fusion products from SHIP
1
2
3
Extraction RFQ
RFQ Buncher
4
Measurement Trap
Purification Trap
5
Detector

Figure 1.4
Schematic view of SHIPTRAP with the gas-filled stopping cell (1), the extraction RFQ (2), the RFQ buncher (3) and the Penning-trap system consisting of a purification trap (4) and a measurement trap (5).

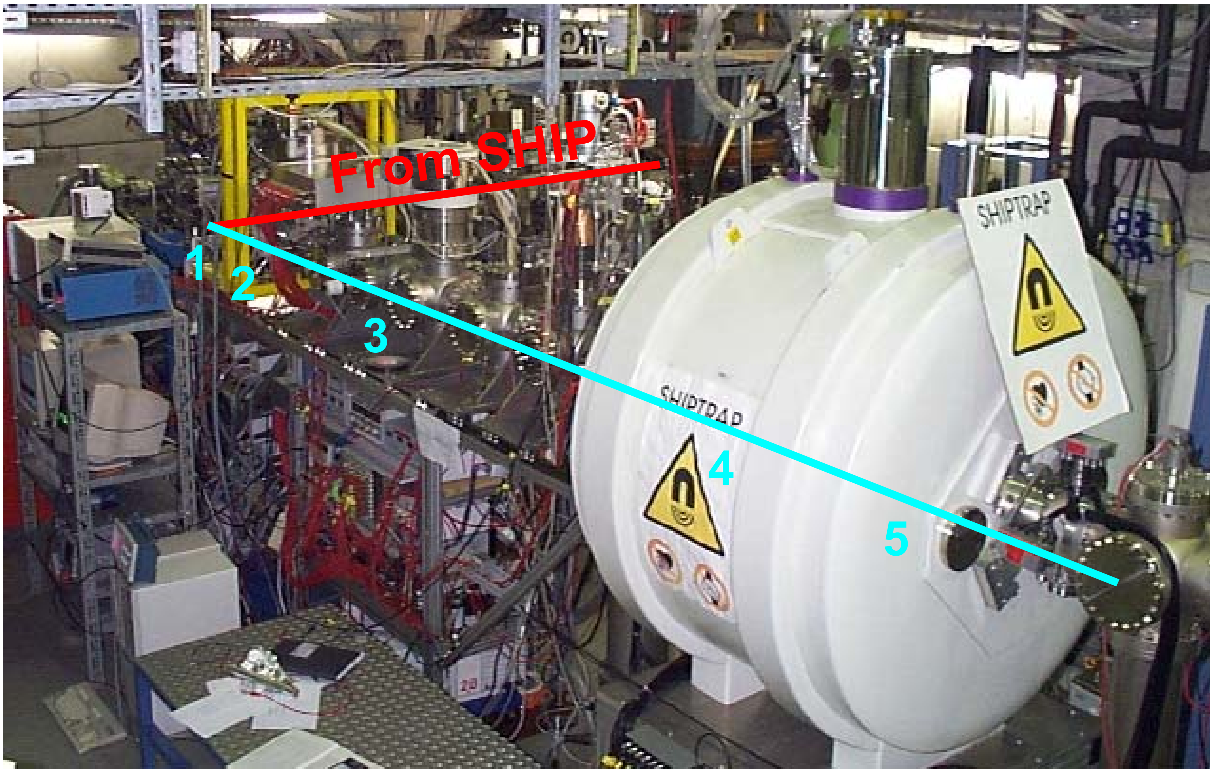
From SHIP
1
2
3
4
5
SHIPTRAP
SHIPTRAP

Figure 1.5
Picture of the SHIPTRAP set-up connected to SHIP with the buffer-gas cell (1), the

extraction RFQ (2), the buncher (3) and the trap system with the purification trap (4) and the measurement trap (5) inside the superconducting magnet. The beam enters the gas cell under an angle of 82.5° relative to the longitudinal axis of SHIPTRAP due to the special geometrical requirements following SHIP.

The He pressure values inside the SHIPTRAP facility decrease from the high-pressure region in the buffer-gas cell with 10 – 200 mbar via the extraction chamber containing the extraction RFQ with 0.01 – 0.2 mbar and the buncher system with 0.001 mbar finally to the low-pressure region in the trap system with 10^{-6} mbar inside the purification trap and 10^{-9} mbar inside the measurement trap [Sik03].

Since the front-end part of SHIPTRAP with the gas cell and the extraction RFQ represents the key issue of the present thesis, it will be presented in more detail in separate chapters. Therefore the following two sections complement the introducing of SHIPTRAP components by discussing the RFQ buncher and the Penning-trap system.

1.2.2.1. The RFQ buncher

The SHIPTRAP buncher consists of a longitudinally-segmented RFQ structure with a total length of 1 m and an aperture of 7.8 mm [Rod03]. Each rod is subdivided into 29 segments and has a radius of 4.5 mm. The rods are kept in position by four ceramic disks as shown on the photograph of Fig. 1.6. The different lengths of the segments depend on the position and function inside the structure, as can be seen in the upper part of Fig. 1.7.

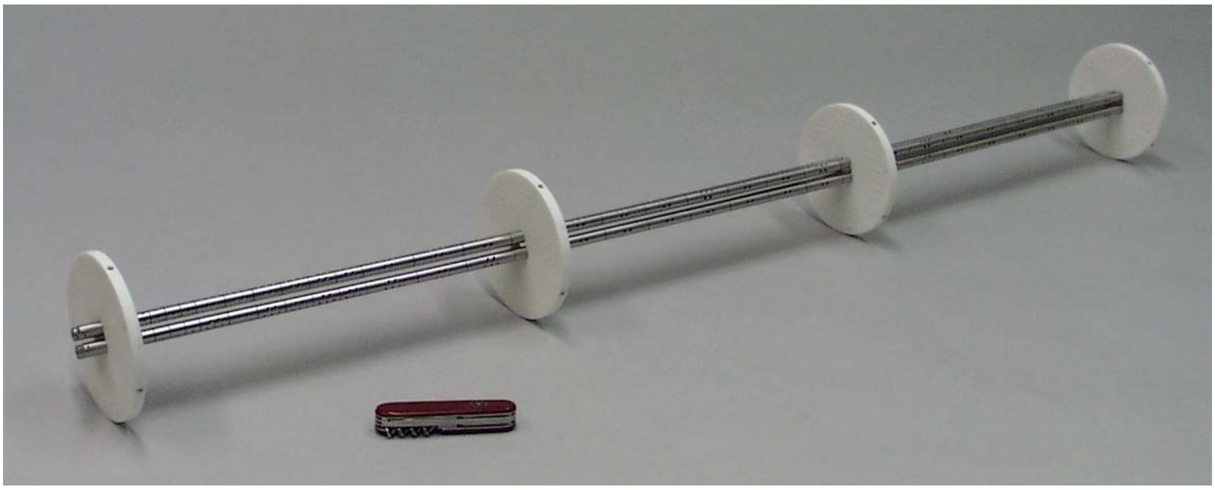

Figure 1.6
Photograph of the SHIPTRAP RFQ buncher. The rods have a diameter of 9 mm and are kept in position (aperture 7.8 mm) by four ceramic disks. The length of each segment (in total 29 per rod) depends on the position and function inside the structure [Rod03].

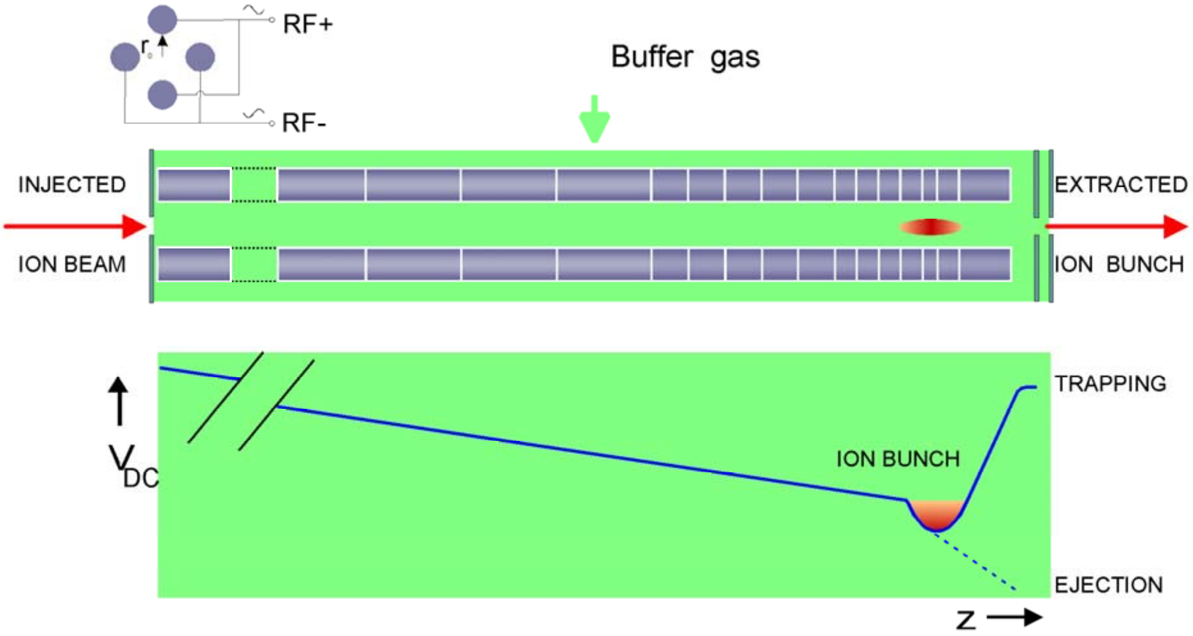

Figure 1.7
The principle of the SHIPTRAP RFQ buncher. The ions extracted from the cell are cooled inside the first part of the RFQ. The RFQ can be operated both in transmission and bunching mode.

The main tasks of the buncher consist of the cooling and the accumulation of the ions for the bunched injection into the first Penning trap. For this purpose the buncher is filled with He buffer gas at a pressure of about 10^{-3} mbar. Since the first part of the RFQ only has to cool the ions, the segmentation of the rods is exclusively used to compensate the longitudinal energy loss in the buffer gas. In order to accumulate the ions a stack of electrodes at the exit part can be supplied with DC potentials creating a potential well, as shown in Figure 1.7. For the creation of the ion bunches the last segments are supplied with a trapping voltage. In the trap well the ions remain in thermal equilibrium with the buffer-gas atoms until the voltage at the last segments is switched down for the extraction of the ion bunches. In the bottom part of Fig. 1.7 the potential gradient applied along the RFQ axis is indicated.

Besides the possibility to operate the RFQ in bunching mode it could also be operated in transmission mode without applying trapping potentials.

The SHIPTRAP RFQ buncher was assembled and tested in the work surrounding the PhD thesis of D. Rodrígues [Rod03]. Typical transport efficiencies of the buncher for argon ions are 95 % when operated in transmission mode and 42 % in bunching mode, respectively.

1.2.2.2. The Penning-trap system

The trap system of SHIPTRAP consists of two cylindrical Penning traps. A picture of the traps with their support structure is shown in the upper part of Figure 1.8, as well as a schematic view of the traps (middle part). The two traps are placed in a distance of 20 cm from each other inside a superconducting magnet with two homogeneous centres of the magnetic field with a flux density of 7 T [Sik03]. The distribution of the magnetic field in the area of the traps is given in the bottom panel of Figure 1.8. The He pressure amounts to 10^{-6} mbar inside the first trap and 10^{-9} mbar inside the second trap. In order to avoid gas flowing from the first into the second trap a diffusion barrier (diaphragm) with a diameter of 3 mm has been installed in-between the two.

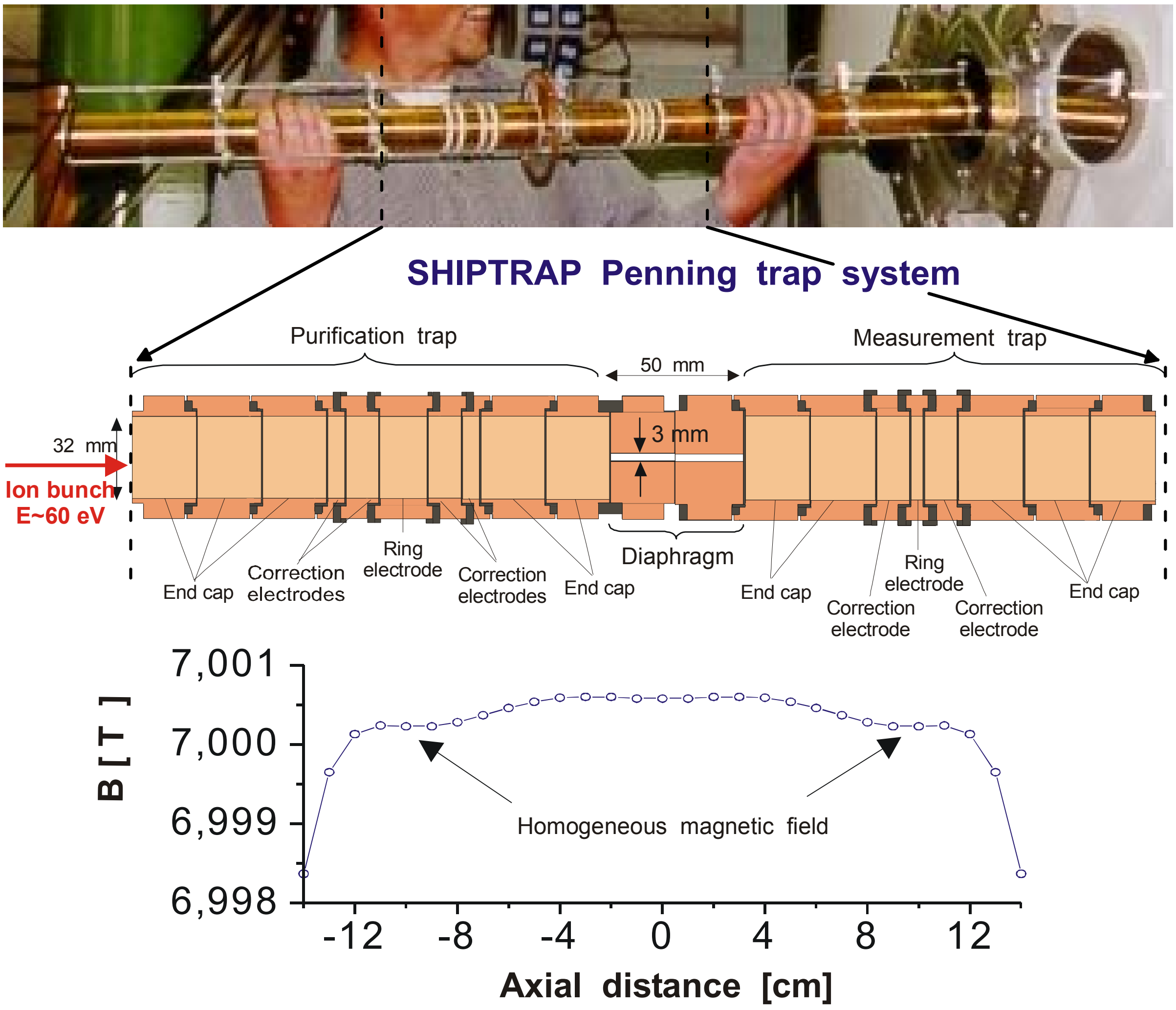
SHIPTRAP Penning trap system
Purification trap
Measurement trap
50 mm
3 mm
32 mm
Ion bunch
E~60 eV
End cap
Correction electrodes
Ring electrode
Correction electrodes
End cap
Diaphragm
End cap
Ring electrode
Correction electrode
Correction electrode
End cap
B [T]
7,001
7,000
6,999
6,998
Homogeneous magnetic field
-12
-8
-4
0
4
8
12
Axial distance [cm]

Figure 1.8
A photograph (upper part) and a schematic view (middle part) of the SHIPTRAP Penning-trap system [Sik03]. Two cylindrical traps are placed at two homogeneous centres of the magnetic field within the superconducting magnet (the field distribution is shown in the bottom panel) with a flux density of 7 T. In order to avoid the buffer gas flowing from the purification trap (left) into the measurement trap a diffusion barrier (diaphragm) is installed between the two and both traps are pumped separately.

The first trap is used for the isobaric purification of the trapped ion bunches. This is done by the mass-selective buffer-gas cooling method using RF fields for the excitation of the ions [Sik03].

Since the cyclotron frequency of singly charged ions in a magnetic field is related to their mass by

$$\omega_c = \frac{e}{m} B \tag{1.1}$$

the mass measurement is based on the precise determination of the cyclotron frequency. This can be achieved by a time-of-flight method, where the ions are extracted from the centre of the precision trap and detected after a given flight path. By applying RF fields inside the measurement trap, kinetic radial energy of the ions can be converted into kinetic axial energy depending on their masses. The time-of-flight of the extracted ions reaches a minimum as a function of the applied RF frequency exactly at $\omega_{RF} = \omega_C$, since at this frequency the conversion of radial kinetic energy into axial kinetic energy has a maximum. In order to determine the minimum of the time-of-flight exactly, several measurements scanning a range of frequencies have to be done. Using this method a typical accuracy of the mass determination of $\delta m/m \approx 10^{-7}$ can be reached.

1.2.3. Physics at SHIPTRAP

SHIPTRAP has been designed to allow for nuclear mass measurements of transuranium isotopes. Presently masses of superheavy ions are determined by the studies of their α-decay chains. However, this method can only be applied for a limited number of isotopes, since it assumes ground-state to ground-state transitions. In addition there are isotopes which decay almost exclusively by spontaneous fission, like all even-even isotopes of Rutherfordium ($Z = 104$). The correlation technique fails, if the α-decay chain ends in daughter isotopes where the decay properties are unknown. For these cases a direct mass measurement as provided by SHIPTRAP is needed.

With the traps also other experiments like studies of nuclear fission and precision nuclear spectroscopy completely free of absorption and backscattering problems caused by the target backing material will become possible.

In addition SHIPTRAP will be used to prepare the ions for other experiments subsequent to the traps. In this context studies on the chemical properties of the produced heavy and superheavy isotopes have to be mentioned in particular. One aim is to compare these properties with homologous elements. In addition the studies can be used for a check of multi-configuration Hartree-Fock-Dirac calculations of the valence-electron configuration. Another point is the measurement of oxidation states that are not accessible by chemical methods [Äys98].

1.2.4. Existing facilities using buffer-gas cells for stopping and extraction of energetic ions

As mentioned in the beginning of this section systems similar to the SHIPTRAP gas cell are actually utilised or are under construction. The principle of the thermalisation of reaction products with energies in the range of MeV in a buffer gas and to extract them from the stopping volume by the use of electrical fields is successfully used at the moment by the groups of G. Savard in Argonne [Sav01] and of M. Wada [Wad03] at RIKEN. Both groups use He as buffer gas and a combination of DC and RF fields inside the gas cell in order to guide the ions towards an extraction nozzle.

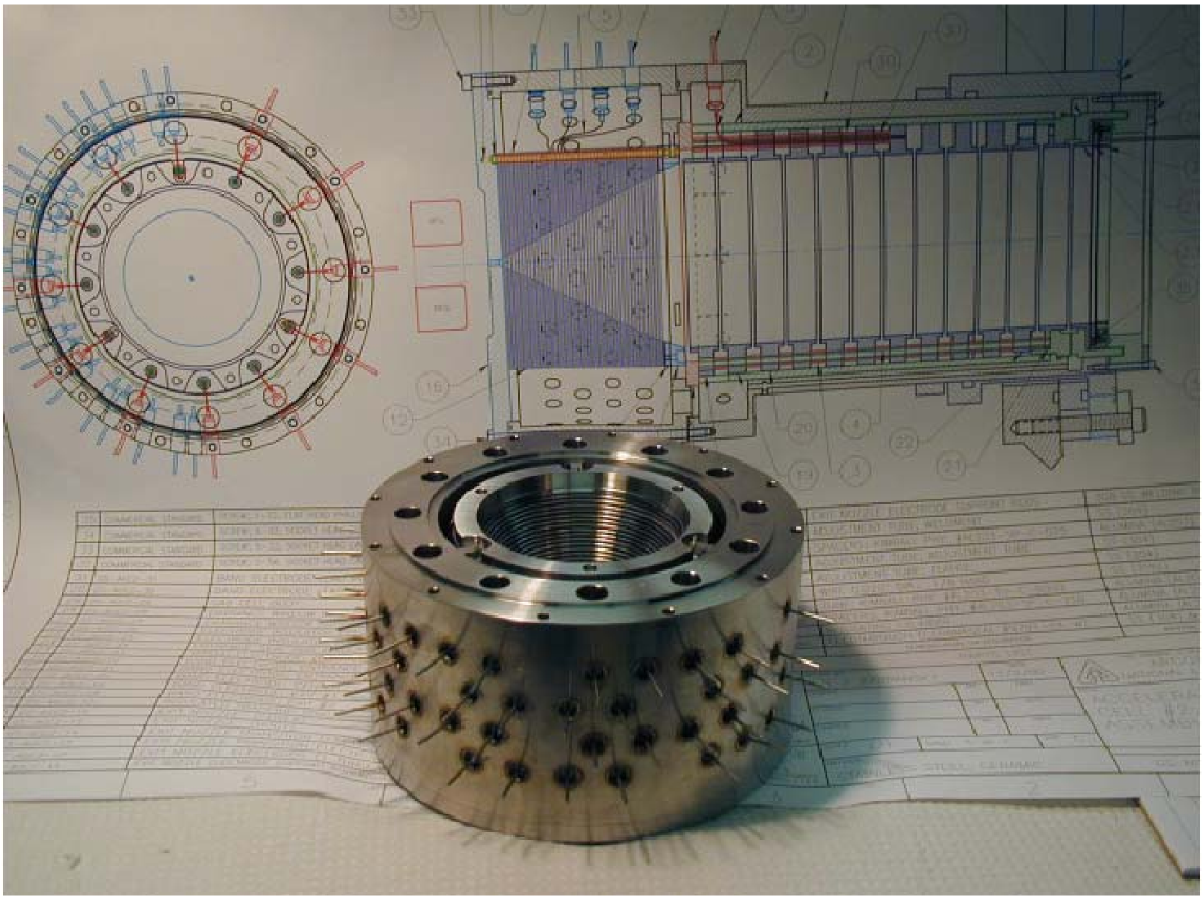

Figure 1.9
Photograph of the extraction part including the RF-funnel structure of the buffer-gas cell presently used in Argonne. In the background a schematic view of the complete cell is visible. The cell is designed for an ion injection along the (longitudinal) extraction axis [Sav01a].

The design of the buffer-gas cell, successfully used for measurements within the CPT at Argonne, is schematically shown on the drawing displayed in the background of Fig. 1.9. It has a total length of around 25 cm at an inside diameter of 7.5 cm and is designed for an ion injection along the extraction axis. The gas cell is operated with helium buffer-gas pressures up to 200 mbar in order to stop ions with energies around 5 MeV/u. At the moment extraction efficiencies up to 45 % at extraction times shorter than 10 ms are reached with this gas cell [Cla03]. In Fig. 1.9 also the extraction region with the RF-funnel structure and the dedicated power feedthroughs is visible. Besides being in use for a nuclear physics program at the ATLAS accelerator facility at Argonne, this gas cell represents the (small) prototype for upcoming buffer-gas cell projects planned to be used at RIA (**R**are **I**sotope **A**ccelerator: US next-generation radioactive ion beam project) [Nol02] and the FRS-ION-CATCHER at GSI [Sav00]. Since the ion energies in those cases will be higher (100 – 1000 MeV/u) than presently at Argonne, the gas cells will have to work at higher pressures (0.5 – 1 bar He) and therefore have a larger size (~25 cm x 125 – 140 cm) in order to consider the larger range straggling during the stopping process. In first test measurements with the buffer-gas cell for the FRS-ION-CATCHER extraction efficiencies between 10 and 40 % were determined [Sav03b].

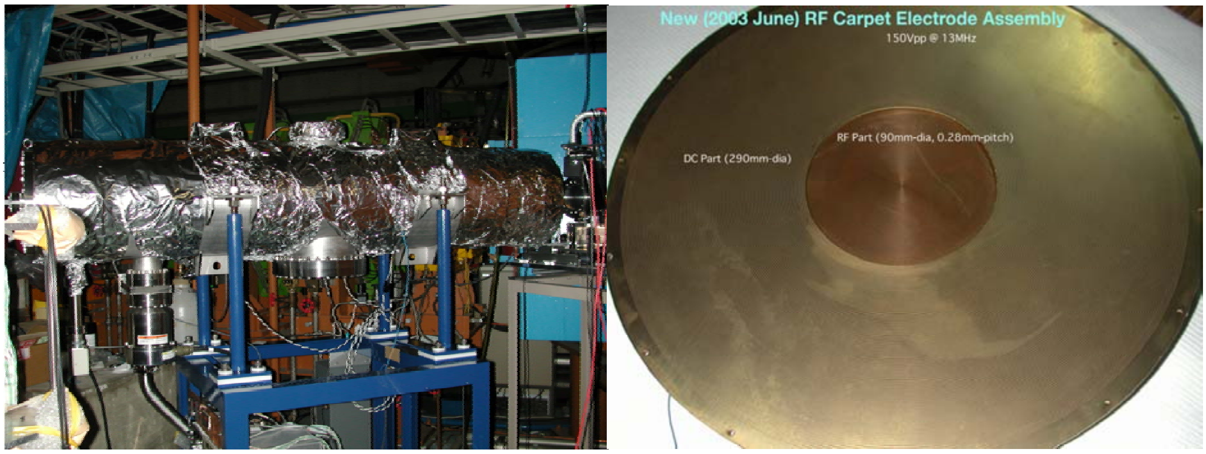
New (2003 June) RF Carpet Electrode Assembly
150Vpp @ 13MHz
RF Part (90mm-dia, 0.28mm-pitch)
DC Part (290mm-dia)

Figure 1.10
Photographs of the buffer-gas cell actually used at RIKEN (left hand side) and the so called RF carpet for the ion extraction (right hand side, see text for details). The buffer-gas cell has a length of 2 m and a diameter of 40 cm [Wad02, Wad03a].

At RIKEN the presently used gas cell has a length of 2 m with a diameter of 40 cm and is shown on the left hand side of Fig. 1.10. The large size was chosen in order to stop ions with an energy in the range of 100 MeV/u in the He buffer gas at pressures around 130 mbar. With its design it is possible to change between a longitudinal and a perpendicular ion injection relative to the extraction axis. Measurements were performed using an RF-funnel structure or the so called RF carpet, shown on the right-hand side of Fig. 1.10 and placed at the extraction side of the gas cell, used in combination with DC electrodes for the extraction of the stopped ions. While the funnel structure is characterised by its conical shape (see Chapter 2), the RF carpet

consists of planar circular electrodes, where the applied RF voltage (alternating by π between adjacent electrodes) creates a repulsive RF force acting perpendicular to the surface. While the RF force prevents the ions from hitting the surface, a DC gradient applied alongside the RF voltage takes care of the ion transport towards the extraction nozzle in the centre of the carpet.
Absolute stopping and extraction efficiencies of 2 – 3 % at intensities of 10^4 – 10^5 incoming ions per second and around 0.1 % at an intensity of 10^7 per second were determined for the gas cell [Wad03a].

For the LEBIT project [Sch03] at MSU a buffer-gas cell with a purely DC-electrode configuration has been designed.
For the stopping of ions with energies around 100 MeV/u He buffer-gas pressures up to 1 bar will be used. The recent design shows a cell with a length of 50 cm and a diameter of 5 cm.

This thesis is organised in 6 chapters. Following the introduction in Chapter 1, where the embedment of this thesis within the SHIPTRAP project was presented, Chapter 2 concentrates on the theoretical background of the behaviour of ions in matter and electric fields. In Chapter 3 the set-up, that has been realised for SHIPTRAP consisting of the buffer-gas stopping cell and the extraction system is presented. Chapter 4 deals with off-line tests of the system, whilst Chapter 5 describes the on-line measurements. The conclusions of the performance and characterisation measurements and an outlook of this work are shown in Chapter 6.

Chapter 2

Behaviour of ions in matter and electric fields

In this Chapter all fundamental mechanisms acting on the ions in the set-up are presented. First the energy loss of ions in matter will be discussed. The second section deals with the behaviour of ions in a buffer gas, while the third section is dedicated to the behaviour of ions in the specific electric-field configurations of the SHIPTRAP set-up.

2.1. Energy loss of ions in matter

As the main task of the gas cell is to thermalise the incoming ions, the energy loss in the entrance window and the buffer gas is of fundamental interest. Besides being slowed down, the ions are also deflected from their incident direction when passing through matter.

The energy loss of non-relativistic ions in matter primarily results from two processes depending on the ion energy. The electronic stopping $S_e(E)$ is caused by inelastic collisions between the passing ions and the electrons in the medium resulting in ionisation and excitation. The second process is the nuclear stopping $S_n(E)$ with elastic collisions between the ion and the atoms of the stopping material. The energy loss of an ion after passing through a certain distance in the medium is given by the total stopping power $S_p(E)$ as the sum of the two energy loss contributions

$$S(E) = \left(\frac{dE}{dx}\right)(E) \qquad (2.1)$$

$$S_p(E) = S_e(E) + S_n(E)\,. \qquad (2.2)$$

Figure 2.1 schematically shows the ratio between electronic and nuclear stopping power. While the nuclear stopping is dominant up to ion energies of some 10 keV/u, the electronic stopping completely dominates the energy loss at higher energies.

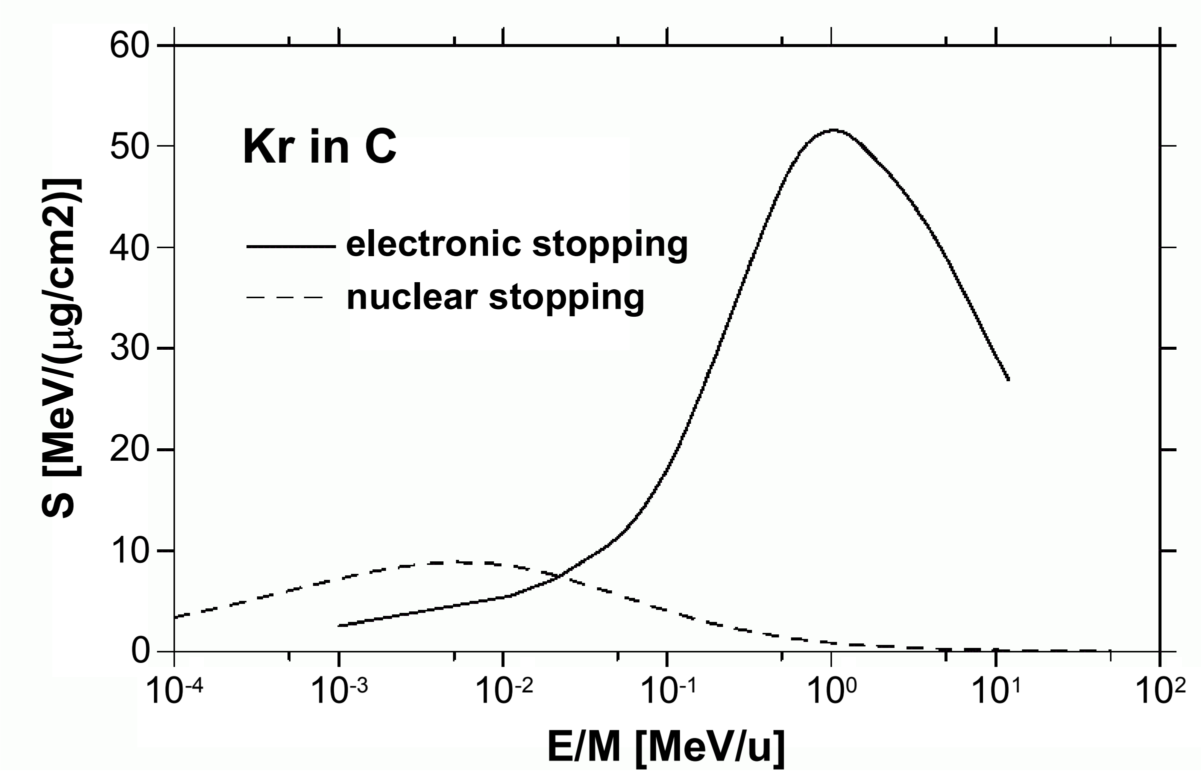

Figure 2.1
The energy dependence of the nuclear and the electronic stopping power for Kr ions stopped in C. While the nuclear stopping is dominant at lower energies up to several 10 keV/u the electric stopping dominates at higher energies.

2.1.1. Nuclear stopping

The nuclear stopping power is caused by elastic scattering of the ions at the nuclear potential of the stopping medium. At small distances the potential is nearly the Coulomb potential $V_{Coul}(r)$ of the nucleus, but with a growing distance more and more bound electrons in the atomic shells shield this potential. Therefore an additional function $\Phi(r)$ describing this shielding is required to solve the equation for the resulting potential $V(r)$, given by

$$V(r) = V_{Coul}(r)\Phi(r) = \frac{Z_p Z_t e^2}{r}\Phi(r) \tag{2.3}$$

with Z_p and Z_t as the nuclear charges of the projectile and target nuclei, respectively, the elementary charge e and the distance r from the target nucleus.

There are different solutions for $\Phi(r)$ given by Bohr [Boh48], Thomas-Fermi [Som32], Molière [Mol47], Lens-Jensen [Len32] and Ziegler-Biersack-Littmark [Zie85]. The last one as the most recent one is given by

$$\Phi(r) = \sum_{i=1}^{4} a_i \exp(-b_i \frac{r}{a_u}) \tag{2.4}$$

with
$$a_u = \frac{0.8854 a_0}{Z_p^{0.23} + Z_t^{0.23}} \tag{2.5}$$

and
$$a_0 = \frac{h^2}{4\pi^2 m_e e^2} \tag{2.6}$$

where m_e is the mass of the electron and the coefficients a_i and b_i are given by

$a_1 = 0.1818$ $a_2 = 0.5099$ $a_3 = 0.2802$ $a_4 = 0.0281$
$b_1 = 3.2$ $b_2 = 0.9423$ $b_3 = 0.4029$ $b_4 = 0.2016$

With this potential the stopping power can be calculated classically as Rutherford scattering, where the differential cross section in the centre-of-mass (*CM*) system is given by

$$\left(\frac{d\sigma}{d\Omega}\right)_{CM} = \left(\frac{Z_p Z_t e^2}{4E_{CM}}\right)^2 \frac{1}{\sin^4(\Theta/2)} \ . \tag{2.7}$$

With the energy E_{trans} transferred from the projectile ion with the incident energy E_p to the scattering partner

$$E_{trans} = \frac{4E_p m_p m_t}{(m_p + m_t)^2} \sin^2(\Theta/2) \tag{2.8}$$

the nuclear energy loss S_n is given by

$$S_n(E_p) = \int_0^{\infty} E_{trans} d\sigma = \frac{8\pi E_p m_p m_t}{(m_p + m_t)^2} \int_0^{b\max} \sin^2(\Theta/2) b db \tag{2.9}$$

where b is the impact parameter and b_{max} is the maximum impact parameter.

Ziegler and Biersack derived the following parameterisation for S_n using the potential from Eq. (2.4)

$$S_n(E_p) = \frac{8.462 \cdot Z_p Z_t S_n^{red}(E_{red})}{(m_p + m_t)(Z_p^{0.23} + Z_t^{0.23})} \frac{eV}{10^{15} atoms/cm^2} \ . \tag{2.10}$$

With the incident ion energy E_p given in keV, the reduced energy E_{red} and the reduced nuclear stopping power S_n^{red} are defined as

$$E_{red} = \frac{32.53 \cdot m_t E_p [\text{keV}]}{Z_p Z_t (m_p + m_t)(Z_p^{0.23} + Z_t^{0.23})} \tag{2.11}$$

where for $E_{red} \leq 30$

$$S_n^{red}(E_{red}) = \frac{\ln(1 + 1.1383 \cdot E_{red})}{2(E_{red} + 0.01321 \cdot E_{red}^{0.21226} + 0.19593 \cdot E_{red}^{0.5})} \qquad (2.12)$$

and for $E_{red} > 30$

$$S_n^{red}(E_{red}) = \frac{\ln(E_{red})}{2E_{red}} \quad . \qquad (2.13)$$

2.1.2. Electronic stopping

In contrast to the nuclear stopping the electronic stopping cannot be calculated classically. The energy loss is mainly caused by inelastic scattering of the projectile ions with the electrons in the stopping medium. The effects contributing to the inelastic energy loss are the excitation of valence and band electrons, the excitation and ionisation of target atoms and the ionisation and electron capture of projectile ions. Thus the stopping power particularly depends on the electronic structure of the target material. There are different analytical approximations for the electronic energy loss .

For high energies Bethe [Bet32] and Bloch [Blo33] derived for the electronic stopping S_e that

$$S_e = 4\pi \frac{Z_p^2 Z_t e^4}{m_e v_p^2} \ln\left(\frac{2m_e v_p^2}{I}\right) \qquad (2.14)$$

with the velocity of the projectile v_p and the mean ionisation potential I.

At low energies Lindhard and Scharff [Lin54] derived the approximation

$$S_e = 4\pi \frac{Z_p^2 Z_t e^4}{m_e v_p^2} c_k \left(\frac{2m_e v_p^2}{I}\right)^{3/2} \qquad (2.15)$$

for the interaction of the projectile ion with a free electron gas. Thereby the free parameter c_k depends only on the target material.

For the intermediate energy region Biersack and Ziegler suggested a harmonic combination of approximations for the high energy and the low energy region, given by

$$S_e = \left(S_{low} + S_{high}\right)^{-1} \qquad (2.16)$$

with

$$S_{low} = c_1 E_p^{c_2} + c_3 E_p^{c_4} \tag{2.17}$$

$$S_{high} = \frac{c_5 n\left(\frac{c_7}{E} + c_8 E\right)}{E^{c_6}}. \tag{2.18}$$

The parameters c_i only depend on the target material.

Moreover, scaling laws can be supplied for the electronic stopping power. As the proton is the ion with the best-known energy loss in matter, the energy loss of other ion species with the same velocity could be calculated by the relation

$$S_e^{ion}(v) = S_e^{proton}(v) q_{eff}^2(v) \tag{2.19}$$

introducing the effective charge q_{eff}.
The effective charge is based on Bohr's assumption [Boh41] that an ion loses all electrons with velocities lower than the ion velocity. The nucleus is then shielded by the remaining electrons depending on the impact parameter b.
The following expression for the effective charge is given by Northcliff [Nor60]

$$q_{eff} = Z_p\left(1 - \exp\left(-\frac{0.92 \cdot v_p}{Z_p^{2/3} v_0}\right)\right) \tag{2.20}$$

where v_0 is the Bohr velocity.
The parameterisation

$$q_{eff} = Z_p\left(\overline{q} + (1-\overline{q})\frac{v_0^2}{2v_f^2}\ln\left(1 + \left(\frac{2\Lambda v_f}{a_0 v_0}\right)^2\right)\right) \tag{2.21}$$

was derived by Ziegler, Biersack and Littmark from experimental and calculated data. v_f is the Fermi velocity of the target medium, the shielding length Λ is given by

$$\Lambda = \frac{2a_0(1-\overline{q})^{2/3}}{Z_p^{1/3}\left(1 - \frac{1-\overline{q}}{7}\right)} \tag{2.22}$$

and the average charge state $\overline{q}$ is given by

$$\bar{q} = 1 - \exp\left(\sum_{i=1}^{4} A_i \left(\frac{\bar{v}}{v_0 Z_p^{2/3}} \right)^{B_i} \right) \tag{2.23}$$

with

$A_1 = 0.803$ $A_2 = 1.3167$ $A_3 = 0.38157$ $A_4 = 0.008983$
$B_1 = 0.3$ $B_2 = 0.6$ $B_3 = 1$ $B_4 = 4$

and $\bar{v}$ as the average projectile velocity relative to the Fermi velocity of the medium.

2.1.3. Stopping range

Amongst the properties of the buffer-gas stopping cell the stopping range and the straggling of the incoming ions in the gas are of primary interest. The average stopping range can be calculated as

$$R = \int_0^E \frac{dE}{S(E)} \tag{2.24}$$

if the total stopping power *S(E)* is known.

Nevertheless calculations for the stopping range using Eq. (2.24) can be wrong by at least a factor of two. For a more accurate estimate of the stopping range, in particular the collisions of the ions with the atoms of the stopping material have to be taken into account. In addition these collisions cause a significant contribution to the angular straggling, which becomes important at low energies. Therefore Monte Carlo-type computer simulations are needed. The widely-used TRIM code by Ziegler et al. [Zie03] offers a full statistical computation of the interactions between the ions and the medium. In this case the mean range projected onto the longitudinal axis as well as the longitudinal and transverse standard deviations are calculated taking into account the angular straggling.

Figure 2.2 shows the results of a TRIM simulation for Ag ions with a total kinetic energy of 23 MeV stopped in 40 mbar helium after passing through a Ti foil of thickness 4 μm (1.8 mg/cm²), corresponding to typical numbers for the buffer-gas pressure and the thickness of the entrance window of the SHIPTRAP gas cell. For this simulation a point-like incident ion beam without divergence and energy spread was assumed. Projected onto the x-axis (longitudinal axis), the mean longitudinal stopping range is given by (174 ± 120) mm. In the radial direction the mean deviation from the axis is (63 ± 49) mm. On the left picture the ions start at the left border along the longitudinal x-axis. The ion trajectories shown lie in the x-y-plane, while on the right-hand picture the trajectories are shown from the transverse view of the y-z-plane.

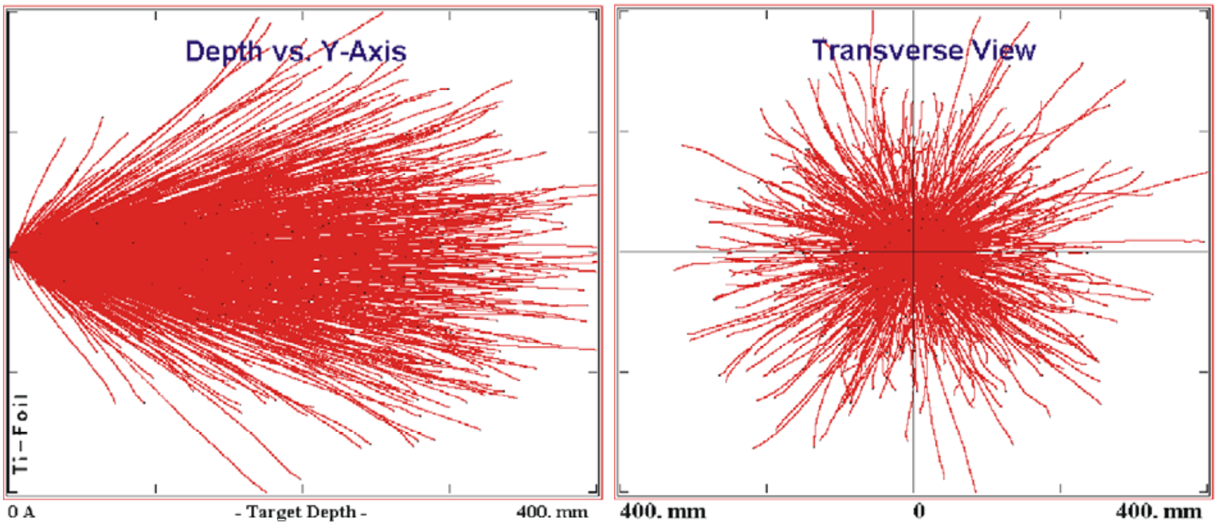

Figure 2.2
TRIM [Zie03] simulation for Ag-ions with a total kinetic energy of 23 MeV, stopped in He after passing through Ti. The left picture shows the calculated ion trajectories for a point-like beam diameter starting at the left border in the x-y-plane with the x-axis as the longitudinal axis. On the right-hand picture the same trajectories are shown in the transverse view of the y-z-plane. The thickness of the Ti of 4 µm (1.8 mg/cm²) and the helium pressure of 40 mbar correspond to typical values for the entrance-window foil and the buffer-gas pressure of the SHIPTRAP gas cell. The calculated mean longitudinal stopping range projected onto the x-axis is (174 ± 120) mm. The result for the radial direction is a mean deviation of (63 ± 49) mm.

Since TRIM calculates the intrinsic range straggling for a sharp ion energy, for a more realistic estimate of the range straggling the energy straggling of the ions to be stopped has also to be taken into account.

2.2. Ions in gas

The buffer gas is the most critical part of the stopping cell as there are some mechanisms leading to a high risk of losing the stopped ions before being able to extract them.

2.2.1. Diffusion

As soon as the ions are stopped in the gas the concentration gradient in the stopping volume disposes them to equilibrate the distribution. This leads to an expansion of the ion cloud. The diffusion follows Fick's law

$$\vec{j} = -D \cdot grad\rho_N \qquad (2.25)$$

with the density-vector of the particle flux $\vec{j}$ oriented along the concentration ρ_N and the diffusion constant D. Together with the continuity equation

$$\frac{\partial \rho_N}{\partial t} + div\vec{j} = \omega\,, \tag{2.26}$$

where ω describes the change in the total number of particles, the diffusion equation is given by

$$\frac{\partial \rho_N}{\partial t} - D\Delta \rho_N = \omega \tag{2.27}$$

where Δ is the Laplace operator.
The diffusion constant can be characterised as

$$D = \frac{1}{3}\bar{v}\bar{l} \tag{2.28}$$

with the mean velocity $\bar{v}$ from the Maxwell-Boltzmann distribution

$$\bar{v} = \sqrt{\frac{8kT}{\pi m_N}} \tag{2.29}$$

and the mean free path length $\bar{l}$ that can be obtained from (2.56).

The expansion of the ion cloud can be counteracted by the application of electric fields inside the gas cell complemented by a fast extraction out of the gas.

2.2.2. Ion loss mechanisms

A special problem for buffer-gas cells is the loss of stopped ions by recombination and molecule formation due to the high amount of ion – electron pairs produced during the stopping process. These processes have been studied in detail by the Leuven group [Kud01].

2.2.2.1. Neutralisation and charge exchange

The mechanism contributing most to the neutralisation of the ions X^+ is the three-body ion-electron recombination

$$X^+ + e^- + He \Rightarrow X^* + He \tag{2.30}$$

$$X^+ + e^- + e^- \Rightarrow X^* + e^- \tag{2.31}$$

which depends strongly on the He gas pressure and the density of electrons. The neutralisation rate depends on the recombination coefficient α and the number of created ion – electron pairs Q. If Q is constant then the charge density n can be expressed as

$$\frac{dn}{dt} = Q - \alpha n^2 \tag{2.32}$$

with the solution

$$n(t) = \sqrt{\frac{Q}{\alpha}} \frac{\exp(2t/\tau) - 1}{\exp(2t/\tau) + 1} \tag{2.33}$$

including the time constant τ

$$\tau = 1/\sqrt{Q\alpha}\ . \tag{2.34}$$

The equilibrium density $n = n_{ion} = n_{electron}$ is given by

$$n = \sqrt{\frac{Q}{\alpha}}\ . \tag{2.35}$$

The dissociative recombination with electrons involves only a two-body interaction, therefore molecular ions can be neutralised very fast following

$$\mathrm{X^+M} + \mathrm{e^-} \Rightarrow \mathrm{X} + \mathrm{M}\ . \tag{2.36}$$

With the electron density n_e the characteristic recombination time can be written as

$$\tau = \frac{1}{\alpha n_e}\ . \tag{2.37}$$

Typical values for recombination coefficients are in the range of ~10^{-7} – 10^{-5} cm^3/s [Kud01] and combined with an assumed electron concentration of ~10^7 cm^{-3} inside the gas cell, characteristic recombination times of 10 – 1000 ms are reached.

During the stopping process in the buffer gas the charge states of the ions to be stopped are reduced by asymmetric electron capture processes between the ions and the He atoms following

$$\mathrm{X}^{\tilde{q}+} + \mathrm{He} \Rightarrow \mathrm{X}^{(\tilde{q}-1)+} + \mathrm{He}^+\ . \tag{2.38}$$

For ions with the charge state $\tilde{q} \geq 2+$ and with energies up to 25 keV/u typical cross sections for the one-electron capture in He are ~10^{-15} – 10^{-17} cm^2 [Ärj87].

For thermalised ions with charge state 1+ and 2+ the charge-exchange reaction with helium is rather unlikely, since the second ionisation potential of only a few elements is higher than the first ionisation potential of the buffer gas. As soon as there are impurities in the buffer gas, the situation changes, as their ionisation potential, typically between 10 and 16 eV, lies between the first and the second ionisation potential of the ions. The corresponding rate coefficients for the charge-exchange reaction

$$\mathrm{X}^{2+} + \mathrm{Y} \Rightarrow \mathrm{X}^{+} + \mathrm{Y}^{+} + \Delta E\,, \tag{2.39}$$

where Y can be an atom or a molecule, are ≤10^{-9} cm^3/s with a maximum of the reaction probability for $2\,\mathrm{eV} \le \Delta E \le 6\,\mathrm{eV}$ [Ärj87].

2.2.2.2. Molecule formation

A main reaction leading to the formation of molecules is an association reaction of a stopped ion X^{+} with a ligand molecule M according to

$$\mathrm{X}^{+} + \mathrm{M} \Leftrightarrow \mathrm{X}^{+}\mathrm{M}^{*}\,. \tag{2.40}$$

The collision complex $\mathrm{X}^{+}\mathrm{M}^{*}$ is not stable and can be dissociated, however, in the presence of the buffer gas (He in the case of SHIPTRAP) it can be stabilised by collisions with the buffer-gas atoms

$$\mathrm{X}^{+}\mathrm{M}^{*} + \mathrm{He} \Rightarrow \mathrm{XM}^{+} + \mathrm{He}\,. \tag{2.41}$$

The time dependence of the number of ions N changing to molecular side bands is given by

$$\frac{dN}{dt} = -kNn_m \tag{2.42}$$

with the reaction rate constant k and the density n_m of ligand molecules. With Eq. (2.34) a reaction time constant

$$\tau = \frac{1}{kn_m} \tag{2.43}$$

can be defined. For a typical rate constant of around $k = 1\cdot 10^{-10}$ cm^3/s [Kud01] and an assumed impurity level of 1 ppm, corresponding to $n_m = 1.35\cdot 10^{12}$ cm^{-3} at a He buffer-gas pressure of 50 mbar (typical value for the SHIPTRAP gas cell), the resulting reaction time becomes 7.4 ms.

The reaction rate constant k depends both on the type of ion and the type of molecule and is tabulated and studied for a multitude of reactants.

Figure 2.3 shows a plot of the mass distribution of ions extracted from the Leuven gas cell following the laser ionisation of Ni atoms [Kud01]. Purified He gas with a water fraction lower than ppb was used for these tests. Even with this small amount of H_2O molecules with Ni ions were formed.

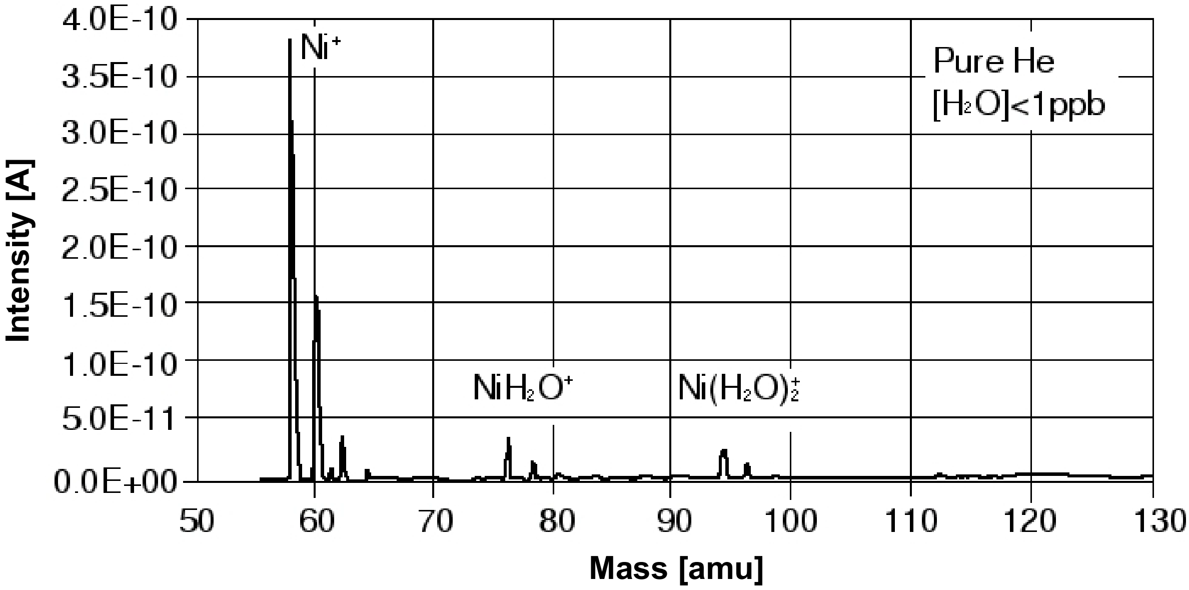

Figure 2.3
Plot of the mass distribution of ions extracted from the Leuven gas cell. The Ni ions were produced via laser ionisation inside the cell. As buffer gas purified He with a fraction of H_2O lower than ppb was used [Kud01].

In further tests at Leuven the gas cell was contaminated in a controlled way in order to investigate the reaction rate constants of different residual gases. Figure 2.4 shows a mass distribution plot for a contamination of the He gas with 0.5 ppm N_2 and 0.045 ppb H_2O (upper part) and a plot with 0.5 ppm O_2 and 0.6 ppb H_2O (bottom part). Comparing the different concentrations with the intensities of the different molecules formed with Ni, the ratio between the reaction-rate constants of H_2O, O_2 and N_2 can be estimated as 2500:2.5:1. Therefore in particular the fraction of water has to be suppressed in order to avoid ion losses due to molecule formation inside the buffer-gas cell.

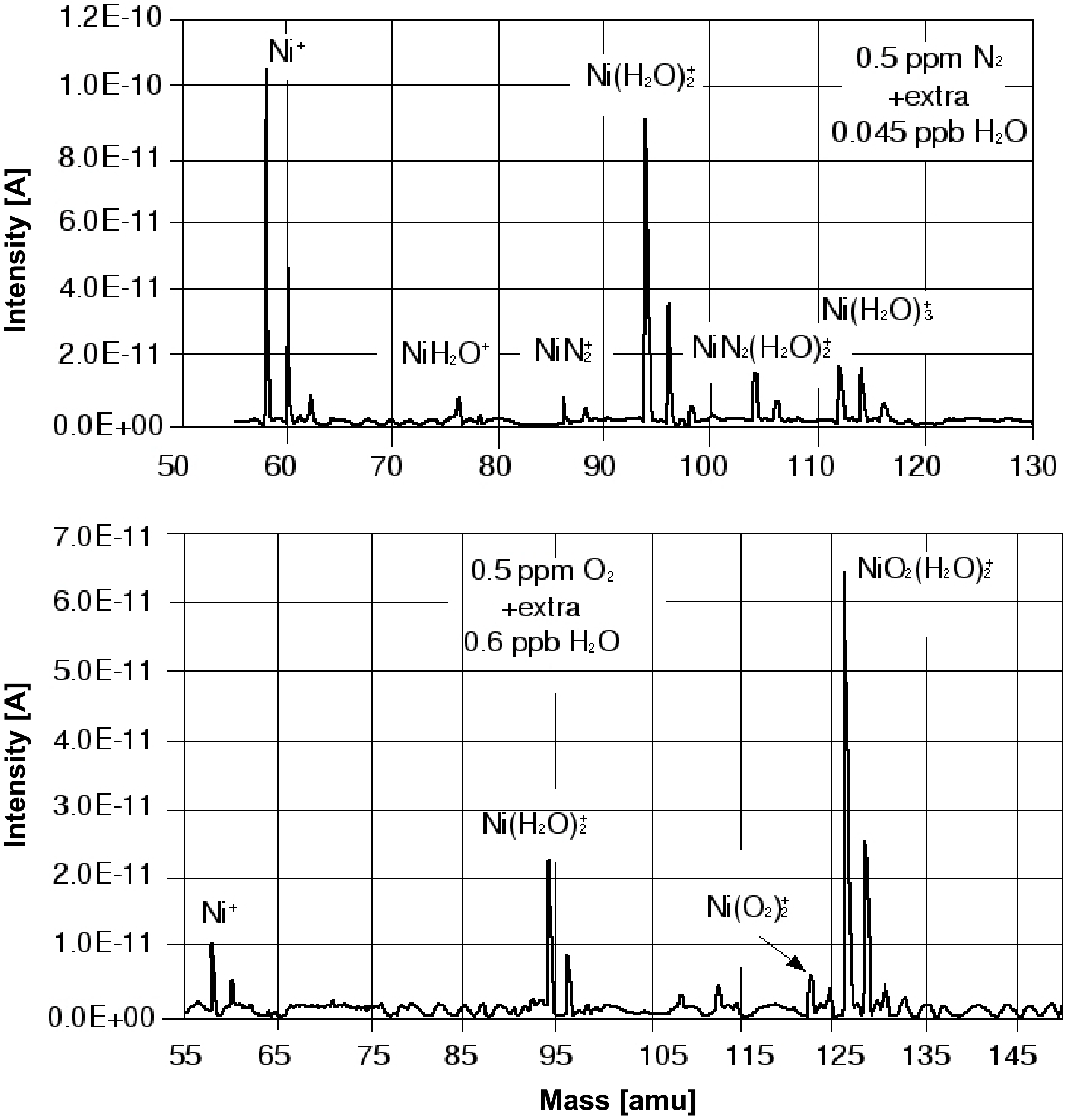

Figure 2.4
Plots of mass distribution for controlled contaminations of the Leuven gas cell based on the situation shown in Fig. 2.3 [Kud01]. Comparing the concentrations of the contaminants the ratios of the reaction rate constants of H_2O, O_2 and N_2 can be estimated as 2500:2.5:1.

2.2.3. Space-charge and plasma effects

Another reason for the large amount of electron-ion pairs created during the stopping process is the effect of free charges, in particular in the case of guiding fields applied inside the cell. The moving positive ions are slower than the electrons attracted by the electrodes, leading to an induced voltage due to the charge separation. This space-charge induced voltage screens the applied electric fields resulting in a reduced dragging force that leads to a reduced velocity of ions and electrons. This effect leads to a higher space charge and to an increase of recombination losses. In order to minimise the recombination effect, minimum field strengths at a given ionisation rate are required. A rough estimate for these fields in He gas at 1 bar [Huy02] is given in Table 2.1, originally calculated for parallel electrode plates. At a given field strength *E* and a distance *d* between the electrodes, the ionisation rate *Q* is calculated for the case that the applied field strength and the space-charge induced field strength are equal.

E [V/cm]	**$d = 1$ cm** **Q [$N_{ion\text{-}e}$/cm^{3}s]**	**$d = 10$ cm** **Q [$N_{ion\text{-}e}$/cm^{3}s]**	**$d = 50$ cm** **Q [$N_{ion\text{-}e}$/cm^{3}s]**
1*	$2.3 \cdot 10^{7}$	$2.3 \cdot 10^{5}$	$9.0 \cdot 10^{3}$
10	$2.3 \cdot 10^{9}$	$2.3 \cdot 10^{7}$	$9.0 \cdot 10^{5}$
50	$5.6 \cdot 10^{10}$	$5.6 \cdot 10^{8}$	$2.3 \cdot 10^{7}$
100	$2.3 \cdot 10^{11}$	$2.3 \cdot 10^{9}$	$9.0 \cdot 10^{7}$
250	$1.4 \cdot 10^{12}$	$1.4 \cdot 10^{10}$	$5.6 \cdot 10^{8}$
500	$5.6 \cdot 10^{12}$	$5.6 \cdot 10^{10}$	$2.3 \cdot 10^{9}$
1000	$2.3 \cdot 10^{13}$	$2.3 \cdot 10^{11}$	$9.0 \cdot 10^{9}$

Table 2.1
Estimated maximum ionisation rate *Q* that should not be exceeded in order to minimise the recombination effect due to space-charge effects for a given field strength. The numbers are calculated for parallel electrode plates placed at a distance *d*. *Q* gives the ionisation rate in He gas at 1 bar for the case that the applied field strength *E* is equal to the field strength induced by the space-charge [Huy02] (* first value scaled).

If the space-charge limit is reached, a weakly-ionised plasma can be formed and in some cases it could even expand over the complete gas cell. Under these conditions the recombination rate is high and the transport efficiency of the cell will decrease rapidly.

Besides recombination also re-ionisation of neutralised reaction products in the plasma via the reactions

$$\mathrm{X} + \mathrm{He}^{*} \Rightarrow \mathrm{X}^{+} + \mathrm{He} + \mathrm{e}^{-} \tag{2.44}$$

$$\mathrm{X} + \mathrm{He}^{+} \Rightarrow \mathrm{X}^{+} + \mathrm{He} \tag{2.45}$$

$$\mathrm{X} + \mathrm{e}^{-} \Rightarrow \mathrm{X}^{+} + \mathrm{e}^{-} + \mathrm{e}^{-} \tag{2.46}$$

can occur, if the concentrations of ionising particles are large enough. At room temperatures the rate coefficients of this ionisation in He are $10^{-10} - 10^{-9}$ cm^3/s [Ärj87].

Space charge and plasma effects are certainly of large importance for gas cells, where the reaction target is placed inside the gas volume [Huy02]. However, also in the case of the SHIPTRAP gas cell with external ion creation these effects have to be taken into account and will be discussed in Chapter 5.

2.3. Ions in electric fields

The conclusion of Section 2.2 is that besides aiming for an optimum purity inside the set-up during operation another requirement to reduce ion losses inside the stopping chamber is to extract the ions as fast as possible. This is also necessary due to the typically short lifetimes of the rare isotopes. Therefore the extraction from the SHIPTRAP gas cell is not only driven by the gas flow, but predominantly by electric DC and RF fields.

Moreover, the application of electric fields is not limited to the cell, as the extraction RFQ is also operated with DC and RF voltages.

2.3.1. Static fields and ion mobility

Due to their charge state ions can be accelerated in electrical fields. In vacuum the resulting force is given by the fundamental equation

$$\vec{F} = \tilde{q}\vec{E} \tag{2.47}$$

where $\tilde{q}$ is the charge state of the ion and $\vec{E}$ is the operating electrostatic field.

In the presence of buffer gas an additional damping force has to be taken into account.

The damping mechanism is caused by two types of interaction of the moving ions with the gas atoms, first a long-range interaction due to atoms polarised by the ions, and second a short-range interaction including collisions between atoms and ions.

In the case of the long-range interaction with induced dipoles the ion is influenced by many atoms at the same time. Provided that

$$E_{ion} \geq kT_{gas} \quad \text{and} \quad m_{ion} >> m_{gas}$$

the multitude of interactions can be averaged by a viscous drag force described by [Lun99, Her01]

$$\vec{F}_{damp} = -\delta m\vec{v} \tag{2.48}$$

with the ion mass m and ion velocity $\vec{v}$ and δ given by

$$\delta = \frac{\tilde{q}}{m}\frac{1}{K} \tag{2.49}$$

where the ion mobility K at a gas pressure P and temperature T is given by

$$K = K_0 \frac{T / T_0}{P / P_0}. \tag{2.50}$$

K_0 is the ion mobility under normal conditions with T_0 = 273 K and P_0 = 1013 mbar. Another term related to δ is the velocity relaxation time

$$\tau_v = \frac{1}{\delta} \tag{2.51}$$

as the solution of the equation

$$\frac{dv}{dt} = -\delta v \tag{2.52}$$

deduced from Eq. (2.48) and considering only the axial motion.

For larger ion drift velocities, where

$$E_{ion} >> kT_{gas}$$

the approach of the viscous damping is no longer appropriate. For this energy region the short-range interaction has to be taken into account. As this interaction is caused by collisions between the ions and the gas atoms, besides the transfer of energy, given by

$$\Delta E_{ion} = -\frac{m_{ion} m_{gas}}{(m_{ion} + m_{gas})^2} E_{ion}\ , \tag{2.53}$$

in particular the number of collisions is related to the damping effect. The number of collisions can be estimated from the collision rate r_c, calculated from

$$r_c = n\sigma v \tag{2.54}$$

with the gas density n, the ion velocity v and the elastic-collision cross section σ given by

$$\sigma = (R_{ion} + R_{gas})^2 \pi \tag{2.55}$$

where R_{ion} and R_{gas} are the radii of the ion and the gas atoms. The number of collisions is also related to the mean free path length of ions

$$\bar{l} = \frac{1}{n\sigma}\ , \tag{2.56}$$

defined as the mean distance between two collisions.
For the damping force due to collisions an ion mobility analogue to the viscous mobility can be defined by [Lun99]

$$K = \frac{1}{\alpha_E}\frac{2\tilde{q}}{m} \tag{2.57}$$

with the energy relaxation time constant α_E given by

$$\alpha_E = -\frac{m_{ion}m_{gas}}{\left(m_{ion}+m_{gas}\right)^2}r_c\ . \tag{2.58}$$

This ion mobility can also be included in Eq. (2.49) and the resulting δ then can be inserted in Eq. (2.48) to get an expression for the damping force due to the ion-atom collisions.

Regarding the SHIPTRAP buffer-gas cell and extraction RFQ there are two different regimes.
In the high-pressure region inside the gas cell the ions are thermalised, therefore the viscous-damping model can be used. For He as buffer gas the ion mobility K_0 of most of the ions is around 20 cm^2/Vs. The most important value influenced by the ion mobility is the extraction time out of the cell. Since the mobility is constant at a fixed gas pressure, the extraction time can only be further affected by the dragging forces of the applied electric fields. As these fields are limited due to the breakdown voltage (Paschen's law [Pas89]) as an upper limit for the applicable voltages there is a lower limit given for the extraction time. The minimum for the breakdown voltage for parallel electrode plates in He is 156 V at 4.0 Torr·cm (5.3 mbar·cm) [Cob58] as the product of the ambient gas pressure and the distance between the electrodes.
In the extraction chamber the gas pressure is much lower than in the gas cell leading to higher ion velocities. The viscous-damping model is no longer applicable and the damping force due to collisions with the atoms of the buffer gas has to be taken into account, therefore Monte-Carlo methods have to be used for calculations.

2.3.2. Radiofrequency structures

In the SHIPTRAP set-up two different types of RF structures are used. The first one is the so-called 'funnel', which is placed inside the gas cell and is used to guide the ions towards the nozzle. In addition the extraction RFQ following the nozzle cools the extracted ions, thus preparing them for injection into the subsequent RFQ-buncher structure.

2.3.2.1. Ions in an RFQ

Radiofrequency quadrupole structures (RFQ) are often used in quadrupole mass spectrometers (QMS) [Daw76] for gas analysis and in recent years they have become more and more important as guiding [Lun99] and accelerating [Kap85] structures for ion beams. As the SHIPTRAP extraction RFQ acts as an ion guide only this aspect will be discussed in an analogue way as the description of the SHIPTRAP RFQ buncher presented in [Rod03].

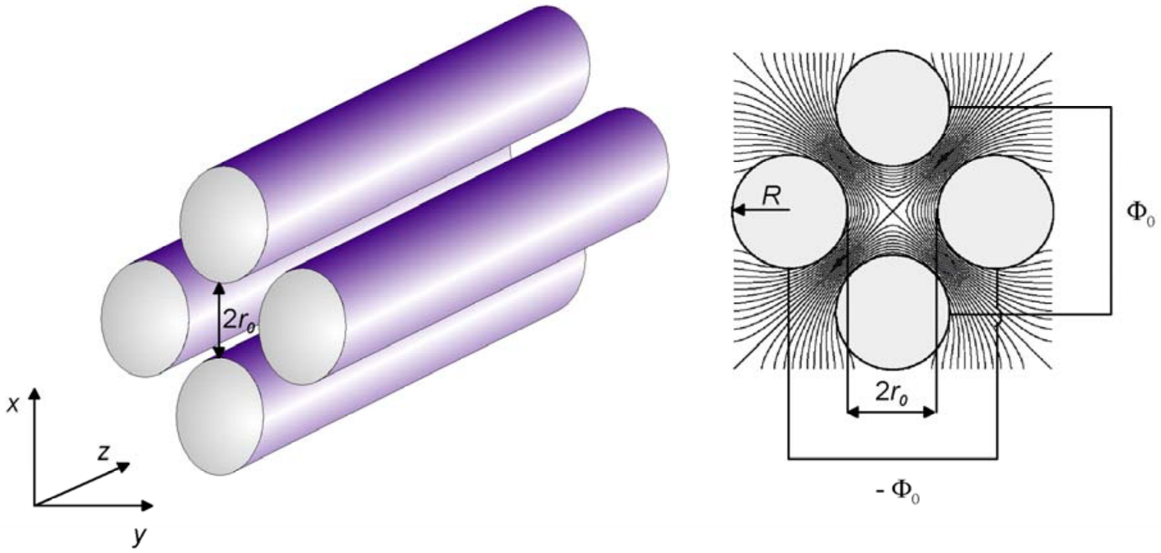

Figure 2.5
Schematic view of an RFQ with 4 cylindrical rods. The ions travel through the RFQ along the z-direction. The picture on the right-hand side shows a front view of the RFQ with the equipotential lines of the electrical fields.

In principle an RFQ consists of four parallel rod electrodes placed in a configuration as shown in Fig. 2.5. The rods can have a hyperbolic shape or, as shown and used more often, a cylindrical shape with a radius *R*. Opposite rods have a minimum distance of $2r_0$ that defines the aperture of the RFQ. An RFQ is operated with RF voltage in order to achieve a confinement of the transmitted ions in the *x*-*y*-plane. Two opposite rods are connected to the same RF potential, while the potentials between the two pairs are shifted by 180°.

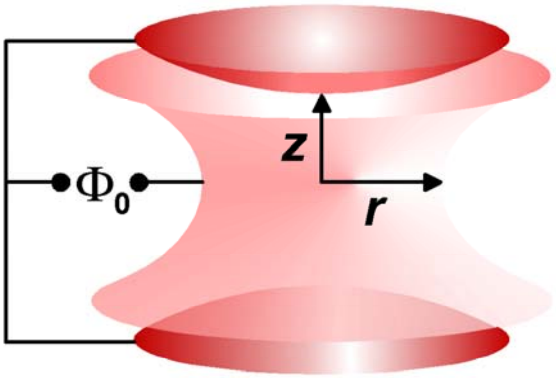

Figure 2.6
Schematic view of a hyperbolic Paul trap. The confining potential is applied between the caps and the ring electrode. Using a static field, where the potential at the ring electrode is

positive, only a radial confinement of positive ions can be achieved. For a confinement in all three dimensions an RF voltage has to be applied. The confinement can also be achieved by a magnetic field directed in the *z*-direction in addition to the static electric fields, as it is realised in the Penning trap [Pen36].

Since an RFQ can be considered as a longitudinal Paul trap, the description of its principle is based on the description of the original hyperbolic Paul trap [Pau53], shown in Fig. 2.6. It consists of three hyperbolically shaped electrodes, where the two cap electrodes have the same potential and the operating voltage is applied between them and the ring electrode.

In general the confinement of ions is achieved by restoring forces restricting the ions to a given position. Regarding a harmonic oscillator in one dimension the ion is affected by the conservative force

$$F_x = -K_x x \tag{2.59}$$

with the constant K_x. Extended to three dimensions the force is

$$\vec{F} = -K_x x\vec{e}_x - K_y y\vec{e}_y - K_z z\vec{e}_z . \tag{2.60}$$

Considering the presence of electric fields with the potential

$$\Phi = \frac{\Phi_0}{2}(\lambda x^2 + \sigma y^2 + \gamma z^2) \tag{2.61}$$

Eq. (2.60) can be written as

$$\vec{F} = -\tilde{q}\Phi_0(\lambda x\vec{e}_x + \sigma y\vec{e}_y + \gamma z\vec{e}_z) \tag{2.62}$$

where $\tilde{q}$ is the charge of the ion.

Without ions being present the electrostatic field has to meet the Laplace equation

$$\Delta\Phi = 0 \tag{2.63}$$

which is fulfilled if

$$\lambda + \sigma + \gamma = 0 . \tag{2.64}$$

For a hyperbolic Paul trap as shown in Figure 2.6 the potential is

$$\Phi = \frac{\Phi_0(r^2 - 2z^2)}{2r_0^2} \tag{2.65}$$

in the case that $\lambda = \sigma = 1$ and $\gamma = -2$ [Daw76].

Using only electrostatic fields allows for a confinement of the ions only in two dimensions. In the case of positive ions in a hyperbolic Paul trap, only a radial confinement can be achieved. To realise a confinement in all three dimensions an RF voltage between the electrodes has to be applied in place or in addition to the static potential.
Another possibility to realise an overall confinement is to use a magnetic field directed in the *z*-direction in addition to the static electric fields, as applied in the case of the Penning trap [Pen36].

For a longitudinal Paul trap consisting of four parallel, hyperbolically shaped rods, the potential is given by

$$\Phi = \frac{\Phi_0 (x^2 - y^2)}{r_0^2}, \tag{2.66}$$

with $\lambda = -\sigma$, $\gamma = 0$ and Φ_0 as the voltage applied between opposite rods. If the rods of the trap are cylindrical the same field can be achieved if

$$\frac{R}{r_0} = 1.14511 \tag{2.67}$$

where *R* is the radius of the rods and r_0 is half of the gap between two opposite rods. The resulting equipotential lines between the rods are shown in Fig. 2.3. With this potential a confinement in two dimensions (*x* and *y*) is achieved by applying an RF field. For the ion confinement in *z*-direction an additional static trap well has to be added. This can be achieved by end caps or by segmented trap rods where the static trap potentials can be applied.

In contrast to the longitudinal Paul trap, in the RFQ used as an ion guide a confinement only in two dimensions (*x* and *y*) is sufficient, so the end caps or the segmentation of the Paul trap can be omitted.

2.3.2.2. Ion motion in an RFQ in vacuum

If RF and DC voltages are combined, the potential for an RFQ is given by

$$\Phi = (U_{DC} + V_{RF} \cos \omega t) \frac{x^2 - y^2}{2r_0^2}, \tag{2.68}$$

with the amplitude U_{DC} of the DC voltage and the amplitude V_{RF} and the frequency ω of the RF voltage.
The resulting equations of motion for an ion with mass *m* and charge $\tilde{q}$ can be

written as

$$\frac{\partial^2 x}{\partial t^2}+\frac{\tilde{q}}{mr_0^2}(U_{DC}+V_{RF}\cos\omega t)x=0 \tag{2.69}$$

$$\frac{\partial^2 y}{\partial t^2}-\frac{\tilde{q}}{mr_0^2}(U_{DC}+V_{RF}\cos\omega t)y=0 \tag{2.70}$$

$$\frac{\partial^2 z}{\partial t^2}=0 \tag{2.71}$$

With the substitution

$$a=\frac{4\tilde{q}U_{DC}}{mr_0^2\omega^2} \tag{2.72}$$

and

$$q=\frac{2\tilde{q}V_{RF}}{mr_0^2\omega^2} \tag{2.73}$$

Eq. (2.69) and Eq. (2.70) can be written as

$$\frac{\partial^2 x}{\partial t^2}+\frac{\omega^2}{4}(a+2q\cos\omega t)x=0 \tag{2.74}$$

$$\frac{\partial^2 y}{\partial t^2}-\frac{\omega^2}{4}(a+2q\cos\omega t)y=0 \tag{2.75}$$

known as the Mathieu equations with the stability parameters *a* and *q*.

With the substitution of *u* for *x* and *y* and with $\zeta=\omega t/2$ the solutions for

$$\frac{d^2 u}{d\zeta^2}\pm(a-2q\cos(2\zeta))u=0 \tag{2.76}$$

are given by

$$u(\zeta)=A\exp(\mu\zeta)\sum_{n=-\infty}^{\infty}C_{2n}\exp(i2n\zeta)+B\exp(-\mu\zeta)\sum_{n=-\infty}^{\infty}C_{2n}\exp(-i2n\zeta) \tag{2.77}$$

with the integration constants *A* and *B* depending on the initial conditions, while the constants C_{2n} and μ depend only on *a* and *q*. Therefore the motion of an ion depends on *a* and *q*.

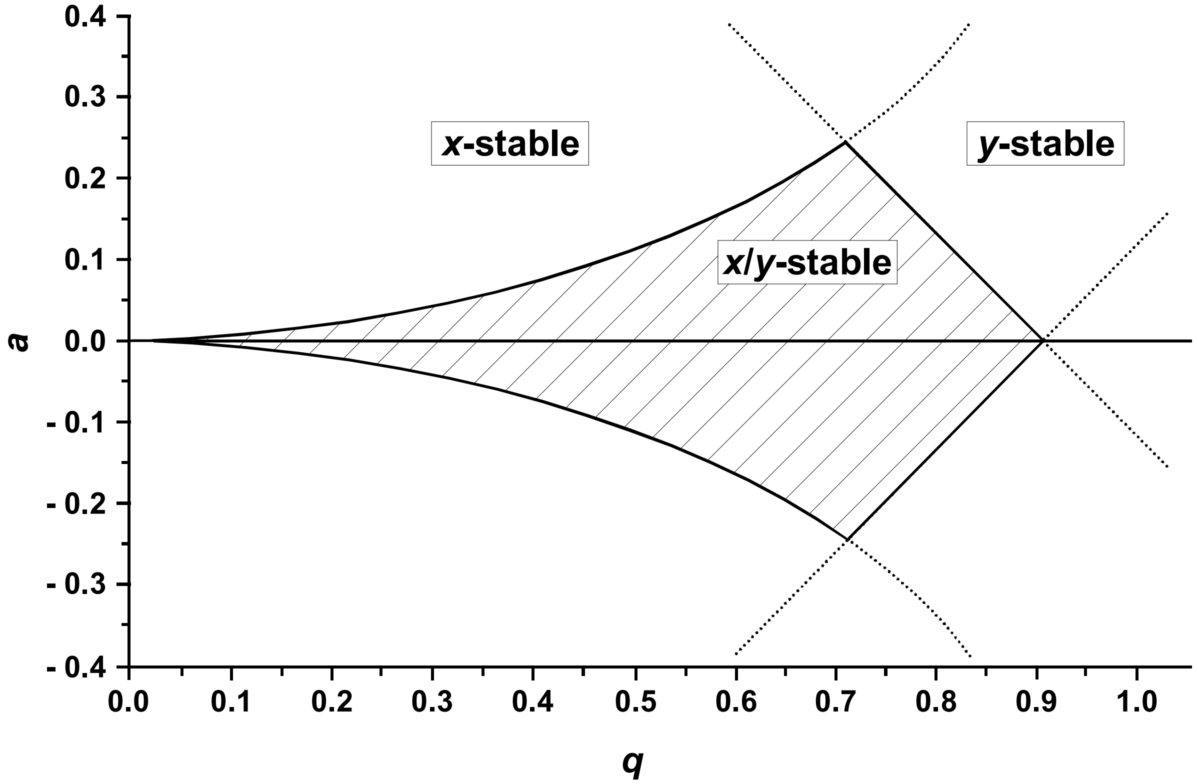

Figure 2.7
The first stability region in the *a*-*q* plot. Only for values of *a* and *q* within the hatched area a stable transmission of the ion through the RFQ is possible. For outside values the trajectories are unstable and the ion gets lost.

As only ions are transmitted if their amplitudes of the oscillating motion remain inside the RFQ structure, stable and unstable solutions of the equations have to be distinguished. The areas of stability or instability in *x* and/or *y*-direction can be plotted in an *a*-*q*-diagram as shown in Figure 2.7. The hatched area represents the first stability region for *x* and *y.*

Since the parameters *a* and *q* depend on the ion mass, an RFQ structure can be used as a mass filter. The operational mode of a QMS is to vary *a* and *q* in such a way, that only the trajectories for the ion mass to be determined are stable. Figure 2.8 shows the first stability region for positive *a*-values with operational conditions for an RFQ. It has to be noticed that if the values for U_{DC}, V_{RF}, r_0 and ω are fixed all ions with the same ratio of $\tilde{q}/m$ have the same operating points in the *a*-*q*-plot. For a fixed charge state the operating points of all ions lie on a line through the origin in the *a*-*q*-plot, the so-called mass-scan line [Daw76]. The position of this line within the *a*-*q*-plane provides information about the transmission through and the resolution of the QMS. Without any overlap with the stability region no ion is transmitted as all trajectories are unstable. If the line is tangent to the peak of the stability region (as for line (1) in Figure 2.8) only an ion with a specific ratio $\tilde{q}/m$ is transmitted with a resolution of $m/\Delta m = \infty$. For the case $a = 0$, when the line has a zero slope, all ions with $q \leq 0.908$ have stable trajectories and are transmitted. In this case the resolution $m/\Delta m$ is zero. All lines between the two extremes allow for the transmission of ions in a range of $\tilde{q}/m$ values between the limiting q-values q(low) and q(high) (line (2) in Fig. 2.8 as an example).

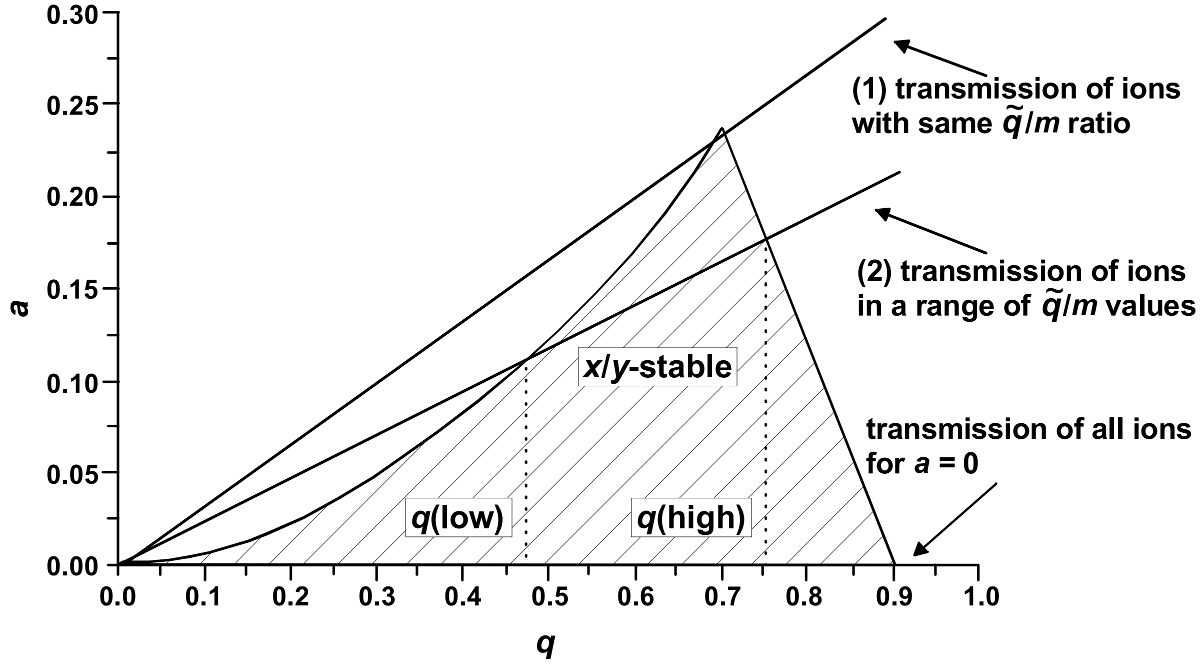

Figure 2.8
The first stability range (hatched area) with the operating points of an RFQ used as a mass filter.

From a more general point of view the ion trajectories resulting from the stable solutions of the Mathieu equations can be seen as the superposition of two oscillations. While the so-called micro-motion of the ions is influenced directly by the applied RF frequency ω_{RF}, the macro-motion or secular motion can be explained by the influence of a pseudopotential. Compared with the micro-motion the frequency of the macro-motion is lower and can be described by

$$\omega_{\sec} \cong \frac{1}{2} \omega_{RF} \beta \tag{2.78}$$

in the case that the RFQ is operated with low values of q and a. The stability parameter β depends on a and q and can be approximated by [Car72]

$$\beta = \left(a - \frac{(a-1)q^2}{2(a-1)^2 - q^2} - \frac{(5a+7)q^4}{32(a-1)^3(a-4)} - \frac{(9a^2+58a+29)q^6}{64(a-1)^5(a-4)(a-9)} \right)^{1/2} \tag{2.79}$$

or, for the underlying assumption of $|q| << 1$ and $|a| \cong 0$

$$\beta = \sqrt{a + \frac{q^2}{2}} \quad . \tag{2.80}$$

The pseudopotential model [Daw76] is commonly used in the case of RF structures. Assuming that the structure is used in RF-only mode, where $a = 0$, and that the micro-motional amplitude can be neglected in comparison to the amplitude of the macro-motion, the Mathieu equations can be written as

$$\frac{d^2u}{dt^2} \pm \frac{\omega^2 q}{2} \cos(\omega t) u = 0 \tag{2.81}$$

with the substitution $u = x, y$.
As the amplitude u of the ion motion is the sum of the amplitudes of macro- and micro-motion

$$u = u_{mic} + u_{\sec} \tag{2.82}$$

Eq. (2.81) results in

$$u_{mic} = -\frac{q u_{\sec}}{2} \cos(\omega t) \tag{2.83}$$

if it is provided that

$$u_{mic} << u_{\sec} \text{ and } \frac{du_{mic}}{dt} >> \frac{du_{\sec}}{dt}$$

for a given time interval. With Eq. (2.83) the amplitude u is given by

$$u = u_{\sec} - \frac{q u_{\sec}}{2} \cos(\omega t) \tag{2.84}$$

and can be included in Eq. (2.81), resulting in

$$\frac{d^2u}{dt^2} = \mp \frac{q u_{\sec}}{2} \omega^2 \cos(\omega t) \pm \frac{q^2 u_{\sec}}{4} \omega^2 \cos^2(\omega t) . \tag{2.85}$$

Since d^2u_{mic}/dt^2, the acceleration due to the RF, is equal to zero when averaged over an RF period, the macro-motion averaged over the same period can be written as

$$\left\langle \frac{d^2 u_{\sec}}{dt^2} \right\rangle_{av} = \frac{\omega}{2\pi} \int_0^{2\pi/\omega} \frac{d^2 u}{dt^2} dt \tag{2.86}$$

with the solution

$$\frac{d^2 u_{\sec}}{dt^2} = \pm \frac{q^2 \omega^2}{8} u_{\sec} \tag{2.87}$$

corresponding to a harmonic motion of u_{sec}.
The harmonic pseudopotential now can be derived using the equation of motion of an ion in an electric field

$$m \frac{d^2 u_{\sec}}{dt^2} = m \frac{q^2 \omega^2}{8} u_{\sec} = -\tilde{q} \frac{d\Phi}{du_{\sec}} \tag{2.88}$$

resulting in

$$\Phi = -\frac{qV}{8 r_0^2} r^2 \tag{2.89}$$

for the motion in the direction of *r*. For Eq. (2.88) the effective electric field E_{eff} is given by

$$E_{eff} = \frac{qV}{4 r_0^2} r = \frac{\tilde{q} V^2}{2 m \omega^2 r_0^3} \left(\frac{r}{r_0} \right) \tag{2.90}$$

It should be noted that the effective field does not provide any information on the stability of the ion trajectory.

2.3.2.3. Ions in a gas-filled RFQ

In Sect. 2.3.2.2. the ion motion inside an RFQ in vacuum has been explained. Since the RFQ structures used at SHIPTRAP are filled with He gas, the damping of the gas has to be considered. Including Eq. (2.48) and (2.49) into the equation of motion and with the substitution

$$p = \frac{\tilde{q}}{m K \omega} \tag{2.91}$$

equation (2.76) can be transformed into

$$\frac{d^2 u}{d\zeta^2} + 2p \frac{du}{d\zeta} \pm (a - 2q \cos(2\zeta)) u = 0 \tag{2.92}$$

with the Mathieu equation as border line case in the absence of damping.
There are different methods for solving this equation, like the one by Hasegawa and Uehara [Has95]. The result for the ion trajectories in a quadrupole field in the presence of the gas damping is given by an enlargement and a shift of the stability region in the *a*-*q*-plane.

Using the pseudopotential model the damping force Eq. (2.48) included in Eq. (2.91) results in

$$\frac{d^2u}{dt^2}+\delta\frac{du}{dt}\pm\frac{\omega^2 q}{2}\cos(\omega t)u=0\,. \qquad (2.93)$$

With the same formalism as used in Eq. (2.81) – (2.90) and with

$$u_{mic}=-\frac{q\omega^2}{2(\delta^2+\omega^2)}\left(\frac{\delta}{\omega}\sin(\omega t)+\cos(\omega t)\right)u_{\sec} \qquad (2.94)$$

the pseudopotential considering the damping by the gas is given by

$$\Phi=-\frac{qV\omega^2}{8r_0^2(\delta^2+\omega^2)}r^2 \qquad (2.95)$$

with the effective field

$$E_{eff}=\frac{qV\omega^2}{4r_0^2(\delta^2+\omega^2)}r=\frac{\tilde{q}V^2}{2mr_0^3(\delta^2+\omega^2)}\left(\frac{r}{r_0}\right). \qquad (2.96)$$

In the extreme case of an quadrupole operated in vacuum where δ is equal to zero, Eq. (2.96) agrees with Eq. (2.91).
Since δ is related to the velocity relaxation time τ_v (given in Eq. (2.51)), the effective field can also be written as

$$E_{eff}=\frac{\tilde{q}V^2\tau_v^2}{2mr_0^3(1+\omega^2\tau_v^2)}\left(\frac{r}{r_0}\right). \qquad (2.97)$$

Inside the RFQ structures of SHIPTRAP the damping forces of the gas are used for the buffer-gas cooling technique [Maj68]. Cooling of ions is thereby related to the reduction of the phase space by the loss of kinetic energy during the interactions with the gas atoms. As the damping forces act on both the motion in longitudinal and in transversal direction, the ions can be cooled down to the thermal equilibrium with the gas. This is important in case the ions have to be stored, but as soon as the RFQ structure is used to transport the ions electric guiding fields in longitudinal direction have to be applied.

2.3.2.4. Ions in the funnel

The funnel system represents another type of RF ion guide. Basically it consists of a stack of ring electrode plates, where the applied RF voltage alternates by π between adjacent plates. The device is named by the shape created by the varying inner diameters of the rings.

The principle of the funnel is based on the RF gradient field near the electrodes. Due to this field ions experience an effective field E_{eff} resulting in a repulsive force driving them away from the electrodes. In order to avoid undirected reflection of the ions at the repulsive field, buffer gas is used to damp the ion motion. Since the ions have to be guided towards the constricted opening of the funnel, a DC gradient is applied additionally.

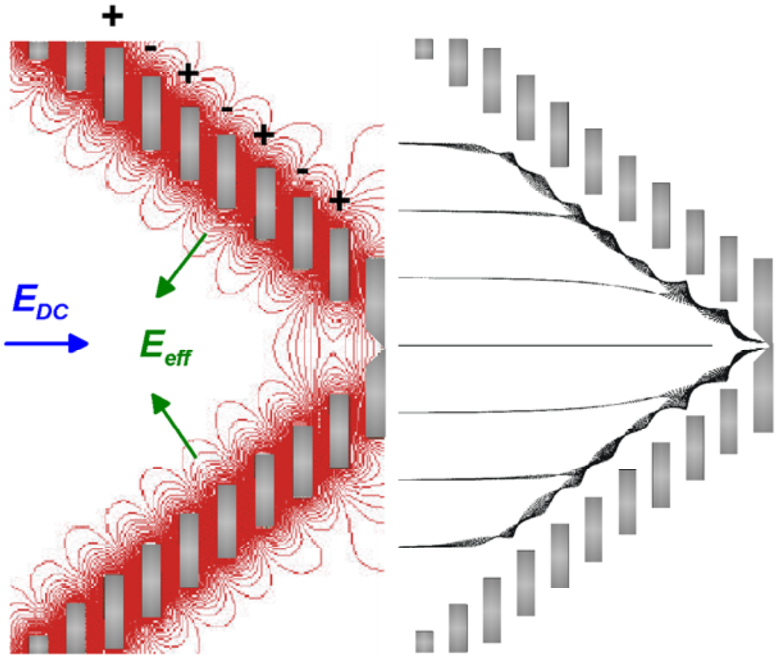

Figure 2.9
Left: electric field for a funnel structure with RF equipotential lines indicated. Right: simulation for the ion motion in a gas-filled RF funnel. Both DC and RF fields are applied at the electrodes to combine the repulsive RF force that helps to avoid the ions hitting the electrodes with the dragging force due to the DC gradient.

Figure 2.9 on the left-hand side shows the direction of the forces acting on an ion due to the DC gradient (E_{DC}) and the RF voltage applied at the electrodes (E_{eff}). On the right-hand side a simulation for the ion motion in a gas-filled RF funnel is shown.
Wada [Wad03] assumes that the resulting RF field near the electrodes can be described as a quadrupole field. With d_0 as the half-distance between the centre-lines

of adjacent electrodes (shown in Figure 2.5) and the RF voltage *V,* the effective field E_{eff} due to the RF potential is given by

$$E_{eff} = \frac{\tilde{q} V^2 \tau_v^2}{2 m d_0^3 (1 + \omega^2 \tau_v^2)} \left(\frac{r}{d_0} \right) \tag{2.98}$$

In the high-pressure region, where the velocity relaxation time is much shorter than the period of the RF

$$\omega^2 \tau_v^2 << 1$$

the effective field can be written as

$$E_{eff} = \frac{\tilde{q} V^2 \tau_v^2}{2 m d_0^3} \left(\frac{r}{d_0} \right) \tag{2.99}$$

and with the definition of τ_v (Eq. (2.51), (2.49))

$$E_{eff} = \frac{m V^2 K^2}{2 \tilde{q} d_0^3} \left(\frac{r}{d_0} \right) \tag{2.100}$$

which is independent from the RF frequency but directly dependent on the ion mass, resulting in a more efficient transport of heavier ions.

Since the RF amplitudes are limited by the breakthrough voltage in the buffer gas, a way to optimise the effective force is to minimise the distances between the electrodes. Another possibility to affect the efficiency of the repulsive force is given by the choice of the aperture angle of the funnel structure, since the direction of the repulsion is perpendicular to the funnel surface. Therefore the larger the angle the more the repulsive force has to counteract the dragging force of the applied DC ramp.

With regard to the funnel structure used inside the SHIPTRAP buffer-gas cell, the optimisation of the funnel parameters is tied to boundary conditions. In the case of the dimensions of the funnel the perpendicular injection of the ions with respect to the cell symmetry axis as well as the size of the stopped ion cloud has to be taken into account. Therefore a steeper opening angle of the funnel structure had to be chosen compared to the optimum solution in the case of longitudinal ion injection. The thickness of the electrodes and with it the distances between them are a compromise between the efficiency of the repulsive forces, the mechanical stability of the used UHV-compatible materials and a manageable number of electrodes, since all have to be individually electrically connected in order to create a smooth DC ramp.

Chapter 3

The experimental set-up

In this chapter the technical design of the SHIPTRAP buffer-gas cell and the extraction-RFQ will be described.

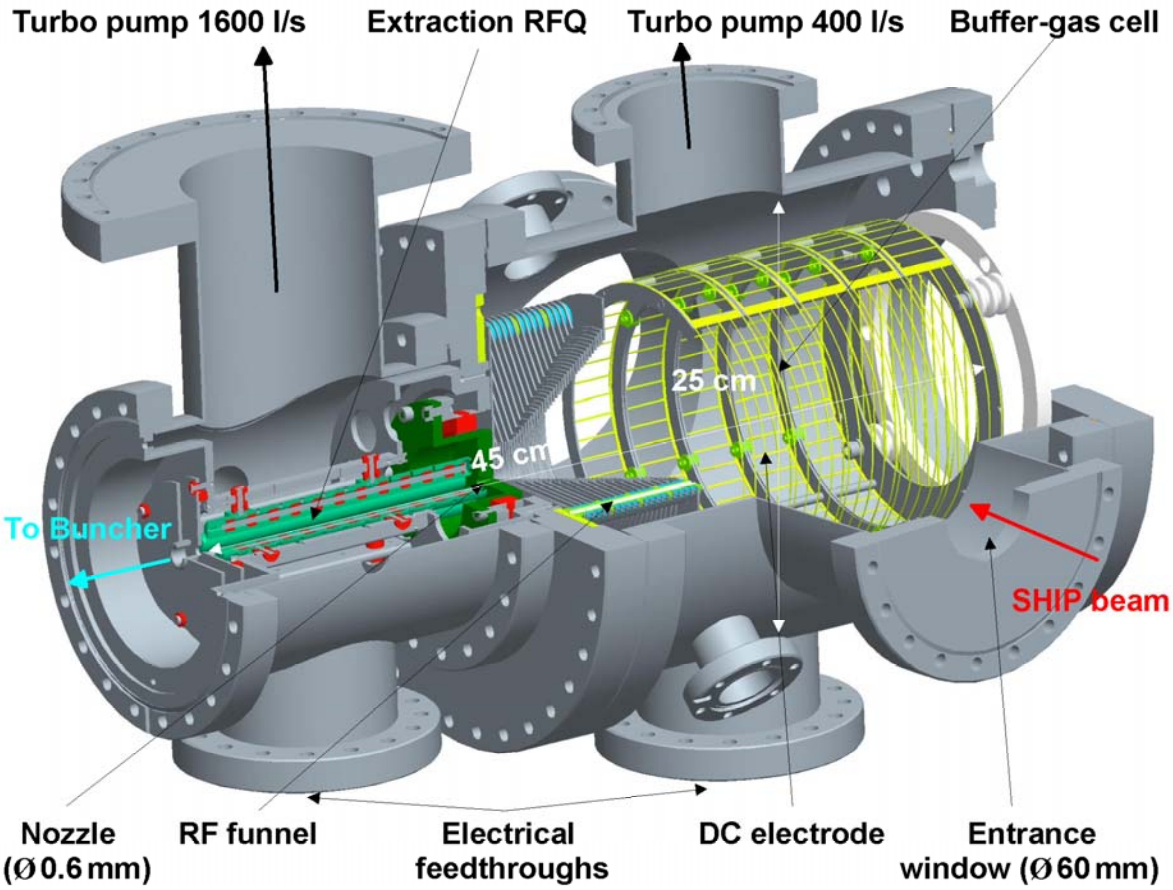
Turbo pump 1600 l/s
Extraction RFQ
Turbo pump 400 l/s
Buffer-gas cell
25 cm
45 cm
To Buncher
SHIP beam
Nozzle (Ø0.6 mm)
RF funnel
Electrical feedthroughs
DC electrode
Entrance window (Ø60 mm)

Figure 3.1
Schematic view of the SHIPTRAP buffer-gas cell and extraction RFQ. Visible are the electrode system inside the cell, the entrance window, the extraction nozzle and the extraction chamber with the segmented RFQ.

3.1. Overview

A schematic view of the stopping and extraction system is given in Figure 3.1. After passing through the entrance window the ions are thermalised inside the stopping chamber. An electrode system generating DC and RF fields inside the chamber guides the ions towards the extraction nozzle. Here the ions are transported into the extraction chamber via the gas flow. The extraction RFQ following the nozzle is used for separating the ions from the neutral gas and for cooling the ions transversely for the transfer into the RFQ buncher (see Sect.1.2).

3.2. Design requirements

The design of the set-up is based on requirements given by the beam properties delivered from SHIP and by the properties of the specific transuranium reaction products intended to be studied. The need of a fast and efficient extraction of the ions towards the RFQ buncher following the gas cell is the key design goal. Additional technical boundary conditions are set by the maximum available pumping speed for the buffer gas. The design as discussed in this section already incorporates the experiences from a first-generation prototype [Eng01].

Table 3.1 shows a list of exemplary transuranium fusion products planned to be investigated with SHIPTRAP [Dil01]. Based on these numbers the cell is designed to be able to stop heavy ions at energies between 10 keV/u and 500 keV/u in helium. The gas pressure inside the cell is limited by the achievable pumping speed in the extraction chamber, resulting in a usable helium buffer-gas pressure range up to 200 mbar.

Nuclide	$T_{1/2}$	Energy	Cross section	Ions at SHIPTRAP
^{245}Cf	43.6 m	~17 keV/u	370 nb	0.05/s
^{250}Md	52 s	~150 keV/u	10 nb	0.001/s
^{262}Db	34 s	~240 keV/u	20 nb	0.002/s
^{264}Bh	740 ms	~240 keV/u	100 pb	0.00001/s

Table 3.1
List of exemplary transuranium fusion products to be stopped in the SHIPTRAP buffer-gas cell. Listed are the isotopes and the values for their half-life, the recoil energy, the production cross section measured at SHIP and the expected number of ions at SHIPTRAP.

Moreover, optimum purity of the whole set-up is decisive as any impurities can drastically worsen the extraction efficiency by the formation of molecules and recombination and by limiting the electrical guiding field strengths. Thus UHV conditions ($<10^{-9}$ mbar) and low outgassing rates have to be achieved by effective pumping, baking and the usage of only metallic and ceramic components. During operation additionally the purity of the used buffer gas is very important.

Another requirement is given by the SHIP beam dimensions of at least 50 x 30 mm² that have to be accepted by the cell. This leads to a diameter of the entrance window of 60 mm. Together with the need to be able to accept reaction products with rather low recoil velocities, very thin (pinhole-free) entrance foils have to be used, which in addition have to be bakeable due to the ultra-high purity requirements in the gas cell. The entrance foil represents a major technical challenge in the gas cell set-up that will be discussed in Section 3.3.2.

3.3. The buffer-gas cell

The two tasks of the SHIPTRAP buffer-gas cell are the stopping of the ions and the ion transport towards the extraction nozzle. The gas cell consists of the vacuum chamber itself, the entrance window, the electrode system and the gas-supply system.

3.3.1. The vacuum chamber

The design and the dimensions of the vacuum chamber are based on the requirements given in Sect. 3.2. Simulations with the code TRIM [Zie03] were used to get a first approximation of stopping ranges and the range straggling in longitudinal and radial direction for different settings of ion energy, He pressure as well as entrance window material and thickness.

As shown in Figure 3.1 the chamber is based on a tube with a diameter of 250 mm and a total length of 320 mm with flanges for different purposes (pumping, electrical feedthroughs, vacuum diagnostics, bypass) connected to the tube. All parts are made of stainless steel and silver-plated CF-sealings are used to guarantee the tightness to reach UHV conditions.
The entrance window is mounted on the end flange of a DN150 tube that acts as an angular adapter between the gas cell and the SHIP beam line, which enclose an angle of 82.5°. Thus the final distance between the entrance window and the longitudinal axis of the gas cell amounts to 195 mm.

3.3.2. The entrance window

The entrance window (not shown in Fig. 3.1) has to separate the gas inside the cell from the beam-line vacuum with optimum transmission of the incoming ions. In addition the window material acts as an energy degrader for the ions, since the stopping power of the gas at the achievable pressures is not sufficient for most of the recoil energies. Regarding the highest possible purity of the set-up only metallic window foils and sealings can be used, since the complete set-up has to be baked to about 180 °C to reach UHV conditions. The window thickness is given on the one hand by the recoil velocity of the ions that have to be transmitted. For the typically low-energy fusion products to be expected at SHIPTRAP this leads to the requirement of the lowest thickness achievable for metallic foils (typically Ti, Ni) in pinhole-free quality, typically a few µm. On the other hand the foil has to sustain the gas pressure in the cell of up to about 200 mbar, which together with the large diameter of 60 mm leads to the requirement of a high-transmission supporting grid.

The window foil for the SHIPTRAP gas cell is mounted in the centre of a DN63-CF flange (Fig. 3.2). The flange carries also a supporting grid with 7 ligaments in *x* and *y*-direction to relieve the foil from the pressure forces. The ligaments have a thickness of 0.4 mm resulting in an geometrical transmission of 95 %. The grid is etched in a stainless steel plate with a diameter of 68 mm and a thickness of 0.5 mm.
A gold wire with a diameter of 1 mm is used between the flange and the foil to seal the window. Foil and sealing are pressed onto the sealing surface with a screwed ring.

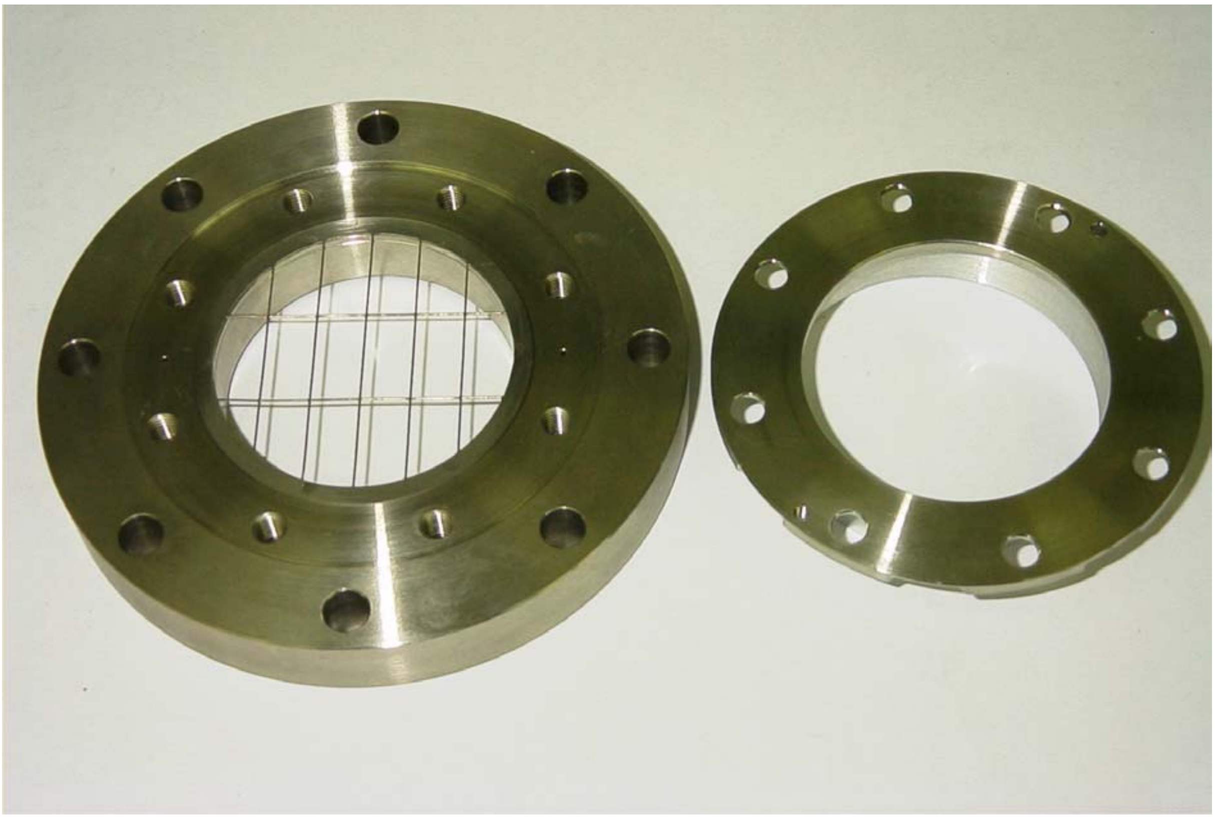

Figure 3.2
Picture of the flange containing the entrance window (not shown) with the support grid and the ring for pressing the foil and the sealing. All parts are made of stainless steel in order to enable baking.

3.3.3. The electrode system

The electrode system in the SHIPTRAP gas cell has to guide the ions towards the nozzle. Two different types of electrodes are used, an exclusive DC electrode for the ion acceleration and the focussing funnel structure using DC and RF fields. Fig. 3.3 shows this electrode system together with the support structures.

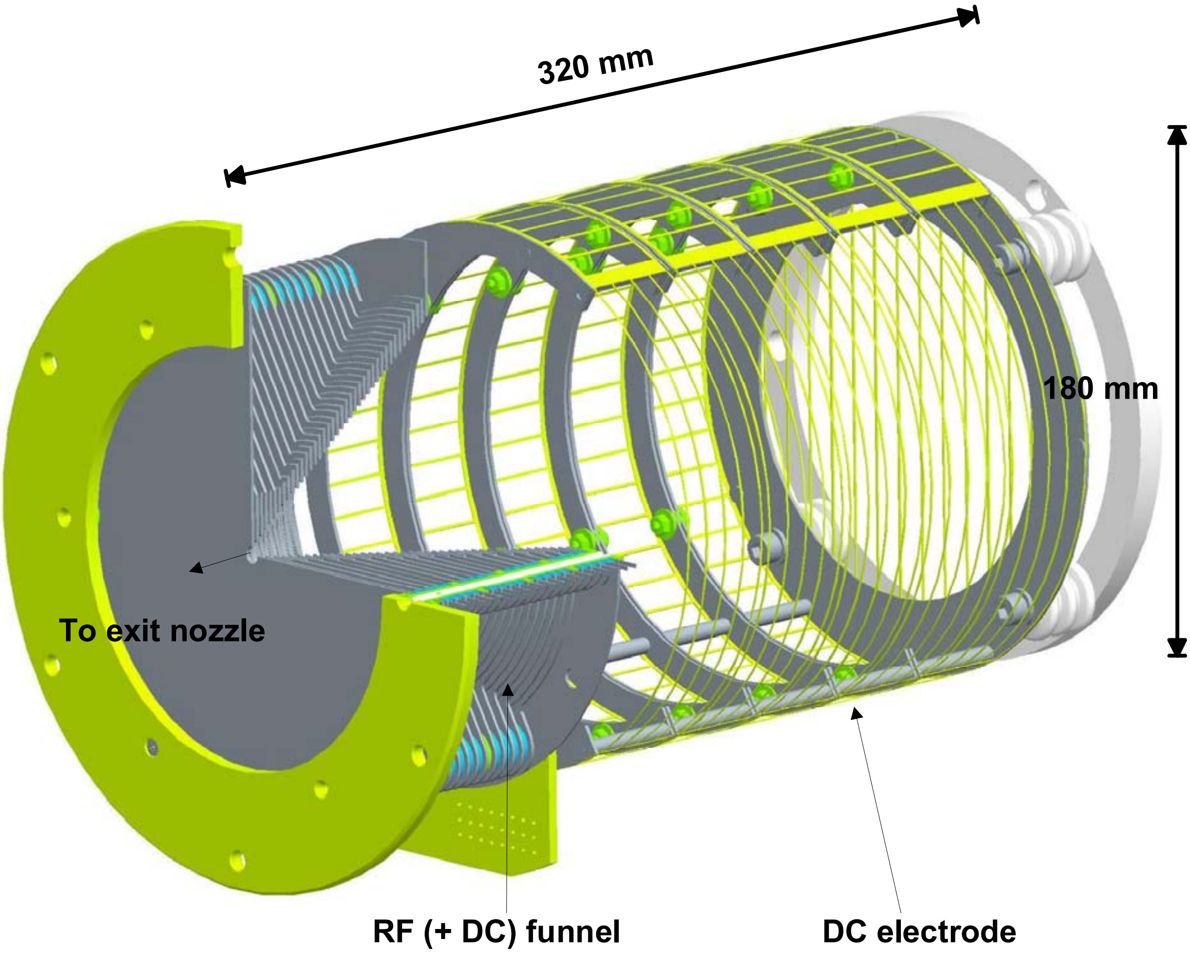

Figure 3.3
The electrode system of the SHIPTRAP buffer-gas cell with the RF (+ DC) funnel (40 ring electrodes) and the DC electrode system (5 segments).

3.3.3.1. The DC electrode

The DC-electrode system contains the stopping volume for the ions and is responsible for the fast acceleration towards the funnel structure. As the beam enters the cell almost perpendicular to the extraction direction, the transmission of the incoming ions through the electrodes has to be considered.

The system consists of 5 cylindrical electrodes with an outer diameter of 180 mm, an inner diameter of 160 mm and a moulded depth of 35 mm. In order to ensure high transmission of the ions into the stopping volume, the electrodes form an open structure at the entrance side of the ion beam as visible in Figure 3.4, resulting in a geometrical transmission of 93 %. The mesh structure of the outside is etched in a stainless-steel strip (thickness of 0.2 mm) welded onto the support structure. The different electrode segments are connected together via ceramic screws at a distance of 1 mm.

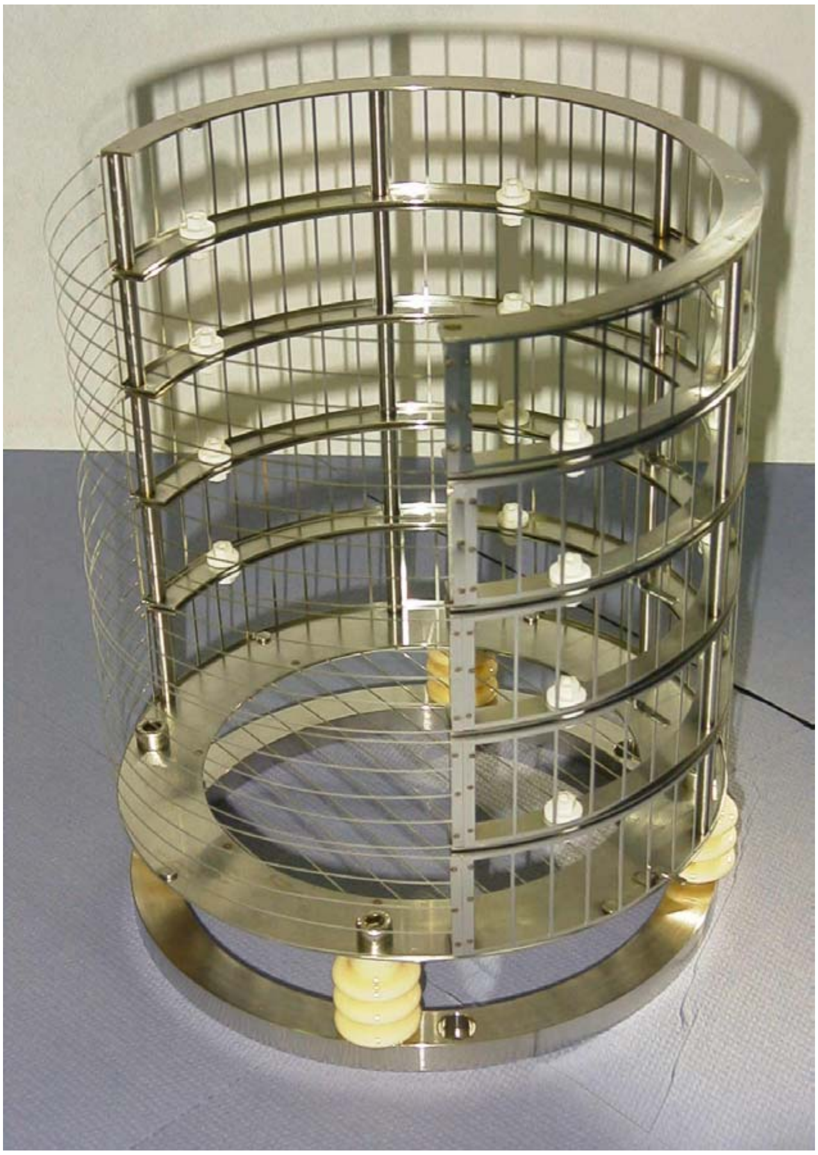

Figure 3.4
The DC-electrode system, consisting of 5 segments to achieve a homogeneous electric field gradient for the acceleration of the ions. The open shape to one side (achieved by an etched strip structure) ensures high transmission of the ions into the stopping volume when entering under 82.5° at SHIPTRAP. The system is fixed to the backside end flange via four ceramic stands.

The stack of electrodes is fixed via four ceramic insulators to the backside flange, where the five voltage feedthroughs are also placed. Electrodes and feedthroughs are coupled via stainless-steel rods with crimp connections. The voltage, typically 150 – 350 V, is applied via five channels of an iseg HV module (model EHQ F025p).

Figure 3.5 shows a distribution of equi-potential lines calculated with SIMION for the used DC-electrode geometry. At the left and the bottom part the mesh structure of the electrode is visible. With these simulations the maximum distances between the wires were determined in order to avoid penetrations of the fields. At the right part of the picture the first two electrode rings of the funnel structure are visible (see next section).

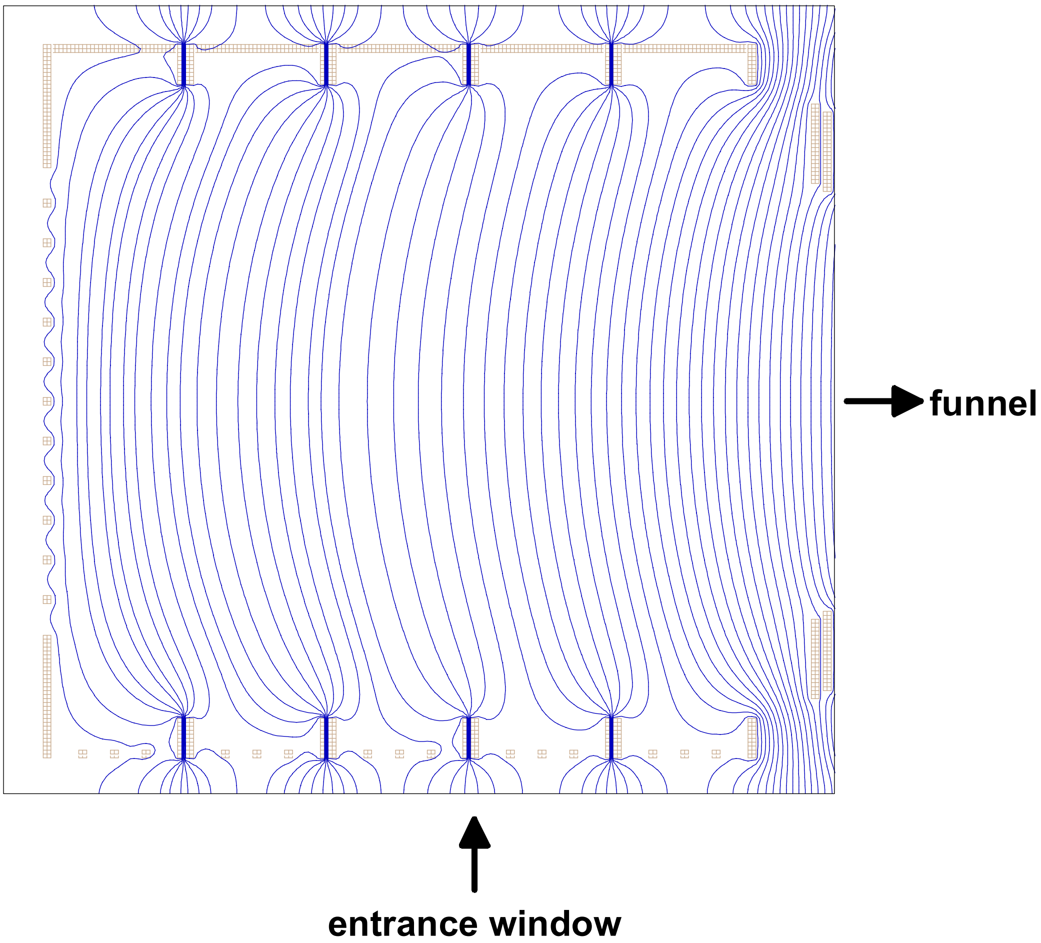

Figure 3.5
Distribution of equi-potential lines generated with SIMION. Besides the five segments of the DC electrode the first two electrode rings of the funnel structure are visible.

3.3.3.2. The funnel structure

The SHIPTRAP funnel structure consists of 40 stainless-steel ring electrodes with inner diameters between 130 and 5 mm. The rings have a thickness of 1 mm each and a distance of 1 mm between adjacent rings. Each ring is supported at three positions each enclosing an angle of 120°.

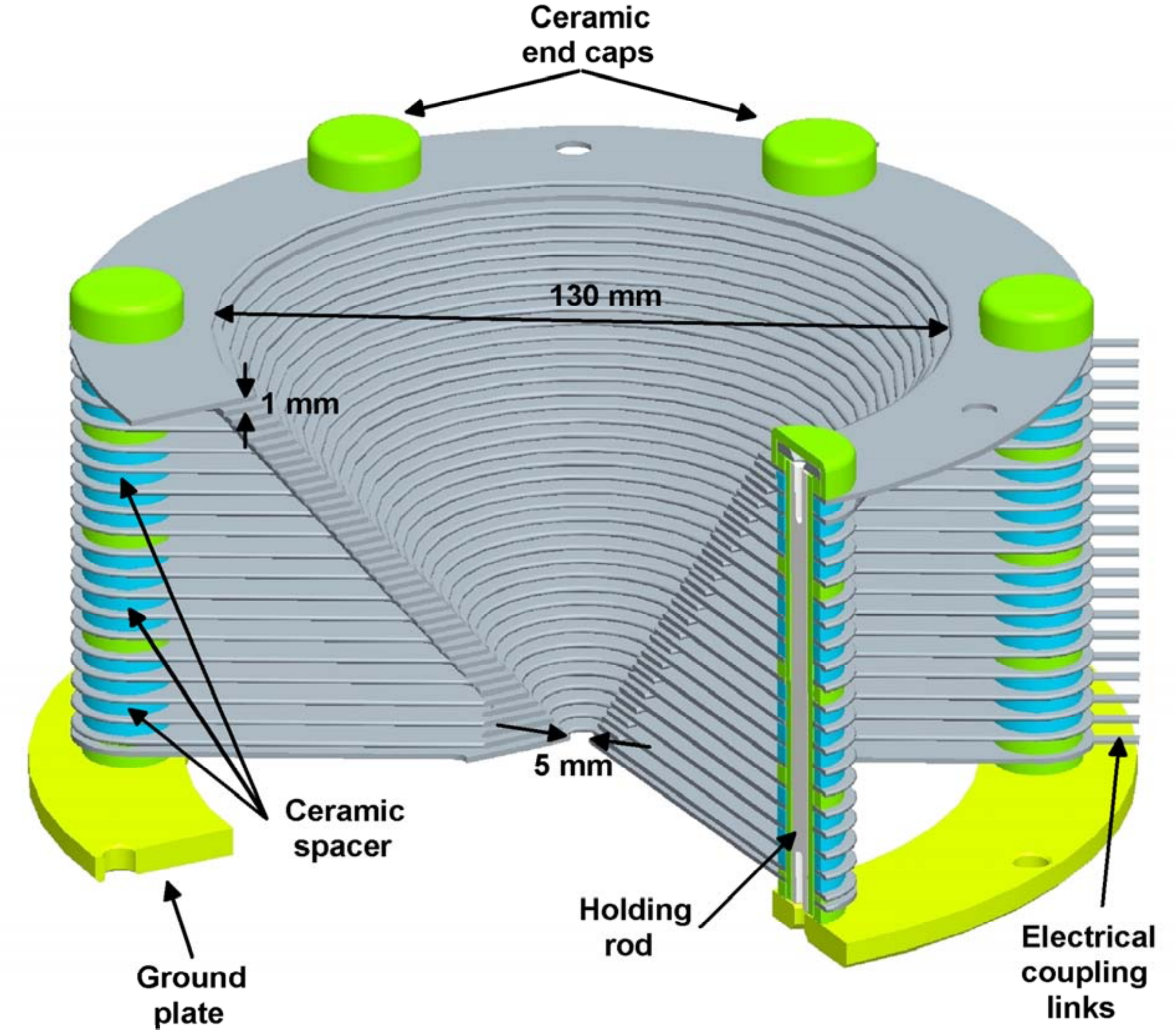
Ceramic end caps
130 mm
1 mm
5 mm
Ceramic spacer
Holding rod
Ground plate
Electrical coupling links

Figure 3.6
The SHIPTRAP funnel structure in a schematic view with the 40 ring electrode plates and the ceramic spacers (blue/green) between adjacent plates.

In order to decrease the electrical capacitance of the system (in the present configuration about 850 pF), adjacent rings are not fixed to the same holding rod. Since all ring electrodes are individually electrically coupled, ceramic spacer plates are used to isolate the rings. In total six holding rods are mounted to a ground plate to guarantee mechanical stability.

As the rods themselves are grounded, they are covered at the ends by ceramic end caps that prevent sparking between the rods and the adjacent electrodes.

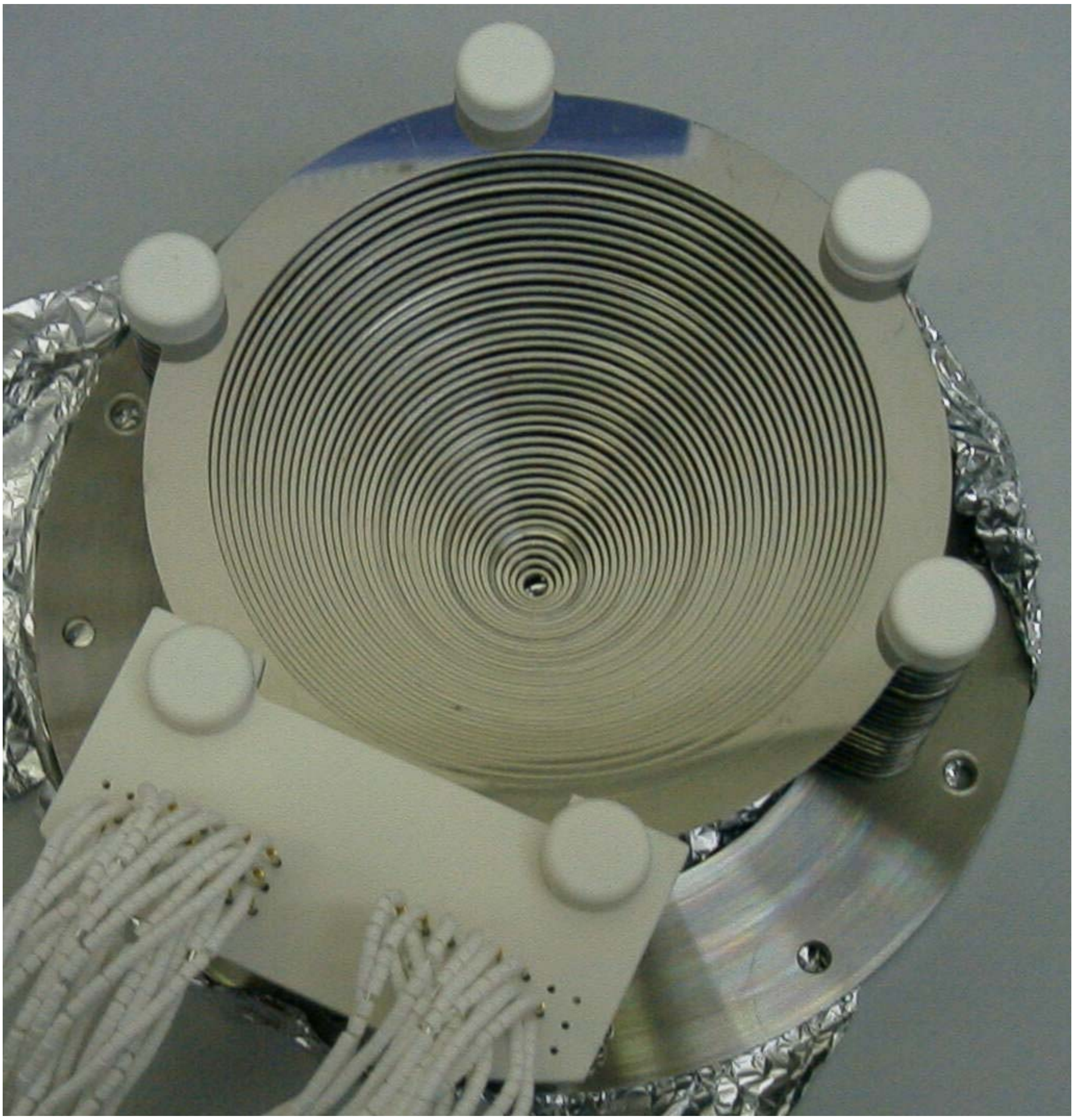

Figure 3.7
Photograph of the funnel structure. The 40 wires for the electrical connections are visible. In order to avoid short-cuts the wires are covered with ceramic beads acting as insulating spacers. The six holder rods (sitting on ground potential) wear ceramic caps in order to avoid discharges.

Two 25-pin SUB-D feedthroughs, one for each RF phase and both placed on a DN100-CF flange, are used for the electrical connection from outside the chamber. In order to avoid impurities and to enable baking the SUB-D plugs inside the chamber are made of aluminium oxide. The electrical coupling to the individual ring electrodes is done via stainless-steel rods (diameter 1 mm), bent in such a way to fit to a ceramic stress-relief plate attached to the funnel. From there silver-plated copper wires, mutually insulated by ceramic beads, are used to connect to the feedthroughs. This can be seen in Fig. 3.7, showing a photograph of the funnel structure and the electrical connections. The wires are connected to the funnel and the feedthroughs via crimp connectors in order to avoid soldering within the chamber. Outside the chamber an electronic circuit ('RF-DC Mixer') is attached to generate the combination of DC and RF voltages supplied to the funnel electrodes. Figure 3.8 schematically shows the principle of this electronic component.

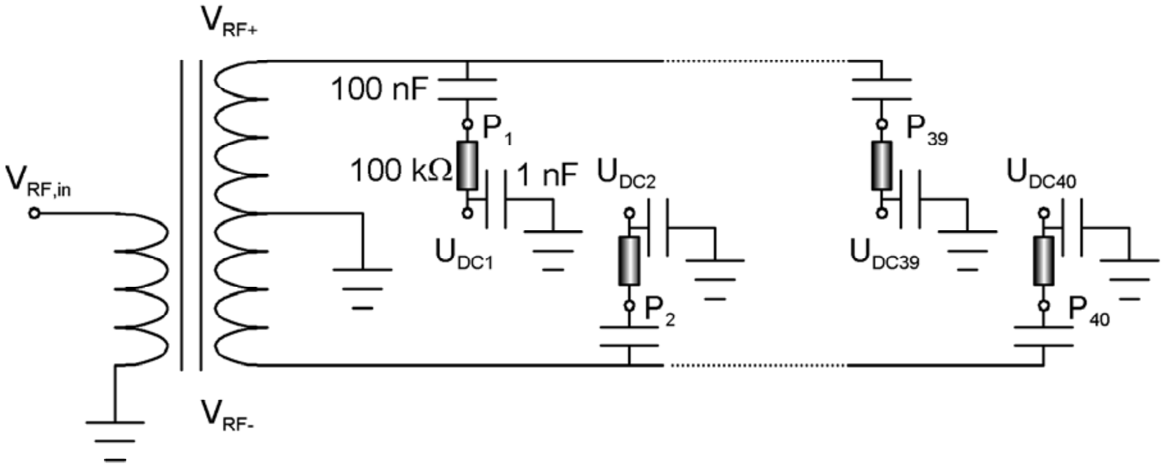

Figure 3.8
Principle of the electrical circuit for the RF funnel. All 40 ring electrode plates (P_1 – P_{40}) are connected separately to the 40 DC supply channels.

The sinusoidal function of the RF voltage is supplied by a function generator (SRS DS345). As higher amplitudes (typically 100 – 200 V_{pp}) are needed than delivered by the DS345, the signal is amplified by an RF power amplifier (KALMUS 170F, 200 W maximum power). Since the funnel has been tested at different RF frequencies, the RF has not been coupled resonantly. Therefore the high output power of the amplifier was chosen in order to deal with the capacitance of the funnel of 850 pF, leading to a required RF power in the range of 50 – 100 W, and in order to deal with the reflection of the RF power back to the amplifier. Behind the amplifier the two RF phases (shifted by π) are separated by coils on a toroidal core. The separated RF amplitudes are then fed to the mixing circuit.

The different DC voltages (typically in the range from 30 to 150 V) are provided by a 40-channel DC power supply.

3.3.4. The gas-supply system

Figure 3.9 shows the principle of the gas-supply system of the gas cell. The main parts are the gas-flow control valve (AERA FC-780CHT), the gas-purification system

(SAES MonoTorr Phase II) and an additional LN_2 cryo trap. The combination of the purifiers is used to remove impurities to a level below 1 ppb and is supported by the usage of ultra-clean gas (He 7.0).
The tubing of the gas-supply system is made of electropolished stainless steel with a diameter of 1/4”. Additional valves (Swagelok 4BG) included in the gas line allow for manipulations at the gas line without venting the whole system. As all parts, including all valves, are made of stainless steel, the whole supply system is bakeable up to 150 °C limited by the highest temperature allowed for the mass-flow control valve (FC-780CHT).

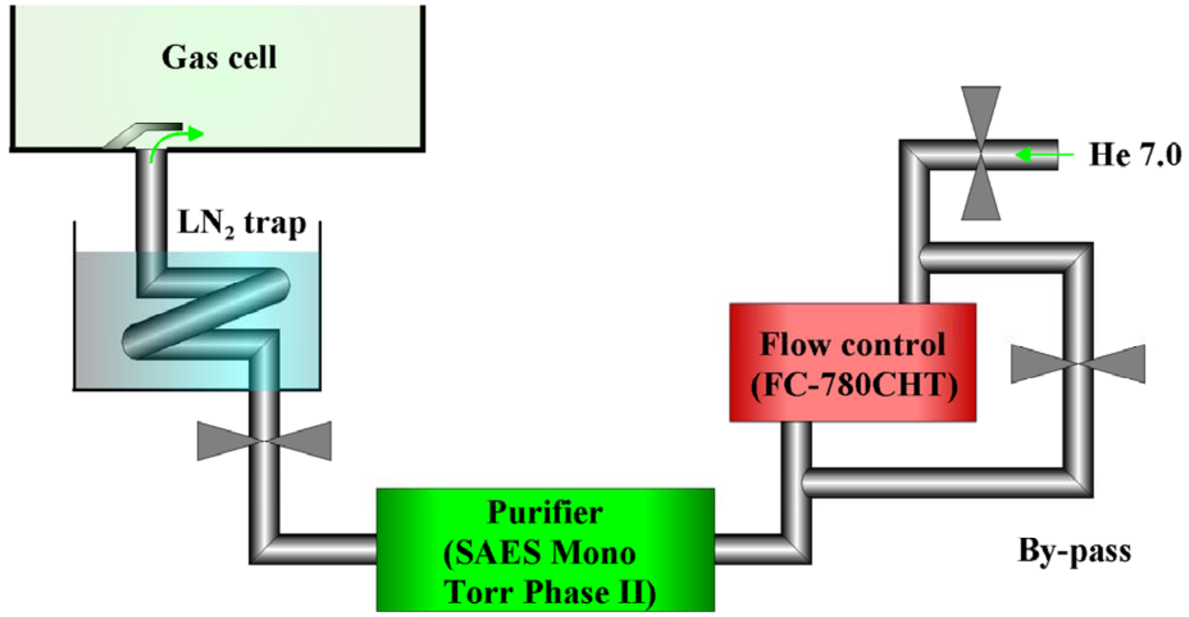

Figure 3.9
The gas-supply system consisting of the flow control valve (AERA FC-780CHT), the purifier (SAES MonoTorr Phase II) and a LN_2 trap directly in front of the cell. All tubes and valves are made of stainless steel in order to enable baking. The gas inlet inside the chamber is covered by a steel strip in order to avoid a gas jet caused by the expanding gas.

The FC-780CHT is controlled via a 0 – 10 V DC ramp (manually or PC-controlled, see Appendix) and is closed without current to avoid an uncontrollable gas flow in case of an electrical power failure. As the valve must not be operated during the baking procedure, a by-pass for pumping is added.

The gas inlet is done via a DN35-CF flange connected to the vacuum chamber. In order to avoid a jet caused by the gas expanding out of the gas line into the cell the inlet is covered by a steel strip at a distance of 3 mm from the flange surface.

3.4. The extraction nozzle

The nozzle provides the transition between the high-pressure area inside the cell and the low-pressure region in the extraction chamber. The shape of the nozzle (displayed in Figure 3.10) was optimised with gas-dynamical simulations using the code VARJET [Var98] (see next paragraph).

The nozzle throat has an inner diameter of 0.6 mm and both sides of the nozzle throat have a conical shape. The convergent nozzle entrance starts with an open diameter of 2 mm and an angle of 90°. It was optimised to achieve subsonic gas velocities high enough to drag the ions through the nozzle. The divergent nozzle exit ends in a diameter of 6 mm with an angle of 38°. The shape was optimised to perform a supersonic gas jet for an effective transfer of the ions into the extraction RFQ and an effective transversal cooling within the first RFQ segments.

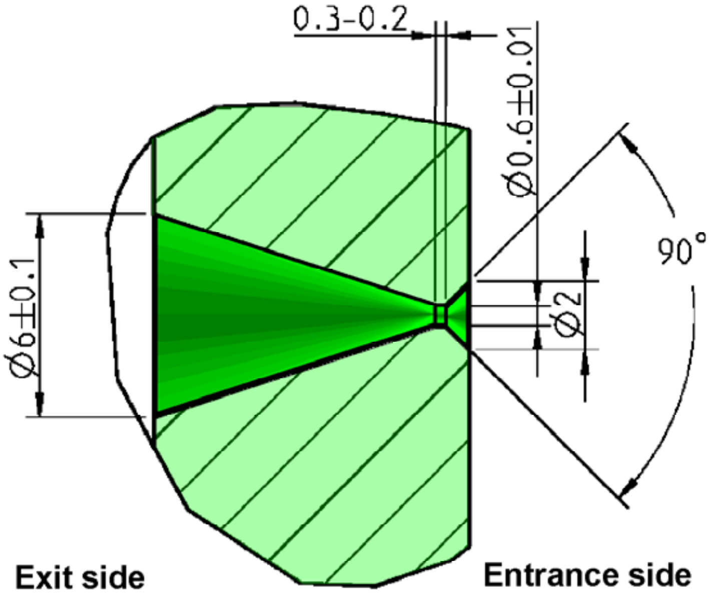

Figure 3.10
Technical drawing of the extraction nozzle. The inner diameter is 0.6 mm, while the diameters of the entrance and exit cones are 2 mm and 6 mm, respectively.

Figure 3.11 displays the design of the nozzle and the support structure. The nozzle flange (green) is mounted on a nozzle holder (grey) that itself is mounted to the end flange of the gas cell. Both the nozzle and the nozzle holder are sealed with gold wires with a diameter of 0.5 mm. Besides shaping the gas flow the nozzle acts as the last DC electrode of the gas cell and as the first electrode of the extraction chamber. Therefore the nozzle holder made of stainless steel consists of two parts connected by an insulating ceramic ring (red). The connection is done by silver soldering between the ceramic ring and the stainless-steel parts. The electrical coupling of the nozzle is done via a silver-plated copper wire insulated by ceramic beads and connected to an SHV feedthrough.

The pocket-like shape of the nozzle flange is a relic of an earlier design of the electrode structure inside the gas cell, using a pure DC-field configuration that led to the need of a large surface of the nozzle electrode.

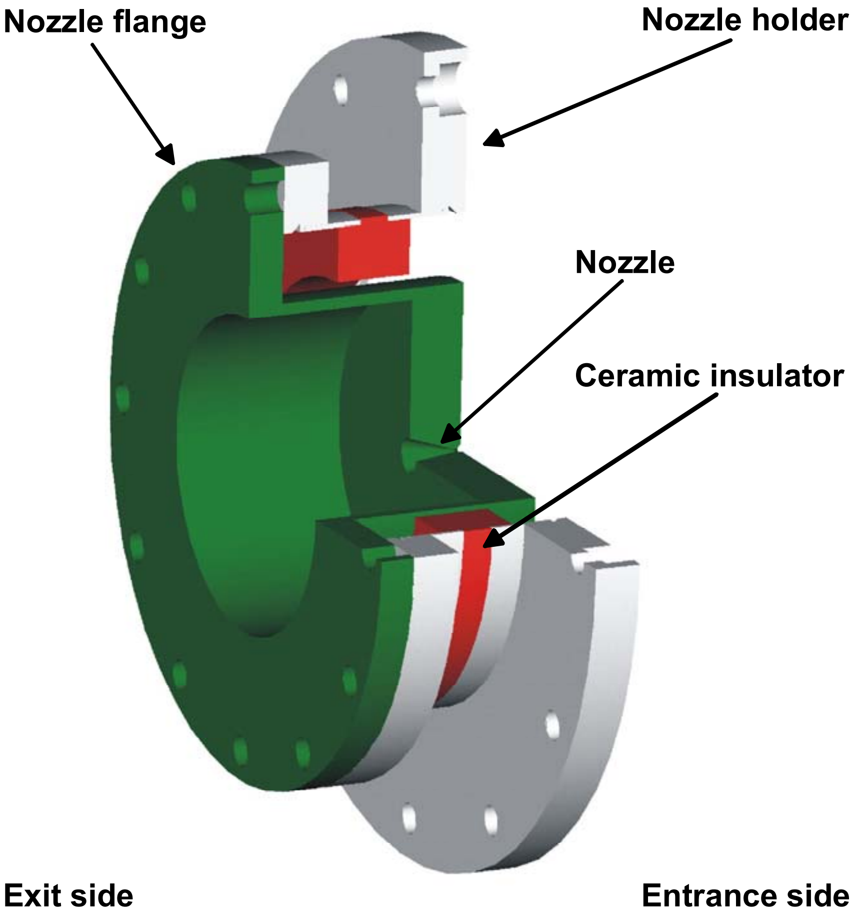

Figure 3.11
View of the nozzle flange (green) and the nozzle holder made of two stainless-steel parts (grey) connected by an insulating ceramic ring (red). Nozzle and holder are vacuum-sealed with gold wires (diameter 0.5 mm).

3.4.1. Gas-dynamical simulations with VARJET

The fast and efficient transfer of the stopped ions from the gas cell into the extraction RFQ is achieved both by electrical guiding fields as well as by the dragging gas flow through the exit nozzle. Therefore not only the electrical field geometries had to be considered in the design phase of the buffer-gas cell, but also the gas-dynamical conditions.

The VARJET code by V. Varentsov [Var98] is based on the solution of the fully time-dependent Navier-Stokes equations and allows to simulate the gas flow inside the complete set-up at given pressures, pumping speeds and geometries. Since the gas velocities inside the gas cell are negligible, except in the vicinity of the nozzle, only this region is of interest and will be discussed further on.

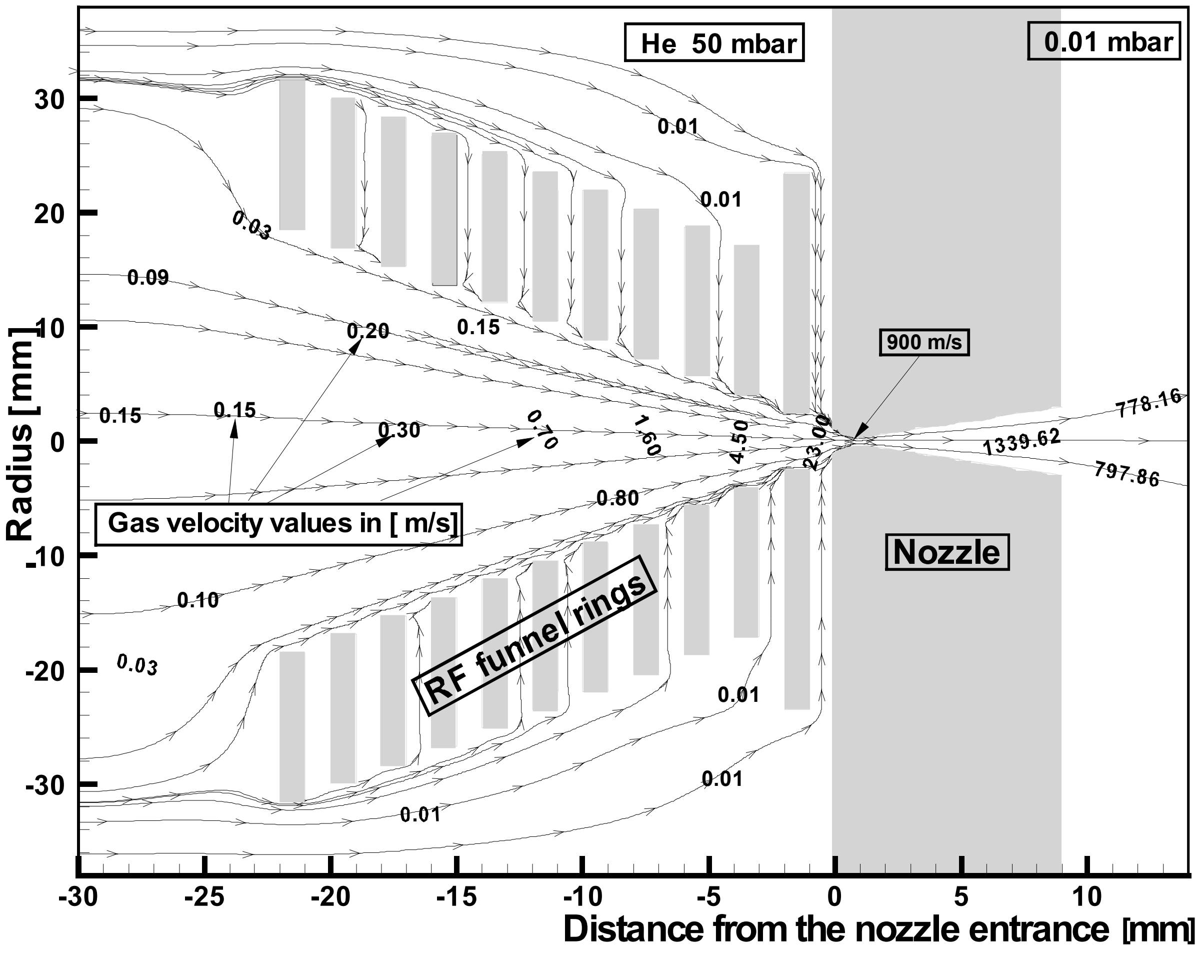

Figure 3.12

VARJET simulation [Var98] for the gas velocities inside the gas cell in the area around the extraction nozzle. The arrows represent the direction of the flow, while the numbers give the local gas velocity in m/s. The gas velocities inside the cell can be neglected, except in the vicinity of the nozzle. Inside and behind the nozzle the jet has supersonic velocities. The centring of the jet helps to inject the ions into the following RFQ.

Figure 3.12 shows a simulation for the gas velocities inside the gas cell taking into account the last 11 funnel plates and the nozzle. The numbers represent the local gas velocities, while the arrows show the direction of the flow. Besides the realistic geometry the simulation takes into account the resulting pressure difference due to the gas flow and the pumping speed, since a He pressure of 50 mbar inside the cell creates a background pressure of 0.01 mbar at the outer wall of the extraction chamber. The most important value for the gas velocity is given for the area directly in front of the nozzle, as it describes the ability of the gas flow to separate the ions from the electrical field lines, thus taking over the transport of the ions. This requires the ion velocity caused by the electrical guiding fields to be comparable to the gas velocity in front of the cell.

A simple expression for the mass flow rate Q through the nozzle, obtained from a one-dimensional model of isentropic flow of an ideal gas, is given by [Var03]

$$Q = 14.2 \cdot \frac{d^2}{\sqrt{mT_0}} [l/s] \times P_0 , \tag{3.1}$$

with the nozzle throat diameter d (in mm), the atomic mass m of the gas, the stagnation gas temperature T_0 (in K) and the stagnation pressure P_0 in the gas cell. Using Equation (3.1) for a He ($m = 4$) pressure of 50 mbar inside the gas cell at a temperature of 293 K and the SHIPTRAP nozzle hole diameter of 0.6 mm, a flow rate of the buffer gas into the relative vacuum of the extraction chamber of

$$Q = 7.5 \,\text{mbar l/s}$$

can be obtained. With the known pumping speed V_p at the extraction chamber, the resulting background pressure P_1 at the outer wall of the extraction chamber can be estimated with

$$P_1 = \frac{Q}{V_p} , \tag{3.2}$$

resulting in

$$P_1 = 7.5 \cdot 10^{-3} \,\text{mbar}$$

for an assumed pumping speed of 1000 l/s. The value is in good agreement with the measured value of $9 \cdot 10^{-3}$ mbar.

3.4.2. Impact-pressure measurements

The VARJET simulations were tested with impact-pressure measurements of the supersonic gas jet. A small pressure probe, comparable to Prandtl's pitot tube [Ger95] and movable in horizontal and vertical direction, was positioned at the nozzle exit to measure the profile of the jet. Figure 3.13 shows a comparison between calculated and measured values of the impact pressure at various distances. Ar with a pressure of 100 mbar was used as buffer gas inside the cell. Taking into account the diameter of the pitot tube of 2 mm, which is in the range of the jet dimensions, the values are in good agreement. The apparent sideways shift of the jet from the longitudinal axis is an effect of the measurement, as the pitot tube was slightly pushed aside by the jet.

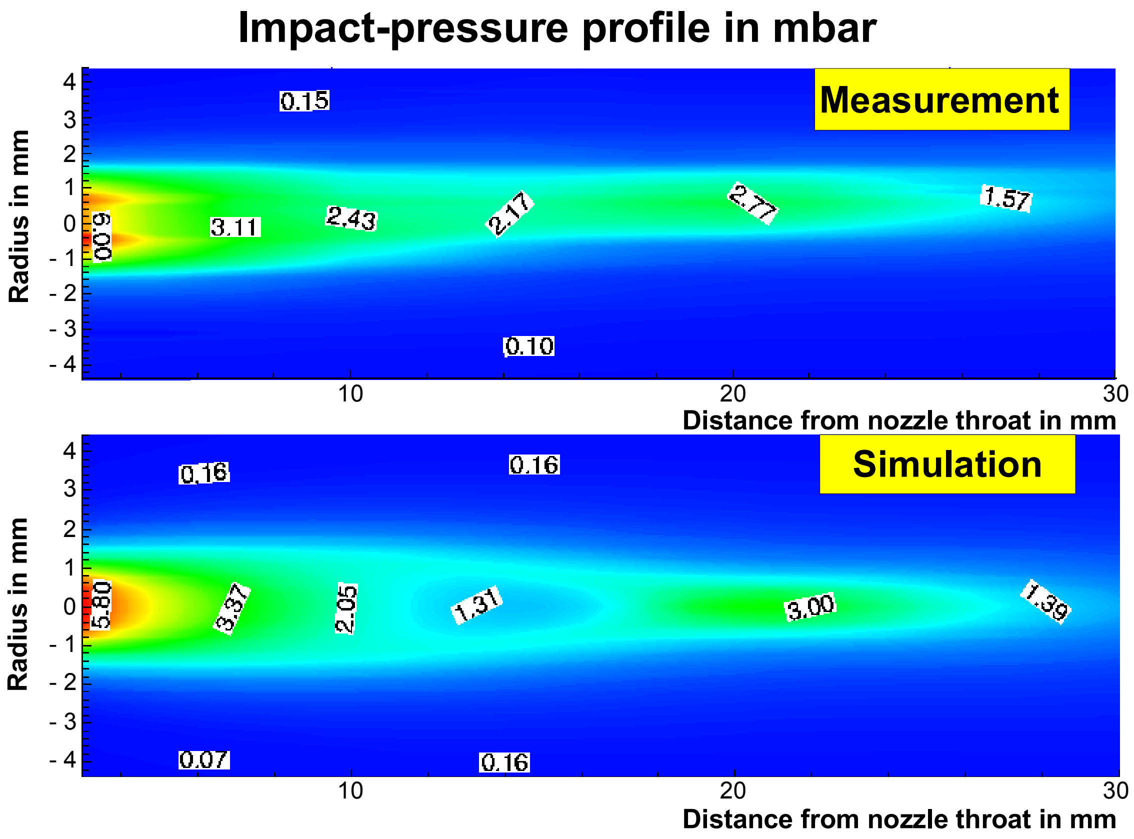

Figure 3.13
Comparison between calculated and measured impact-pressure values of the gas jet for an Ar pressure of 100 mbar inside the cell and the given geometry and pumping speed. The numbers give the local pressure values in mbar. Taking into account the size of the pitot probe (diameter 2 mm) there is a good agreement between simulation and measurement.

For simulations of ion trajectories inside the gas cell the code SIMION [Dah00] is used. Since the pressure regime inside the cell enables to use the viscous-damping model (see Section 2.3.1), the damping by the buffer gas is simulated as an additional force included in the SIMION calculations. As long as the gas velocities inside the cell are negligible, the simulations can be used for an optimisation of the electrode system. In the last part of the funnel and in vicinity of the nozzle the situation changes, since the gas velocities become more important. For a realistic simulation in this region the calculations have to take into account the velocity and the direction of the gas flow. Therefore the results of the VARJET calculations can be inserted into simulations of SIMION as additional forces acting on the ion. The accuracy of these combined simulations will be discussed in Chapter 4.

3.5. The extraction system

The main purpose of the extraction system is the separation of the ions from the neutral buffer gas and the transverse cooling of the ions. A segmented RFQ is used to be able to apply a DC ramp in order to compensate for the damping by the buffer gas inside the extraction chamber.

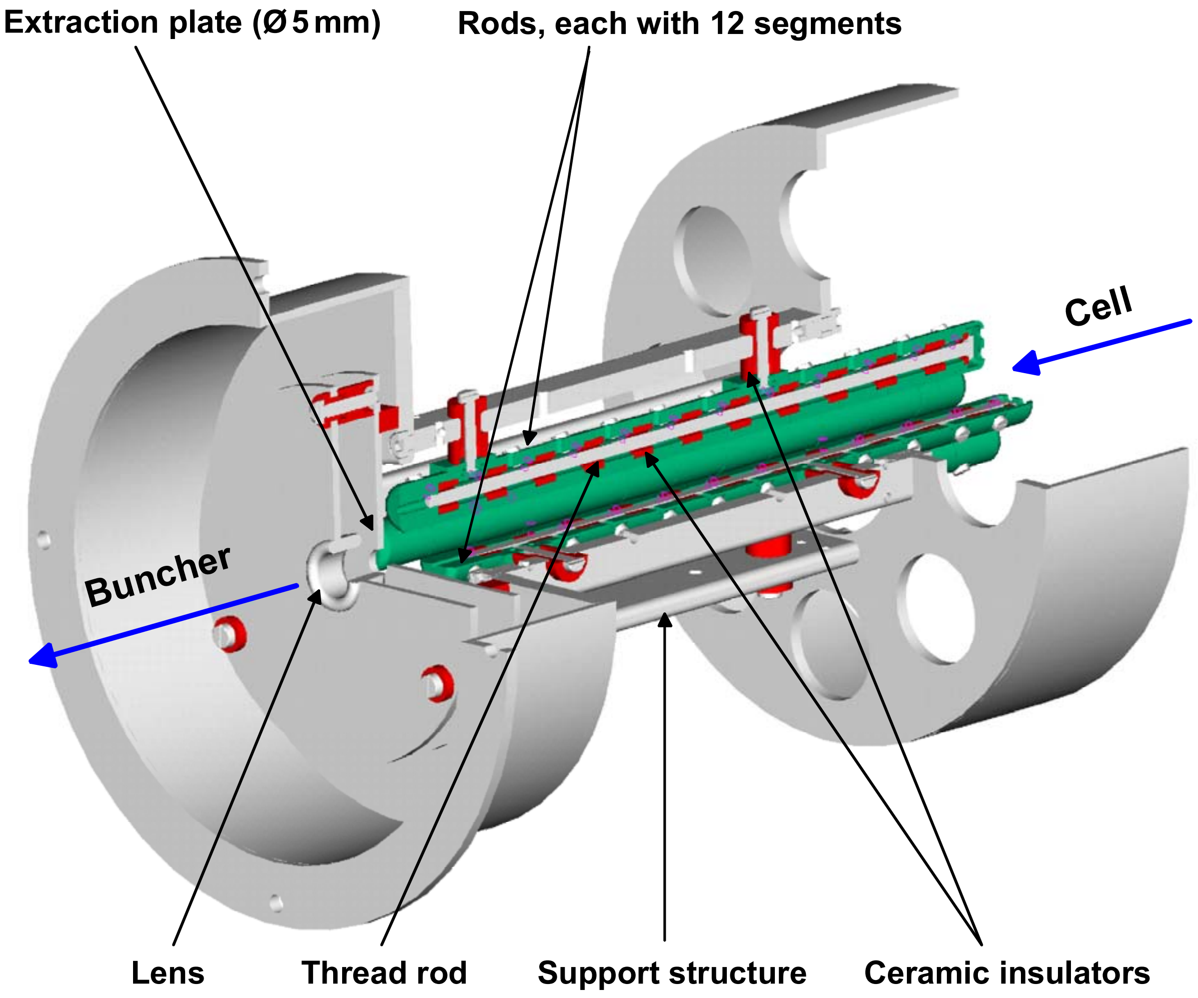
Extraction plate (Ø5 mm)
Rods, each with 12 segments
Cell
Buncher
Lens
Thread rod
Support structure
Ceramic insulators

Figure 3.14
Three-dimensional schematic view of the RFQ from the exit side. The segments (green) are separated by ceramic sleeves (red). The segmented RFQ rods are kept together by threaded rods (grey), each of them mounted to the support structure (grey) at two points, insulated by ceramic tubes. Behind the RFQ an extraction plate and an electrostatic Einzel-lens are mounted for the coupling to the subsequent components.

Figure 3.14 shows a three-dimensional schematic view of the extraction RFQ from the exit side. The RFQ consists of four rods (green) with a total length of 180 mm, a rod diameter of 11 mm and an aperture of 10 mm. Each rod is subdivided into 12

segments of the same length, separated by ceramic sleeves (red). The segments are kept together by pressing onto a threaded rod from both ends.
Each rod is electrically insulated with respect to the support structure. This structure is fixed on one side to the extraction chamber by screws (Figure 3.13), while the open shape of the opposite side (Figure 3.15) fits to a recess inside the (nozzle) end flange of the gas cell. This helps to centre the RFQ when connecting the vacuum chambers of the cell and the RFQ.

As the extraction chamber acts as a differential pumping stage, the entrance side of the RFQ ends in an insulated extraction plate with a central hole of 5 mm diameter to prevent the gas to flow directly into the following RFQ buncher. After the plate a lens with an inner diameter of 10 mm and a length of 20 mm is included to allow for a focusing of the ions into the RFQ buncher.

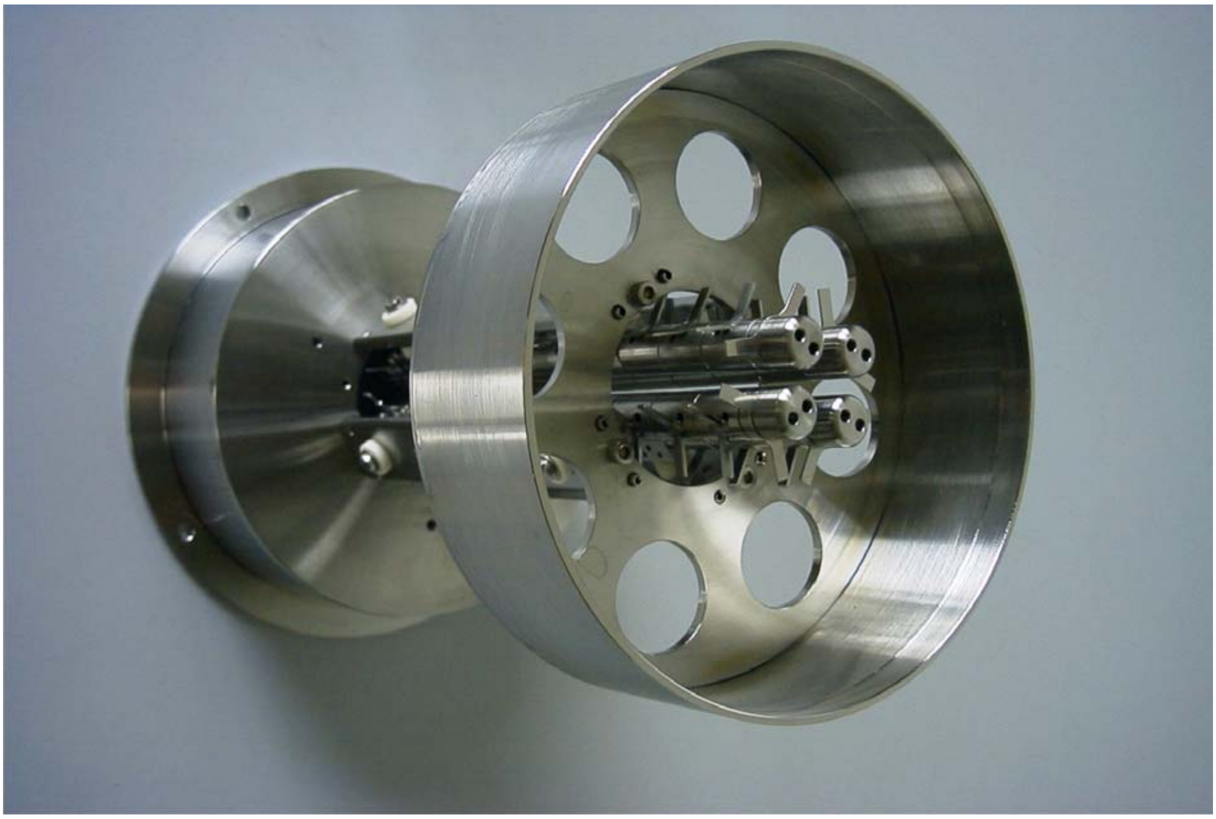

Figure 3.15
Photograph of the RFQ from the entrance side. The open shape of the support structure fits into a recess in the end flange of the stopping chamber. The metal strips sticking out from the segments act as contact surfaces for the electrical connectors.

Since the electrodes of two opposite rods are connected to the same potential, only one rod per phase is connected to the power supply. Inside the vacuum chamber the electrical connection is done by Kapton-coated wires, headed by two 15-pin SUB-D plugs (one for each phase) made out of PEEK, a plastic material suitable for UHV-conditions. It should be mentioned that purity requirements are less stringent inside the extraction chamber compared to the gas cell, since the extracted ions are not stopped and ionisation due to energy loss mechanisms has not to be expected. Therefore it is not mandatory to avoid all kind of organic materials and Kapton-coated cables as well as multi-pin connectors from organic materials can be accepted in the extraction chamber. Nevertheless all cable connections are crimped in order to avoid any problems with solder, especially when the set-up is baked.

The two SUB-D feedthroughs are mounted onto a DN100-CF flange attached to the extraction chamber. As the RF and DC voltages are applied in a combined way, a circuit for the DC/RF-mixing is connected, as schematically shown in Figure 3.16.

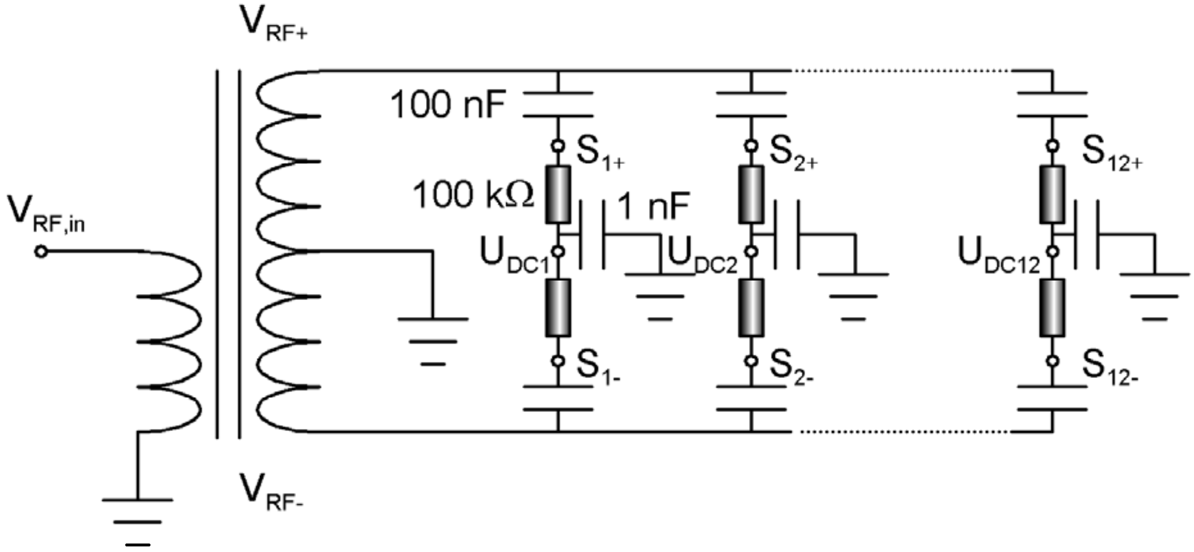

Figure 3.16
Principle of the electronics circuit for the mixing of the RF (V_{RF}) and the DC (U_{DC}) voltages applied at the different segments ($S_{1+/-}$ - $S_{12+/-}$) of the RFQ. The circuit is similar to the one used for the RF funnel. The main difference is the number of the different DC voltages, as longitudinally equivalent segments at different rods are connected to the same DC potential, even if they are operated with different RF phases. Therefore only 12 DC high voltage power supply channels are needed, supplied by an iseg HV module (model EHQ F005p).

Whilst for the sinusoidal function of the RF voltage another DS345 function generator is used, the signal amplification and the phase separation is performed with only one unit. This amplifier by BERTRONIX is customised to the SHIPTRAP RFQ with a maximum power of 350 W and maximum amplitudes of 400 V_{pp} for both phases in a frequency range from 500 to 1500 kHz. The high maximum power was chosen, as the RFQ is not operated on resonance, which was not possible due to the wide range of operating frequencies applied during the test and optimisation phase of the set-up.

3.6. Realisation of UHV conditions

The different requirements for the vacuum system are discussed separately in view of the different tasks of the gas cell and the extraction RFQ. While the vacuum system for the cell has to provide optimum vacuum conditions prior to the flooding of the cell with the buffer gas, the vacuum system of the RFQ also has to remove the mass flow of the buffer gas during the operation of the system. In general the vacuum system consists of oil-free pre-vacuum and turbomolecular pumps, assisted by a computer-controlled baking system, and of getter material placed inside the gas cell.

3.6.1. The vacuum system

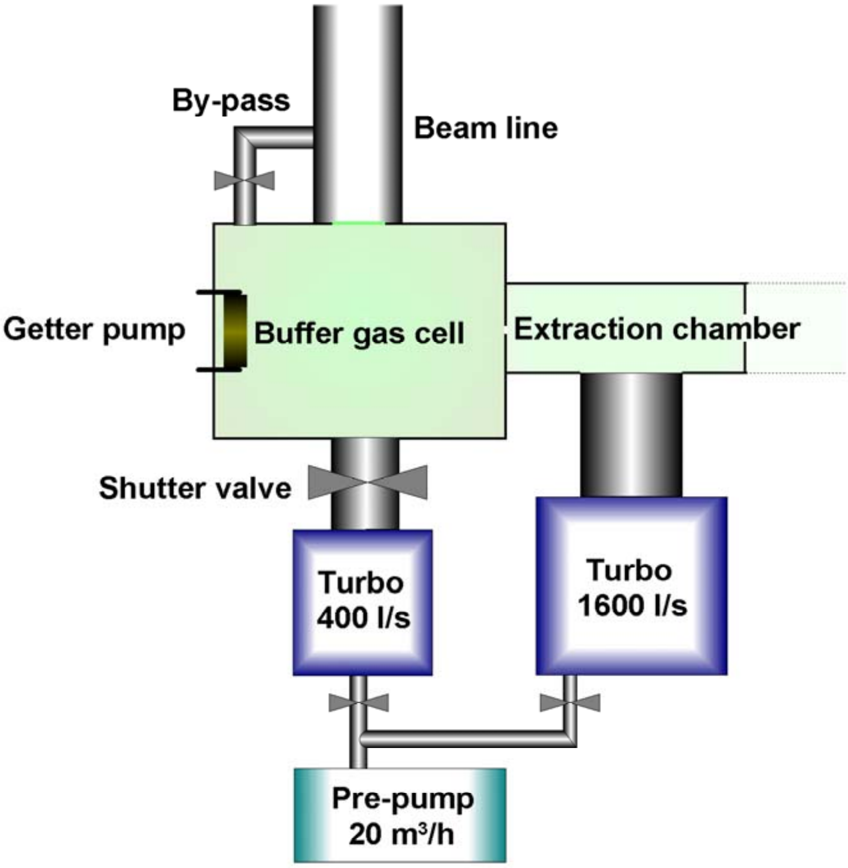

Figure 3.17
Schematic view of the vacuum system of the gas cell and the extraction chamber. The cell and the extraction chamber are pumped by magnetically levitated turbomolecular pumps with 400 l/s and 1600 l/s. A shutter valve between buffer-gas cell and pump is used to disconnect both during operation. Getter material (NEG) inside the gas cell is used to compensate the surface outgassing rate during operation of the gas cell. Between the beam line and the cell a by-pass line is installed in order to avoid pressure differences on both sides of the entrance window during pumping and venting.

In order to guarantee a high purity of the vacuum system, schematically shown in Figure 3.17, a completely oil-free pumping system is used to evacuate the gas cell and the extraction chamber. Thus the gas cell is pumped by a magnetically levitated turbomolecular pump (Pfeiffer TMU400, 400 l/s) and an oil-free scroll pump (VARIAN TriScroll 600, 20 m³/h). In order to avoid direct contact to organic material, a bakeable full-metal gate valve (VAT 48240-CE74, DN100) is used to separate the gas cell from the pump during operation with buffer gas.
In order to ensure an efficient removal of the buffer gas behind the extraction nozzle, a high pumping speed is required. Therefore a turbomolecular pump (Pfeiffer TMU1600, 1600 l/s) is used to pump the extraction chamber. The same roughing pump as for the gas cell is also used for this turbo pump.

Special attention has to be paid when the set-up is pumped down from ambient pressure to pre-vacuum pressure or when the set-up is vented. Due to the highly-sensitive entrance window a by-pass line between the stopping chamber and the beam line is installed to avoid pressure differences on both sides of the foil during pumping and venting. A bakeable full-metal valve is used to close the bypass after reaching the pre-vacuum regime.

For the control of the gas pressure inside the buffer-gas chamber two different gauges are installed. A full-range gauge (Pfeiffer PKR 261) is used for the low-pressure measurement up to 1 mbar, while the helium pressure during operation is measured with a capacitance gauge (Pfeiffer CMR 261). The pressure inside the extraction chamber is monitored by a full-range gauge (Pfeiffer PKR 261).

During operation with buffer gas outgassing from the inner gas-cell surfaces is the dominant source of impurities contaminating the stopping volume. The only way to remove residual gas components besides the buffer gas is to apply getter materials inside the gas cell. Therefore a NEG (**N**on **E**vaporable **G**etter) pump is placed inside the cell. This pump consists of a stainless-steel strip of 500 mm length, covered on both sides with St707^{TM} (Zr-V-Fe alloy, from SAES Getters). The advantage of the getter pump is that the buffer gas He is not affected by the getter material. For an effective pumping of the unwanted residual gas components the getter material has to be activated, thus the steel strip is connected on both sides to electrical feedthroughs in order to allow for heating of the material by applying a DC current of 35 A for several hours.

Pressure values down to the range of $5 \cdot 10^{-9}$ mbar for both the cell and the extraction chamber can be reached with turbomolecular pumps. However, not only the nominal pressure values but also the composition of the residual gas has to be considered. Therefore a small quadrupole mass spectrometer temporarily attached to the gas cell chamber was used to determine the partial pressures inside the cell. Figure 3.18 shows a mass distribution of the residual gas inside the cell after one day of pumping with the turbo pump. The distribution of contaminants is typical for a non-baked chamber with water (H_2O^+) being the dominant contribution. Further contaminants are H_2^+ (m = 2), OH^+ (m = 17), N_2^+/CO^+ (m = 28), O_2^+ (m = 32) and CO_2^+ (m = 44).

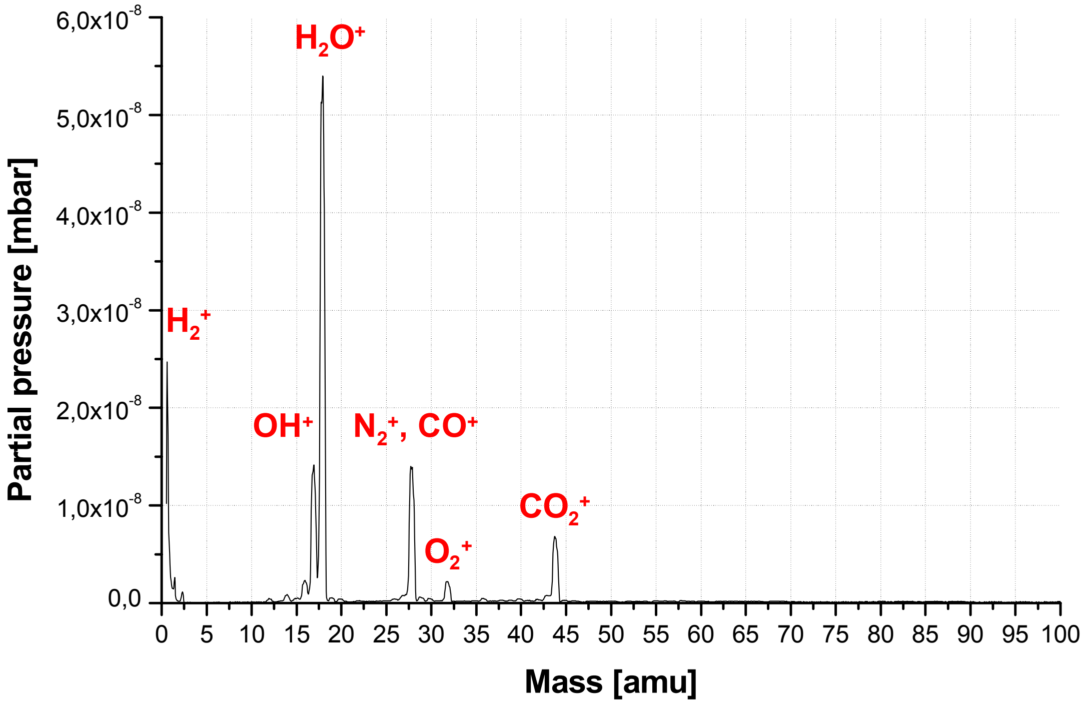

Figure 3.18
Mass distribution of the residual gas inside the gas cell at a $P_{tot} = 8 \cdot 10^{-8}$ mbar measured with a directly connected QMS. The chamber was only pumped by the turbo pump and not baked.

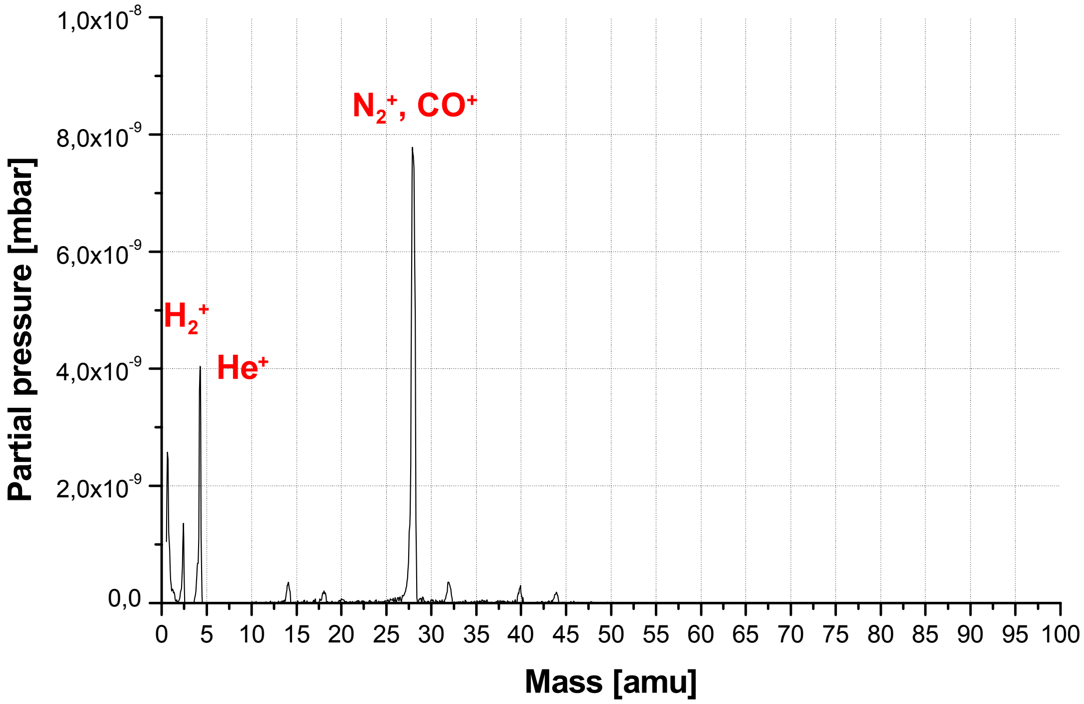

Figure 3.19
Mass distribution of the residual gas inside the cell after four days of baking at 150 °C.

After baking the system for four days at a temperature of 150 °C the resulting mass spectrum is shown in Figure 3.19. For this measurement the getter pumps were not activated. Clearly visible is the difference to Figure 3.18, since especially the fraction of water decreased by more than two orders of magnitude. The dominant remaining background component originates from mass m = 28 mainly consisting of N_2^+. The small peak at mass 40 is caused by a contamination with argon.
Since the baking procedure was performed by simultaneously applying a constant flow of He gas (~0.1 mbar l/s) to facilitate the removal of outgassing contaminations, a residual background component at m = 4 is visible in Fig. 3.19.

Nevertheless the realistic operating condition for the buffer-gas cell is represented by a closed gate valve to the turbo pump. In this case the outgassing residual gas components from the inner cell surface are no longer removed, leading to a drastic contamination of the gas-cell vacuum if no countermeasures are foreseen. For this purpose the getter material is included in the cell. Figure 3.20 shows a comparison of the mass distribution of the residual gas before (black curve) and after (red curve) the activation of the getter material.

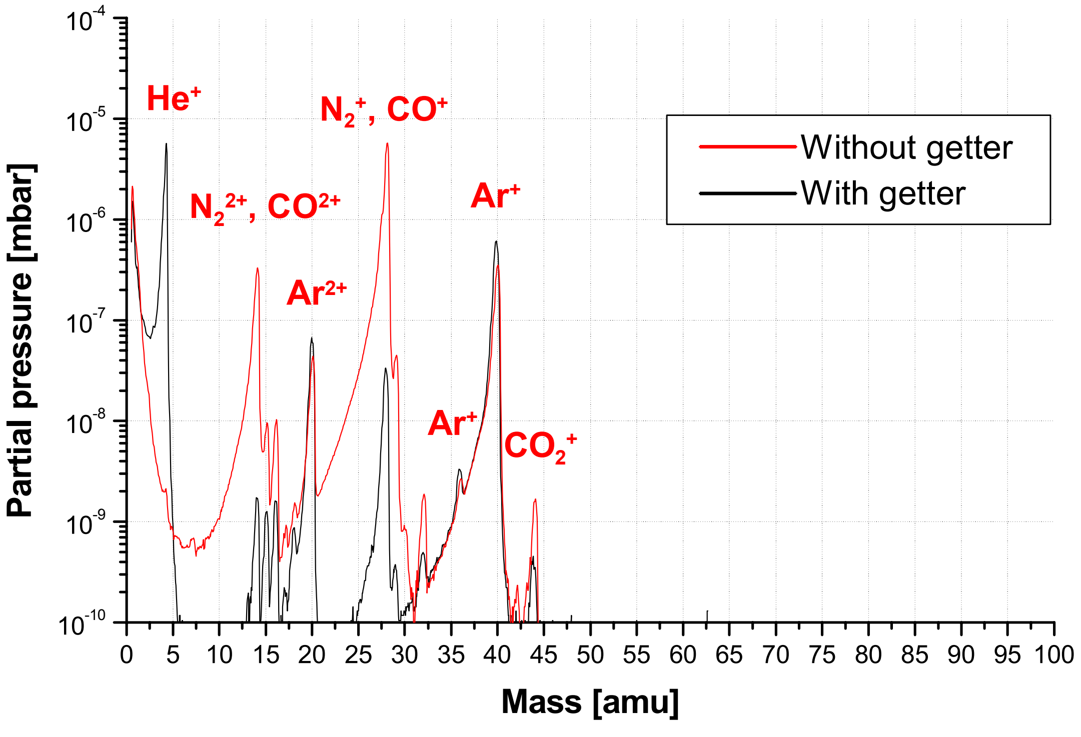

Figure 3.20
Mass distribution of the residual gas inside the buffer-gas chamber comparing the situation of a closed shutter valve to the turbo pump without (black line) and with (red line) activated getter. It is clearly visible that all residual gas components are pumped very efficiently. Since the getter material cannot pump noble gases, the peaks at m = 40 ($^{40}Ar^{1+}$), m = 36 ($^{36}Ar^{1+}$) and m = 20 ($^{40}Ar^{2+}$) have not changed. The peak at mass 18 contains both H_2O^+ and $^{36}Ar^{2+}$. The dominant $^4He^+$ peak in the black curve is due to a flow of buffer gas inside the gas cell while the getters were being activated (and the gate valve to the turbo pump was still open).

Clearly visible is that the partial pressures of $^{36}Ar^+$ and $^{40}Ar^+$ have not changed, since noble gases are not pumped by the getter material. Very efficient is the pumping of N_2^+/CO^+ (masses 28 and 14), visible in the decrease of the partial pressure by two orders of magnitude, and of CO_2^+ (mass 44), where the pressure decreases by a factor of two. Since also $^{36}Ar^{2+}$ is measured, the efficiency in pumping water cannot be estimated quantitatively and also the peak at mass 2 consists of H_2^+ and $^4He^{2+}$. The peak of $^4He^+$ in the red curve is caused by a flow of buffer gas inside the gas cell during the activation of the getters.

3.6.2. The baking system

As mentioned in Sect. 3.2, baking of the set-up is of prime importance in order to guarantee optimum purity. Thus the whole set-up, including the pumps and the gas-supply system, can be baked with customised heating jackets and standard heating bands. Due to the size and shape of the vacuum chamber altogether 28 separate heating jackets are used. The maximum temperature applicable at the chambers must not exceed 200 °C, since some critical parts like the shutter valve connected to the gas cell cannot sustain higher temperatures.

The baking system is closed-loop controlled via temperature sensors (one for each heating element), which will be described in more detail in the Appendix. In general the system allows to choose between two options, a time ramp in order to reach a homogeneous heating and a control of all individual heating elements with static temperature values, respectively. The time ramp is used for the heating-up procedure, with 40 °C/h up to 100 °C and 20 °C/h up to the end temperature, and the cooling-down procedure, with 10 – 20 °C/h down to room temperature. The static temperature control is used for the continuous heating in order to keep the set temperature. The actual set-up is commonly baked at temperatures between 150 °C and 180 °C for at least three days.

3.7. The control system

The PC-control system for the gas cell and the RFQ is based on LabVIEW [Lab98], a program that provides a graphical user interface. The individually controlled systems communicate with LabVIEW via different interfaces using PROFIBUS, CAN-Bus and GPIB (General-Purpose-Interface-Bus).

In the actual set-up, as shown in Figure 3.21, three parts are computer-controlled, the iseg high voltage power supplies (CAN-Bus), the SRS DS345 function generators (GPIB) and the control system of the baking system (PROFIBUS). In the near future besides these parts the whole vacuum and gas-supply system will be added via PROFIBUS and an SPS unit. A more detailed description is given in the Appendix.

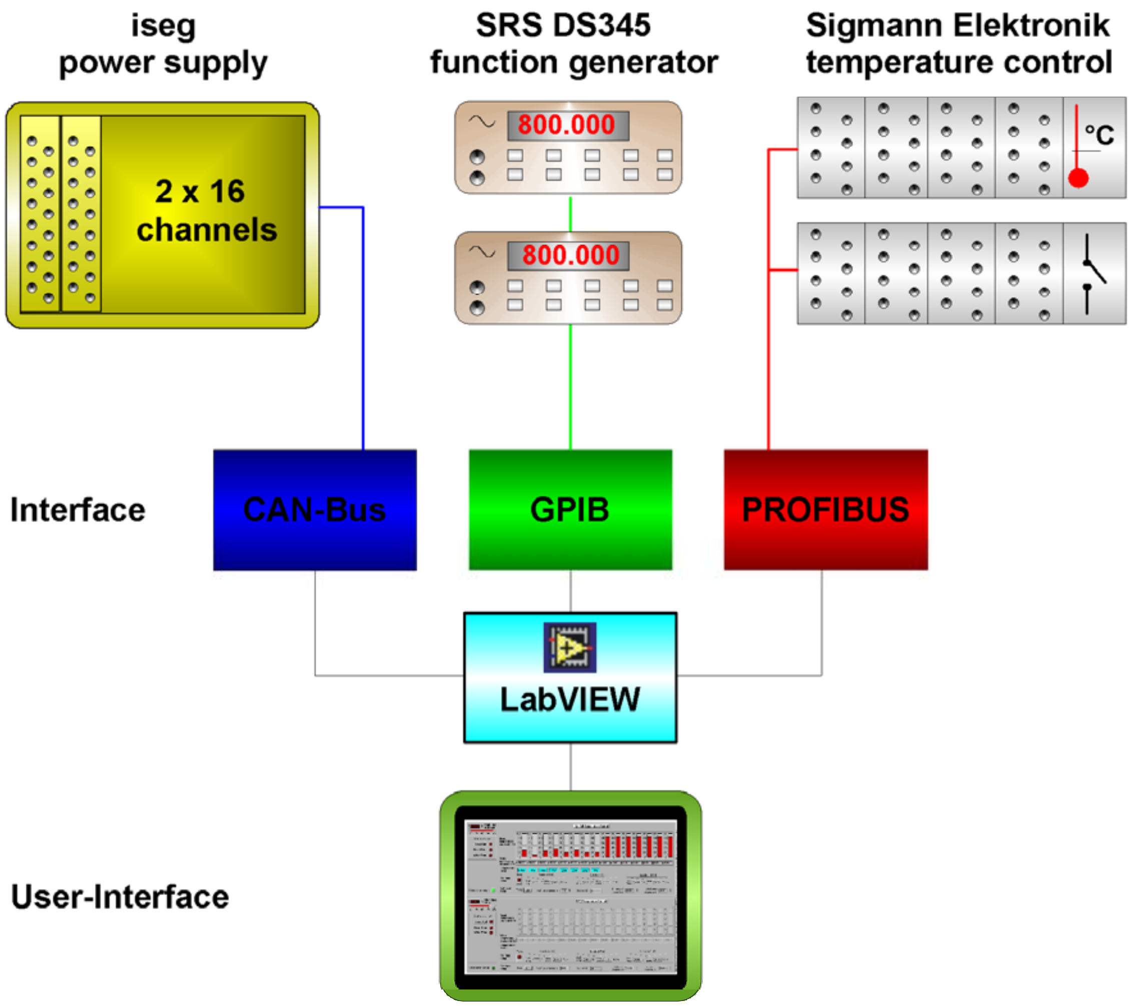
iseg
power supply
SRS DS345
function generator
Sigmann Elektronik
temperature control
2 x 16
channels
800.000
800.000
°C
Interface
CAN-Bus
GPIB
PROFIBUS
LabVIEW
User-Interface

Figure 3.21
The PC control system, used for the SHIPTRAP gas cell and extraction RFQ. The system is based on LabVIEW, communicating with the controlled modules via interfaces using CAN-Bus, GPIB and PROFIBUS.

Chapter 4

Characterisation of the ion extraction in off-line measurements

The off-line measurements using laser induced ions were performed at the Maier-Leibnitz Laboratory (MLL) at Garching and at GSI in order to optimise the field configurations for both a high extraction efficiency and a fast ion extraction. Compared with on-line measurements the advantage of this method is its flexibility concerning the availability of the tests ions and the independence of stopping efficiencies.

Nevertheless, as the number of created ions is not well defined, a determination of the absolute extraction efficiency using this method is not possible and only relative efficiencies can be compared.

4.1. The test set-up

Figure 4.1 shows the test set-up used for the laser measurements, performed at the MLL and at GSI. In both cases a pulsed, frequency-doubled Nd-YAG laser (CONTINUUM, 532 nm, MLL: 25/50 Hz, 200 mJ max, GSI: 1 – 5 Hz, 100 mJ max) and a filament, placed inside the gas cell at the inner side of the back-side electrode opposite to the entrance window were used for the ion production. The laser beam was routed by mirrors through a glass viewport placed at a side flange of the gas chamber. A movable lens in front of the window served to create the beam focus inside the cell.

The laser acts in two steps. At first the beam heated up the filament thus evaporating metal atoms into the gaseous environment. Some of these atoms were then ionised in the laser beam focus and were available for the studies of the acting fields and the gas flow.

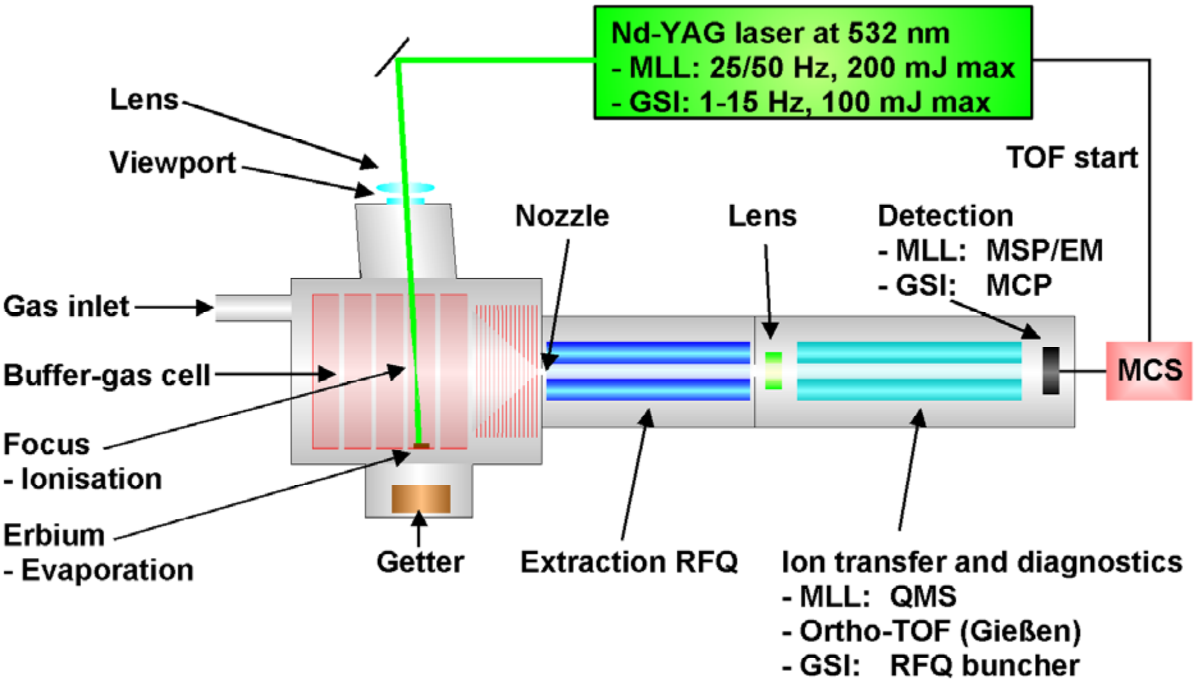
Nd-YAG laser at 532 nm
- MLL: 25/50 Hz, 200 mJ max
- GSI: 1-15 Hz, 100 mJ max
Lens
Viewport
TOF start
Nozzle
Lens
Detection
- MLL: MSP/EM
- GSI: MCP
Gas inlet
Buffer-gas cell
MCS
Focus
- Ionisation
Erbium
- Evaporation
Getter
Extraction RFQ
Ion transfer and diagnostics
- MLL: QMS
- Ortho-TOF (Gießen)
- GSI: RFQ buncher

Figure 4.1
Schematic view of the test set-up used for the laser measurements at the MLL and at GSI. The pulsed beam of a frequency-doubled Nd-YAG laser was routed by mirrors through a glass viewport, placed at a side flange of the chamber, onto a filament, placed inside the gas cell at the inner side of the back-side electrode opposite to the entrance window. With a movable lens in front of the window a beam focus inside the cell was created. The laser beam heated up the filament thus evaporating metal atoms into the gaseous environment. Then some of these atoms were ionised in the laser beam focus. At the MLL the ions were detected mass-selectively after the extraction out of the cell and after the transmission through the RFQ. At GSI the ions were transported by the SHIPTRAP RFQ buncher towards the detector.

At the MLL the ions were detected mass-selectively after the extraction out of the cell and after the transmission through the RFQ. In first tests a system consisting of a commercial QMS (Balzers) and a subsequent MSP (**M**icro **S**phere **P**late) [Naa96] was used. Later the MSP was replaced by a secondary electron multiplier type Hamamatsu R8810.
The set-up at GSI was different, since the SHIPTRAP RFQ buncher was used in transmission mode for the ion transport to an MCP (**M**icro **C**hannel **P**late) [Lad79] detector. As the buncher was only guiding the ions there was no effective mass-selectivity.
Since the various detectors gave different output data (current, single ion signals) and the conditions during the measurements varied, the spectra of Chapter 4 contain only relative efficiencies, normalised to the maximum value determined within one series of measurements.

Besides special tests, where different filament materials were used for a calibration of the QMS, usually erbium ions were produced inside the gas cell. Figure 4.2 shows a

plot of ion masses extracted out of the cell at a He pressure of 40 mbar, using natural erbium as filament material. The determined masses as well as their measured intensities correspond well to the four naturally most abundant Er isotopes (^{166}Er, ^{167}Er, ^{168}Er and ^{170}Er) with their natural abundances indicated in Fig. 4.2.
The substructure visible in the mass peaks is an artefact of the measurement with the QMS [Daw76].

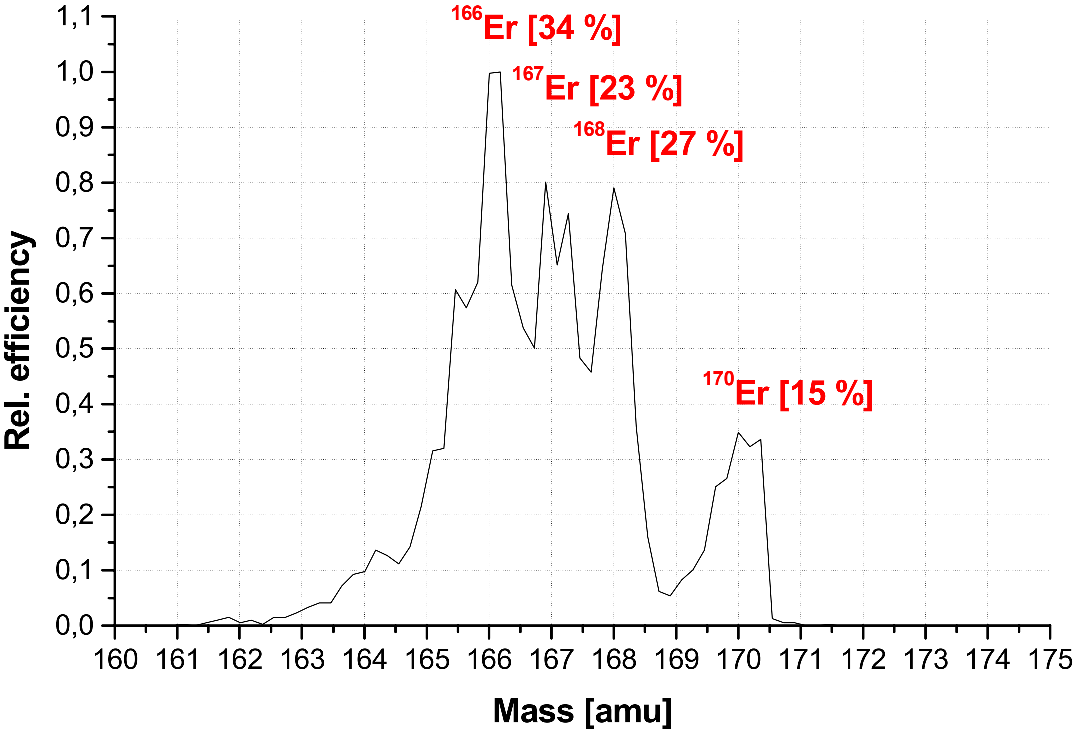

Figure 4.2
Plot of the extracted masses from the tests with laser-ionised ions in 40 mbar He using natural Er as filament material. Indicated are the natural abundances of the Er isotopes ^{166}Er, ^{167}Er, ^{168}Er and ^{170}Er, which correspond well to the measured intensities. The substructure in the mass-peaks is a measurement artefact of the QMS [Daw76].

4.2. Field optimisations

In a first step the laser-induced Er-ions were used to investigate and to optimise the electrical fields inside the cell and the RFQ as a function of the buffer-gas pressure.

Starting from the origin of the laser-induced Er-ions, the first point of interest is the ion transfer from the DC electrodes to the RF funnel. Figure 4.3 shows a plot of the relative extraction efficiency as a function of the voltage difference between the exit of the DC electrode and the first RF-funnel electrode at its entrance at a distance of 25 mm. The measurement was done at a He gas pressure of 52 mbar and an RF voltage of 160 V_{pp} at a frequency of 400 kHz and a DC gradient of 1 V/mm applied at the funnel. Between a voltage difference of 40 V and 80 V an almost constant maximum in the extraction efficiency is visible. This maximum may be explained by an optimum balance between the extraction time and the ion velocity, on the one hand a high field strength leading to a rapid ion extraction helps to avoid ion losses caused by neutralisation and molecule formation. On the other hand, however, too large ion velocities may exceed the repulsive RF force thus leading to ion losses on the funnel electrodes.

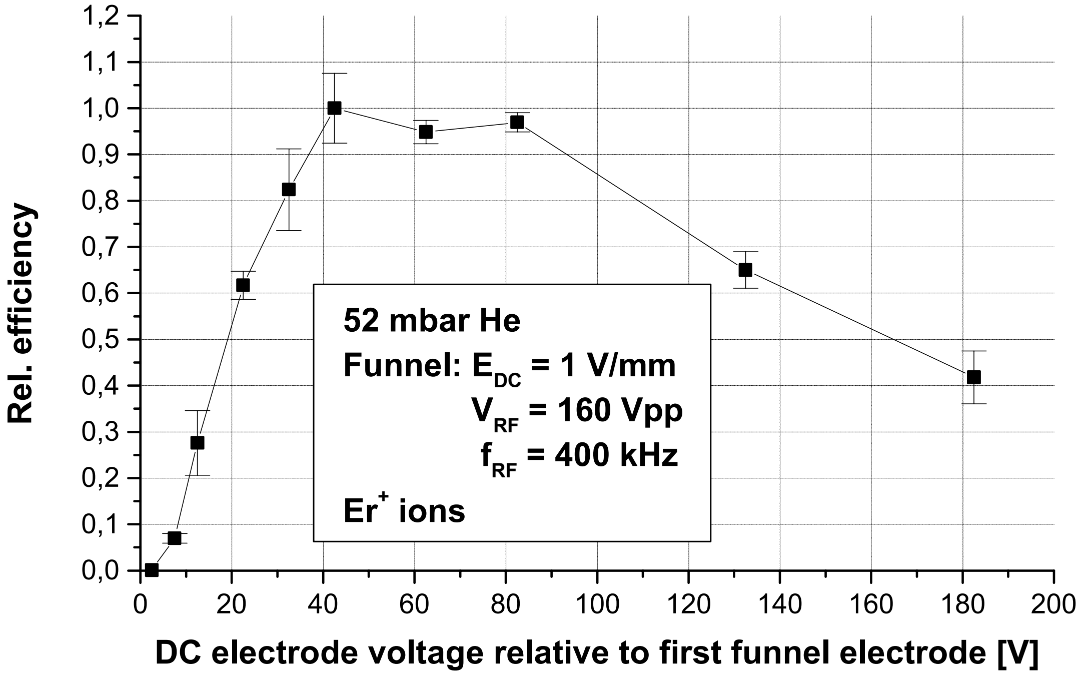

Figure 4.3

Normalised extraction efficiency of Er^+ ions as a function of the DC voltage difference between the DC electrode and the first funnel electrode. Between 40 V and 80 V a nearly constant maximum of the efficiency is visible.

Figure 4.4 shows a plot of the relative extraction efficiency of Er^+ ions as a function of the RF amplitude applied at the funnel at a fixed helium gas pressure of 25 mbar (exemplarily chosen) and a DC field of 10 V/cm. The measurements were done at different RF frequencies, two of them are shown exemplarily in Fig. 4.4. During the measurements the amplitude applied at the funnel was increased until discharges occurred inside the cell.

Clearly visible in Fig. 4.4 is the lower breakthrough voltage of 160 V_{pp} at 1000 kHz in comparison with 190 V_{pp} at 500 kHz during this measurement.

The comparable characteristics of the normalised extraction efficiency curve for both frequencies shows the independence of the applied frequency, as predicted by Eq. (2.100). The flat behaviour at 500 kHz beyond ~180 V_{pp} could be a hint for a plateau of the transport efficiency at higher amplitudes.

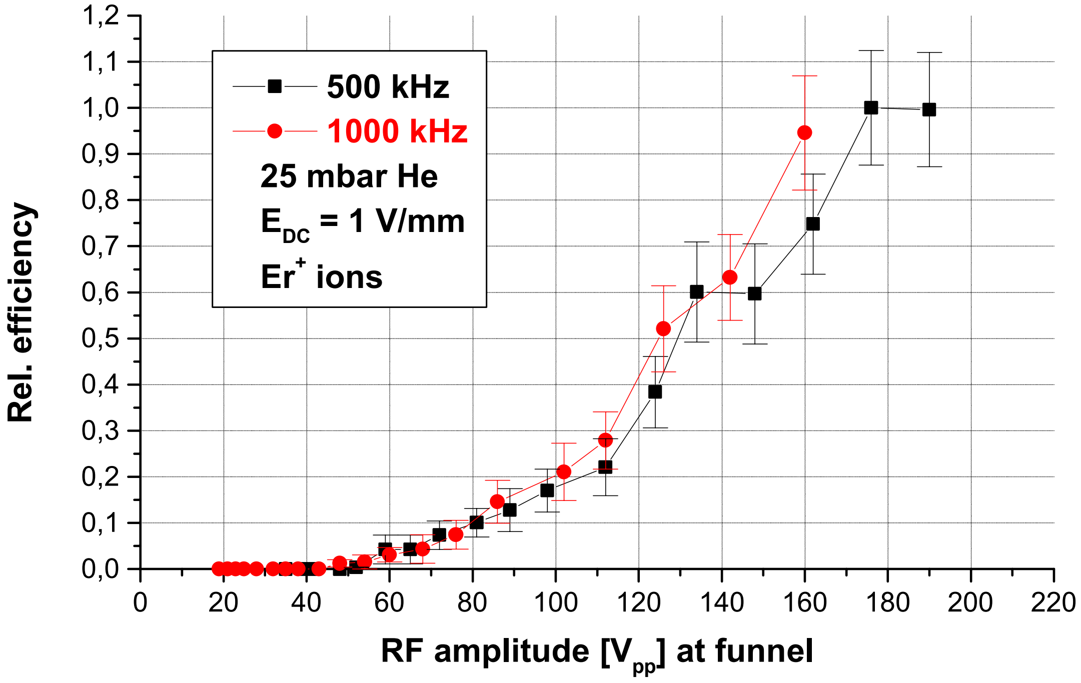

Figure 4.4
Normalised extraction efficiency of Er^+ ions as a function of the RF amplitude applied at the funnel for two different RF frequencies at a buffer-gas pressure of 25 mbar. For the measurements the amplitude was increased until discharges occurred inside the funnel structure, thus marking the upper end of the two curves.

This effect was seen by chemists using an RF-funnel device for the ion focusing during mass spectrometry measurements [Sha98]. There the RF amplitude was varied over a wide range at fixed RF frequencies. The measured currents of transported ions showed a maximum at a certain amplitude, while for higher amplitudes the efficiency decreased drastically. This can be explained by a trapping potential created by the RF voltage at the exit part of the funnel, an effect that occurs not only at large RF amplitudes but also at large RF frequencies.

Using again Eq. (2.100), the RF amplitudes required at higher gas pressures in order to create the same effective electrical field can be estimated with the amplitude value of around V_{RF} = 180 V_{pp} at the transport maximum of Figure 4.4. Together with an assumed ion mobility $K_0 = 20\,\mathrm{cm^2/Vs}$ and taking into account the distance $d_0 = 1$ mm of the ring electrodes of the funnel the depth of the optimum effective potential for singly charged ($q = 1$) Er ions ($m \approx 170$) in the SHIPTRAP funnel is given by

$$\Phi_{eff}(d_0) = \frac{mV_{RF}^2 K^2}{4qd_0^2} \approx 90\,\mathrm{V}.$$

Since the needed RF amplitude increases quadratically with the gas pressure an amplitude of 2880 V_{pp} would be required for a buffer-gas pressure of 100 mbar in order to reach the same effective potential of around 90 V. As the breakthrough voltage increases not quadratically with the pressure the transport efficiency will decrease at higher values of the buffer-gas pressure due to limitations given by discharges.

Figure 4.5 shows the same type of measurement as Fig. 4.4, however in this case the gas pressure is 52 mbar and the RF amplitude at the funnel of 170 V_{pp} is fixed, while the frequency is varied. As before, also this measurements proves (within experimental uncertainties) that the extraction efficiency due to the repulsive RF field of the funnel is independent of the frequency (above a lower limit of about 400 kHz) as predicted by Eq. (2.100).

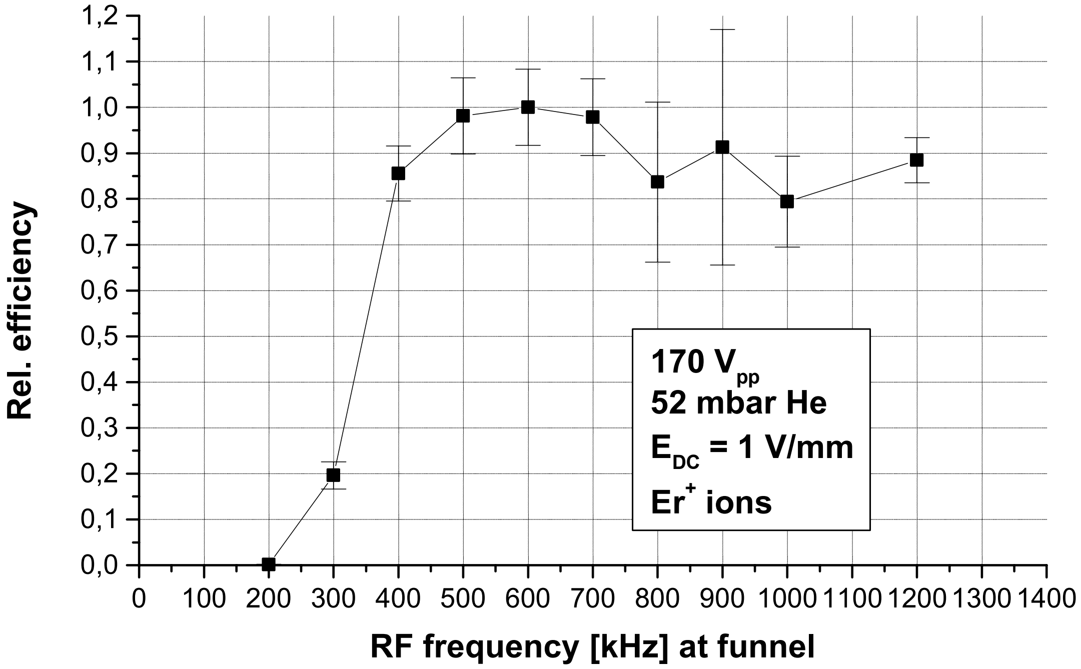

Figure 4.5
Extracted laser-ionised Er^+ ions at a gas pressure of 52 mbar as a function of the RF frequency applied to the funnel electrodes at a fixed RF amplitude of 170 V_{pp}. The transport efficiency of the funnel does not depend on the RF frequency, as predicted by Eq. (2.100).

As mentioned in Sect. 3.4 the ion velocity directly in front of the extraction nozzle determines the efficiency of the transition of the ion transport from electrical guiding fields to the gas flow in the vicinity of the nozzle. In case of the ion velocity being higher than the gas flow velocity the ions will continue to follow the electrical field lines and will be lost after hitting the nozzle surface. Therefore a deceleration of the ions in front of the nozzle by applying a higher DC voltage at the nozzle relative to the last funnel electrode has to be considered. Figure 4.6 shows a plot of the relative extraction efficiency as a function of the relative voltage between the extraction nozzle and the adjacent funnel electrode for three different values of the buffer-gas

pressure. For 32 mbar and 43 mbar the extraction exhibits a maximum at a voltage difference of +2 V, while this maximum is shifted to +3 V at 21 mbar helium pressure. Beyond these values the efficiency decreases rapidly. The different slope at negative relative voltages for the three pressure values can be explained by the increasing damping of the gas at higher pressure values. For voltages below the efficiency maximum the efficiency decreases with a steeper slope for increasing gas pressure. The behaviour at 21 mbar may be caused by a combination of gas damping, gas flow and electrical fields. For a quantitative explanation of these effects further simulations at different gas pressures using VARJET and SIMION are required.
All measurements shown further on have been performed with a relative voltage of +2 V between the last funnel electrode and the nozzle.

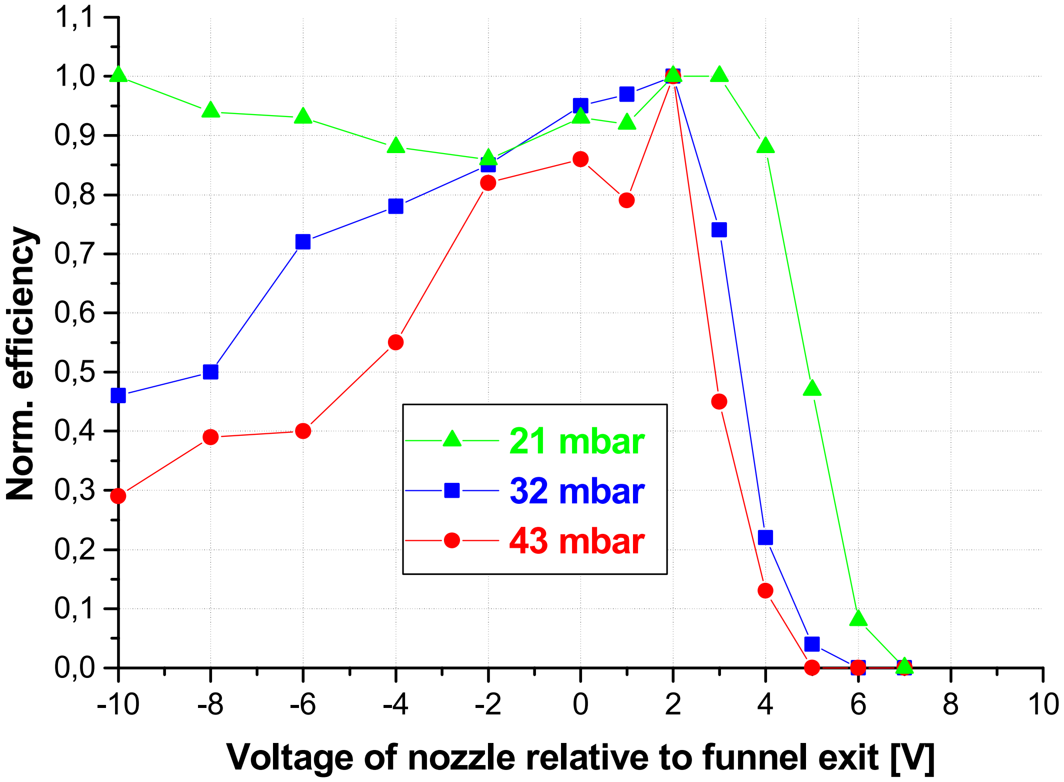

Figure 4.6
Normalised efficiency for laser-induced Er ions as a function of the relative voltage between the last funnel plate and the nozzle. The voltage applied at the last funnel plate was 60 V. For all three pressure values the extraction efficiency exhibits a maximum at a difference of about +2 V. The behaviour at voltages below the maximum seems to reflect the interplay of gas damping and electrical fields and has to be quantitatively clarified with simulations.

Another point of interest is the transfer of the ions from the nozzle into the extraction RFQ. Besides the gas jet, the transfer efficiency is also influenced by the voltage between the nozzle and the first segment of the RFQ. Figure 4.7 shows the relative extraction efficiency as a function of the potential difference and the gas pressure.

For these measurements the voltage applied at the nozzle was fixed to 62 V, while at the extraction RFQ an amplitude of 100 V_{pp} at a frequency of 800 kHz and a DC ramp of 0.3 V/cm were applied.

The efficiency shows for all three pressure values a comparable trend. The ion transfer starts at a relative voltage of -4 V, corresponding to the maximum energy of the ions extracted by the gas flow. In the 'deceleration regime' between -4 V and 0 V potential difference almost no influence of the helium pressure in the gas cell is visible. This may be explained by a compensation of the faster and thus more efficient extraction at higher gas-cell pressures by the consequently larger damping of the ambient buffer-gas pressure in the entrance region of the RFQ. Then a transfer maximum is reached, where the corresponding relative voltage depends on the gas pressure. The higher the helium pressure in the gas cell and consequently also the ambient pressure in the extraction chamber, the lower the relative voltage between nozzle and first RFQ segment needed to achieve an extraction maximum. This behaviour as well as the efficiency behaviour for higher voltage differences reflects the influence of the gas jet. Higher values of the gas pressure inside the stopping cell will result in higher velocities of the gas flow through the nozzle, thus less acceleration is needed for the optimum transfer into the extraction RFQ.

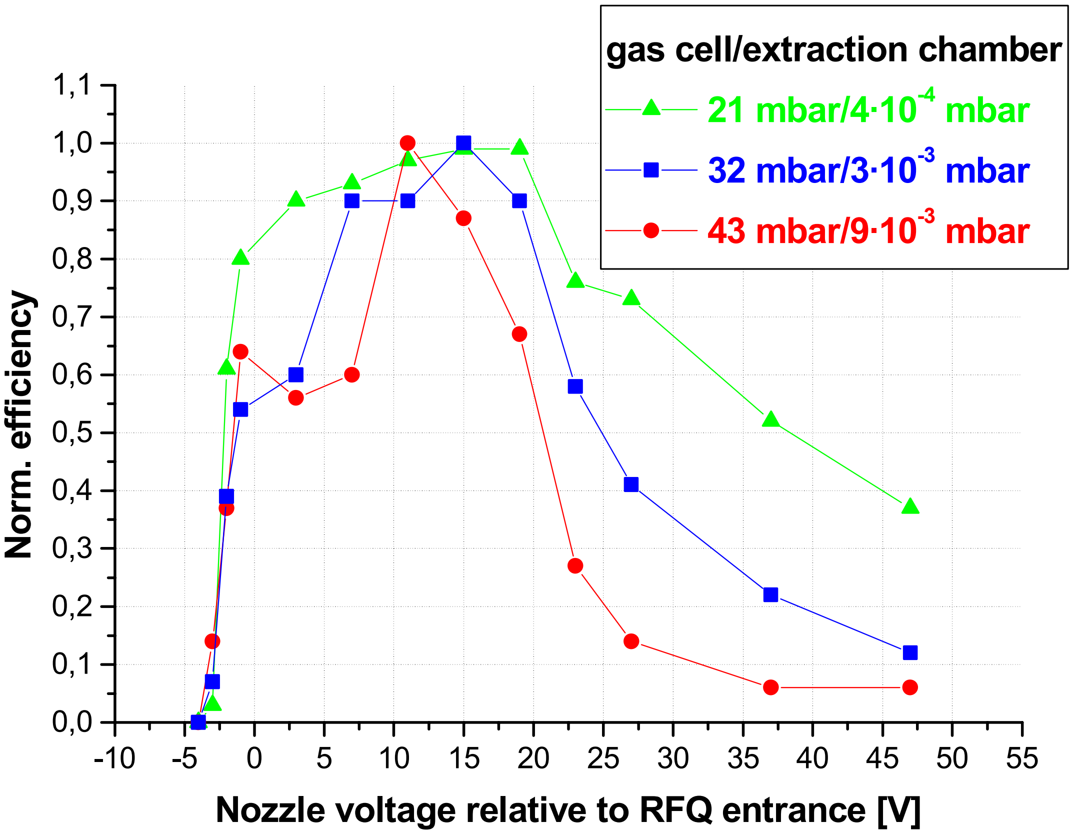

Figure 4.7

Normalised extraction efficiency for laser-induced Er ions as a function of the voltage difference between the first RFQ segment and the extraction nozzle for three combinations of the buffer-gas pressure inside the gas cell and the extraction chamber. The voltage applied at the nozzle was 62 V.

Besides the extraction of the ions out of the cell the transport inside the RFQ structure has to be optimised. The transfer inside the RFQ can be determined by a scan of the applied RF amplitude at a fixed RF frequency resulting in a relation between *q* value (see Sect. 2.3.2) and the corresponding relative transfer efficiency. Figure 4.8 shows a plot of the relative transfer efficiency for Er^+ ions detected behind the RFQ as a function of the *q* value at a pressure of around 10^{-3} mbar inside the extraction chamber. A fixed RF frequency of 800 kHz and a DC ramp of 0.3 V/cm were applied to the RFQ, while the RF amplitude was varied between 0 and 400 V_{pp}.
As visible in Fig. 4.8, a transmission of the ions can be achieved for *q* values between about zero and 0.9, as expected from the theory for an RFQ in vacuum. However, in contrast to theoretical expectations, the transmission maximum occurs at *q* values around 0.2 instead of 0.6 as expected. A similar transmission behaviour has been observed for the Jyväskylä RFQ structure [Nie01].
Besides the shifted maximum the transmission curve shows a staggering with subsequent local maxima and minima. There are two possible explanations for the ion losses in the minima. One reason may be the occurrence of instabilities in the RFQ trajectories due to anharmonics caused by higher-order contributions to the ideal pure quadrupole potential [Gud96]. These contributions could be caused by the finite electrode structure, by the non-hyperbolic shape of the electrodes and by misalignments.

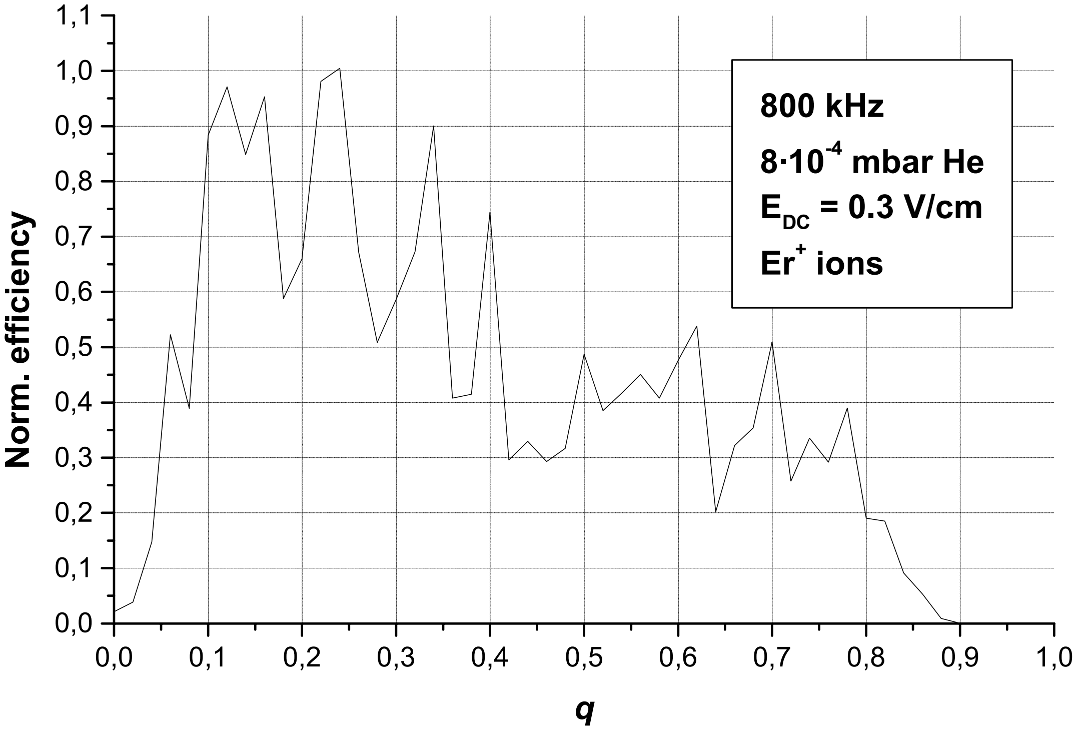

Figure 4.8
Plot of a scan for the *q* value of the RFQ, showing the normalised transfer efficiency measured from laser-induced Er^+ ions extracted from the gas cell and detected behind the RFQ. For a fixed RF frequency of 800 kHz the RF amplitude was varied between 0 V_{pp} and 400 V_{pp}. Ion losses at different positions are clearly visible and may be explained by

instabilities in the ion trajectories due to anharmonics or by losses at the exit aperture of the RFQ.

Another reason could be attributed to losses due to the diameter of the exit aperture of the RFQ. Simulations for transmission studies on RF-only quadrupoles [Mun95] showed a similar staggering in the transmission curve for certain sizes of the aperture. For different *q* values antinodes of the stationary wave form of the ion beam inside the RFQ are placed near the exit aperture. As a result the number of ions passing through the exit is reduced.

4.3. Extraction time measurements

The second characteristic parameter of the gas cell performance besides the extraction efficiency is the extraction time of the stopped ions. In order to measure this extraction time a photo diode is added to the test set-up. The signal induced by the laser pulse in the photo diode is used as start trigger for the time measurement with a multi-channel scaler (MCS). Extraction times were measured as a function of the gas pressure inside the cell for different field configurations. Figure 4.9 shows as an example time-of-flight spectra for Er^+ ions at a buffer-gas pressure of 40 mbar. The voltage applied at the DC electrode was 180 V, 280 V and 340 V, respectively, while at the funnel a DC gradient of 1 V/mm and an RF voltage of 160 V_{pp} at 400 kHz were applied. With these configurations minimum extraction times between 3.2 ms and 5.2 ms were reached.

Besides the peak of ions created in the laser focus on the longitudinal axis of the gas cell a second peak for every voltage is visible. This peak corresponds to another area placed off-axis near the DC electrode where ions were produced by the laser. However, removing the focussing lens and directly shining the laser onto the Er filament resulted in the loss of any signal from extracted ions, thus contradicting the assumption of the second component being produced at the filament position. Further investigations with a shifted laser focus are needed to clarify the origin of the second component.

In contrast to the peak of ions produced near the axis, which has a nearly constant contents for all three DC voltages, the contents of the second peak clearly depends on the applied voltage, i.e. the ion velocity. For higher acceleration voltages not only the extraction time difference between the two components is decreasing, in addition the intensity of the second (off-axis) component is gradually vanishing, while the intensity of ions extracted from the laser focus stays constant. This may be explained by the same effect as shown in Fig. 4.3, where the extraction efficiency as a function of the relative voltage between DC electrode and funnel entrance was shown. In this case the lower efficiency at voltage differences larger than 80 V could be explained by losses of ions created near the surface of the DC electrode which are accelerated due to the electrical field to the funnel electrodes near the entrance of the funnel. In both situations with increasing ion velocities due to increasing field strengths the efficiency of the repulsive RF forces will decrease at a fixed RF voltage. These losses have to be considered during on-line measurements when the cloud of stopped ions is not centred on the extraction axis or when the centred cloud fills the volume of the DC electrodes (as especially given in the case of an ion injection perpendicular to the extraction axis).

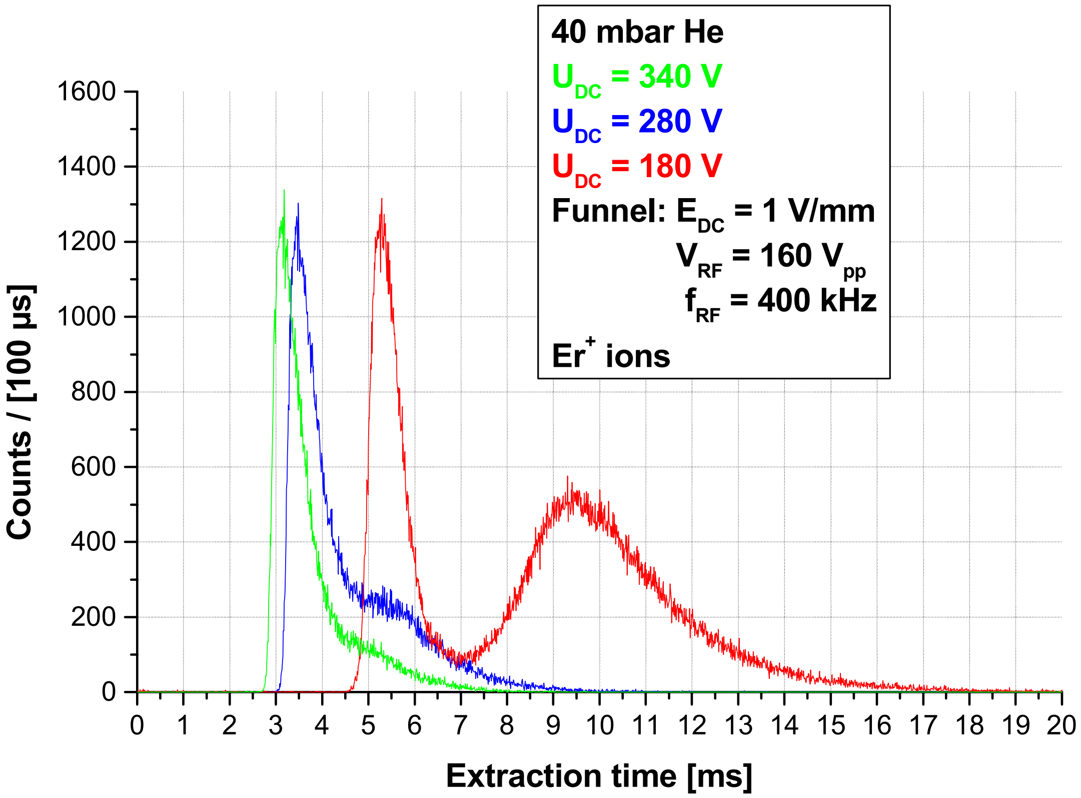

Figure 4.9
Time-of-flight spectra determined for Er^+ ions at a buffer-gas pressure of 40 mbar inside the gas cell. Minimum extraction times between 3.2 ms and 5.2 ms were determined. Besides the ions produced along the gas cell axis a second group of ions is visible. They may be produced off-axis at the filament.

In Figure 4.10 the mean extraction times for the situation shown in Fig. 4.9 are displayed. The extraction times for ions produced on axis or (potentially) at the filament are shown as a function of the relative voltage between the DC electrode and the first funnel electrode. The extrapolated values show that for voltages higher than 220 V only negligible improvements of the extraction time can be expected. In particular with regard to the efforts required for higher voltages, where discharges in the buffer gas have to be avoided, an optimum is reached at voltages around 220 V.
Taking into account the results showed in Fig. 4.3, where an optimum extraction was found at a voltage difference in the range of ΔU ≈ 60 – 80 V, while at 220 V the efficiency decreased dramatically, it has to be considered which setting would cause higher ion losses.

In particular when regarding the need of a fast extraction in order to avoid molecule formation and losses due to neutralisation, a compromise depending on the particular situation has to be found.

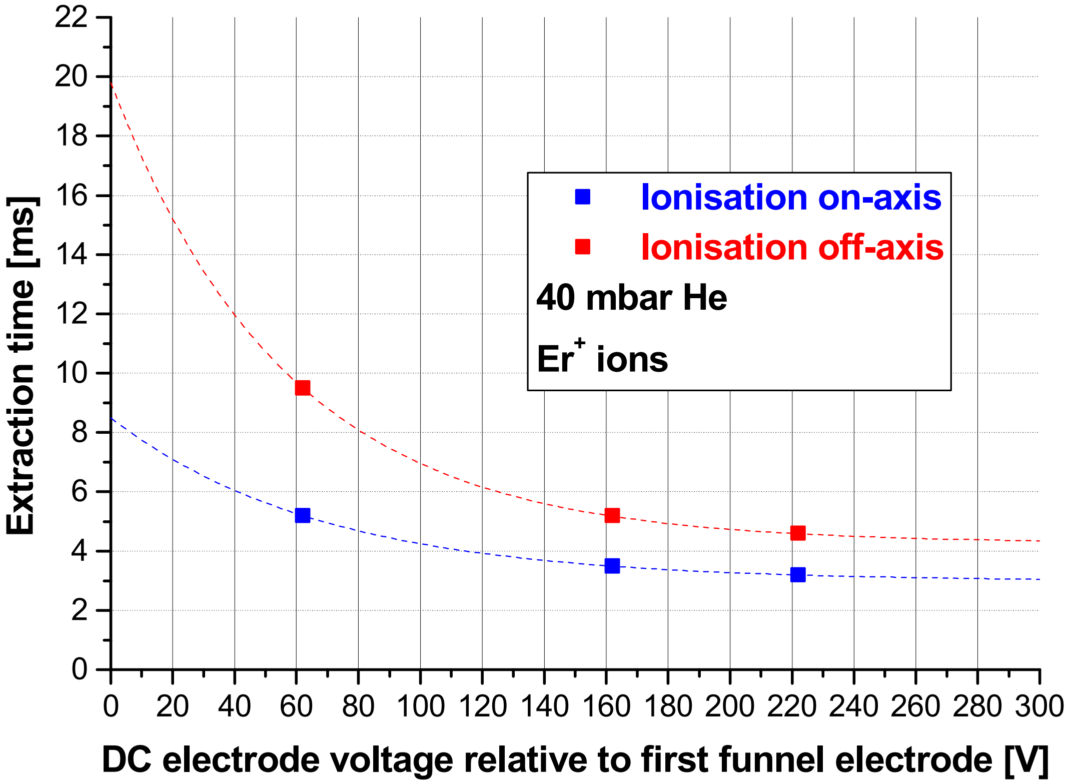

Figure 4.10
The extraction times for the two components of extracted ions shown in Fig. 4.9 as a function of the voltage between DC electrode and first funnel electrode. The dashed lines correspond to (exponential) fits to guide the eye. The extrapolated extraction times for voltages higher than 220 V show that the achievable gain in the rapidity of the extraction is low compared to the efforts necessary in order to reach these potentials due to possible discharges in the buffer gas.

Figure 4.11 shows the results of time-of-flight measurements for three different settings as a function of the gas pressure for ions produced on the extraction axis. The voltages applied at the backside DC electrode were varied between 145 V and 280 V. In all cases the same voltage was applied to all segments of the backside electrode structure. The DC ramp applied to the funnel started at maximum voltages of 100 V and 130 V, respectively, with a decrease of 10 V/cm.

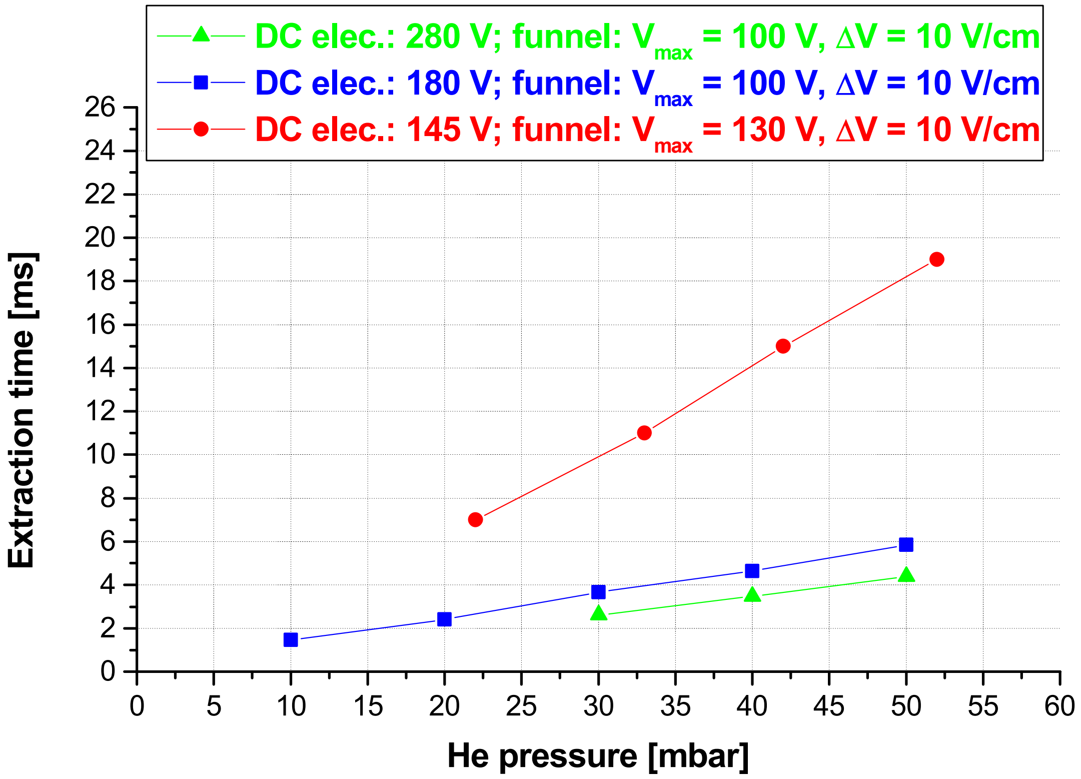

Figure 4.11

Measured extraction times of laser-induced Er^+ ions as a function of the helium buffer-gas pressure at different voltages applied at the cell electrodes.

For the highest accelerating fields extraction times around 5 ms at a buffer-gas pressure of 50 mbar were measured, whilst for a low-field configuration an extraction time around 20 ms was observed. Since the electrical fields typically applied inside the gas cell range between these extreme values, mean extraction times around 10 ms at a gas pressure of 50 mbar can be achieved for ions stopped in the centre of the stopping volume. As the relation between the extraction time and the gas pressure is linear at fixed applied potentials, values for higher pressures can be extrapolated from the measured results.

Figure 4.12 schematically shows the optimum distribution for the DC potentials within the set-up found during the optimisation measurements with laser-induced ions. Since the influence of the first DC electrodes on the ions produced within the last two electrodes is small, an optimum value for the DC gradient is not given.

A significant dependence of the extraction efficiency on different DC gradients in the RF funnel was not observed. This could be explained by the small ionisation region of the laser focus near the extraction axis, where the transport characteristic of the funnel is not as important as for a broad ion distribution.

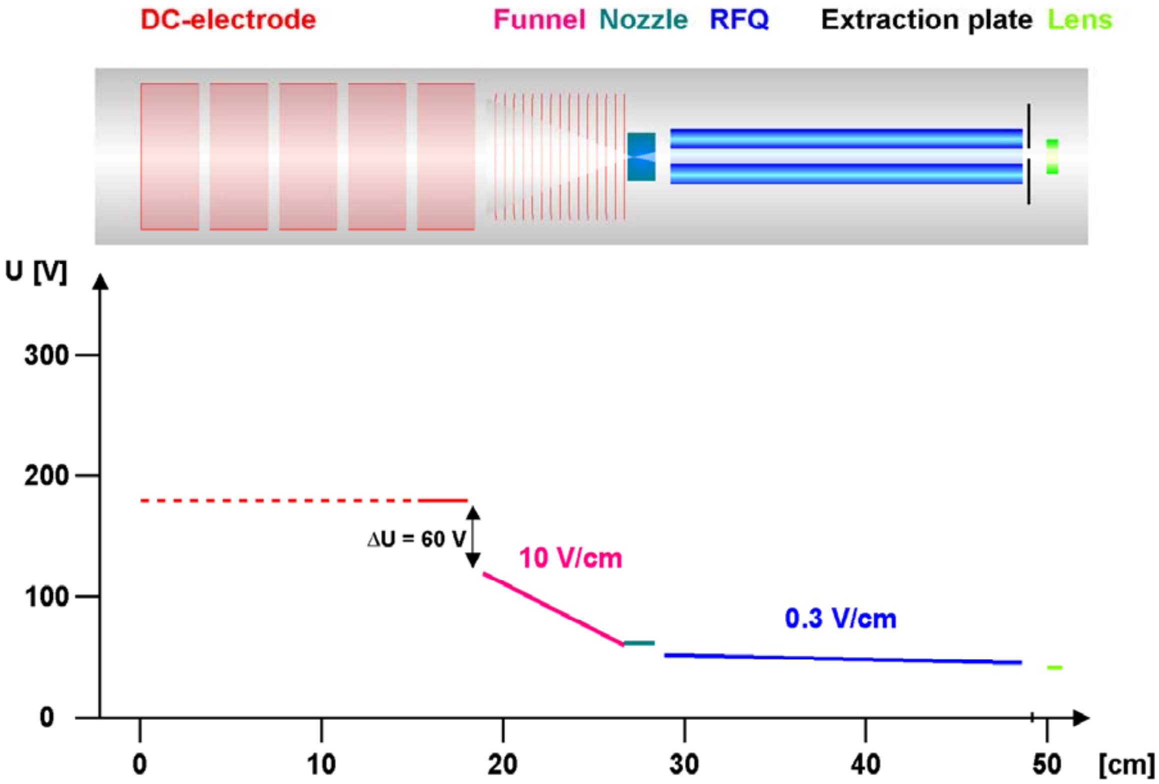

Figure 4.12
Schematic view of the optimum distribution for the DC potentials found during the optimisation measurements with laser-induced ions. An optimum value for the DC gradient is not given, since the influence of the first DC electrodes on the ions produced within the last two electrodes is small.

Chapter 5

Determination of the extraction efficiency via on-line measurements

The on-line measurements were performed in order to add the stopping behaviour to the extraction characteristics of the gas-cell/RFQ system. For these studies both stable primary ion beams and radioactive secondary ions were used.

The on-line tests with the gas cell and the extraction system were performed at the accelerator facilities of the Maier-Leibnitz Laboratory (MLL) in Garching and at GSI. For some experiments at GSI the gas-cell and RFQ set-up was integrated into the SHIPTRAP set-up, mainly using the RFQ buncher and its diagnostics system.

In contrast to the measurements under SHIPTRAP conditions at GSI with an almost perpendicular ion injection, the experiments at the MLL were performed with a longitudinal injection into the gas cell.

5.1. On-line measurements at the MLL in Garching

The dominant part of the measurements to characterise the performance of the gas-cell and extraction-RFQ combination was performed using ion beams delivered to a dedicated beam line by the Tandem accelerator of the MLL in Garching. Besides the flexible availability of beam time, allowing for frequent beam measurements, the capability of rapid changes of the ion species and beam energies is a major advantage of the Garching test installation.

Stable primary ion beams were used as well as radioactive fusion reaction products. In order to separate the latter from the non-reacting primary beam a large 90° dipole magnet was added to the beam line, as will be discussed in Section 5.1.2.

5.1.1. Measurements with stable ion beams

The tests performed with stable ions were done in collaboration with the Gießen group and their Ortho-TOF spectrometer [Zho00, Eli04] in order to allow for a high-resolution mass-selective ion diagnostics.

Figure 5.1 schematically shows the components of the Ortho-TOF spectrometer and the trajectories of the ions inside. The ion mass is determined via the measurement of the time of flight at a fixed kinetic energy.

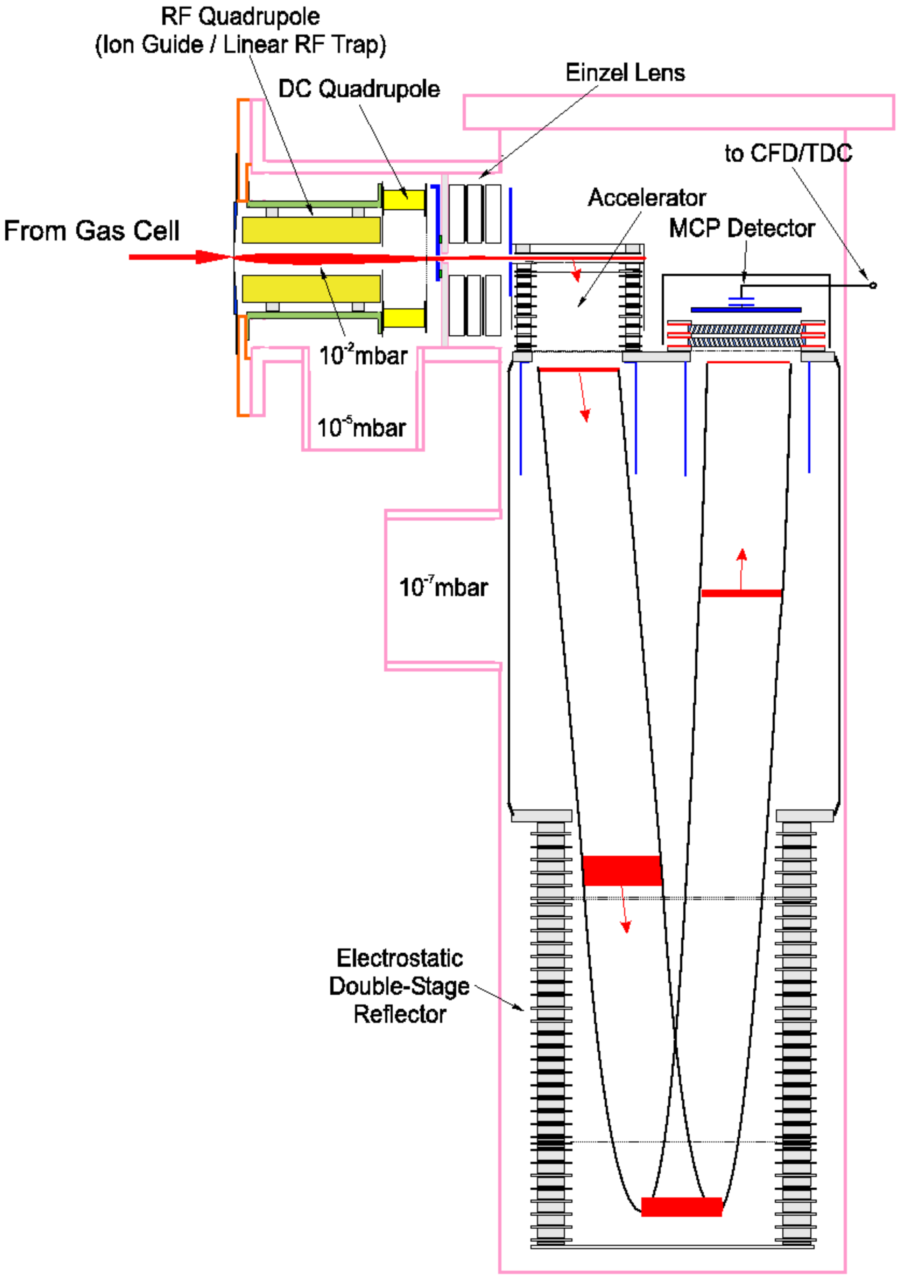
RF Quadrupole
(Ion Guide / Linear RF Trap)
DC Quadrupole
Einzel Lens
to CFD/TDC
Accelerator
MCP Detector
From Gas Cell
10^{-2}mbar
10^{-5}mbar
10^{-7}mbar
Electrostatic
Double-Stage
Reflector

Figure 5.1
Schematic view of the Gießen Ortho-TOF spectrometer [Zho00]. The ions are injected into the RFQ where they are cooled. The ions are then accelerated, reflected and detected with an MCP detector. Thereby the time of flight is measured in order to determine the ion mass. Using the working area twice helps to improve the accuracy without having to enlarge the set-up.

In order to improve the accuracy of the measurement without an enlargement of the set-up, the spectrometer is designed as a so-called multi-TOF spectrometer, where the working section is traversed several times by the ions. The naming of the Ortho-TOF spectrometer is based on the working area attached perpendicular to the longitudinal axis of the incoming ions.
The Gießen Ortho-TOF typically has a mass resolution of $\delta m/m \approx 10^{-4}$ and an overall transmission efficiency of about 1 – 3 % [Pla03].

For the measurements at the MLL the spectrometer was directly connected to the extraction chamber, as shown in Figure 5.2 and Figure 5.3. Prior to the on-line measurements the detection efficiency of the TOF was determined to be in the range of $2.5 - 3.5 \cdot 10^{-3}$, which has to be taken into account for the characterisation of the overall efficiency of the gas-cell/RFQ set-up.
Although the ion transfer between extraction RFQ and TOF was optimised by using laser-induced ions (see Chapter 4), the transfer efficiency is not quantitatively known and is therefore assumed to be 100 % for the determination of the system efficiency.

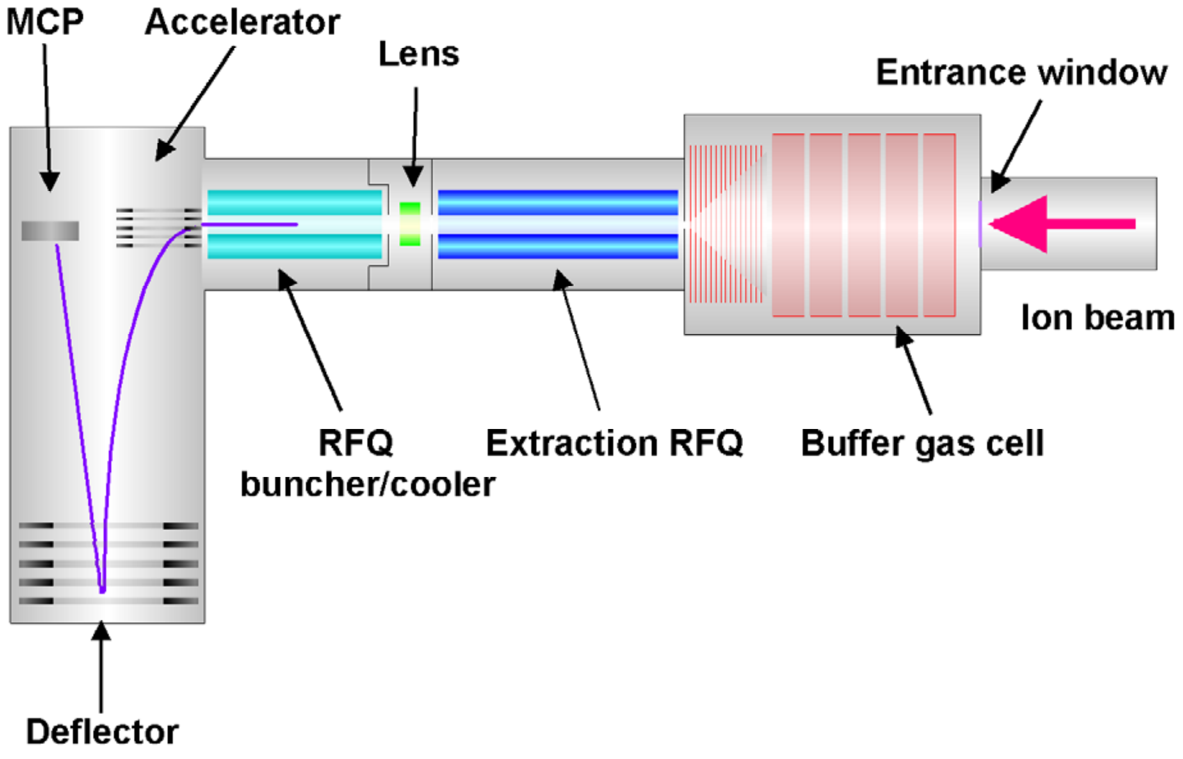

Figure 5.2
Schematic view of the set-up used for the on-line measurements with stable ions at the MLL. Following the extraction chamber the Gießen Ortho-TOF spectrometer was connected to the system.

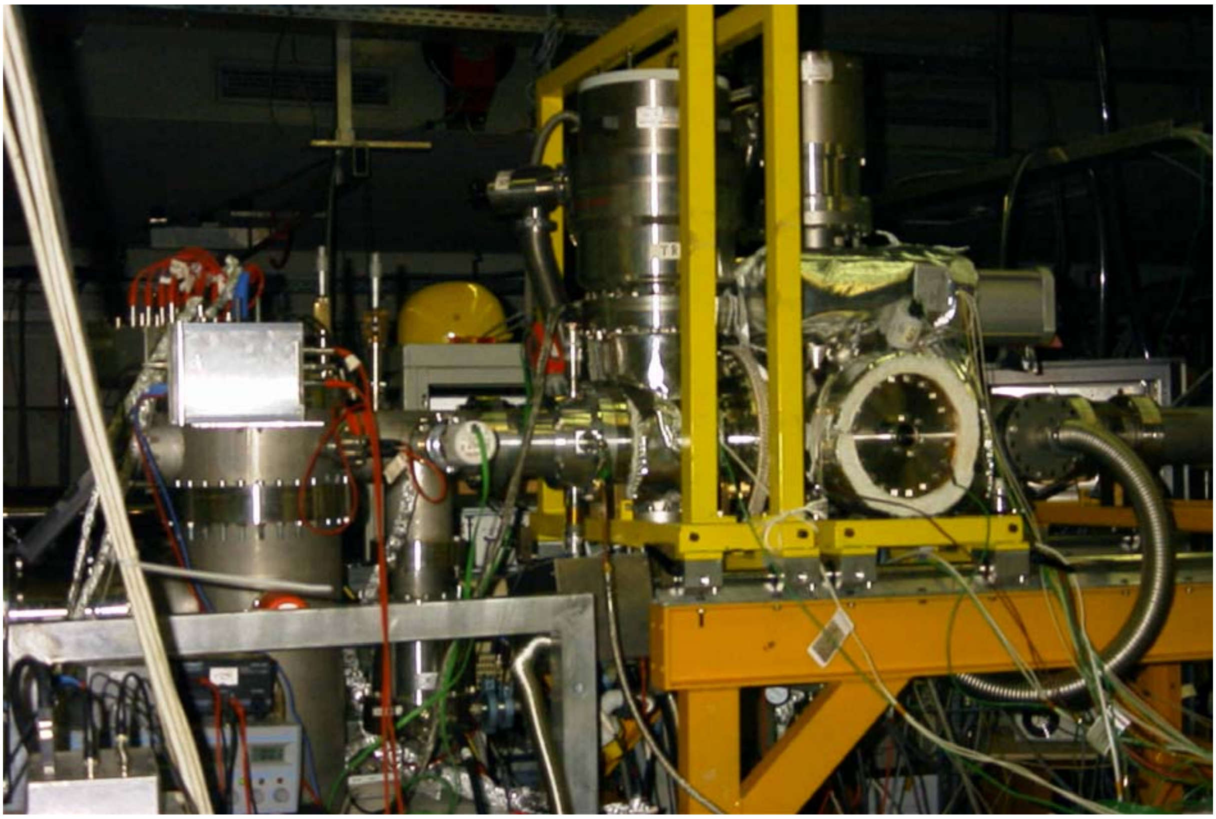

Figure 5.3
Photograph of the set-up with the Gießen Ortho-TOF mass spectrometer (left hand side) connected to the extraction chamber.

The measurements together with the TOF spectrometer were performed with a ^{107}Ag beam at different intensities from the Tandem accelerator. The initial energy of the ^{107}Ag^{3+} ion beam from the accelerator was 24 MeV. A carbon stripper foil (25 µg/cm^2) placed in front of the dipole magnet was used to increase the charge state in order to allow for a transport of the ions across the 90° bending magnet, optimised for the transmission of ^{107}Ag^{17+} ions. The energy loss of 1 MeV in the carbon foil finally reduced the Ag ion energy in front of the gas cell to 23 MeV.
The He buffer-gas pressure inside the cell was fixed at 40 mbar for all measurements, which is the optimum value for the beam energy in combination with the Ti window foil with a thickness of 4 µm (1.8 mg/cm^2).

Figure 5.4 shows a mass spectrum of ions detected in the range of 70 – 220 amu. Besides the dominant peak of the ^{107}Ag test ions also molecules of silver with water and ionised contaminants are visible. While the noble gases Kr and Xe could be attributed to the gas-supply system, the source of the mercury contributions (the most abundant natural isotopes are determined exactly with their natural relative abundances) is not clear. One possibility is the soldering between the stainless steel and the ceramic ring of the nozzle holder (see Sect. 3.4), potentially containing an amalgam component.

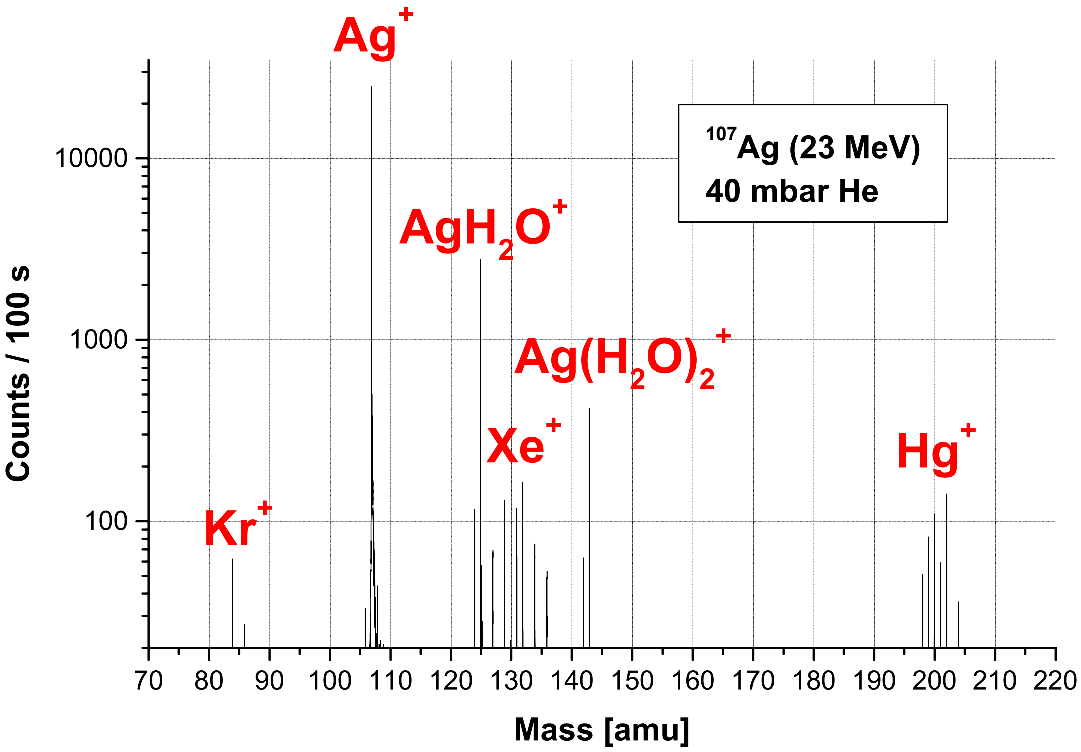

Figure 5.4
Plot of the extracted masses during an on-line test with a ^{107}Ag beam. Besides the ^{107}Ag peak, peaks around the masses 84, 125, 130, 142 and 200 are visible. The peaks correspond to the noble gases Kr and Xe, to compounds between water and Ag and to a series of mercury isotopes possibly resulting from a metal/ceramic soldering connection at the nozzle holder.

Similar to measurements with laser-induced ions, the silver ions were used for electrical-field optimisations. In contrast to the off-line measurements, where the ions were created in a small area around the laser focus, the stopping of the ions during the on-line tests allow for studies of a broad ion distribution.
All following measurements were performed unless otherwise stated at a beam intensity of $3.7 \cdot 10^7$ ^{107}Ag^{17+} ions per second corresponding to 5.9 ppA.

In a first measurement the transfer efficiency from the DC electrode to the RF funnel as a function of the potential difference between them was studied. Figure 5.5 shows a plot of the stopping and extraction efficiency of Ag$^+$ ions as a function of the relative voltage between the last DC electrode and the first funnel electrode at a He gas pressure of 40 mbar. An RF voltage with an amplitude of 160 V_{pp} at a frequency of 700 kHz and a DC gradient of 1 V/mm were applied to the funnel. Compared to Fig. 4.3 a similar behaviour with an efficiency maximum at a voltage difference of around 40 V is visible. Reasons for the narrower maximum compared to the situation with laser-induced Er-ions may be found in the broader distribution of the stopped Ag ions compared to the compact distribution of the laser-induced ions and in the lower buffer-gas pressure. The broader ion distribution on the one hand leads to a larger fraction of ions transported close to the funnel electrodes, with a larger probability of losses (previously shown in the laser measurements of Sect. 4.3).

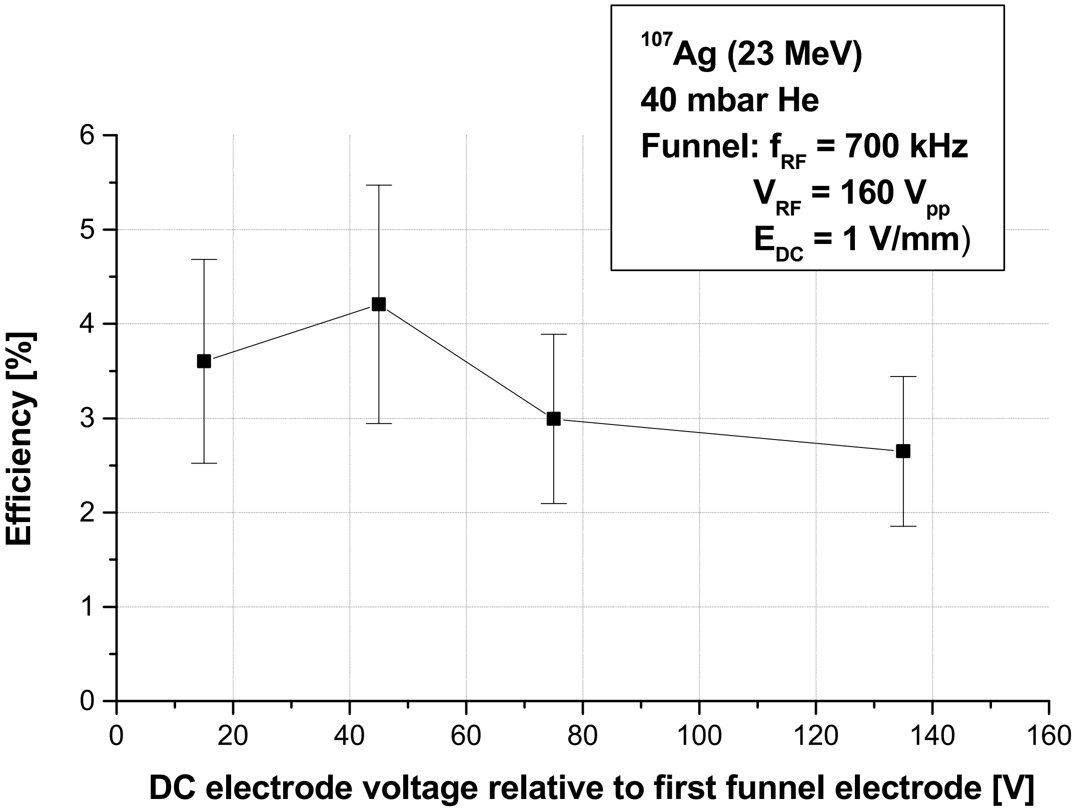

Figure 5.5
Plot of the absolute stopping and extraction efficiency for ^{107}Ag ions as a function of the relative voltage between the last DC electrode and the first funnel electrode. A maximum in the efficiency is reached at a voltage difference of around 40 V.

Besides by the RF voltage applied at the funnel the transport efficiency is influenced by the applied DC ramp. The corresponding behaviour of the efficiency is shown in Fig. 5.6, where the absolute stopping and extraction efficiency for Ag ions is plotted as a function of the DC ramp. The applied RF voltage had a frequency of 700 kHz and an amplitude of 160 V_{pp}. Clearly visible is the higher efficiency for the lower values of the field strength. This can be explained by the lower repulsion forces needed inside the funnel for lower ion velocities which are directly related to the accelerating forces of the DC ramp. The repulsive RF forces have to act against the velocity component of the ions directed towards the funnel electrodes. The probability of ion losses on the funnel electrodes for a given RF amplitude and frequency increases with an increase of this velocity component.

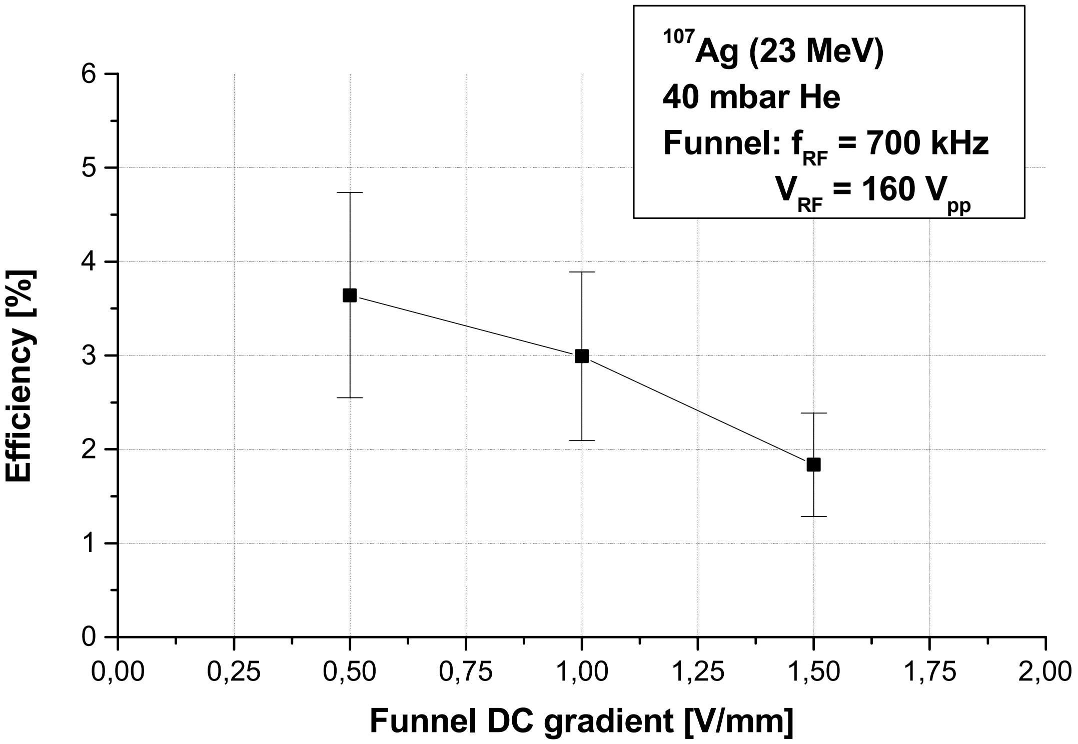

Figure 5.6
Plot of the absolute stopping and extraction efficiency for Ag^+ ions as a function of the DC ramp applied at the funnel. The higher efficiency at lower accelerating DC fields can be explained by the lower repulsion forces needed at the funnel surface, acting against the ion velocity component directed towards the funnel electrodes.

Figure 5.7 shows a plot of the overall stopping and extraction efficiency for ^{107}Ag ions as a function of the RF amplitude applied at the funnel electrodes at a fixed frequency of 700 kHz and a DC ramp of 1 V/mm. Compared to Fig. 4.4, where the same type of measurement was shown for laser-induced Er^+ ions in 25 mbar He gas, the behaviour is similar. The higher initial RF amplitude of nearly 80 V_{pp} needed for an ion transport can only partially be explained by the higher buffer-gas pressure compared to the off-line measurements, as according to Eq. (2.100)

$$E_{eff} = \frac{mV_{RF}^2K^2}{2\tilde{q}d_0^3}\left(\frac{r}{d_0}\right)$$

$$K = K_0\frac{T/T_0}{P/P_0}$$

higher amplitudes should be expected due to the quadratic dependence of the effective field strength on the gas pressure *P* (via the ion mobility *K*). The reason can be found in the effect shown in Fig. 5.6, where the extraction is more efficient for lower ion velocities. In this case the lower ion velocity compared to the laser

measurements is caused by the higher damping forces of the buffer gas.
The use of RF amplitudes beyond 160 V_{pp} was limited due to discharges at the funnel electrodes.

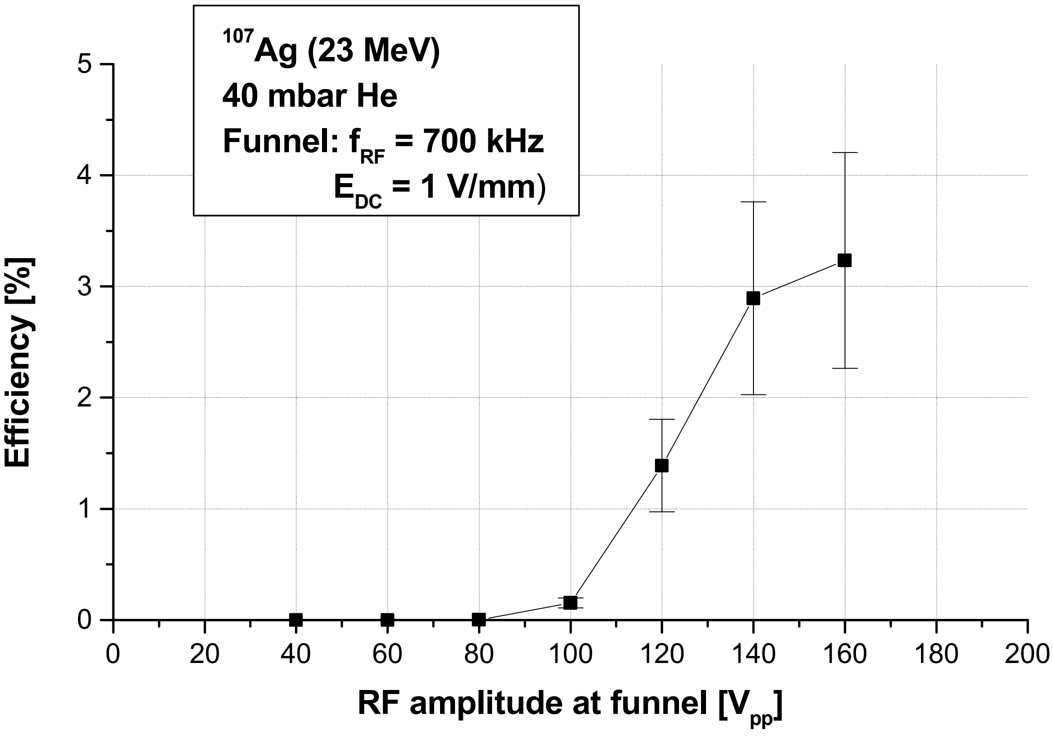

Figure 5.7
Plot of the stopping and extraction efficiency for ^{107}Ag ions as a function of the RF amplitude applied to the funnel at a frequency of 700 kHz and at a buffer-gas pressure of 40 mbar. The use of RF amplitudes beyond 160 Vpp was limited due to discharges at the funnel electrodes.

In Fig. 5.8 a plot of the stopping and extraction efficiency for $^{107}Ag^+$ ions is shown as a function of the RF frequency applied at the funnel. The RF amplitude of 160 V_{pp} was fixed as well as the DC ramp of 1 V/mm. Visible is a maximum of the transport efficiency at a frequency of 800 kHz, which is comparable to the results of the laser measurements.

The difference to the results obtained with the laser-induced ions is the rapidly decreasing efficiency for increasing frequencies. This effect can again be explained by the lower ion velocities at 40 mbar He gas. Trapping potentials inside the funnel at large RF amplitudes or frequencies, as mentioned in Sect. 4.2, may be acting more efficiently compared to the off-line measurements due to the lower repulsive forces which are needed for the lower ion velocities.

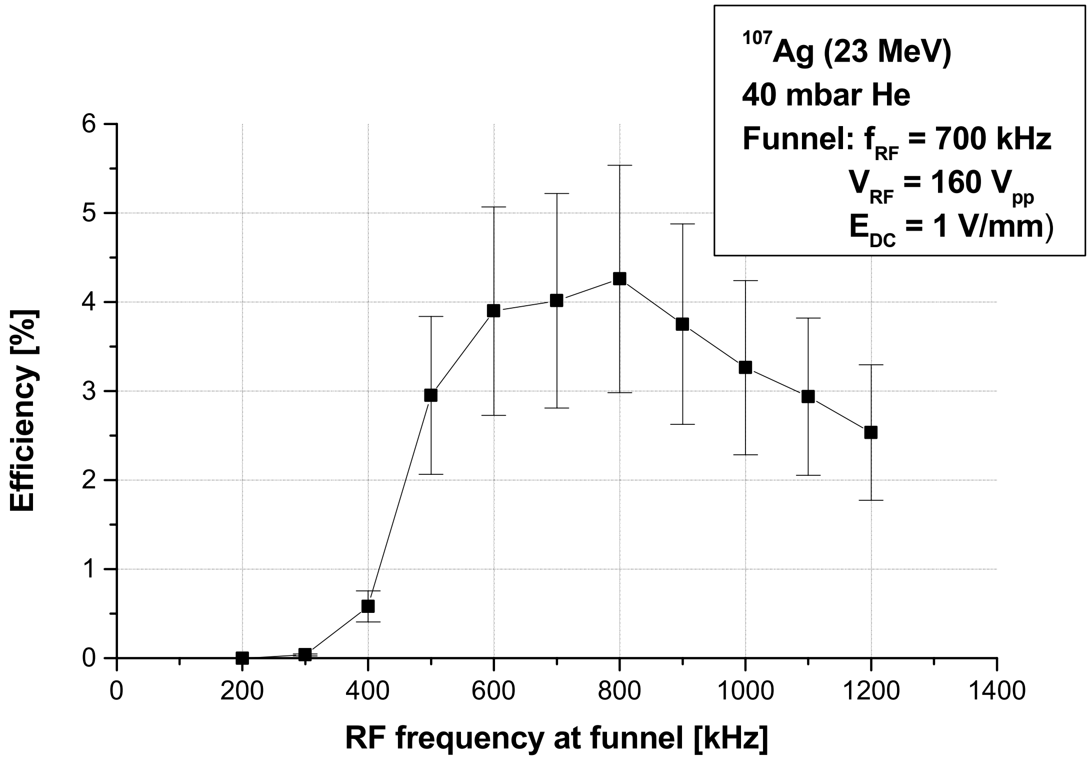

Figure 5.8
Plot of the absolute efficiency for ^{107}Ag ions as a function of the RF frequency applied at the funnel at a fixed amplitude of 160 V_{pp} and a buffer-gas pressure of 40 mbar.

When discussing the performance of a buffer-gas cell, the dependence of the extraction efficiency on the intensity of the incident ions deserves special attention. The amount of electrical charges involved and produced during the stopping process can significantly influence the survival probability of the ions of interest within the buffer gas.

The behaviour of the SHIPTRAP gas cell is shown in Fig. 5.9. While up to an intensity of around $2.5 \cdot 10^8$ ^{107}Ag^{17+} ions per second the stopping and extraction efficiency is nearly constant, it decreases rapidly at higher beam intensities. Taking into account the deposited energy of around 800 keV per stopped Ag ion (behind the 4 µm Ti entrance window, where more than 22 MeV of the initial 23 MeV beam energy get lost) and a mean ionisation energy for ion-electron pair creation of around 41 eV for He, the beam intensity of $2.5 \cdot 10^8$ s^{-1} corresponds to $4.9 \cdot 10^{12}$ electron-ion pairs produced per second inside the cell. Assuming that these charge carrier pairs are all created within the electrode system with a volume of around 4000 cm³, the ionisation rate is given by $Q = 1.2 \cdot 10^9$ cm^{-3}s^{-1}. Taking into account the maximum field strength of 10 V/cm during the measurements and typical distances between the electrodes of around 10 cm, the derived Q value corresponds to the predictions from Table 2.1, assuming that the influence of the buffer-gas pressure of 40 mbar scales linearly.

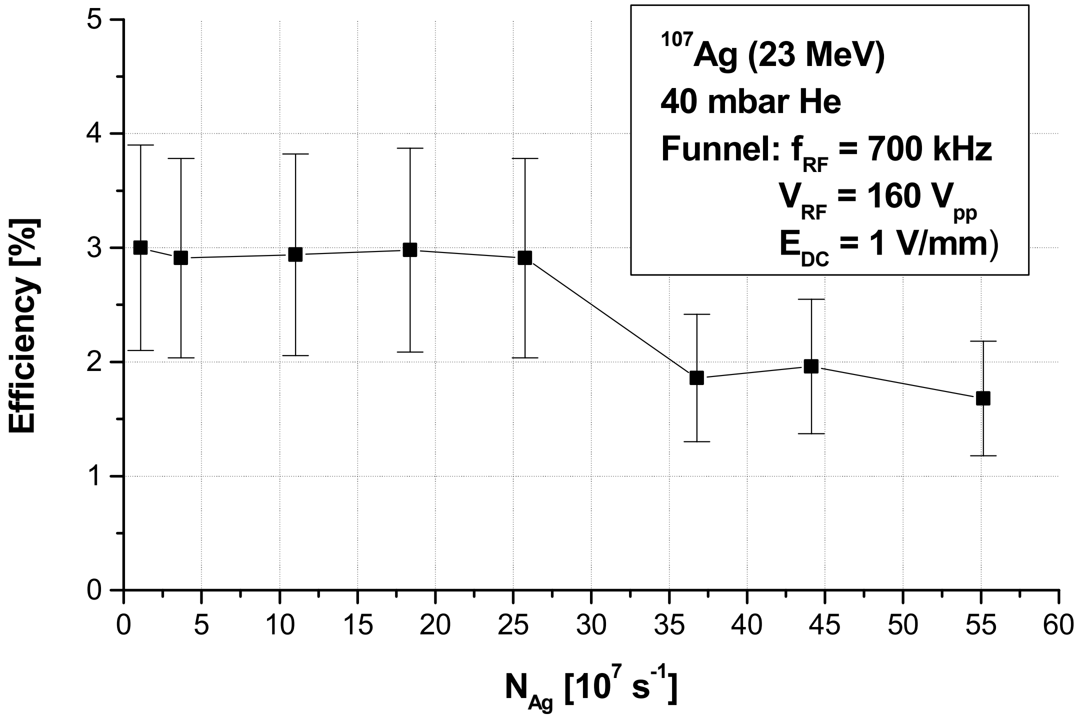

Figure 5.9
Plot of the absolute extraction efficiency for ^{107}Ag ions as a function of the intensity of the incoming ion beam, measured with the Gießen Ortho-TOF spectrometer [Eli04].

Due to fluctuations in the buffer-gas pressure in the TOF spectrometer and due to beam intensity variations the various maximum efficiencies obtained in different series of measurements spread between 3 and 4 %. Nevertheless within the error margin the efficiency values showed a good reproducibility of the measurements.

It should be noted that the already rather high value of the gas-cell extraction efficiency of about 4 % was obtained under rather unfavourable conditions, since due to vacuum problems optimum experimental conditions could not be reached, especially limiting the maximum electrical guiding fields. Therefore it is fair to expect even increased values for the efficiency under optimised conditions.

Analogue to the measurements with the laser-induced ions an optimum distribution for the DC potentials within the set-up can be found, shown in Fig. 5.10. The main difference to the results of the measurements with the laser-induced ions is the lower DC gradient of the funnel which could be explained by the broader distribution of the ions inside the gas cell. This is also the reason for the different potentials that have to be applied at the DC electrodes in order to avoid losses during the stopping process. The decelerating potential applied at the lens was found to be an optimum for the ion transfer from the extraction chamber to the TOF spectrometer.

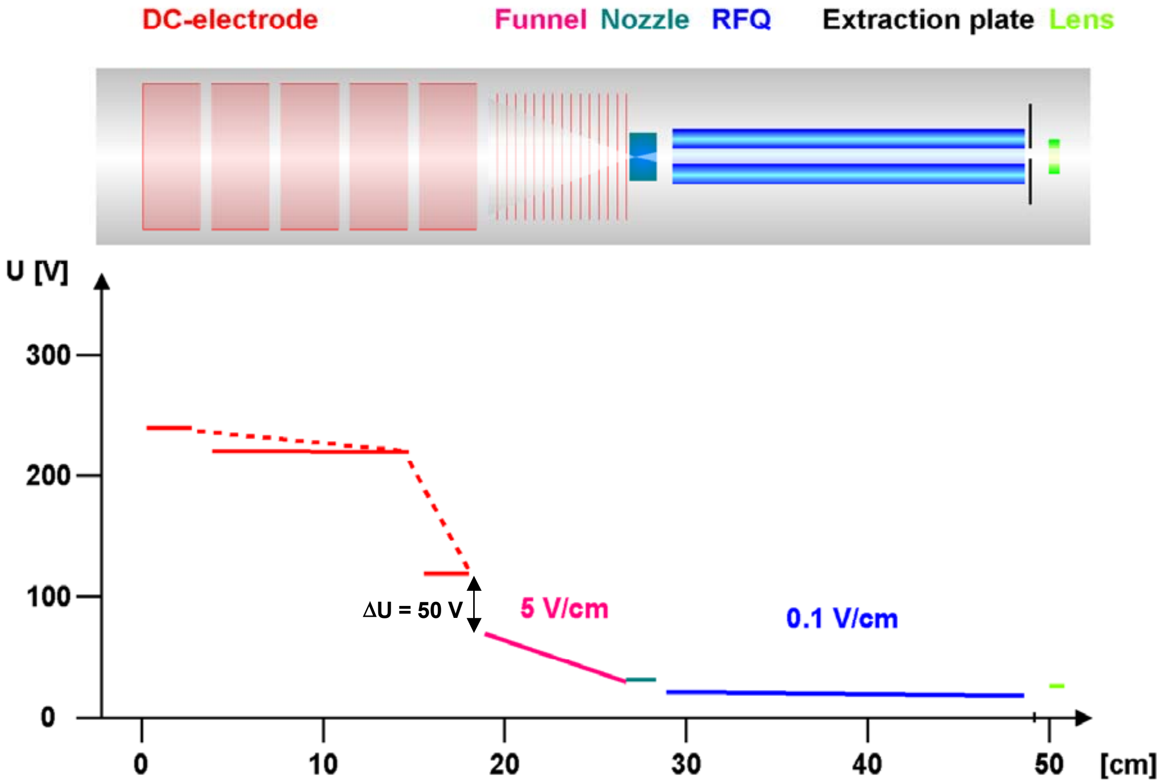

Figure 5.10
Schematic view of the optimum distribution for the DC potentials found for the measurements including the Gießen Ortho-TOF spectrometer.

5.1.2. Direct efficiency measurements using α-emitting reaction products

Using the Gießen Ortho-TOF spectrometer, an experimental determination of the absolute stopping and extraction efficiency of the SHIPTRAP gas cell set-up could be achieved. However, due to the limited detection efficiency of the Gießen Ortho-TOF spectrometer, only primary beam ions could be used at rather high intensities. In order to determine the gas cell efficiency for the more realistic situation of reaction products with much lower intensities, a completely different concept for the isotope-specific ion detection was applied, making use of the specific decay properties of radioactive ions.

One possibility is to perform off-line measurements with a ^{252}Cf fission-source in front of the cell. The stopped and extracted fission products can be detected directly after the extraction from the gas cell or behind an additional TOF mass measurement by determining their β-decay electrons. This method is used by the group of G. Savard at Argonne [Mai00, Sav02], where extraction efficiencies up to 45 % were determined. However, there are severe drawbacks connected to this method, mainly arising from the wide distribution of masses, half-lives and decay energies amongst the fission fragments. Moreover, only a few isotopes exhibit a characteristic discrete

β-decay energy spectrum, which in turn has to be distinguished from the prominent background of γ rays originating in the fission process. Thus any attempt to determine the gas-cell extraction efficiency has to cope with large uncertainties introduced by necessary assumptions on the stopping efficiency in the buffer gas or the influence of daughter-nuclide decays on the number of detected β particles.
The determination of the gas-cell extraction efficiency via the β decay can also be done with ions produced on-line, as also performed by the Argonne group [Sav02]. There the number of ions entering the cell was determined with a PPAC counter in front of the gas cell, while the number of extracted ions was determined at different positions behind the cell. Besides the detection of the beta particles also TOF measurements were implemented. Extraction efficiencies of the stopped ions up to 40 – 45 % were measured, with the best values obtained for Ba and Cs [Sav02].

On-line tests also offer the possibility to produce α emitters with the advantage of using the specific α-decay energies as an isotope-specific diagnostics tool. In the group of M. Wada at RIKEN a (radioactive) beam of ^{8}Li is used for the measurements with the gas cell, where the lithium ions are identified via their delayed α decay following their extraction out of the buffer-gas cell. Presently stopping and extraction efficiencies up to 2 – 3 % at incoming beam intensities between 10^4 – 10^5 particles per second have been reported [Wad03a].

In our own measurements for the direct experimental determination of the absolute stopping and extraction efficiency of the SHIPTRAP buffer-gas cell/extraction-RFQ combination α-emitting reaction products have also been used. In order to avoid any systematic errors and uncertainties, the measured values of the system efficiency directly were derived from the relation between the number of specific α decays detected in front of the gas cell and behind the extraction RFQ, respectively.

5.1.2.1. Production of α-emitting ions

The ^{121}Sb(^{35}Cl,4n) reaction was chosen to produce ^{152}Er, an α emitter in the rare earth region with a ground-state α-decay energy of 4.8 MeV and a half-life of 10.3 s (see Fig. 5.11). The advantages of this isotope are the absence of competition by the fission decay channel and the branching ratio of 90 % for the α decay. In addition, as shown in Figure 5.11, displaying a part of the nuclidic chart around ^{152}Er, only four α-emitting isotopes that can be produced in the region around ^{152}Er have comparable half-lives and branching ratios. Therefore, since the daughter nuclide ^{148}Dy decays by electron capture, the number of detectable α energies is rather limited.

Moreover, a ^{35}Cl ion beam can easily be produced by the Tandem accelerator with sufficient intensity and energy variability.

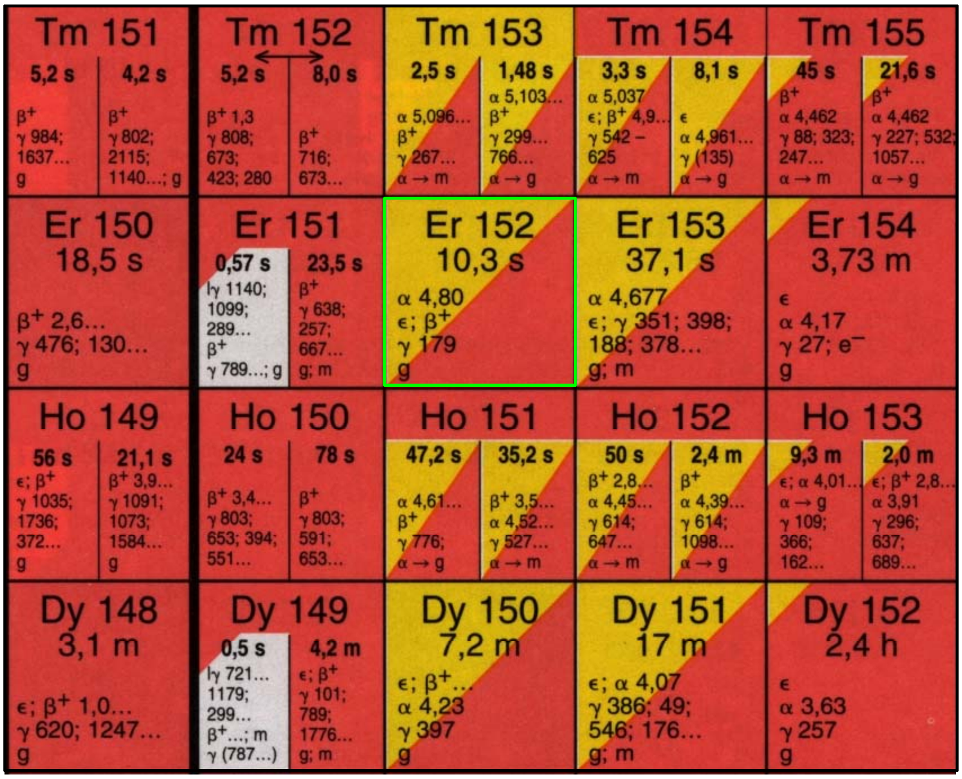
Tm 151
5,2 s
β+
γ 984; 1637…
g
4,2 s
β+
γ 802; 2115; 1140…; g
Tm 152
5,2 s
β+ 1,3
γ 808; 673; 423; 280
8,0 s
β+
716; 673…
Tm 153
2,5 s
α 5,096…
β+
γ 267…
α → m
1,48 s
α 5,103…
β+
γ 299… 766…
α → g
Tm 154
3,3 s
α 5,037
ε; β+ 4,9…
γ 542 – 625
α → m
8,1 s
ε
α 4,961…
γ (135)
α → g
Tm 155
45 s
β+
α 4,462
γ 88; 323; 247…
α → m
21,6 s
β+
α 4,462
γ 227; 532; 1057…
α → g
Er 150
18,5 s
β+ 2,6…
γ 476; 130…
g
Er 151
0,57 s
Iγ 1140; 1099; 289…
β+
γ 789…; g
23,5 s
β+
γ 638; 257; 667…
g; m
Er 152
10,3 s
α 4,80
ε; β+
γ 179
g
Er 153
37,1 s
α 4,677
ε; γ 351; 398; 188; 378…
g; m
Er 154
3,73 m
ε
α 4,17
γ 27; e−
g
Ho 149
56 s
ε; β+
γ 1035; 1736; 372…
g
21,1 s
β+ 3,9…
γ 1091; 1073; 1584…
g
Ho 150
24 s
β+ 3,4…
γ 803; 653; 394; 551…
78 s
β+
γ 803; 591; 653…
Ho 151
47,2 s
α 4,61…
β+
γ 776;
α → g
35,2 s
β+ 3,5…
α 4,52…
γ 527…
α → m
Ho 152
50 s
β+ 2,8…
α 4,45…
γ 614; 647…
α → m
2,4 m
β+
α 4,39…
γ 614; 1098…
α → g
Ho 153
9,3 m
ε; α 4,01…
α → g
γ 109; 366; 162…
2,0 m
ε; β+ 2,8…
α 3,91
γ 296; 637; 689…
Dy 148
3,1 m
ε; β+ 1,0…
γ 620; 1247…
g
Dy 149
0,5 s
Iγ 721… 1179; 299…
β+…; m
γ (787…)
4,2 m
ε; β+
γ 101; 789; 1776…
g; m
Dy 150
7,2 m
ε; β+…
α 4,23
γ 397
g
Dy 151
17 m
ε; α 4,07
γ 386; 49; 546; 176…
g; m
Dy 152
2,4 h
ε
α 3,63
γ 257
g

Figure 5.11
Part of the nuclear chart in the rare earth region around ^{152}Er, which was chosen as a test case for the determination of the gas-cell extraction efficiency.

5.1.2.2. The MLL test set-up

For the on-line measurements with ^{152}Er fusion-reaction products a large 90° dipole magnet (1.2 T, bending radius 0.7 m, gap width 100 mm x 45 mm) and a quadrupole doublet lens (18 T/m) were added to the beam line at the MLL. This set-up, shown in Figure 5.12 and 5.13, allows to perform nuclear reactions in front of the magnet, where the primary beam is separated from the secondary reaction products.
In the case of ^{152}Er the specific nuclear structure of this isotope has to be taken into account for the design of the experimental set-up. Figure 5.15 displays a part of the nuclear level scheme of ^{152}Er with the yrast band. Typical for isotopes in the rare earth region around A ~ 150 is the occurrence of high-spin isomers, as can be seen in Fig. 5.15 (highlighted by the red colour). Those high-spin isomers may exhibit strong conversion-decay branches, thus drastically changing the charge state of the reaction products and thus preventing their transport to the detector behind the 90° dipole magnet. A standard technique to compensate for conversion-decay transport losses is the use of a 'charge-reset foil', a thin carbon foil placed between the target and the entrance aperture of the dipole magnet. Like in a stripper foil, the charge-state distribution behind this charge-reset foil is centred around an equilibrated average charge state that can be described by the expression given in Eq. (2.23).

The distance from the target has to be determined by the lifetime of the most relevant isomers and the recoil velocity of the reaction products. In our case with typical recoil velocities of $\beta = v/c \sim 2\,\%$ and isomeric lifetimes up to 40 ns a minimum flight path of 240 mm to the charge-reset foil is required. Therefore the thin C reset foil (25 µg/cm², Ø 45 mm) was placed at a distance of 330 mm behind the target.

The detection system consists of two Si surface-barrier detectors, one in front of the gas cell with a diameter of 2.4 cm (active area 450 mm^2) and a thickness of 100 µm, and one following the lens behind the extraction RFQ at a distance of 2 mm with a diameter of 2 cm (active area 300 mm^2) and a thickness of 300 µm. The detector in front of the gas cell is movable in y-direction as is the α source ('mixed nuclides', ^{239}Pu/5.155 MeV, ^{241}Am/5.486 MeV, ^{244}Cm/5.805 MeV) close-by that allows for an on-line calibration.

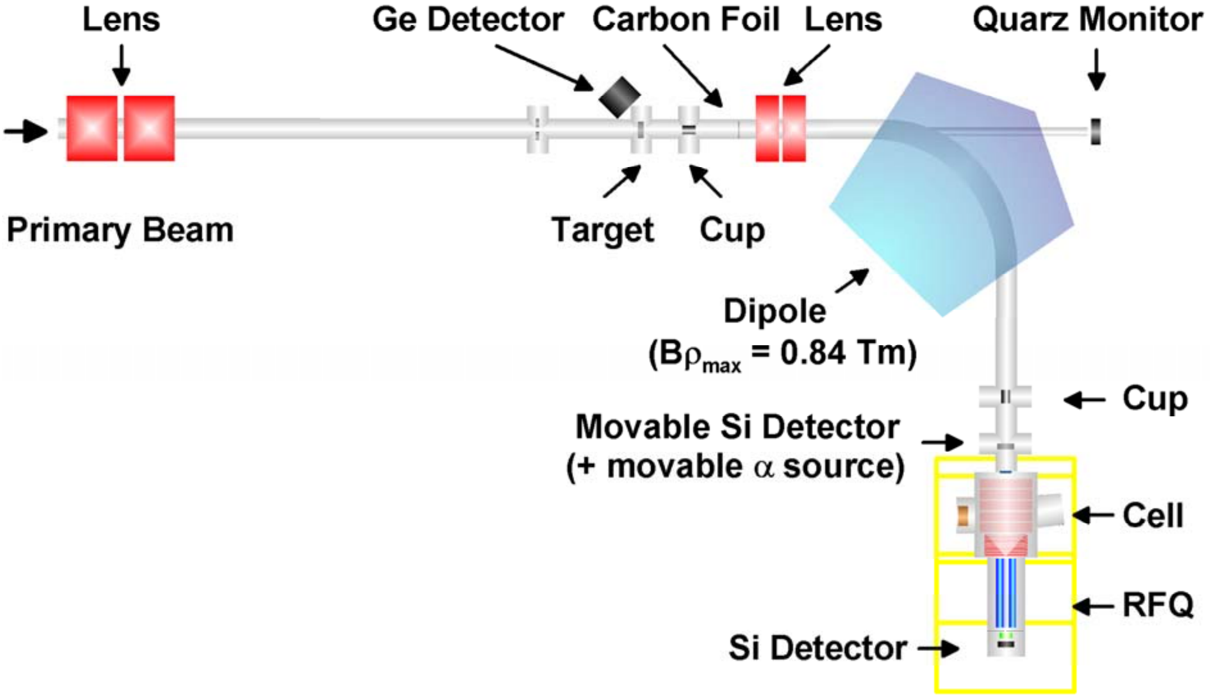

Figure 5.12
Schematic view of the MLL test set-up. The radioactive ions are produced in a fusion-evaporation reaction at the target position, while with the 90° dipole the primary beam is separated from the reaction products. The carbon foil after the target is used to equilibrate the charge states of the secondary ions in order to compensate for conversion processes following isomeric decays. In front of the cell the test ions are determined with a movable Si detector that can be on-line calibrated with a movable α source. For the tests at the MLL the test ions enter the gas cell on the longitudinal axis, therefore the entrance window is mounted on the end flange of the stopping chamber. After the extraction of the ions they are detected with a Si detector placed behind the extraction chamber.

Behind the Si detector the gas-cell/extraction-RFQ set-up was connected to the beam line in a longitudinal geometry, allowing for the recoil ions to enter the gas cell along the extraction axis.

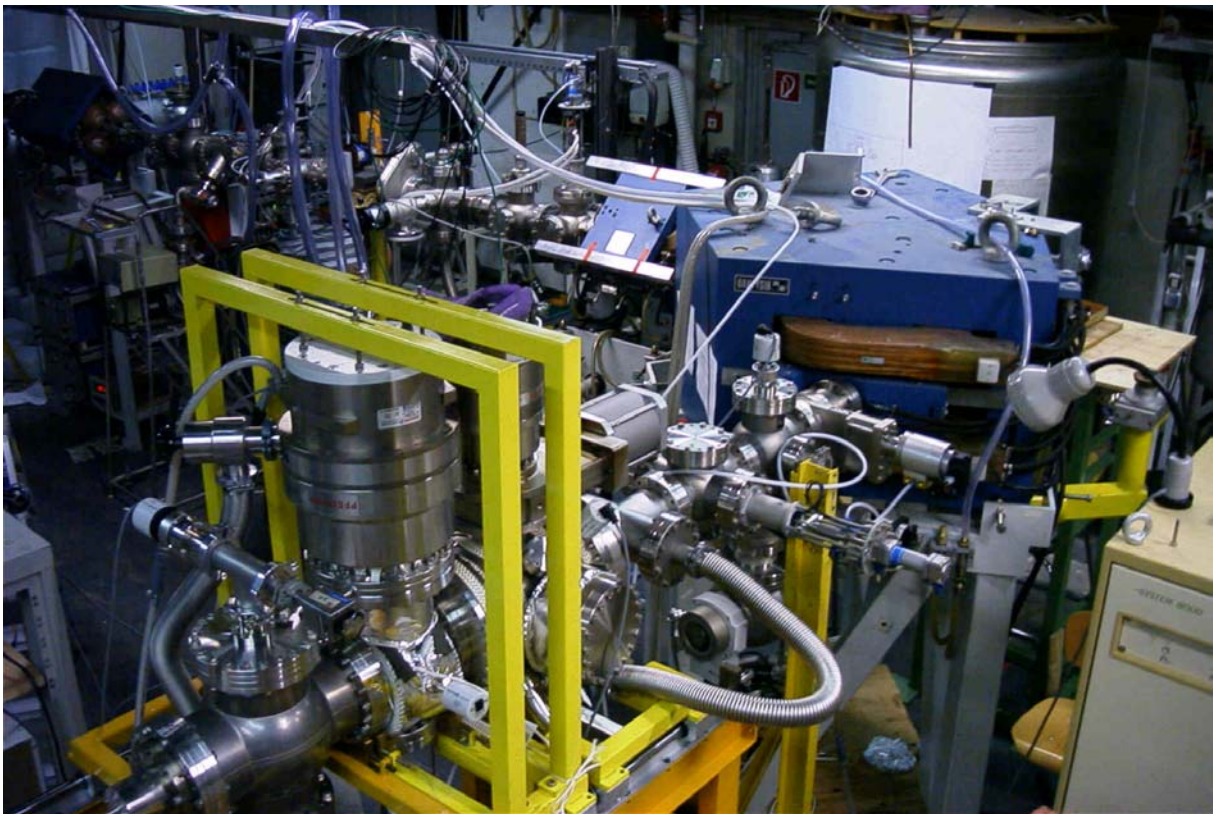

Figure 5.13
Photograph of the MLL test set-up with the gas-cell/extraction-RFQ system in the foreground and the beam line with the 90° dipole magnet and the quadrupole doublet lens following the production target.

In order to suppress scattered primary beam particles behind the dipole magnet, an aperture (opening $40 \times 40\,\mathrm{mm}^2$) was placed at the exit of the magnet chamber.

The ^{121}Sb targets used for the efficiency measurements typically had a thickness of 260 µg/cm^2. Since antimony has a low sublimation temperature of ~300 °C under the vacuum conditions of the beam line, the target material was sandwiched within carbon layers with a thickness of 25 – 40 µg/cm^2. Therefore, together with a limitation of the beam intensity of ~1 pnA, stable ion production conditions for several days could be reached.

In order to determine the optimum ^{35}Cl beam energy an excitation function was measured using a germanium γ-ray detector positioned close to the target. In a first step the γ-ray detection properties of the germanium counter were determined. Figure 5.14 shows the plot of the absolute photopeak efficiency as a function of the γ energy, measured with a ^{152}Eu source placed at the target position.

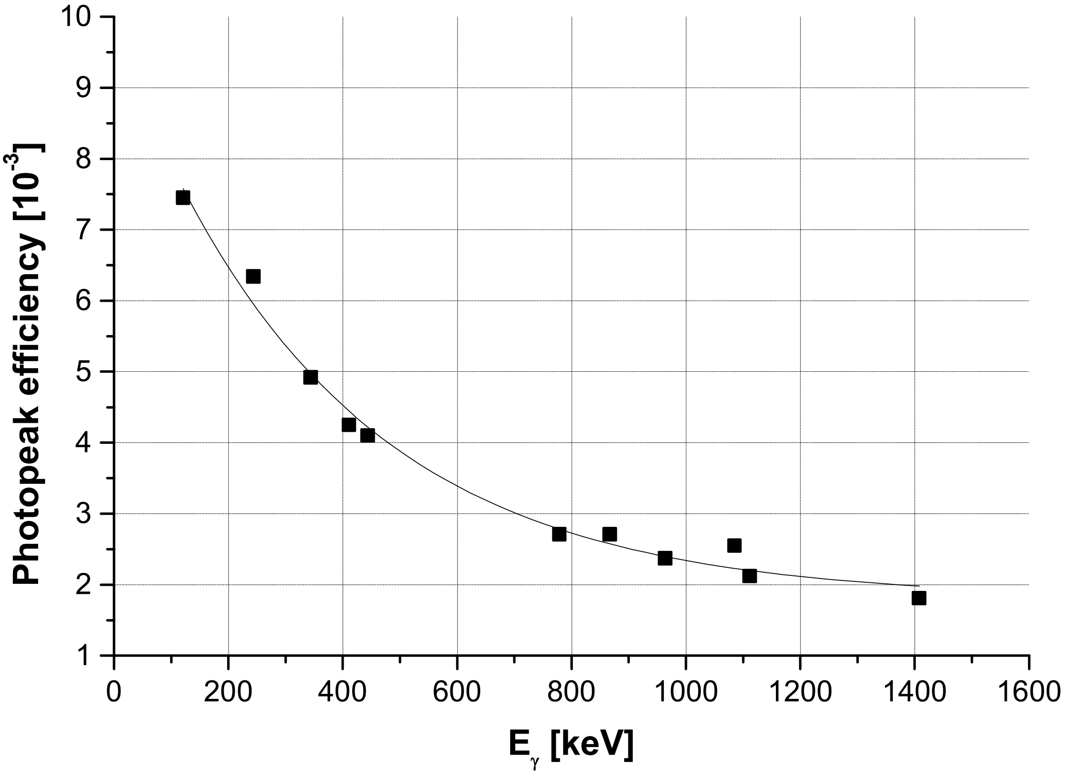

Figure 5.14
Plot of the germanium-detector photopeak efficiency as a function of the γ energy. For the measurement a ^{152}Eu source was used, placed at the target position.

For the γ-ray studies a ^{121}Sb target (260 µg/cm^2) on a thick lead backing (10 mg/cm^2) was used, in order to stop the recoil nuclei prior their γ decay. Sublimation of the target material was prevented by a carbon front layer of 40 µg/cm^2. The γ-ray energy spectrum measured with the Ge detector following the ^{121}Sb(^{35}Cl,xn)$^{156-xn}$Er reaction is shown in Fig. 5.16. The arrows mark the position of yrast transitions in ^{152}Er, shown in Fig. 5.15.

In addition γ-ray transitions corresponding to fusion products like ^{151}Ho, ^{152}Ho, ^{151}Er and ^{153}Er and transitions of recoils produced in fusion reactions of the primary beam with the carbon layer material are visible.

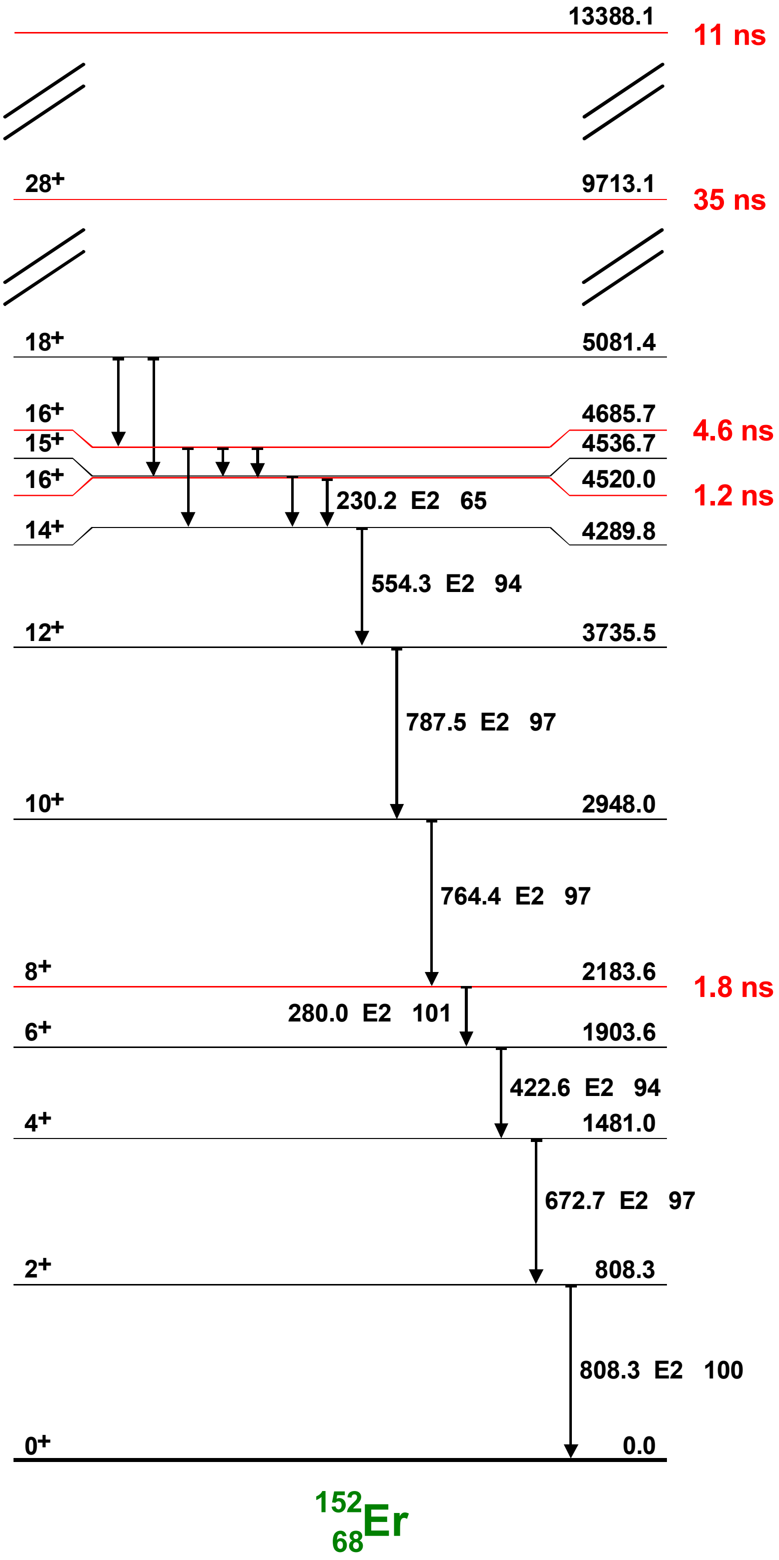
13388.1
11 ns
28+
9713.1
35 ns
18+
5081.4
16+
4685.7
4.6 ns
15+
4536.7
16+
4520.0
1.2 ns
230.2 E2 65
14+
4289.8
554.3 E2 94
12+
3735.5
787.5 E2 97
10+
2948.0
764.4 E2 97
8+
2183.6
1.8 ns
280.0 E2 101
6+
1903.6
422.6 E2 94
4+
1481.0
672.7 E2 97
2+
808.3
808.3 E2 100
0+
0.0
152 68 Er

Figure 5.15
Part of the level scheme of ^{152}Er (taken from [Nuc96]). For each level its spin and parity, excitation energy as well as transition energy and corresponding multipolarity and intensity is indicated. In the case of isomeric states also the lifetime is given.

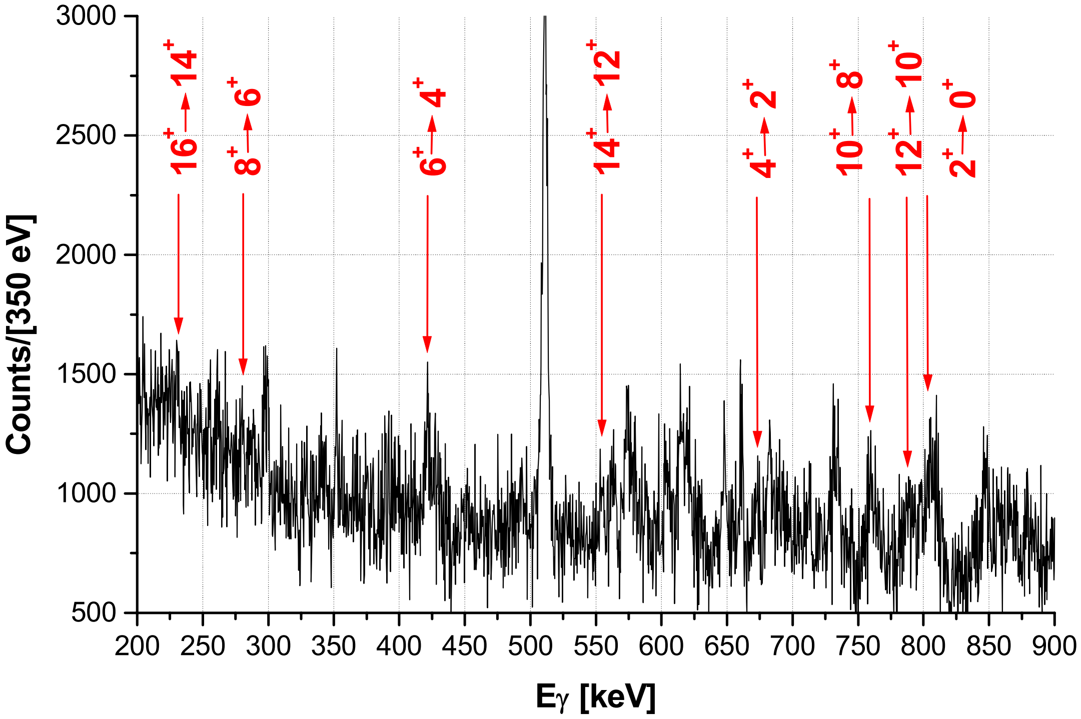

Figure 5.16
γ-ray energy spectrum following the reaction $^{121}\mathrm{Sb}(^{35}\mathrm{Cl},xn)^{156-xn}\mathrm{Er}$ at E_{lab} = 150 MeV. Marked are the yrast transitions from ^{152}Er. Other γ-ray transitions correspond to fusion products like ^{151}Ho, ^{152}Ho, ^{151}Er and ^{153}Er.

For the measurement of the ^{152}Er excitation function the energy of the chlorine ions delivered from the Tandem accelerator was varied between 125 MeV and 150 MeV, limited only by the maximum available terminal voltage of the accelerator. From the (efficiency-corrected) peak intensities of the unambiguously identified γ transitions in ^{152}Er, the production cross-section for this reaction was determined and compared to results calculated using the evaporation codes HIVAP [Rei92] and PACE4 [Gav02]. Due to known intensity ratios within the yrast cascade of ^{152}Er background contributions could easily be identified.
A comparison of the model predictions and the measured values for the production cross section of ^{152}Er is shown in Fig. 5.17. While PACE4 predicts a maximum cross section of σ = 113 mb for ^{152}Er for an energy E_{beam} = 147 MeV, the experimental findings are better reproduced by the HIVAP results with a maximum of the excitation function at E_{beam} = 153 MeV, resulting in a cross section of σ = 59 mb. Nevertheless the experimental result of σ = 37 mb at E_{beam} = 150 MeV is still overpredicted. The measured production cross sections are also in good agreement with published values for the reaction $^{118}\mathrm{Sn}(^{40}\mathrm{Ar},6n)^{152}\mathrm{Er}$ [Gau74].
Whereas the experimental excitation function still exhibits a rising trend at 150 MeV, all further experiments were performed at this beam energy due to restrictions in the operation of the Tandem accelerator.

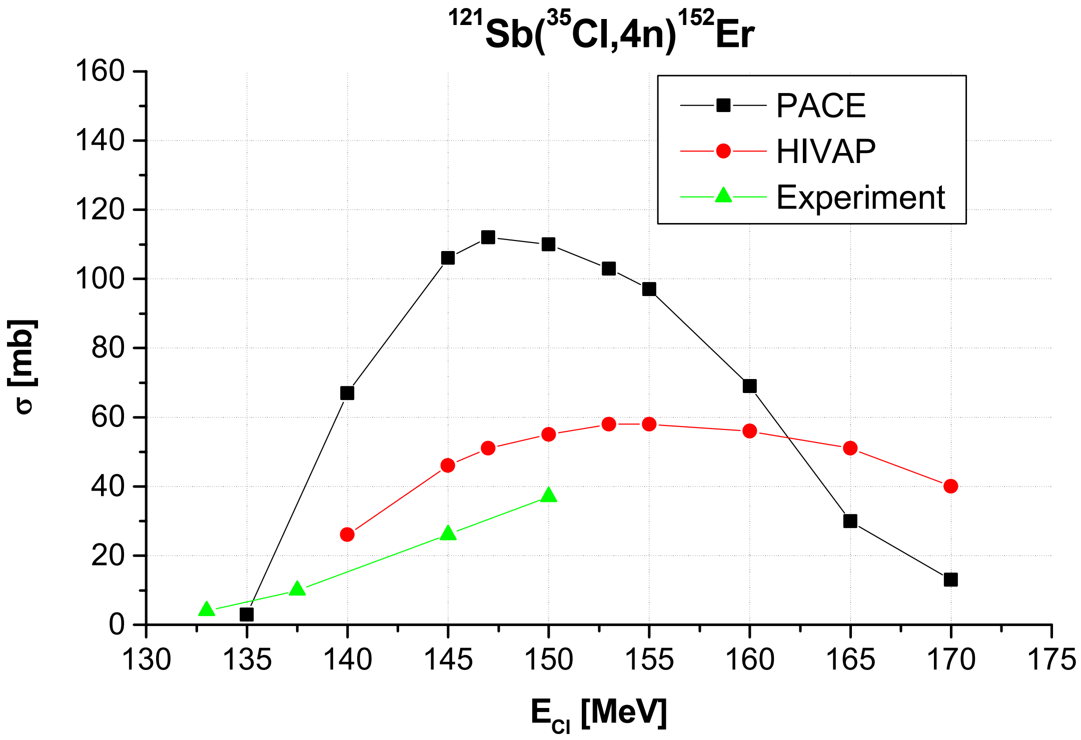

Figure 5.17
Comparison between the calculated and the measured excitation function of ^{152}Er following the reaction $^{121}Sb(^{35}Cl,4n)$.

In order to get an impression of the composition of the α-energy spectrum to be expected following the reaction ^{35}Cl + ^{121}Sb, Table 5.1 shows a list of the residual nuclei following the fusion-evaporation reaction as calculated by PACE4. Where applicable, the α-decay properties have been added.

Decay channel	Residual nucleus	σ [mb]	$t_{1/2}$ [s]	E_α [MeV]
3n	^{153}Er	3.76	37.1	4.677
4n	^{152}Er	113	10.3	4.804
5n	^{151}Er	38.7	23.5	-
1p3n	^{152}Ho	31.4	161.8/49.5	4.389/4.456
1p4n	^{151}Ho	12.9	35.2/47.2	4.522/4.611
2p2n	^{152}Dy	4.3	2.38 h	3.628
2p3n	^{151}Dy	2.3	17.9 m	4.069
2p4n	^{150}Dy	2.9	7.2 m	4.235
3p4n	^{149}Tb	10.5	4.13 h	3.967

Table 5.1
List of isotopes produced in the fusion-evaporation reaction ^{35}Cl + ^{121}Sb at E_{lab} = 150 MeV, as calculated by PACE4.

Besides the dominant contribution to the α-decay spectrum from ^{152}Er (4.804 MeV), also weaker components from ^{153}Er (4.677 MeV), ^{152}Ho (4.456 MeV/4.389 MeV), ^{151}Ho (4.522 MeV/4.611 MeV), ^{151}Dy (4.069 MeV), ^{150}Dy (4.235 MeV) and also from ^{149}Tb (3.967 MeV) can be expected.

After having optimised the production cross section of ^{152}Er at the target position, optimised transport conditions for the recoiling reaction products to the gas-cell entrance window have also to be found. Therefore ion-optical calculations of the beam line between target and gas cell were performed using the code COSY INFINITY [Be01]. In view of the limited angular acceptance of the quadrupole doublet (beam line diameter 48 mm) and the dipole magnet (gap width 45 mm in *y*-direction, 100 mm in *x*-direction) the angular straggling of the reaction products caused by the target and the charge-reset foil as well as their energy and charge-state distribution had to be thoroughly studied as input parameters for the ion-optical calculations.
While the recoil energy can be calculated with PACE4, energy-loss simulations using TRIM were needed to determine the energy and angular straggling of the reaction products. It turns out that the initial ^{152}Er recoil energy of 33.0 MeV (E_{lab} = 150 MeV) transforms into a wide distribution of (28.4 ± 3.6) MeV behind the reset foil, while the angular straggling amounts to ±4° at the entrance of the quadrupole doublet. Moreover, after passing through the carbon foil the charge-state distribution of the ^{152}Er recoil nuclei with about 0.2 MeV/u can be determined using the tables of Shima [Shi92], resulting in the distribution displayed in Fig. 5.18.

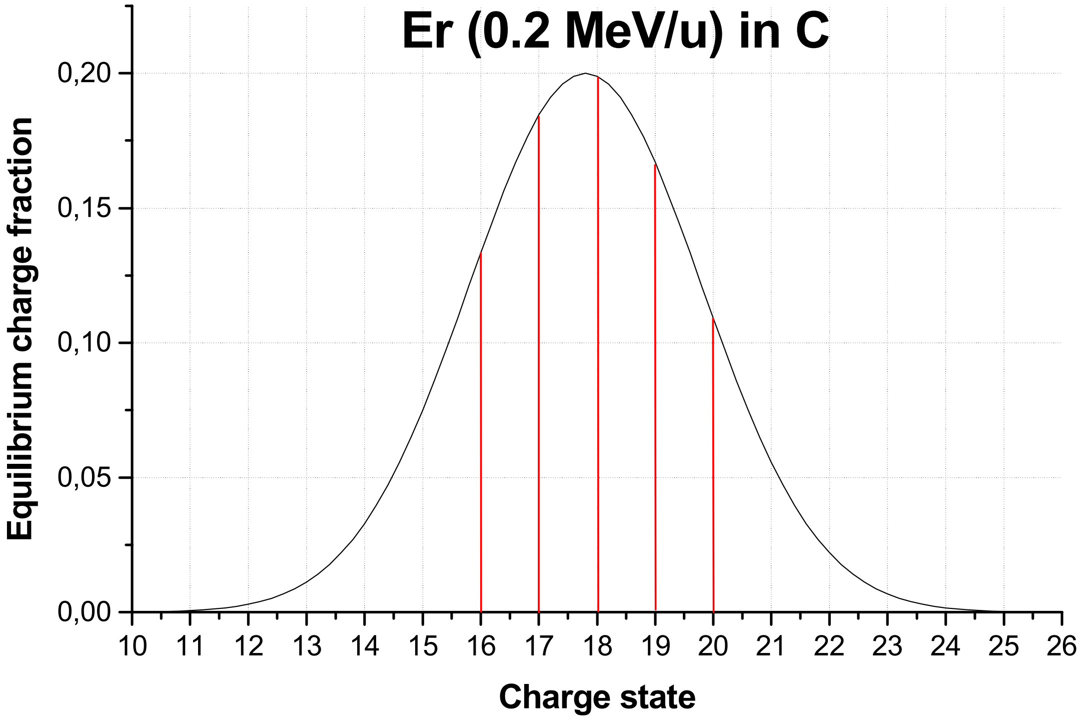

Figure 5.18
Equilibrium charge distribution for erbium ($Z = 68$) at an energy of 0.2 MeV/u after passing through a thin carbon foil [Shi92].

Taking into account the available bending power of the dipole magnet and limitations given in order to avoid the transfer of the 17+ charge state of the primary beam, only the most abundant charge state (18+) and fractions of its neighbours can be transported to the gas cell, resulting in a charge state transmission efficiency of about 20 % for a sharp energy.

Using the properties of the ^{152}Er recoil ions as discussed above as starting values for the ion-optical calculations with COSY INFINITY, optimised settings for the quadrupole lens in front of the dipole magnet were calculated. Figure 5.19 illustrates the resulting ion trajectories in the *x*-plane between the target and the gas-cell entrance window for ^{152}Er^{18+} ions with a well defined energy of 28.4 MeV. Besides the positions of target (ion start), lens, dipole magnet, detector and entrance window the limiting apertures and diameters are given. The trajectories were calculated for ^{152}Er^{18+} with an energy of 28.4 MeV ± 15 % and the optimised lens adjustment. The resulting optimised field settings are displayed in Table 5.2.

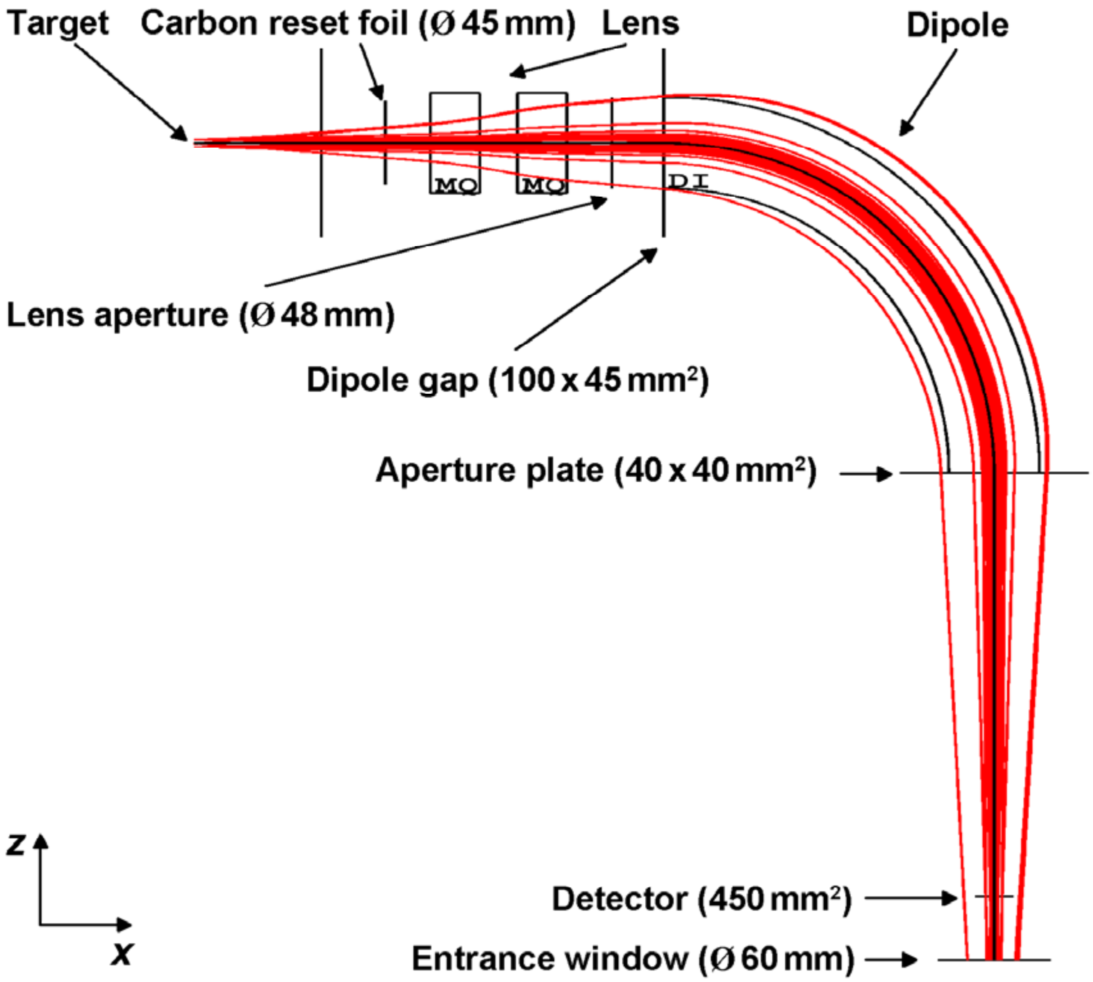
Target
Carbon reset foil (Ø 45 mm)
Lens
Dipole
MQ
MQ
DI
Lens aperture (Ø 48 mm)
Dipole gap (100 x 45 mm²)
Aperture plate (40 x 40 mm²)
z
x
Detector (450 mm²)
Entrance window (Ø 60 mm)

Figure 5.19
Trajectories in the *x*-*z*-plane of ^{152}Er^{18+} recoil ions from the reaction ^{35}Cl + ^{121}Sb at a primary beam energy of E_{lab} = 150 MeV in a COSY INFINITY simulation for a well defined recoil ion energy of 28.4 MeV. Besides the different positions limiting apertures and diameters are shown.

	17+	18+	19+
B_{dipole} [mT]	795	751	711
Q_1 [A]		57	
Q_2 [A]		23	

Table 5.2
List of the optimised field settings for ^{152}Er with an energy of 28.4 MeV for the three most abundant charge states.

Due to the energy straggling of (28.4 ± 3.6) MeV the transfer through the dipole magnet at a flux of 751 mT is not limited to the charge state 18+, also fractions of 17+ and 19+ are transmitted depending on their energy. Therefore, for a realistic estimate not only the energy straggling but also the charge distribution has to be taken into account at a fixed magnet setting.

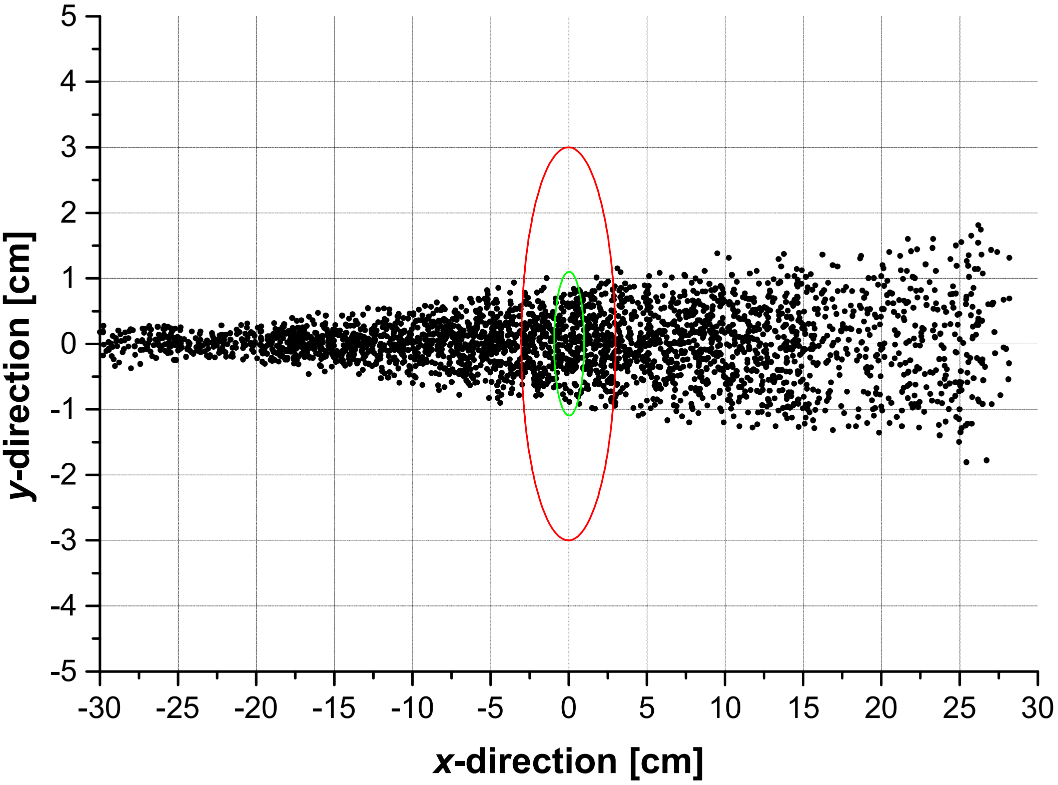

Figure 5.20
Distribution of simulated ion trajectories in a cut of the *x*-*y*-plane at the position of the gas-cell entrance window with the ions flying towards the observer. The ions were started with an energy of 28.4 MeV ± 15 % and a uniform distribution of the charge states 17+, 18+ and 19+. Indicated are the projected contours (elliptical due to the different scaling for *x*- and *y*-axis) of the gas-cell entrance window (red) and the Si detector in front of the cell (green).

Figure 5.20 shows the distribution of simulated ion trajectories in a cut of the *x*-*y*-plane at the position of the gas-cell entrance window with the ions flying towards the observer. The ions were started with an energy of 28.4 MeV ± 15 % and a uniform distribution of the charge states 17+, 18+ and 19+. The angular distribution at the target allows for an optimised transmission through all apertures except the exit aperture of the dipole at the optimised field settings. The losses at the exit aperture has to be taken into account separately since COSY does not consider geometrical losses. Indicated are the projected contours (elliptical due to the different scaling for *x*- and *y*-axis) of the gas-cell entrance window (red) and the Si detector in front of the cell (green).

It turns out that adding-up all geometrical restrictions the transmission efficiency of the ^{152}Er recoils from the target to the gas-cell entrance window can be estimated to about 8 %. Since the Si detector in front of the buffer-gas cell covers only an area of 450 mm^2, only a fraction of 3 % of the transmitted recoil nuclei will be implanted onto its surface. Moreover, only 50 % of the decays will be registered in the Si detector, as the α decay of the implanted ^{152}Er nuclei occurs isotropically.

In Table 5.3 the expected transmission and detection efficiency of ^{152}Er is shown. The rate estimate was done for a primary beam intensity of ~$5.6\cdot10^9$ ^{35}Cl^{11+} per second (= 10 enA) and a target thickness of 260 µg/cm² and the measured reaction cross section of ~37 mb for the production of ^{152}Er.

	Fraction	Rate estimate
Production at target	100 %	250 s^{-1}
Transmitted charge states	60 %	150 s^{-1}
Transmission efficiency and acceptance of window	8 %	12 s^{-1}
Transmission efficiency and implantation on detector	3 %	4.5 s^{-1}
Detection efficiency	50 %	2.3 s^{-1}

Table 5.3
Rate estimate for α-decaying ^{152}Er entering the gas cell and being identified at the Si detector in front of the gas-cell entrance window. The individual reduction factors acting on the initially produced 250 ^{152}Er nuclei per second resulting in the finally expected 2.3 s^{-1} at the detector and 12 s^{-1} at the entrance window, respectively, are listed.

5.1.2.3. Stopping and extraction efficiency measurements

For the determination of the absolute stopping and extraction efficiency of the gas-cell set-up the detectors in front of the cell and behind the RFQ were used to compare the numbers of injected and extracted ions.

The measurements were performed with a primary ^{35}Cl beam having an energy of 150 MeV and an intensity of ~$4.5\cdot10^9$ s^{-1} (8 nA) and a target thickness of 260 µg/cm². For an efficient stopping inside the cell at buffer-gas pressures around 50 mbar a Ti window with a thickness of 4 µm corresponding to 1.8 µg/cm² was used.

In order to reduce background caused by scattered ions the primary beam was pulsed during the measurements. The pulse sequence was given by a period of 10 s where the beam was switched on, followed by a period of 30 s where the beam was switched off and the data acquisition was enabled (duty cycle 25 %). The length of the periods was chosen with regard to the half-life of ^{152}Er (10.3 s).

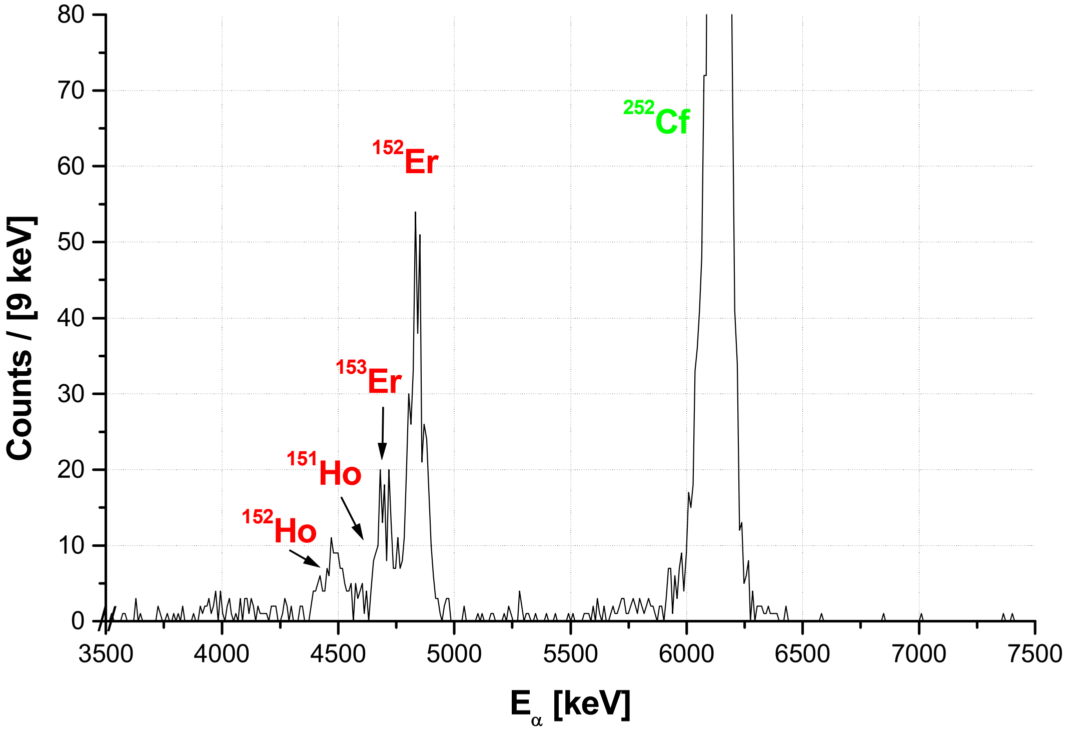

Figure 5.21
α-energy spectrum following the reaction ^{35}Cl + ^{121}Sb at E_{lab} = 150 MeV, measured in front of the gas cell. The peak at ~6.1 MeV represents an on-line calibration line from ^{252}Cf, while the α transition at ~4.8 MeV originates from ^{152}Er. Also smaller fractions of α transitions from ^{153}Er, ^{151}Ho and ^{152}Ho can be observed.

Figure 5.21 shows the α-energy spectrum detected in front of the cell. The peak at ~6.1 MeV corresponds to the α decay of ^{252}Cf, which was used as an on-line calibration reference. The four most abundant α emitters produced in the fusion reaction can be identified via their α ground-state decay energies (see Table 5.1).

The maximum number of ^{152}Er ions detected in front of the gas cell corresponds to an intensity of around 1.0 s^{-1}. Compared to the expected number of 2.3 s^{-1} (see Table 5.3) about a factor of 2 is missing. This discrepancy could be explained on the one hand by the observed sensitive dependence on the ion optics of the beam line. On the other hand simulated values like the energy or the angular straggling of the recoil ions could still be underestimated.

Subsequently the recoil ions entered the gas cell via the 4 µm Ti entrance window and were stopped in the gas cell, operated at a He buffer-gas pressure of 40 mbar. Figure 5.22 shows the α-decay energy spectrum after stopping and extraction. The α transitions of all four isotopes that were detected in front of the cell are clearly visible. The measurements behind the system were performed without pulsing the beam in order to increase the intensity.

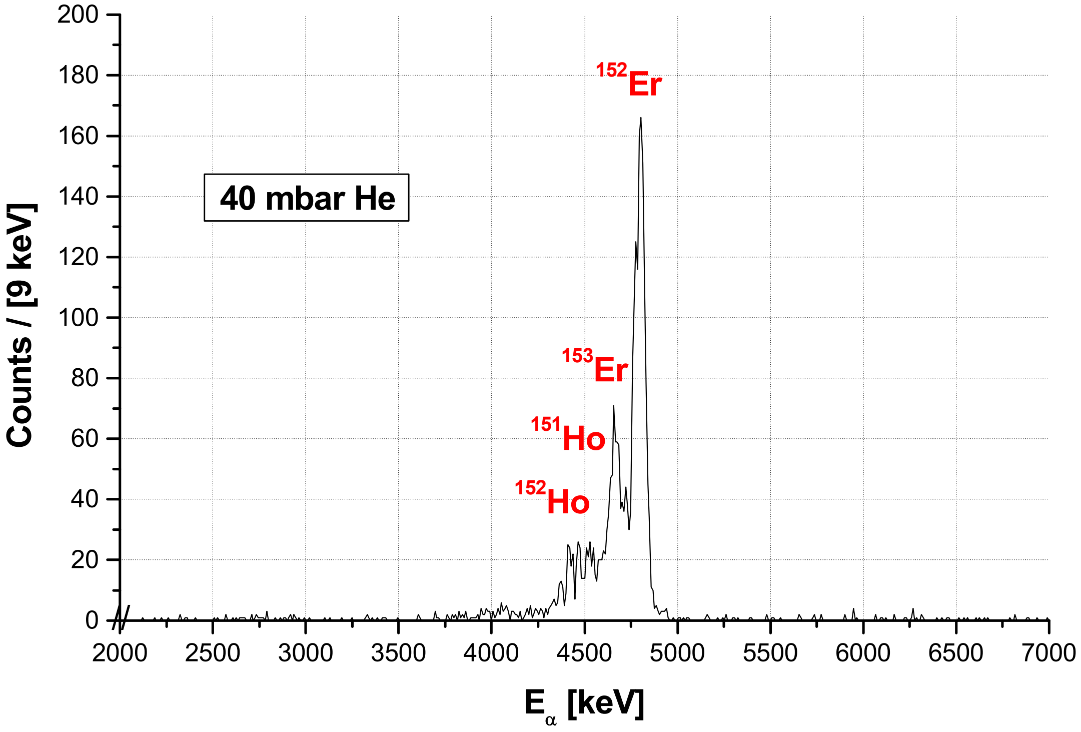

Figure 5.22
α-energy spectrum following the reaction ^{35}Cl + ^{121}Sb at E_{lab} = 150 MeV, measured after stopping the reaction products in the gas cell, extracting them through the nozzle and cooling them in the extraction RFQ.

For the determination of the overall stopping and extraction efficiency only the average number of counts contained in the α peak corresponding to ^{152}Er were used. Before being able to compare the measured rates of ^{152}Er before and behind the gas cell, the measured rate in front of the cell has to be re-normalised, since these measurements were performed using a pulsed beam and a detector which was smaller than the entrance window of the gas cell. This results in different factors that have to be included into the normalisation:

- The duty cycle of the beam of 25 % leads to a factor of 4, since the measurements behind the gas cell were done with a continuous beam.

- Data acquisition was disabled during the beam-on period, therefore decays taking place during this period were not accumulated, resulting in a factor of 1.3.

- The active area of the detector is smaller compared to the entrance window of the cell by a factor of 6.3. Nevertheless, the corresponding normalisation factor was determined to be 2.5, since a scan of the incoming recoil ion distribution using the movable Si detector showed that the diameter of the detector (24 mm) was sufficient to cover the complete ion distribution in *y*-direction (also visible from Fig. 5.20). Thus only the spread in *x*-direction had to be taken into account. Scanning the magnetic field of the bending dipole and the results of the COSY INFINITY simulations (see Fig. 5.19) revealed an almost uniform ion distribution in the *x*-direction due to the wide energy spread.

- The accumulation period of the α decays was 30 s when the beam was pulsed. Within this period of three half-lives of ^{152}Er, 7/8 of the decays took place, giving a factor of 8/7 for the normalisation calculation.

Altogether the number of counts measured in front of the gas cell in a given period of time has to be multiplied with a factor of 14.9 in order to get the number of initial ^{152}Er ion decays at the entrance of the gas cell that has to be compared to the decay rate measured behind the system.

The measurements were done at different He buffer-gas pressures and different settings for the guiding fields inside the cell, as shown in Table 5.4. The DC-field strength is given for the backside electrode surrounding the stopping volume, while at the funnel the electrical field of 10 V/cm as well as the RF amplitude of 195 V_{pp} were fixed. At the RFQ the frequency was fixed to 800 kHz and a DC ramp of 0.3 V/cm was applied.

Pressure inside cell [mbar]	DC field inside cell [V/cm]	Amplitude RFQ [V_{pp}]	N_{Er} in front of cell [1/min]	N_{Er} behind RFQ [1/min]	Efficiency [%]
20	4.5	124	24.83	0.26	1.0 ± 0.5
30	4.5	124	24.83	0.87	3.5 ± 1.0
40	4.5	124	24.83	0.73	2.9 ± 0.9
50	4.5	124	24.83	0.80	3.2 ± 1.0
60	4.5	124	24.83	0.20	0.8 ± 0.4
40	11.5	62	27.81	2.33	8.4 ± 1.5
40	11.5	124	27.81	1.67	6.0 ± 1.3
40	11.5	180	27.81	1.10	4.0 ± 1.0

Table 5.4
Measured stopping and extraction efficiencies as a function of the applied voltages and the He pressures inside the cell. The values N_{Er} for the average number of ions entering the cell have been re-normalised with the factor discussed in the text.

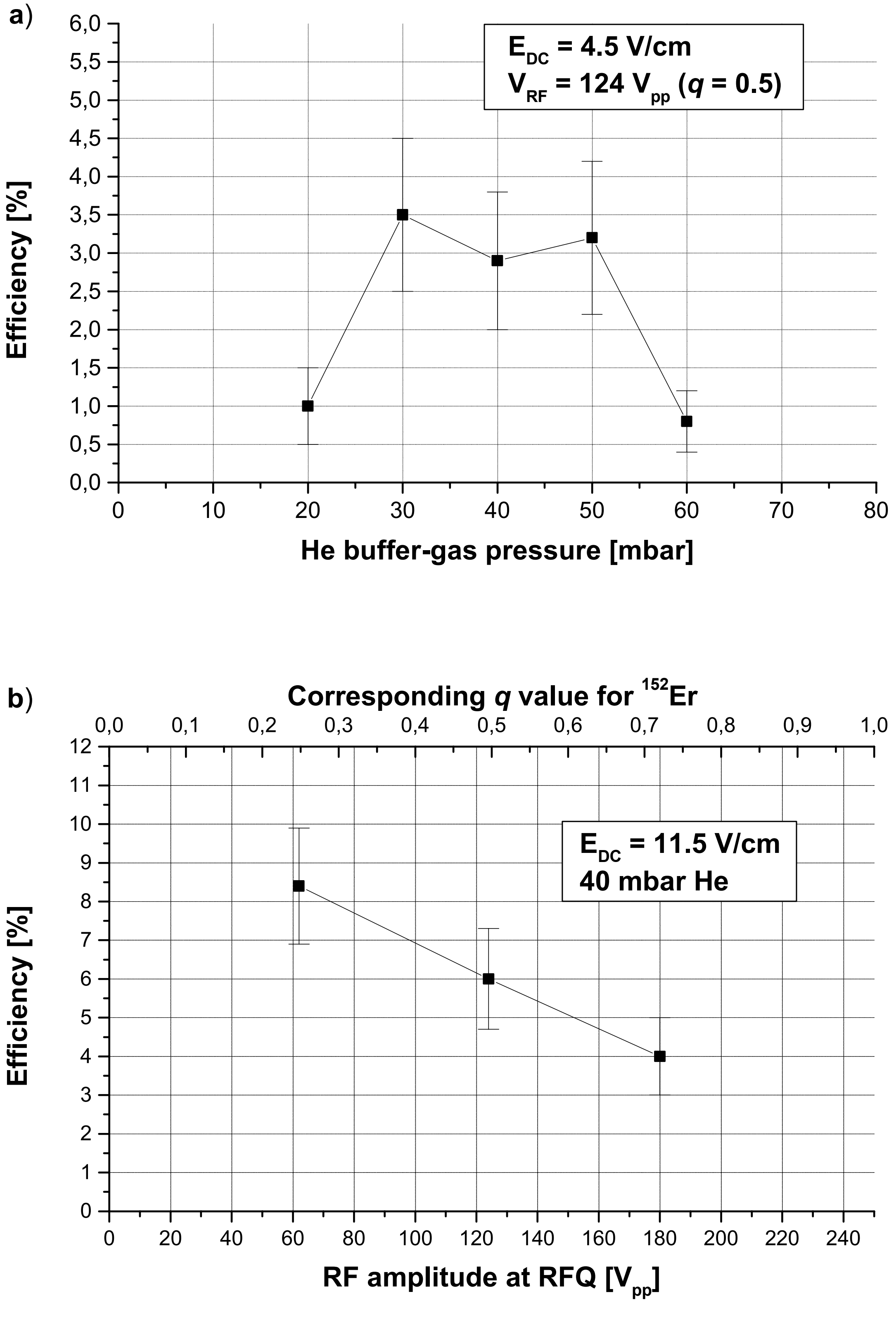

Figure 5.23

Plot of measured stopping and extraction efficiencies as a function of the He buffer-gas pressure in a) and of the RF amplitude applied at the RFQ in b). In addition to the RF amplitude the corresponding q value for ^{152}Er is indicated in part b).

Figure 5.23 shows again the efficiencies as given in Table 5.4, in part a) as a function of the buffer-gas pressure at fixed field strengths inside the cell and the RFQ. In part b) the efficiency is given as a function of the RF amplitude applied at the RFQ and the corresponding *q* value for ^{152}Er with the other settings being fixed.

The numbers given in Table 5.4 and displayed in Fig. 5.23 reflect the overall efficiency of the system including the stopping efficiency in the buffer-gas cell, the extraction efficiency from the gas cell and the transport efficiency of the RFQ. In addition the efficiency of the (low-energetic) ions sticking on the detector surface is intrinsically included, which here is assumed to be 100 %.

Besides the overall efficiency the listed numbers contain additional information. The wide pressure range between 20 mbar and 60 mbar where an efficient extraction can be achieved clearly reflects the wide energy distribution of the ions entering the gas cell. This distribution is in good agreement with stopping-range simulations using TRIM (SRIM version 2003.17) for ^{152}Er ions with a kinetic energy of 29 MeV stopped in helium gas after having passed through 4 μm of Ti, displayed in Table 5.5 for different buffer-gas pressures and shown exemplarily for 40 mbar He in Fig. 5.24.

He pressure inside cell [mbar]	Longitudinal stopping range [mm]	Radial mean deviation [mm]
20	205 ± 192	70 ± 68
30	138 ± 128	48 ± 47
40	106 ± 98	35 ± 34
50	83 ± 77	29 ± 28
60	69 ± 64	24 ± 23

Table 5.5
Stopping-range simulations using TRIM (SRIM version 2003.17) for ^{152}Er ions with a kinetic energy of 29 MeV stopped in helium gas after having passed through 4 μm of Ti.

The dimensions of the cylindrical DC electrode of the buffer-gas cell with a length of 180 mm and a diameter of also 180 mm should be remembered, in particular for the case of a perpendicular ion injection as realised at SHIPTRAP.

The nearly constant efficiency between 30 mbar and 50 mbar reflects the result of the superposition of the behaviours of the stopping and the extraction efficiency, since the extraction efficiency at fixed values for the field strengths is expected to decrease for increasing pressures, while the opposite behaviour for the stopping efficiency is expected.

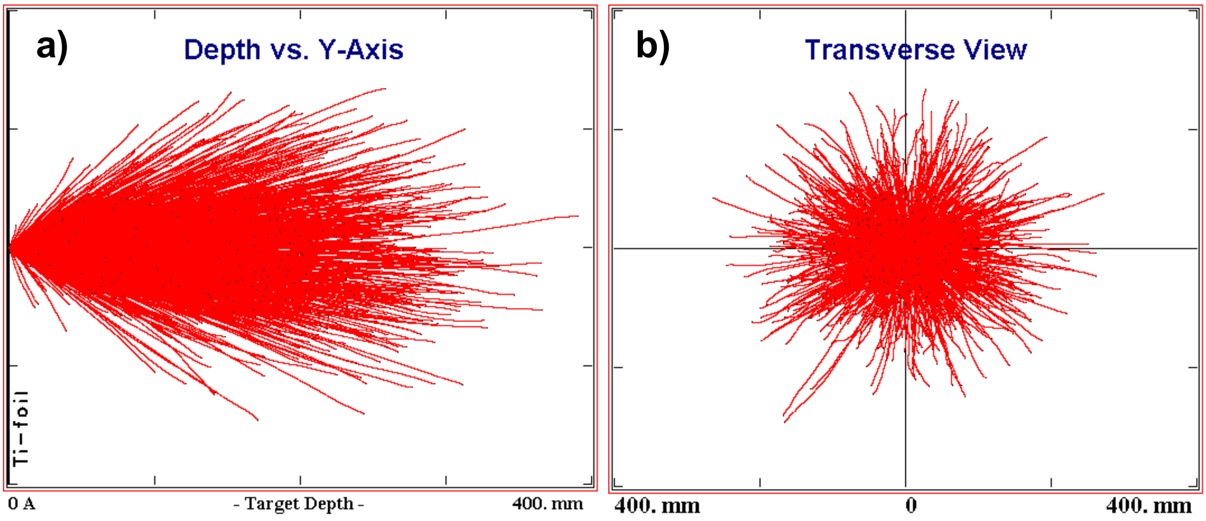

Figure 5.24
TRIM simulation for Er ions with a total kinetic energy of 29 MeV, stopped in 40 mbar of He after passing through Ti with a thickness of 4 µm. a) The calculated mean longitudinal stopping range projected onto the *x*-axis is (106 ± 98) mm. B) The result for the radial direction is a mean deviation of (35 ± 34) mm.

The increase in efficiency by raising the accelerating DC-field strength and thus decreasing the extraction time as visible from a comparison of the efficiencies obtained at $E_{DC} = 4.5$ V/cm and 11.5 V/cm, respectively, could be a hint for ion losses caused by impurities inside the gas cell. Therefore the improvement of the efficiency is directly connected to the improvement of the purity conditions inside the gas cell.
The efficiency dependence on the RF voltage applied to the RFQ shows a similar behaviour as shown in Fig. 4.8, where the transport efficiency for laser-induced ions through the RFQ as a function of the q value was displayed. In this case the optimum transfer efficiency through the RFQ was obtained for a q value between 0.1 and 0.2. About the same q value was measured for the optimised extraction of ^{152}Er ions as shown in Fig. 5.23 b). In view of the decreasing efficiency measured below the optimum q value in Fig. 4.8 it is clear that the apparent linear trend visible in Figure 5.23 b) may not be extrapolated to lower RF amplitudes.
Thus in conclusion the optimum value for the overall stopping and extraction efficiency of the SHIPTRAP gas cell determined in the measurements at the MLL amounts to (8.4 ± 1.5) %.

One important point to be mentioned is that the measurements via the α decay cannot distinguish between the extraction of 'pure' ions and molecular ^{152}Er ions. Nevertheless, the measurements with the Ortho-TOF described in Section 5.1.1. showed that at comparable conditions the contribution of molecules to the complete number of detected ions is rather low. Therefore the efficiencies given in Table 5.2 can reliably be attributed to the extraction of the 'pure' ^{152}Er ions.

5.2. On-line measurements at GSI

Besides the on-line experiments at the MLL the gas-cell/RFQ combination was also operated in first commissioning experiments together with the SHIPTRAP RFQ buncher and the Penning traps at GSI. Both stable isotopes and recoil products from SHIP were used for the measurements.

5.2.1. Measurements with stable ions

For the first operation of the complete SHIPTRAP set-up including the gas cell and the extraction RFQ a primary ^{40}Ca beam at an energy of 5.9 MeV/u was used. Since this energy is too high to be stopped directly in the cell, the beam energy was degraded by a stack of Mylar foils in front of the entrance window. The incoming ions were detected with a Si detector placed inside the cell opposite the entrance window. With this method the number of detected ions and their energy were measured as a function of the incident ion energy behind the degraders and the He gas pressure inside the cell in order to determine the centre of the stopped ion cloud.

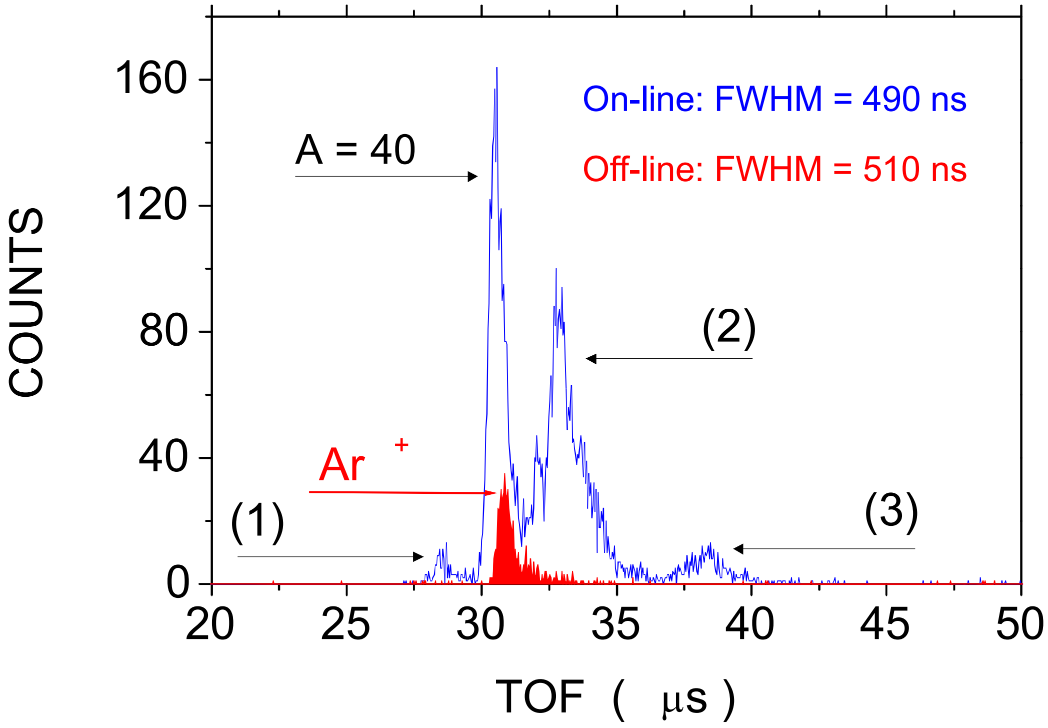

Figure 5.25
Blue: Time-of-flight spectrum of ions extracted from the gas cell and detected behind the RFQ buncher of SHIPTRAP, equivalent to a mass spectrum. Red: Off-line calibration measurement using an argon test ion source.

Figure 5.25 shows a time-of-flight spectrum of the ions extracted from the buffer-gas cell and detected behind the RFQ buncher (blue), equivalent to the mass spectrum of the extracted ion species. For comparison off-line measurements using an argon test-ion source are shown in red. Besides the peak at mass 40 several other peaks are visible. These peaks correspond to the masses $32 < A < 36$ (1), $44 < A < 48$ (2) and $61 < A < 65$ (3), assumed to originate from impurities inside the gas cell.

Several factors prevented a realistic estimate of the buffer-gas cell extraction efficiency from these measurements. Although helpful in the off-line characterisation of the gas-cell performance, the usage of the Ar test-ion source left the cell with remaining argon contaminations that could not be removed quantitatively by the pumping system before the experiment performed with a beam of the same mass number A = 40. Therefore the number of extracted m = 40 amu ions cannot be unambiguously attributed to the extraction of $^{40}\mathrm{Ca}^{+}$ ions. Moreover, a significant energy straggling of the ^{40}Ca ions entering the gas cell was introduced by the degraders in front of the entrance window, thus the stopping efficiency in the gas cell could not be calculated reliably enough for an efficiency estimate.

5.2.2. Measurements with reaction products

For the measurements with reaction products at GSI the same isotope ^{152}Er was chosen, in order to be able to compare the results of this experiment and the beam time at Munich. Different from the measurements at the MLL, the radioactive ions were produced via the reaction $^{40}\mathrm{Ar}(^{116}\mathrm{Sn},4n)^{152}\mathrm{Er}$ at an energy of 168 MeV of the primary beam and a target thickness of 440 µg/cm^2. According to PACE4 and HIVAP calculations, this reaction provides a production cross section for ^{152}Er of about 50 % higher compared to the reaction $^{35}\mathrm{Cl} + {}^{121}\mathrm{Sb}$ used at Garching.

Taking into account the ^{116}Sn target thickness, the calculated cross section of 60 mb (HIVAP) [Heß04] and an average intensity of the primary beam of 10 pnA, around 8600 ^{152}Er ions were produced per second at the target during the beam time. Since around 2700 ^{152}Er ions were determined per second in front of the gas cell, a transmission efficiency of around 31 % through the SHIP facility can be calculated, in good agreement with the simulated value of 35 % [Heß04].
Concerning the experimental set-up the main difference of this beam time compared with the measurements at the MLL was the nearly perpendicular ion injection into the gas cell at SHIPTRAP, as indicated by the schematic view of the experimental set-up in Fig. 5.26.

The measurements were performed in two configurations. The first one corresponds to a similar set-up as used for the measurements at the MLL and is shown in Fig. 5.26. Here the Si detector was placed directly behind the extraction RFQ. In the second configuration the SHIPTRAP RFQ buncher was connected to the extraction chamber, as shown in Fig. 5.27 and Fig. 5.28. For the identification of the transferred ions a Si detector was placed at the exit of the buncher.

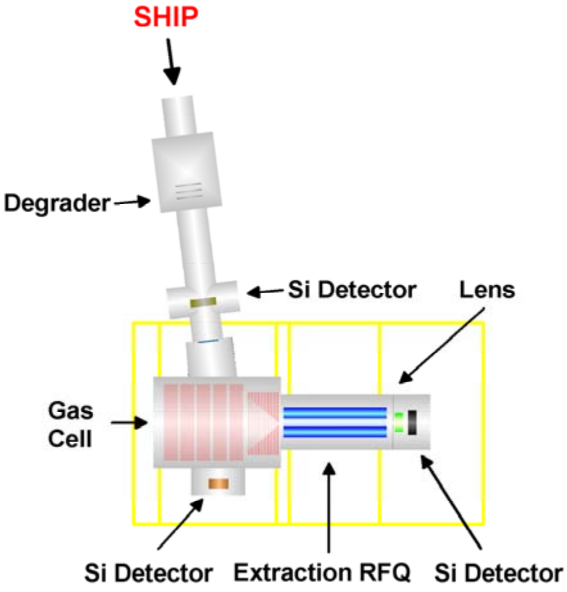
SHIP
Degrader
Si Detector
Lens
Gas Cell
Si Detector
Extraction RFQ
Si Detector

Figure 5.26
Schematic view of the set-up used at GSI behind SHIP for the efficiency measurements of the gas-cell/extraction-RFQ system. The number of incoming ^{152}Er ions was determined by a movable Si detector in front of the entrance window. For the on-line monitoring of beam intensity fluctuations the number of incident ions was related to a current measurement at the (primary) beam dump of SHIP. With the movable stack of degrader foils (Mylar) the recoil energy was reduced in order to optimise the position of the stopped ion cloud inside the gas cell.

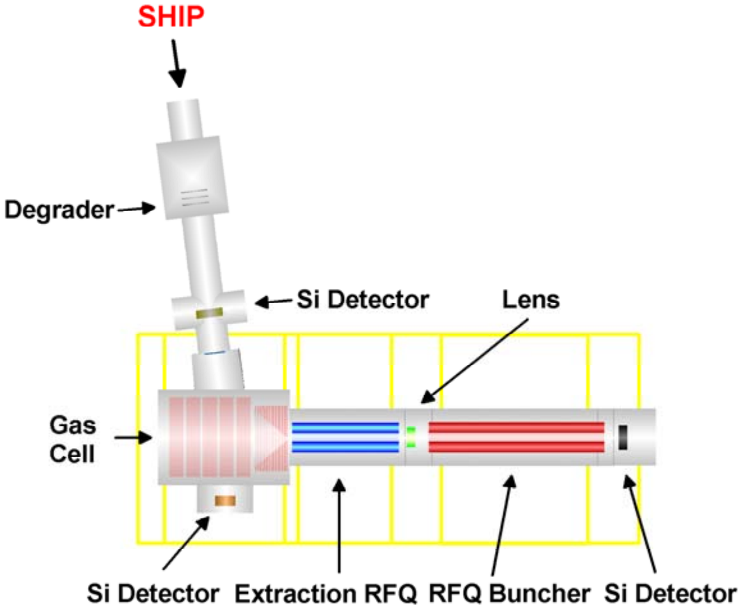
SHIP
Degrader
Si Detector
Lens
Gas Cell
Si Detector
Extraction RFQ
RFQ Buncher
Si Detector

Figure 5.27
Schematic view of the set-up including the SHIPTRAP RFQ buncher. In this case the Si detector for the identification of the extracted ions was placed directly behind the buncher.

In order to be able to determine if the injected ions were stopped near the longitudinal axis, an additional detector was placed inside the cell opposite the entrance window, as indicated in Fig. 5.26 and 5.27. For the determination of the number of ions entering the cell a movable Si-strip detector was placed in front of the entrance window. The detector was read out by eight channels segmented in *x*-direction with an overall size of 80 mm x 35 mm.

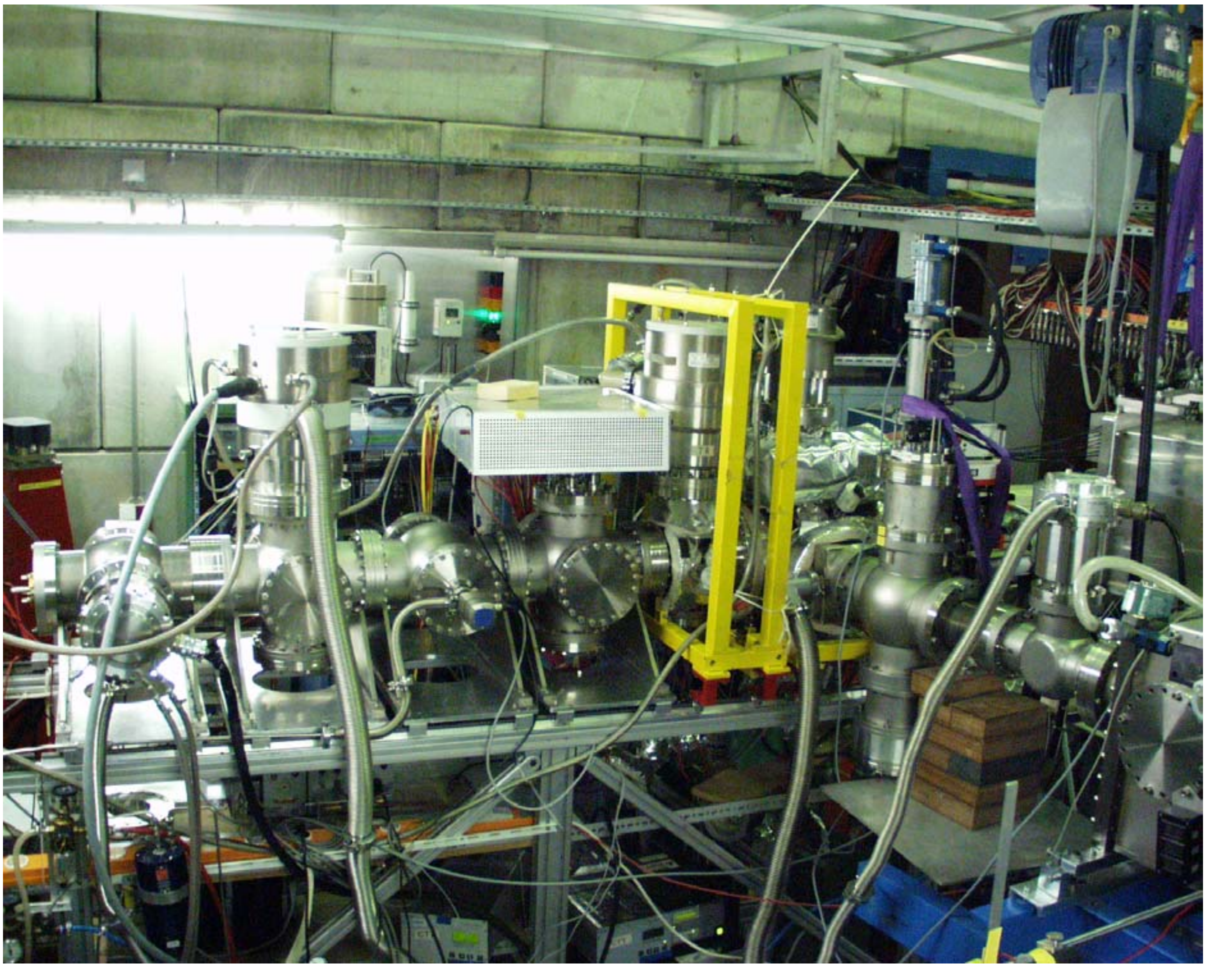

Figure 5.28
Photograph of the set-up used at GSI. On the right-hand side the SHIP beam line connected to the SHIPTRAP buffer-gas cell is visible. Following the extraction chamber (yellow support structure) the RFQ buncher and the last beam line section containing the Si detector are visible.

Figure 5.29 shows an α-decay energy spectrum detected in one of the Si-detector channels in front of the gas cell with the same structure as for the reaction used at the MLL. Besides the α ground-state decays of ^{152}Er, ^{153}Er, ^{151}Ho and ^{152}Ho also the decays of ^{150}Dy, ^{151}Dy and ^{149}Tb are visible.

A movable stack of degrader foils (Mylar, in steps of 0.5 µm) was placed in front of the entrance window in order to be able to reduce the energy of the recoil ions thus enabling the optimisation of the position of the stopped ion cloud inside the gas cell.

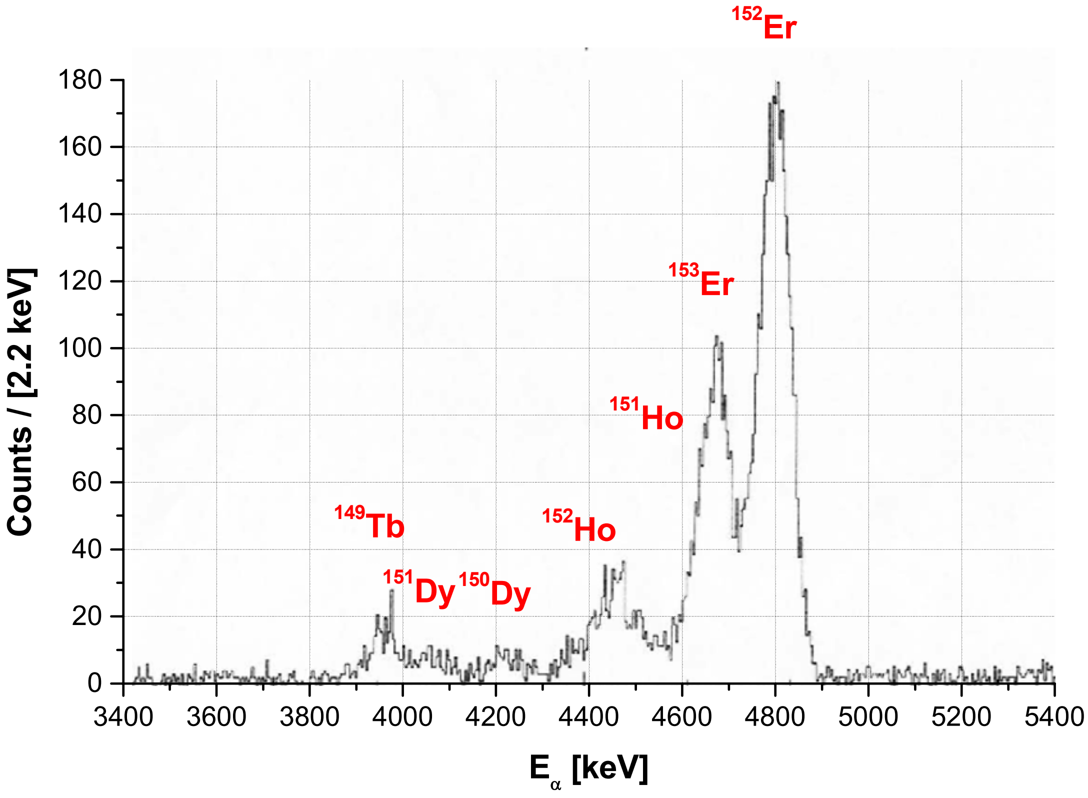

Figure 5.29
α-decay energy spectrum measured with one of the eight channels of the Si-strip detector in front of the gas cell, following the reaction ^{40}Ar + ^{116}Sn at E_{lab} = 168 MeV. The spectrum exhibits the same structure as obtained from the reaction ^{35}Cl + ^{121}Sb displayed in Fig. 5.20. Besides the α ground-state decays of ^{152}Er, ^{153}Er, ^{151}Ho and ^{152}Ho also the decays of ^{150}Dy, ^{151}Dy and ^{149}Tb are visible.

For the on-line monitoring of the primary-beam intensity a current measurement at the (primary-) beam dump of SHIP was used. Before extracting the absolute value of the gas-cell stopping and extraction efficiency, the numbers of injected and extracted ions, respectively, were always normalised to the same primary-beam intensity. Since the detector in front of the cell had a different size compared to the entrance window, another correction factor had to be taken into account. The resulting number of detected ^{152}Er was then directly compared to the number of ^{152}Er ions detected behind the extraction RFQ or behind the buncher, respectively.

Figure 5.30 shows an α-decay energy spectrum measured with the Si detector placed behind the extraction RFQ. Compared to the spectrum taken in front of the cell the lower number of detected α decays of ^{149}Tb and the lower height of ^{153}Er relative to ^{152}Er are visible. This could be explained by a lower stopping efficiency in the buffer gas for both isotopes due to their different incident energies.

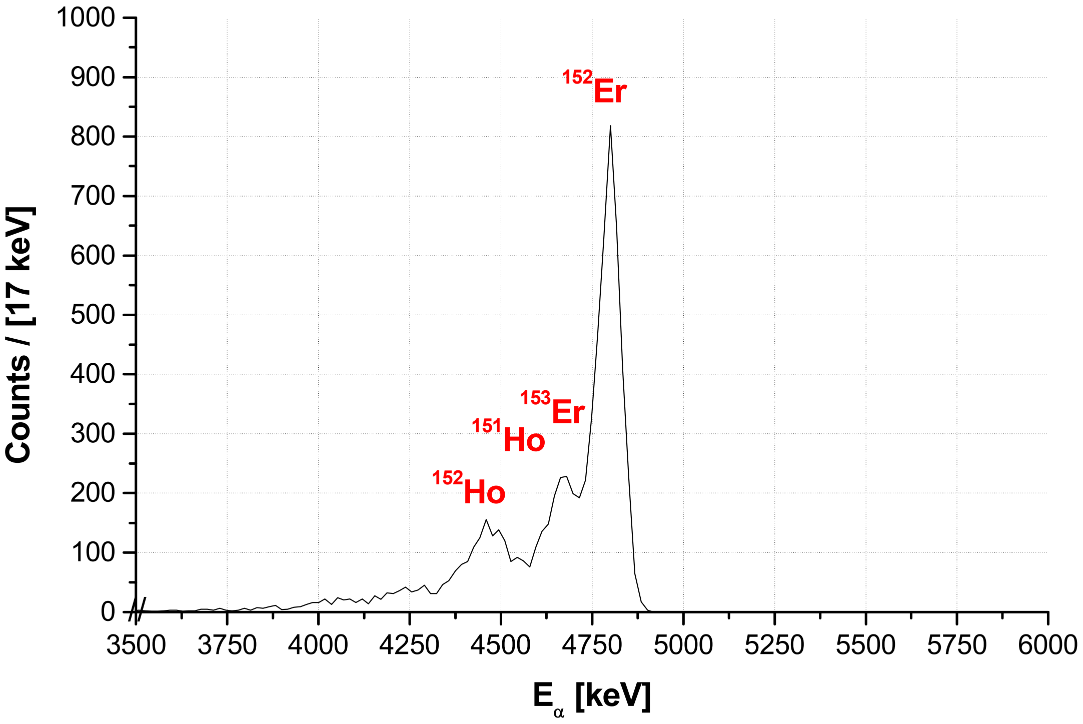

Figure 5.30
Plot of α energies detected behind the extraction RFQ with the same peaks as detected in front of the cell. The main differences to Fig. 5.29 are the lower contributions of ^{149}Tb and ^{153}Er.

The first measurements were done only with the gas-cell/extraction-RFQ set-up in order to optimise stopping and extraction before the combined operation with the RFQ buncher. Since the (rapidly fluctuating) intensity of the primary beam was not monitored continuously during the measurement, several of the following plots do not show the absolute but a relative efficiency, where the values were normalised to the maximum within the plot.

In Table 5.5 the measured absolute efficiencies for ^{152}Er at different electrical-field and gas-pressure settings are shown. All displayed efficiencies were measured for an RF voltage of 200 V_{pp} at 800 kHz applied to the funnel and an RF frequency of 1100 kHz applied to the extraction RFQ. The DC gradients were 0.5 V/mm at the funnel and 0.3 V/cm at the RFQ and the degrader thickness in front of the entrance window in all cases was 0.5 µm (Mylar). DC 5 describes the voltage applied to the DC electrode segment close to the funnel, while DC 3 is the corresponding voltage for the segment in the middle of the electrode. Since most of the ions are stopped within the last three segments of the DC electrode, the influence of a DC gradient between the first three segments is low. Therefore the first three electrodes were supplied with the same voltage. At the nozzle a voltage of 62 V was applied for a buffer-gas pressure of 62 mbar, while for 47 mbar 62.5 V were found as optimum for the used DC gradient at the funnel. The lower efficiency at 62 mbar is explained by the lower transport efficiency of the RF funnel, while the stopping efficiency is assumed to be comparable due to the energy straggling of the recoil ions. The gain in efficiency at 47 mbar at two different voltage settings is caused by both a higher transmission through the extraction RFQ and a more efficient extraction due to the higher fields, while the influence of the fields inside the gas cell is assumed to play the main part.

Pressure inside cell [mbar]	DC 5/DC 3 [V]	Amplitude RFQ [V_{pp}]	N_{Er} in front of cell [1/s]	N_{Er} behind RFQ [1/s]	Efficiency [%]
47	210/275	250	1090	30.6	2.8 ± 0.4
47	235/280	275	1260	60.6	4.8 ± 0.7
62	250/300	275	1770	67.8	3.8 ± 0.5

Table 5.5
Measured stopping and extraction efficiencies as a function of the applied voltages and the He buffer-gas pressures inside the cell.

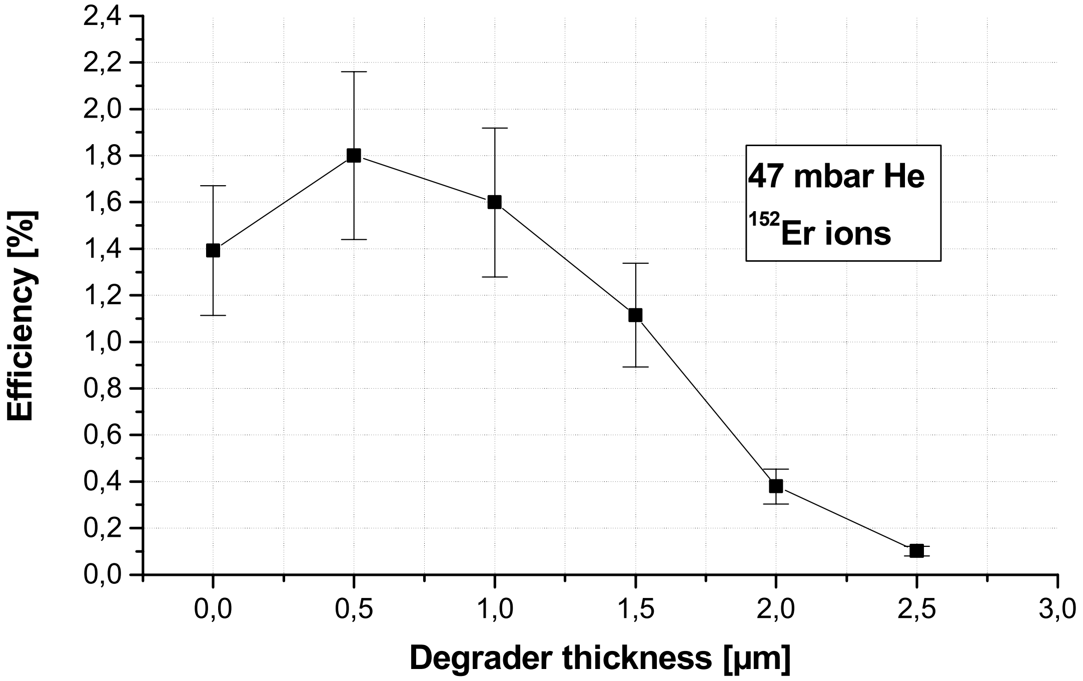

Figure 5.31
The absolute efficiency for ^{152}Er ions as a function of the degrader (Mylar) thickness. The buffer-gas pressure inside the cell was 47 mbar.

Besides the optimisation of the absolute efficiency several characteristics of the gas cell and the extraction were studied.

Figure 5.31 and Figure 5.32 show plots of the absolute efficiency for ^{152}Er ions as a function of the degrader thickness in front of the entrance window at a buffer-gas pressure of 47 mbar and 62 mbar, respectively. The efficiency maximum corresponds in both cases to a thickness of 0.5 µm of Mylar, resulting in an estimated kinetic energy of the ^{152}Er ions of (32.2 ± 5.5) MeV in front of the entrance window, taking into account all energy losses between target and degrader. TRIM calculates for these parameters a mean stopping range of (106 ± 90) mm where most of the ions would be stopped inside the DC electrode.

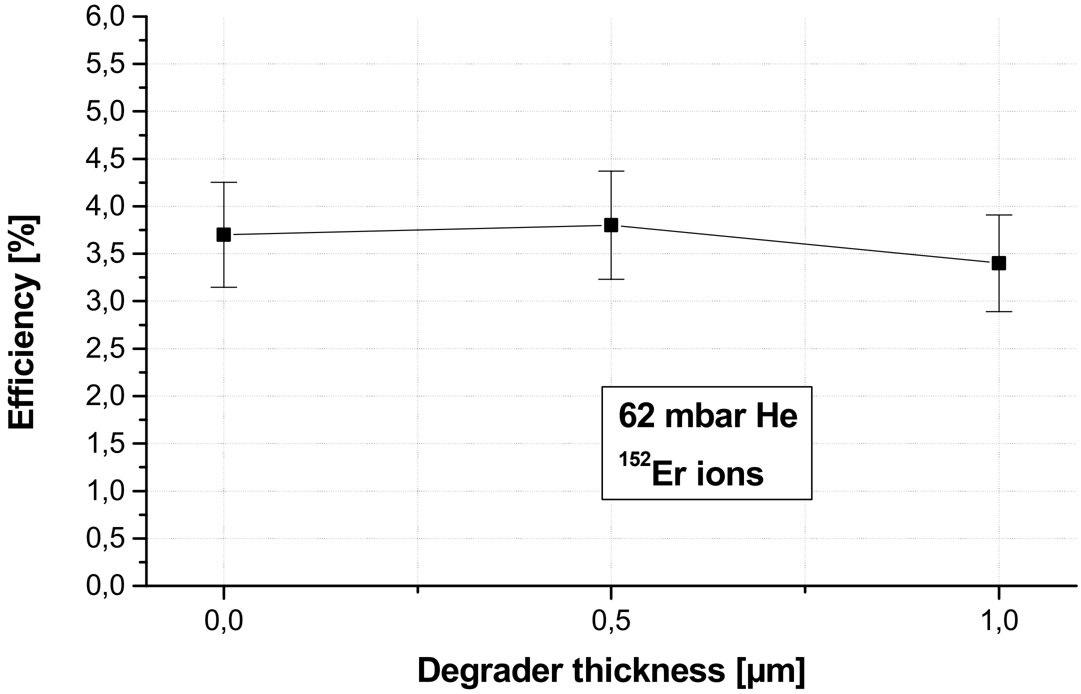

Figure 5.32
The absolute efficiency for ^{152}Er ions as a function of the degrader (Mylar) thickness. The buffer-gas pressure inside the cell was 62 mbar.

The lower efficiency values at a buffer-gas pressure of 47 mbar compared to the values determined at 62 mbar are explained by two different series of measurements. The settings at 47 mbar had not been optimised when the dependence of the absolute stopping and extraction efficiency on the degrader thickness was studied.
The efficiency decrease at degrader thicknesses beyond 0.5 µm Mylar are well reproducible with simulations showing that more and more ions will get lost in the entrance window foil for recoil-ion energies affected by the degrader.

In addition to the stopping efficiency the extraction efficiency was optimised in several steps. The systematics of the optimisation procedure allows to show some correlations that can be compared to results from the off-line measurements in Chapter 4.

Figure 5.33 shows the relative efficiency for ^{152}Er as a function of the voltage difference between the last segment of the DC electrode and the first funnel plate for two different DC gradients applied to the funnel. The relative efficiency is calculated for each gradient separately, therefore the values of two gradients cannot be compared.

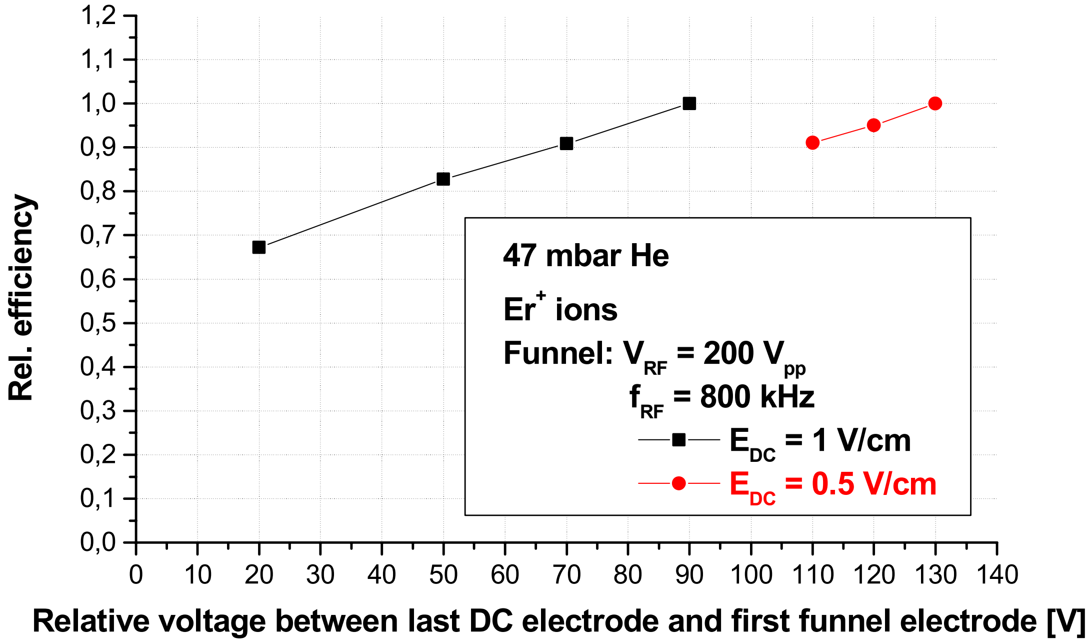

Figure 5.33
The relative efficiency for ^{152}Er ions as a function of the voltage difference between the last DC electrode segment and the first funnel electrode at a buffer-gas pressure inside the cell of 47 mbar for two different DC gradients applied to the funnel. The relative efficiency is calculated for each gradient separately, therefore the values of two gradients cannot be compared

Compared to Fig. 4.3 and Fig. 5.5 the almost linear rise of the efficiency shown in Fig. 5.33 is different, since the voltage difference for the extraction optimum with 90 V and 130 V, respectively, is different from the value of about 40 V in the off-line measurements and in addition no plateau shows up beyond the maximum. This may be explained by the non-optimised vacuum conditions during these measurements, where the getter pump could not be used. Therefore, as mentioned in the discussion of Fig. 4.10, the gain in extraction efficiency due to shorter extraction times for the higher voltage difference is assumed to be higher than the corresponding efficiency decrease due to ion losses on the funnel surface. In addition the gain in efficiency may be supported by less ion losses due to neutralisation for higher ion velocities, since the area of a high charge-carrier density due to the stopping process is shifted towards the region between the DC electrode and the funnel for the case of the perpendicular ion injection.

Figure 5.34 shows the relative efficiency for ^{152}Er as a function of the decelerating voltage between the last funnel electrode and the nozzle. The plot proves the results shown in Fig. 4.6, as in both cases for comparable gas pressures the extraction optimum is reached for a difference of +2 V. In addition the behaviour of the efficiency for voltage differences above and below the optimum is similar.

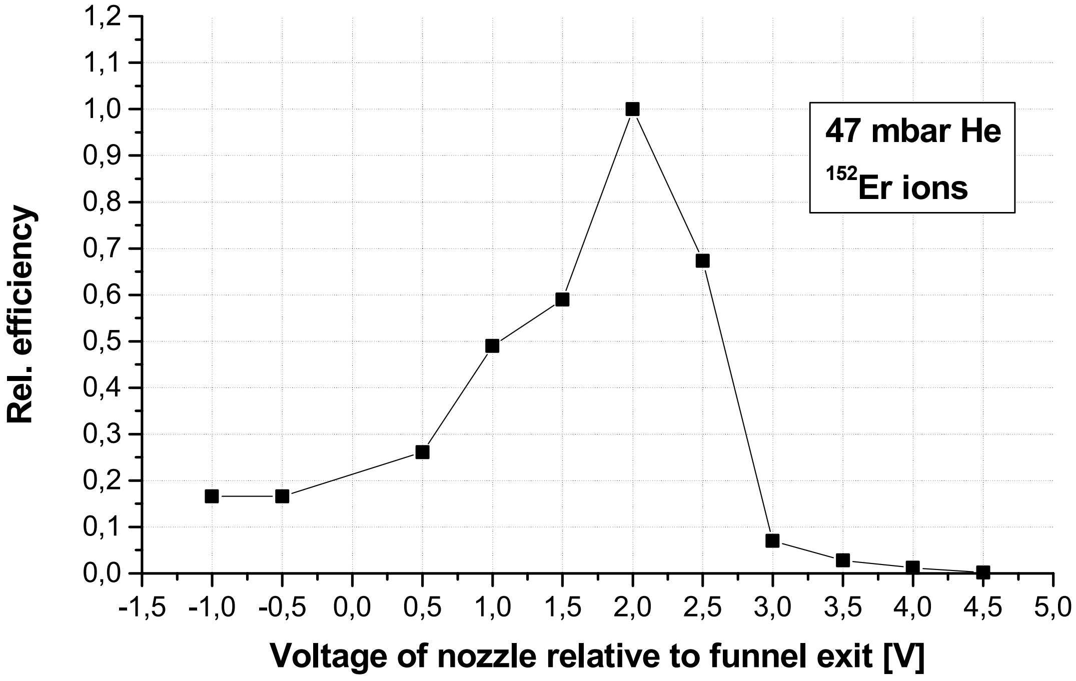

Figure 5.34
The relative efficiency for ^{152}Er ions as a function of the voltage difference between the last funnel electrode and the nozzle at a buffer-gas pressure of 47 mbar inside the cell.

In Figure 5.35 the relative efficiency as a function of the RF amplitude applied to the extraction RFQ is displayed. In addition the corresponding q value for ^{152}Er is presented, showing an extraction maximum at ~0.59. This behaviour is different compared to the former measurements, since Fig. 4.8 and Fig. 5.23 show an extraction maximum for a q value around 0.2.

Concerning the transport optimum in addition to the shifted q value a higher RF frequency of 1100 kHz instead of 800 kHz had to be applied. Measurements at a frequency of 800 kHz showed a drastically decreased efficiency, even for the same q value. Since the effective potential increases with an increasing RF frequency at a fixed q value, this behaviour may be amongst other things a hint that the emittance of the extraction RFQ still has to be optimised, which has to be investigated in further measurements.

Variations in the DC gradient applied to the extraction RFQ showed that the transport efficiency is completely independent of it. In addition the efficiency did not change even if no DC voltage at all was applied to the RFQ.

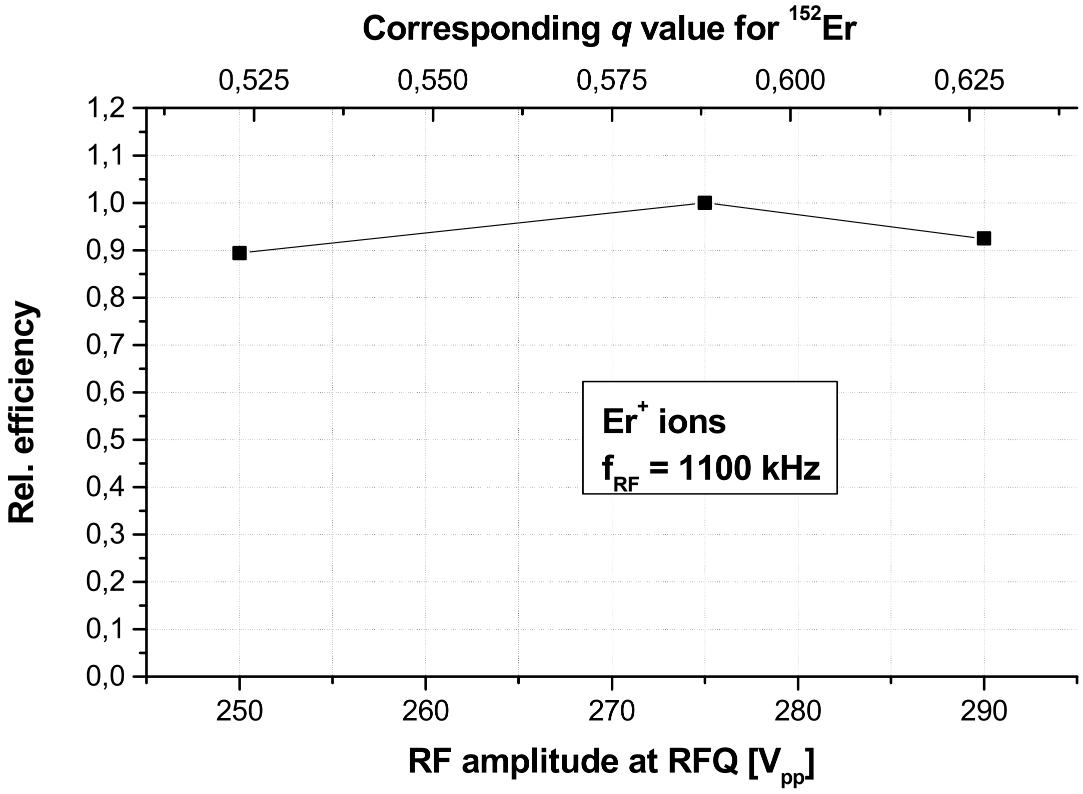

Figure 5.35
The relative efficiency for ^{152}Er ions as a function of the RF amplitude applied to the extraction RFQ at a frequency of 1100 kHz. In addition the corresponding *q* value for ^{152}Er is displayed.

In table 5.6 the absolute efficiency for ^{152}Er for the measurements with the set-up including the RFQ buncher at different settings is shown. The parameters for the gas-cell/extraction-RFQ correspond to the values where the maximum efficiency was reached (see Table 5.3) at a buffer-gas pressure of 47 mbar. The optimum potential applied at the lens between the two RFQs was found to be 50 V.
The transmission mode was used for two cases, with and without buffer gas inside the RFQ buncher. Without gas only an RF voltage of 128 V_{pp} at 950 kHz without any DC potentials was applied. During the operation without buffer gas the optimum extraction efficiency of (3.2 ± 0.4) % was found, while with buffer gas and with a DC gradient of 0.5 V per segment the value was (2.7 ± 0.4) %.
For the bunch mode, where the ions were accumulated and ejected as ion bunches, the optimum values for the measurements were an accumulation time of 20 ms, a closing voltage of 48 V and a DC gradient of 0.25 V per segment. The optimum overall extraction efficiency for this case was (2.7 ± 0.4) % which is as high as in the case for the transmission with a buffer gas.

Pressure inside RFQ buncher [mbar]	Mode	Amplitude RFQ buncher [V_{pp}]	N_{Er} in front of cell [1/s]	N_{Er} behind RFQ buncher [1/s]	Efficiency [%]
$< 10^{-5}$	transmission	128	1722	54.7	3.2 ± 0.4
10^{-3}	transmission	128	1607	42.8	2.7 ± 0.4
10^{-3}	bunch	128	1516	40.7	2.7 ± 0.4

Table 5.6
Measured stopping and extraction efficiencies for different settings of the RFQ buncher.

For an estimate of the transport efficiency of the RFQ buncher the measured stopping and extraction efficiency of the gas-cell/extraction-RFQ set-up of 4.8 % for the same settings has to be taken into account. The efficiency values shown in Table 5.6 therefore result in transport efficiencies of around 67 % in transmission without buffer gas and around 56 % with buffer gas in both transmission and bunch mode. Within the uncertainties these values are in good agreement with efficiencies measured off-line with an ion source coupled to the buncher [Rod03], assuming the same *q* value of 0.6 for both measurements.
Nevertheless, since in addition the transfer between the extraction RFQ and the RFQ buncher is included in these efficiencies further investigations are required in order to clarify if there is actually an optimum transfer or if chemical aspects of the test ions have also got to be taken into account.

Comparing the measured absolute stopping and extraction efficiencies for the measurements at the MLL and at GSI and taking into account the non-optimum conditions at GSI such as the vacuum purity and the energy spread of the recoil ions, the set of operation parameters found at GSI actually reflects the optimum. This set is displayed together with the main design parameters of the set-up in the Appendix and is the foundation for future measurements.

5.3. Discussion of the buffer-gas cell performance

In order to evaluate the actually determined performance of the SHIPTRAP buffer-gas cell it has to be compared to the performance of the buffer-gas cell (gas catcher) of the CPT at Argonne, which is based on a similar concept concerning the dimensions and the electrode configuration (see Section 1.2.4). For this cell an extraction efficiency of up to 45 % for Cs and Ba ions was reported [Sav02]. For a comparison of the performance of both cells stopping calculations were performed, since the efficiency reported for the Argonne gas cell contains only the extraction out of the cell. TRIM (SRIM version 2003.17) calculations for the ^{152}Er recoil-ion energies produced at the MLL and at GSI, taking into account the buffer-gas pressures and entrance-window foil thickness, resulted in stopping efficiencies of about 30 % (MLL) and 25 % (GSI), respectively, at the SHIPTRAP buffer-gas cell. Including an estimated efficiency of the extraction RFQ of 85 %, extraction efficiencies of the

SHIPTRAP buffer-gas cell of about 32 % for the measurements at the MLL and of about 23 % for the measurements at GSI can be deduced. The difference between the two measurements can be explained by different vacuum conditions and by the higher buffer-gas pressure during the measurements at GSI, leading to a lower transport efficiency of the funnel. In view of the gain potential under optimised operational conditions extraction efficiency values comparable to the Argonne gas cell are within reach.

The direct comparison between both cells is based on similar operational parameters of both cells, displayed in Table 5.7. A main difference between both cells concerns the RF funnel, since the structure used at Argonne has an electrode plate thickness of around 0.3 mm and a distance between adjacent plates of 0.3 mm. With regard to Eq. (2.100) the resulting effective fields are around 30 times higher than the effective fields of the SHIPTRAP RF funnel at the same buffer-gas pressure and the same RF amplitude. Therefore the Argonne gas cell provides a higher ion-transport efficiency at higher gas pressures.

	SHIPTRAP gas cell	CPT gas catcher
Absolute efficiency	~4 – 8 %	-
Extraction efficiency	~23 – 32 %	~40 – 45 %
Dimensions	32 cm x 25 cm	25 cm x 8 cm
Stopping volume	18 cm x 18 cm	~18 cm x 7.5 cm
Entrance window	1.8 mg/cm^2 Ti	1.9 mg/cm^2 HAVAR
Funnel plates: thickness/distance	1 mm	~0.3 mm
Diameter of the nozzle throat	0.6 mm	1.7 mm
RF voltage at funnel	200 V$_{pp}$ @ 800 kHz	~180 V$_{pp}$ @ 900 kHz
DC fields	~5 – 10 V/cm	~20 V/cm
Buffer-gas pressure	~50 mbar He	~150 – 200 mbar He
Typical stopped and extracted isotopes	^{107}Ag: stable beam (23 MeV) ^{152}Er: ^{121}Sb(^{35}Cl (150 MeV),4n) ^{116}Sn(^{40}Ar (168 MeV),4n)	$^{141\text{-}145,147}$Ba: $^{143\text{-}149}$La: $^{145,147\text{-}149,151}$Ce: ^{149,151}Pr: ^{252}Cf-fission source ^{68}Se: ^{12}C(^{58}Ni (220 MeV),2n) ^{64}Ge: ^{12}C(^{54}Fe (185 MeV),2n) ^{120}Cs: ^{63}Cu(^{60}Ni (220 MeV),2p1n)

Table 5.7
Operational parameters for the SHIPTRAP buffer-gas cell and the CPT gas catcher. The values for the gas catcher are taken from [Sav02], [Sav03], [Sav03a] and [Sav03b].

With regard to the vacuum system of both cells the main difference is given by the ability to pump directly at the gas-cell volume via a turbo pump being directly connected to the SHIPTRAP gas cell, while the CPT gas catcher is only pumped through the extraction nozzle. However, this difference is only of importance when the cells are pumped down during the preparation phase for subsequent measurements. During regular operation a more crucial influence on the cell performance is given by the outgassing rate of vacuum impurities from the surface area of the cell, therefore the smaller surface area of the CPT gas catcher compared to the SHIPTRAP gas cell may be advantageous. In order to remove the impurities from the cell, for the CPT gas catcher only the pumping speed of 50 – 200 l/s created by the gas flow inside the gas catcher and through its nozzle is used. Due to the larger surface area of the SHIPTRAP gas cell and the lower pumping speed through the smaller extraction nozzle, getter pumps placed inside the stopping chamber have to be used in order to remove the gaseous impurities with a comparable efficiency as for the CPT gas catcher.

The performance of the SHIPTRAP buffer-gas cell concerning the optimum vacuum conditions is actually not well defined. A hint for optimum conditions would be given by the identification of extracted ions with higher charge states than 1+, as observed at the Argonne cell for fission fragments of a ^{252}Cf source placed in front of the gas-cell window [Sav03]. There Ba^{1+} ions were extracted with an efficiency of 10 %, while simultaneously 20 % were reached for Ba^{2+} ions [Sav02]. Since Ba and Er have similar ionisation potentials, the identification of the charge states of ^{152}Er behind the SHIPTRAP buffer-gas cell could help to assess the vacuum conditions inside, however in the present test set-up the determination of higher charge states would be limited by the rather low efficiency of the mass-selective diagnostics using either a QMS or the Gießen Ortho-TOF spectrometer. A hint of the occurrence of higher charge states during the measurements at the MLL may be given by the different RF amplitudes that had to be applied at the extraction RFQ compared to the optimum RF amplitude used during the measurements at GSI (see Sect. 5.2.2), nevertheless further studies on this issue have to be performed.

With an improved design of the gas stopping cell, using a thinner entrance foil and a larger stopping volume, the stopping efficiency could be increased by a factor of 2 – 3 resulting in correspondingly larger absolute efficiencies.

Chapter 6

Conclusion and outlook

6.1. Conclusion

Within this work the buffer-gas cell and the extraction RFQ for the SHIPTRAP facility were designed, assembled and characterised. The characterisation measurements showed that a fast (~5 ms at 50 mbar) and efficient (up to 8 % absolute) extraction of the stopped ions is achievable with the present system. With regard to measured efficiencies of gas cells of other groups (see Sect. 5.1.2 and Sect. 5.3) the overall efficiency of the SHIPTRAP gas-cell/extraction-RFQ combination is comparable, taking into account that also the stopping efficiency in the gas cell is included.

In the recent commissioning measurements at GSI together with the RFQ buncher absolute efficiencies of almost 3 % in bunch mode were obtained. This performance enables physics experiments with the complete SHIPTRAP facility.

Besides the results of the efficiency measurements, which were performed both with stable and radioactive ions, optimum operational settings for the actual set-up have been determined.
With regard to optimised extraction efficiencies the accelerating potentials applied to the DC electrodes have to be as high as possible in order to guarantee a fast extraction and therefore less ion loss due to neutralisation and molecule formation. This motivates the requirement of utmost purity in the vacuum system and the He buffer gas. However, the voltage applied at the DC electrode segment in front of the RF funnel should not exceed certain values (depending on the gas damping) in order to avoid ion losses due to the lower transport efficiency in the funnel at higher ion velocities caused by higher electrical fields.
The ion-transport efficiency inside the funnel is also affected by the applied DC gradient, as for lower ion velocities the repulsive RF forces are more efficient. Nevertheless a fast ion extraction has to be guaranteed, therefore the DC gradient has to be a compromise between the transport efficiency and the prevention of ion loss in the buffer gas.
Concerning the ion extraction by the buffer gas the voltage difference between the last funnel electrode and the nozzle is of prime importance for the extraction efficiency. At an ion velocity higher than the gas flow velocity the ions will be lost after hitting the nozzle surface, as they continue to follow the electric field lines. Therefore

a deceleration of the ions in front of the nozzle by applying a DC voltage at the nozzle of around 2 V higher than the voltage applied to the last funnel electrode has to be considered.

The transport efficiency in the extraction RFQ in contrast to the RF funnel is not affected by the applied DC gradient. The transport depends only on the voltage difference between the extraction nozzle and the first electrodes of the RFQ. Ion losses at certain settings of the RF at the RFQ can be explained by anharmonics due to imperfections of the quadrupole geometry and by an influence of the aperture of the extraction plate. In order to reduce this influence a larger aperture should be used if the higher gas flow from the extraction chamber into the RFQ buncher can be handled by the vacuum system.

The measurements including the Ortho-TOF spectrometer showed that the extraction efficiency is nearly constant up to beam intensities of around $2.5 \cdot 10^8$ ions per second, allowing for measurements with a high background level of ions.

The fact that even with a non-optimised vacuum purity good absolute stopping and extraction efficiencies could be achieved shows that the influence of chemical properties on the efficiency has to be characterised in more detail.

The availability of metallic and pin-hole free entrance-window foils with appropriate thickness and diameter actually limits the energy acceptance of the gas cell. The Ti foil with a thickness of 4 µm used for all on-line measurements presently sets a lower limit for the ion energy of around 0.2 MeV/u. For lower ion energies another concept has to be found. One possibility is given by the use of Kapton foils, where the influence on the gas purity has to be investigated.

In addition to the thickness of the window its homogeneity has also to be considered, since variations in the foil thickness will not be averaged in the stopping process but will rather lead to ion loss in the foil itself (too thick) or on the stopping-cell walls (too thin). This is one of the major problems concerning the stopping efficiency inside the buffer gas, as well as the energy distribution of the incoming ions.

6.2. Outlook: Next-generation set-up

As described in the previous chapters, the crucial front-end components of the SHIPTRAP facility, gas stopping cell and extraction RFQ, could successfully be commissioned and their performance was characterised in on- and off-line measurements. Consequently the commissioning of the complete SHIPTRAP set-up has now started with the permanent installation of the gas-cell/extraction-RFQ combination in the SHIPTRAP beam line at GSI.

However, successful mass measurements of rare transuranium isotopes will require the highest achievable efficiency of the whole facility, so continuous optimisation of the existing components is mandatory. This goal will be pursued in Munich with a next-generation set-up of gas cell and extraction RFQ, while at the same time the existing installation at GSI will proceed towards the start of the physics programme. The new Munich set-up will also lay the foundation for the upcoming MAFFTRAP facility [Sze03] at the new Munich reactor FRM-II, which will be designed in close analogy to SHIPTRAP.

Moreover, results and improvements originating from the measurements with the new Munich installation will directly be transferred to SHIPTRAP, eventually resulting in modifications of the existing set-up.

6.2.1. Improvements of the SHIPTRAP gas cell

With regard to an efficient stopping and extraction of fusion reaction products, the advantage of a longitudinal ion injection scheme as realised at the MLL, in contrast to the perpendicular injection in the case of SHIPTRAP, facilitates the ion extraction, since the stopping volume is automatically centred around the extraction axis. Therefore there is no need to centre the ion cloud on this axis by an accurate choice of the buffer-gas pressure and degraders as it is presently done at SHIPTRAP. This may not lead after all to a drastic increase of the extraction efficiency, however routine operation during physics experiments will be much simpler and the available beam time may therefore be used more efficiently.

With regard to the next-generation RF-funnel structure, the new design will include ring electrodes with a significantly smaller outer diameter. Thus not only the capacitance will decrease, allowing to use an RF amplifier with lower power in combination with a resonant coupling of the RF, but also the effective surface area will decrease, reducing the rate of outgassing.

6.2.2. The new Munich set-up

With regard to the upcoming MAFFTRAP gas cell [Sze03] and in order to continue the development of buffer-gas cells at the MLL in Garching, a new set-up is presently under construction. The design is based on the SHIPTRAP cell/RFQ set-up and the experiences gained with it. Figure 6.1 shows a schematic view of the new set-up. As the new stopping chamber is initially designed for a longitudinal beam injection, in particular the dimensions differ significantly from the design parameters of the SHIPTRAP cell.

Therefore the main difference of the new gas cell compared to the SHIPTRAP cell is the absence of the radial entrance window and the modified overall dimensions of the cell. With the ions entering the cell on its longitudinal symmetry axis, the radius of the cell can be reduced (from 180 mm to 140 mm) compared to SHIPTRAP, while the requested flexibility in stopping ranges leads to an increase of the gas-cell length (from 330 mm to 500 mm). The decrease in diameter demands a modified RF-funnel geometry, leading to a smaller aperture angle with the advantage of lower RF amplitudes required.

Special attention will be paid to the purity of the system. Therefore the amount of getter material placed inside the gas cell will be increased, whilst the amount of flange connections to the outside will be minimised by concentrating various functionalities such as vacuum gauges and electrical feedthroughs on a few outlet flanges, thus improving the pumping and baking conditions.

The whole system of vacuum chambers and outlet flanges will be manufactured from UHV-compatible stainless-steel material (type 316L), allowing to anneal the complete set-up at around 1000 °C, in order to improve the vacuum quality.

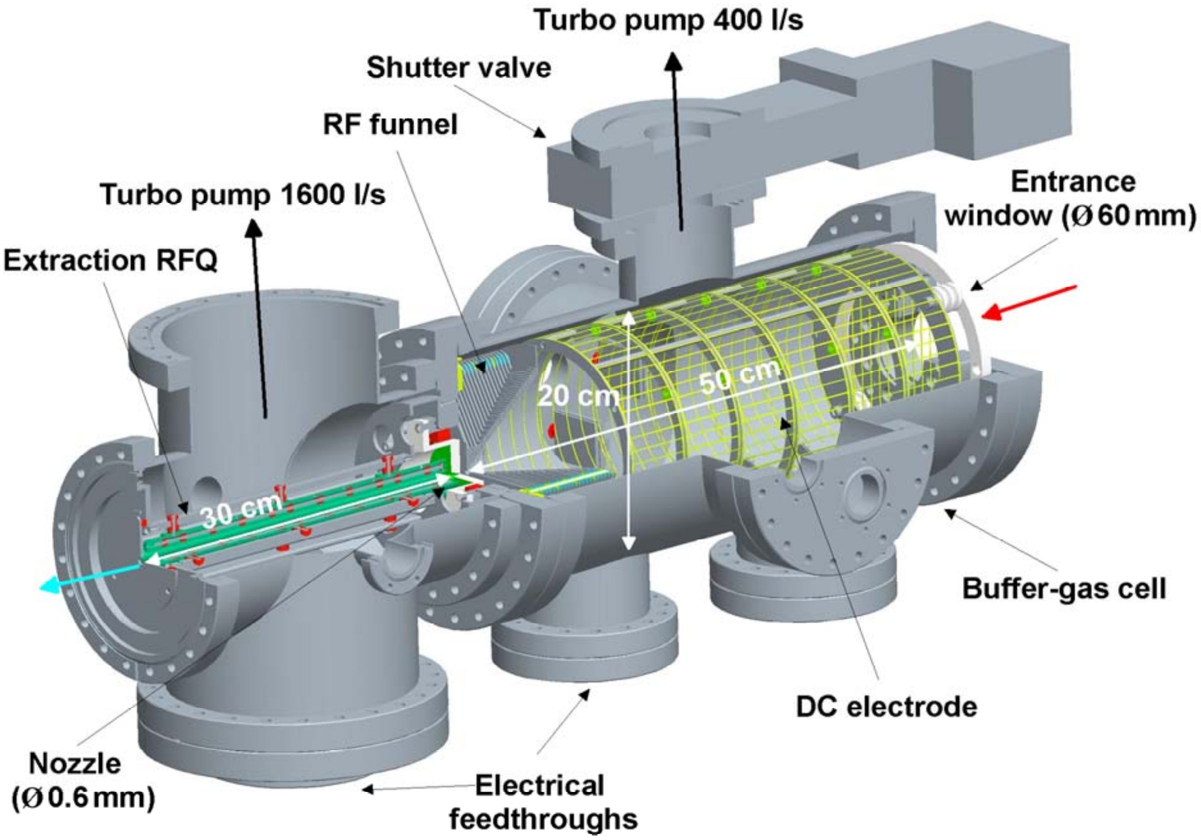
Turbo pump 400 l/s
Shutter valve
RF funnel
Turbo pump 1600 l/s
Entrance window (Ø60 mm)
Extraction RFQ
20 cm
50 cm
30 cm
Buffer-gas cell
DC electrode
Nozzle (Ø0.6 mm)
Electrical feedthroughs

Figure 6.1
Schematic view of the new Munich gas-cell and extraction-RFQ set-up. The buffer-gas cell has a length of 50 cm and a diameter of 20 cm, while the extraction chamber has a length of 30 cm.

In order to improve the pumping conditions the new extraction chamber will be larger compared to the present one. By enlarging the flange diameter of the connection to the 1600 l/s turbomolecular pump at the extraction chamber the full pumping speed of this pump can be exploited, thus avoiding the present reduction of the conductance. The resulting increase in size of the extraction chamber will be compensated by an increased length of the extraction RFQ from presently 18 cm to 30 cm, whilst the number of segments (12) will be kept constant. Compared to the SHIPTRAP RFQ the new version is based on the same structure and has the same aperture and rod diameter. In order to improve the mechanical stability of the rods, a third attachment point to the support structure has been added.

6.2.3. Optimisation program with the new set-up

The priority given to the optimisation program with the upcoming set-up at the MLL is the optimisation of the absolute ion extraction efficiency. The successful method using α emitters will thereby further be used for the efficiency measurements.

An issue of prime importance with regard to the absolute efficiency of the buffer-gas cell is the improvement of the stopping efficiency. Therefore the effect of the orientation of the ion injection relative to the extraction axis will be studied, potentially resulting in a modification of the SHIPTRAP set-up at GSI.

Concerning higher buffer-gas pressures, which could help to reduce the stopping volume of the ions and to improve the energy acceptance of the buffer-gas cell, new concepts will be studied. This includes new nozzle concepts as well as new RF-funnel geometries.

Another point with regard to the improvement of the stopping efficiency concerns the entrance window. Since the available thickness of the used metal foils is limited, it has to be clarified if thin Kapton foils could be used instead. Since the measurements with the SHIPTRAP set-up showed that even with a non-optimised vacuum purity good efficiencies could be achieved, it has to be tested in how far organic materials can be accepted in the buffer-gas cell. For foils of both materials, metals or Kapton, especially the homogeneity of thickness has to be checked in order to minimise ion losses.

This property will also be included in the planned study on the influence of the residual-gas composition inside the buffer-gas cell on the extraction efficiency. Here especially the outgassing rate from the chamber surface during operation and the effect of getter pumps inside the gas cell are of interest. In addition the influence of the material (e.g. the type of stainless steel 316L used) and prior treatments of the set-up (e.g. annealing at high temperatures) will be studied.

Related to the purity of the buffer gas is the charge distribution of the extracted ions, as according to the ionisation potential of 24.58 eV for pure helium strong contributions from higher charge states (2+, 3+) besides the singly-charged ions for many elements should be expected, provided that charge-exchange, recombination or molecule-formation processes are negligible.

The combination of the new set-up with the Gießen Ortho-TOF spectrometer will allow for studies of chemical processes inside the buffer-gas cell. Especially the molecule formation for various elements being stopped and extracted may be studied, since the Tandem accelerator at the MLL offers an extensive variety of different projectile ions.

Besides the optimisation of the set-up its systematic experimental characterisation has to be completed. This comprises systematic studies of the correlation between electric fields and the gas pressure, as started for the SHIPTRAP set-up, as well as the emittance behind the extraction RFQ. These measurements have to be done both with laser-induced ions and ions from the Tandem accelerator.

6.2.4. A new extraction structure

A new extraction structure to replace the existing extraction RFQ has been proposed by V. Varentsov [Var02], based on experiences with the RF-funnel structure and on calculations with VARJET. The basic idea is an ion transport only by the gas flow without dragging DC fields. This would allow to use only the two RF phases with low amplitudes applied at the structure. Another advantage could be that any heating of the ions by the dragging fields can be avoided resulting in a very cold beam.

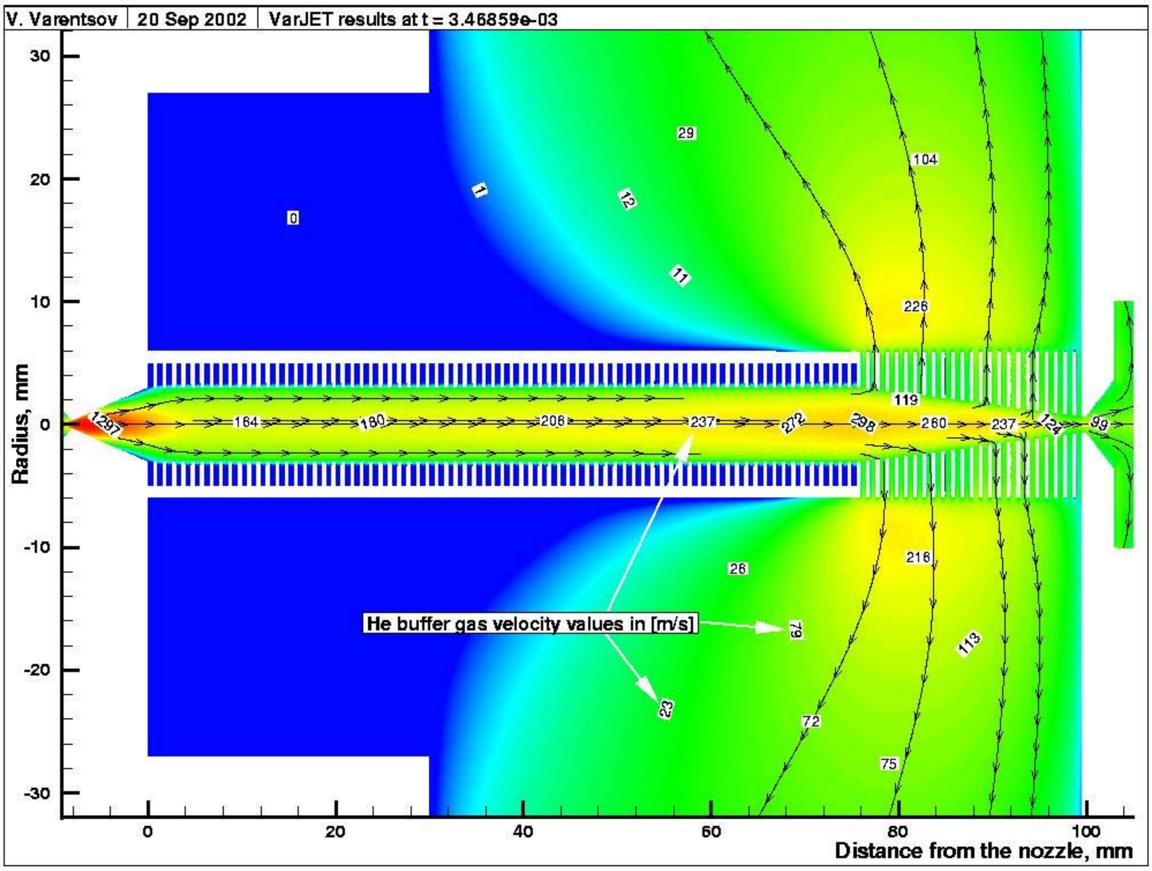

Figure 6.2
VARJET simulation for the proposed extraction structure. Besides the geometry of the structure the simulations shows the direction of the gas flow (arrows) and the He buffer-gas velocity for certain positions.

Figure 6.2 shows the geometry of the proposed structure within a plot of a VARJET gas-dynamical simulation. Analogue to an RF-funnel structure it consists of a stack of ring electrodes, shaping a cylindrical RF channel with a total length of 75 mm (75 ring electrodes) and an inner diameter of around 6 mm, followed by an RF funnel with a length of 25 mm (25 ring electrodes) and an exit aperture of 1.2 mm. The electrode plates have a thickness of 0.5 mm and an outer diameter of 1.2 cm and the distance between adjacent plates is 0.5 mm.

Since the ion transport inside the new structure will be done by the gas flow following the buffer-gas jet after the extraction nozzle, the untimely collapse of the directed flow is avoided by coating the channel region. The open structure of the funnel region afterwards guarantees an effective pumping of the buffer gas in order to avoid a flow of a high amount of gas into the high-vacuum sections following the extraction chamber.

Besides the geometry of the structure the simulation shows the direction of the gas flow (arrows) and the He buffer-gas velocity for certain positions.

The results of the VARJET calculations were also included in ion-optical simulations using SIMION. Since the He pressure inside the RF structure is in the region of some mbar, the viscous-damping model was used for the simulation of the gas damping. Figure 6.3 shows the resulting ion trajectories for the area following the extraction nozzle and the exit RF-funnel region, where the focussing effect of the structure is clearly visible. The trajectory simulations were done for an ion mass of 100 amu, an RF amplitude of 1 V_{pp} at 1 MHz and the assumed He buffer-gas pressures of 50 mbar in the gas cell and $1.5 \cdot 10^{-2}$ mbar in the extraction chamber.

Ion mass: 100 amu
f_{RF}: 1 MHz
V_{RF}: 1 V_{pp}

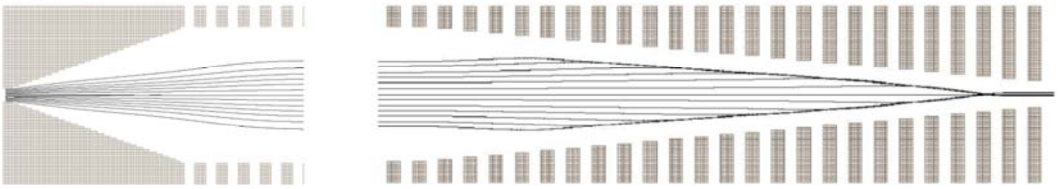

Pressure in the cell: 50 mbar He
Pressure in the extraction chamber: $1.5 \cdot 10^{-2}$ mbar He
Transport time: 500 - 800 μs

Figure 6.3
Ion-optical simulations using SIMION and the results from the VARJET calculations for the proposed extraction structure. Shown are the resulting ion trajectories for the area following the extraction nozzle and the exit RF-funnel region, where the focussing effect of the structure is clearly visible.

With regard to the resulting transport times of 500 – 800 μs and the buffer-gas pressure in the range of 1 – 2 mbar inside the extraction structure, studies have to be performed concerning possible ion losses due to neutralisation by charge exchange.

6.3. Physics program in combination with a Penning-trap system

In parallel to the new gas-cell/extraction-RFQ set-up a double Penning-trap system for the upcoming MAFFTRAP facility [Sze03] is already under construction at the MLL in Garching. In addition a ring-electrode buffer-gas cooler (RF-funnel cooler) has been built and successfully tested [Hei03]. Until the availability of accelerated ion beams at MAFF [Hab03], the different components can be used in combination for measurements using the existing Tandem accelerator of the MLL. The efficiency measurements using ^{152}Er showed, that isotopes in the rare earth region can be produced, stopped and extracted in amounts suitable for mass measurements in a Penning trap.

Nevertheless, in order to improve the efficiency of the measurements, especially the transfer efficiency between target and gas cell has to be increased. Since the energy spread and the resulting charge state distribution is given by the reaction, the number of available recoil ions can primarily be increased by an increase of the primary-beam intensity. In order to avoid the destruction of the target due to heating, one possible solution could be given by a wobbling of the primary beam on the target area allowing for a prevention of selective hot spots on the target material.

Moreover, the transfer efficiency of recoil ions could significantly be increased by replacing the present 90° dipole magnet with a new gas-filled separator magnet with a wider acceptance than the present magnet. With a reaction target placed inside the gas-filled dipole chamber and using the exit window of the magnet simultaneously as the entrance window for the buffer-gas cell, a gain factor of about 5 can be expected for the recoil ion transfer efficiency to the gas cell and hence to the subsequent Penning trap.

The following paragraphs illustrate the physics perspectives opened up by the new facility at the MLL.

6.3.1. High-precision mass measurements

Mass measurements using Penning traps provide the highest achievable accuracies of about $\delta m/m \sim 10^{-8}$, in special cases already reaching the ppb region [Bla04]. The mass m of an ion (charge state $\tilde{q}$) confined in a Penning trap (magnetic flux density B) is obtained via a comparison of its cyclotron frequency ν_c, given by

$$\nu_c = \frac{\tilde{q} \cdot B}{2\pi \cdot m}, \tag{6.1}$$

with that of a well-known reference mass. The recently introduced use of carbon cluster sources [Bla02] has the advantage that sharply defined reference masses in multiples of the mass of ^{12}C can be obtained. Since the unified atomic mass unit is defined as 1/12 of the mass of this nuclide no experimental error has to be taken into account.

Moreover, the advantage of using highly charged ions is obvious from the linear dependency between the cyclotron frequency and the ion charge state. The resolving power achievable in a mass measurement is approximately given by the product of the cyclotron frequency and the duration of the excitation in the trap T_{Ex}. The resulting relative statistical mass uncertainty is then given by

$$\delta m / m \approx m / (T_{Ex} \cdot \tilde{q} \cdot B \cdot N^{1/2}), \tag{6.2}$$

where *N* is the number of detected ions. In order to optimise the precision, i.e. to achieve a low mass uncertainty, high cyclotron frequencies by either strong magnetic fields or higher charge states and longer excitation or observation times are desirable.
The use of highly-charged ions has already been successfully applied at the SMILETRAP facility in Stockholm [Bes02], where ppb mass uncertainties could be realised.
Moreover, further improvements in magnet and trap technology will enable to reach mass uncertainties down to as low as 0.1 eV within the next decade e.g. by increasing the magnetic field of the Penning trap (9 T magnets already being available) or the homogeneity of the magnetic field in the trap region, which can be done by shielding against external stray field components e.g. by applying additional compensation coils [Gab88]. Given these perspectives, mass measurements will gain qualitatively new impact in many areas, where so far only spectroscopic techniques were used, including exciting new prospects to contribute to the field of fundamental interactions (see Sect. 6.3.3).

6.3.1.1. Ground-state masses

Already with the presently achievable mass resolutions significant progress can be contributed to the mass landscape of the nuclidic chart. It should be reminded that presently only 27 of the 3177 nuclides listed in the recent Atomic Mass Evaluation AME2003 [Wap03] with experimentally determined or extrapolated mass values have been determined to an accuracy level of 10^{-9}.
Candidates for future mass measurements at the MLL are shown in Figure 6.4. Indicated by dots are the isotopes, where the experimental mass uncertainty exceeds 130 keV (green) or 470 keV (red), respectively, while mass values obtained from systematical extrapolations are marked by black dots. Only isotopes with lifetimes larger than ~80 ms have been included, which is sufficient for measurements with a buffer-gas cell and a subsequent Penning trap.
Amongst the possible candidates nuclei can be found which have a special relevance for calculations concerning the location of the proton drip-line and for the rp process. These nuclei are ^{65}As, ^{66}As, ^{70}Br and ^{71}Br with regard to the calculations for the binding energies of proton-rich nuclei [Bro02] and ^{80}Zr as an even-even waiting point with $Z = N$.
Studying mass systematics with higher precision will show new dependencies on e.g. deformation, intruder states etc. Large-area surveys will be possible which will also allow to study correlations with quantities like the quadrupole moment of deformed nuclei.

A compilation of possible candidates taking into account the possibilities given by the Tandem accelerator concerning the ion species, the beam intensity and the available energy of the primary beam and with regard to the available target materials is presented in the Appendix.

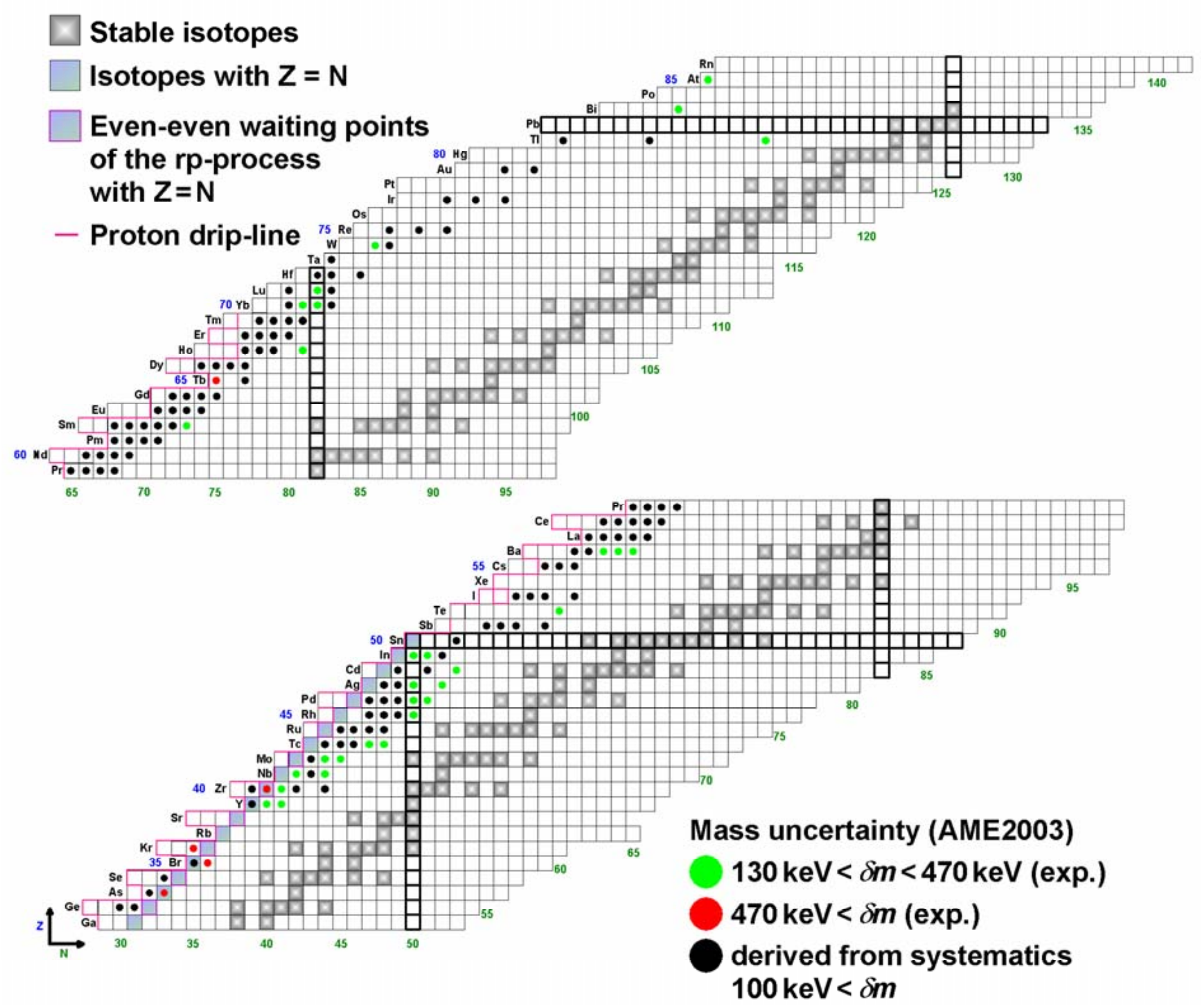

Figure 6.4
Candidates for future precision mass measurements at the MLL. Indicated are the isotopes with a mass uncertainty of more than 130 keV (green), of more than 470 keV (red) and isotopes with masses derived from systematics (black) [Wap03]. All isotopes have lifetimes of more than ~80 ms in order to allow for measurements with a buffer-gas cell and a subsequent Penning trap.

6.3.1.2. Isomer spectroscopy

With the availability of an increased mass resolution isomers will become a key topic of Penning-trap mass spectrometry. While presently many listed mass values have to be considered as forged by isomer contaminations, mass resolutions beyond the ppb region will allow to discriminate isomeric contributions from the ground-state masses. Furthermore, isomers can be targeted in dedicated studies.
Figure 6.5 gives an overview of the occurrence of isomers with half-lives of longer than 1 ms throughout the nuclidic chart.

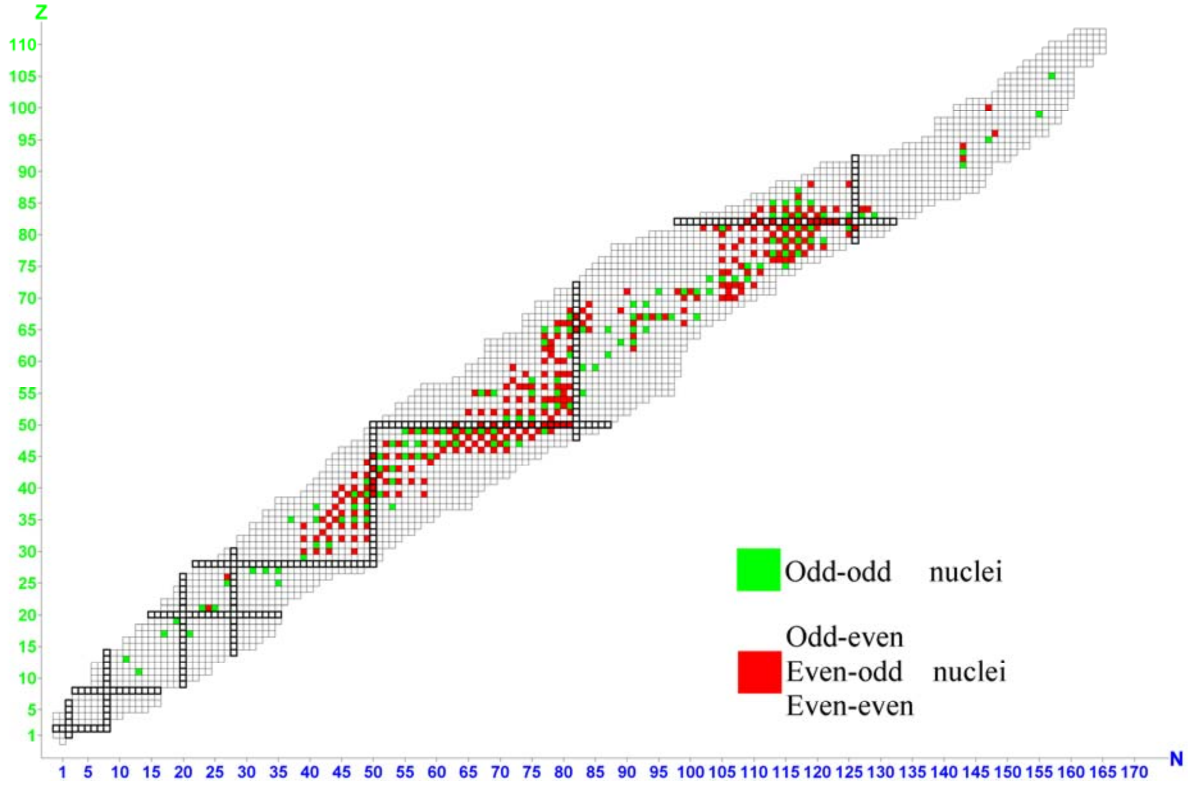

Figure 6.5
Overview of the isotopes having isomers with half-lives larger than 1 ms. Indicated in green are the odd-odd nuclei, while all other combinations are shown in red.

6.3.1.2.1. The α decay of high-spin and K-isomers

The mass region of the rare earth elements ($58 \leq Z \leq 70$ and $80 \leq N \leq 88$) is known for the appearance of high-spin isomers [dVo83] and therefore offers the basis for α-spectroscopy studies on high-spin isomers using the new set-up at the MLL. While the decay characteristics of these isomers have been studied in detail by γ-spectroscopic methods, only few experimental hints about their α-decay channels are existing [Hof79, Hof89].

For a prediction of possible half-lives for the α decay channels the Geiger-Nuttal rule can be used. This rule describes an empiric linear relationship between the logarithm of the (partial) α-decay half-lives and the inverse square root of the α-decay energy for the ground-state α decay of isotopes from a specific element. In Figure 6.6 this relation is shown for isotopes of Tb, Ho, Er, Lu and W. Indicated are the known α decays from high-spin isomers of ^{155}Lu ($I = (25/2^-)$, $E_\alpha = (7379 \pm 15)$ keV, $t_{1/2} = (2.60 \pm 0.07)$ ms [Ho89]) and ^{158}W ($I = (8^+)$, $E_\alpha = (8280 \pm 30)$ keV, $t_{1/2} = 1\ \mu\text{s} - 1$ ms [Ho79]).

The hindrance factor of these isomeric α decays caused by the difference of the angular momentum that has to be bridged ($\Delta I = 8$ for ^{158}W and $\Delta I = 12$ for ^{155}Lu) can be estimated from the Geiger-Nuttal plot, resulting in $10^{2.5}$ – $10^{4.5}$ for ^{158m}W and in $10^{4.65}$ for ^{155m}Lu.

In Fig. 6.6 also the energetic position of the (27/2$^-$)-high spin-isomer of ^{151}Er is indicated. Assuming a partial α half-life of 1 s (which corresponds to an α-decay branching ratio of 60 % at a total half-life of 0.58 s) a comparable hindrance factor of around 10^5 ($\Delta I = 13$) can be found, resulting in comparable hindrance factors per angular momentum unit for the isotopes of Er, Lu and W.

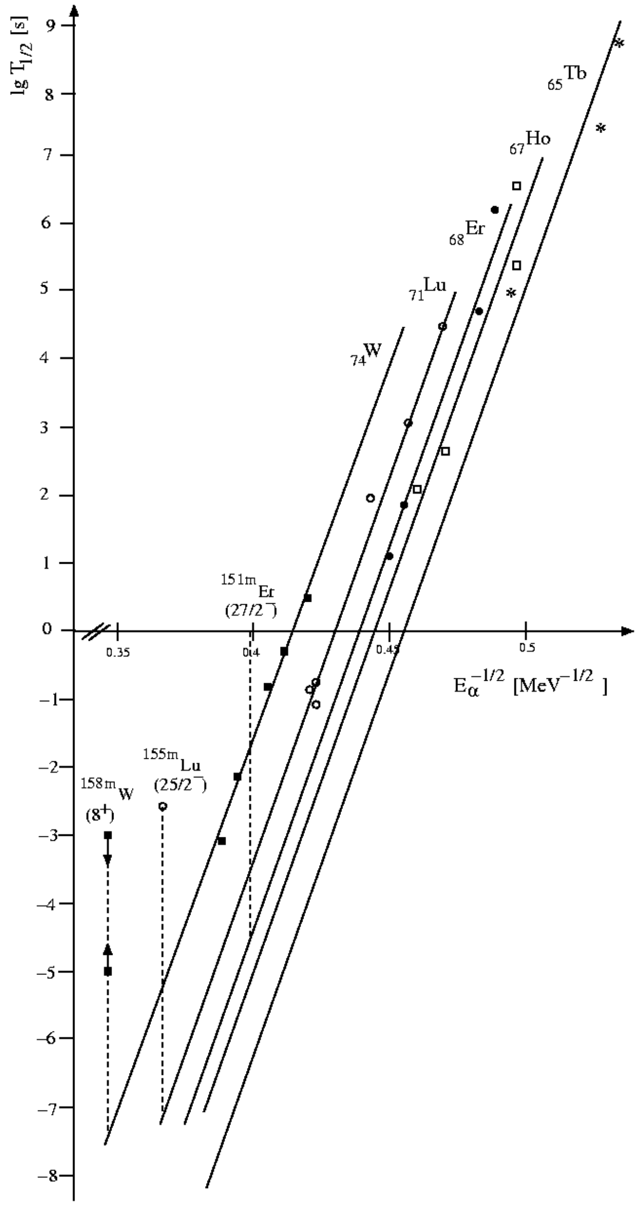

Figure 6.6

Geiger-Nuttal plot describing an empiric linear relation between the logarithm of the (partial) α-decay half-lives and the inverse square root of the α-decay energy for the ground-state α decay of isotopes of one element. The two known α decays from high-spin isomers of ^{155}Lu and ^{158}W are indicated as well as the high-spin isomer ^{151m}Er as one possible candidate for future measurements.

Besides the ground-state decays mentioned above α decays into excited states should also be considered. An example for this type of decay is given by the 18^+-isomer of ^{212}Po ($t_{1/2}$ = 45.1 s, E_x = 2.922 MeV) with α-decay branches into the 3^- (1 %) and the 5^- (2 %) states of ^{208}Pb besides the dominant α ground-state decay branch (97 %). High resolution mass measurements with the Penning-trap system would allow for a definite determination of these isomeric states, since already an accuracy of around 100 keV would allow for a determination of an excitation of the daughter nucleus.

For these measurements the isobaric purified α emitters would be extracted from the precision trap, followed by a TOF measurement (minimised TOF for the cyclotron frequency applied resonantly inside the Penning trap) together with the detection of the α decay. The determination of the TOF of the ions will be done by the detection of secondary electrons produced by the ions flying through a carbon foil. These electrons will be detected by an MCP detector placed under 90° relative to the direction of the ions. After the TOF measurement the ions will be implanted on the surface of a Si detector which will be used for the determination of the α decay.

The combination of the measured α-decay energy and the spectroscopic properties of the daughter nuclide could then allow for an assignment of the initial properties of the high-spin isomer.

6.3.1.2.2. The α decay of fission isomeric states

So far experimental evidence for an α-decay branch from a fission isomer has been obtained only in one case: The 14 ms fission isomer in ^{242}Am has the largest lifetime of all fission isomers. The expected transition from ^{242f}Am close to the ground state of ^{238}Np is estimated to have an energy of (8.4 ± 0.3) MeV. This value is given by the sum of the excitation energy of the isomeric state in ^{242f}Am (2.9 MeV [Bri71]) and the α ground-state decay energy between ^{242}Am and ^{238}Np (5.588 MeV [Fir96]). This high α energy should be sufficient for a measurable α branch for the case that the hinderance factors are not extremely high. On the other hand strong changes of the structure are necessary to get from the highly-deformed isomeric state to the much less deformed ground state of ^{238}Np.

Up to now the only experimental hint for an α-decay branch from this fission isomer has been found in the reaction ^{242}Pu(d,2n) at the Tandem accelerator at Garching, where the fission isomer ^{242f}Am can be produced with a cross section of (8 ± 3) μb at a beam energy of 13 MeV. In order to minimise contaminations from other reactions the reaction products of interest were transported by a helium-jet transport system to an area well shielded against the deuteron beam. In total 6 beam-correlated events with an E_α = 8.64 MeV were observed, which is in good agreement with the expected transition energy of 8.4 MeV. A branching ratio of the α decay relative to the isomeric fission of $\sigma_\alpha/\sigma_f \approx (1.0 \pm 0.4)\cdot 10^{-3}$ was found.

For a confirmation of these hints advanced experiments were performed at Los Alamos using the reaction ^{242}Pu(t,3n)^{242f}Am [Web82]. Thereby the results from the Garching experiments were confirmed by the determination of a shape-isomeric α decay from ^{242f}Am with an E_α = (8.62 ± 0.1) MeV and an α/f branching ratio of $1/1.4(4)\cdot 10^{-3}$. Using these numbers a partial half-life of around 20 s for the α decay

from ^{242f}Am to the ground state of ^{238}Np can be derived, thus resulting in a hinderance factor of ~10^{6} due to the large deformation-change during the decay, since without hinderance a half-life of 10^{-5} s is expected for an allowed transition with an $E_{\alpha} = 8.65$ MeV from the highly-deformed ^{242}Am.
Despite these promising consistent experimental hints these data have never been published.

Using the new experimental set-up at Garching for a confirmation of the α decay of ^{242f}Am would require a target placed inside the buffer-gas cell, since the recoil energy of the ^{242f}Am nuclei from the ^{242}Pu(d,2n) reaction would be too low for a transfer through a metallic entrance window. Such a target arrangement is routinely used by the groups in Mainz [Sew99] and Leuven [Kud96]. Special care has to be taken in order to avoid disturbance of the ion extraction by space-charge and plasma-effects caused by the primary beam. Since a pulsed beam would be used for the measurements, the DC fields inside the gas cell could be applied synchronously to the beam-on periods in order to allow for an extraction of the ions only after the neutralisation of the beam-induced plasma.
For this kind of experiments an ion injection transverse to the extraction as it is presently used at SHIPTRAP would be advantageous, since the primary beam could then be released from the cell. A modification allowing this beam guiding will also be possible with the new buffer-gas cell.

Aside of this specific situation in ^{242}Am a wide variety of longer-lived fission isomers can be expected in odd-even and odd-odd actinides. This is due to the specialisation energy, which describes the increase of the fission barrier of an odd-even nucleus compared to the neighbouring even-even nuclei, thus drastically increasing the fission lifetime. Typically an increase of the lifetime by a factor of 10^{3} for each additional nucleon has to be considered. So far those potentially existing ms – s isomers escaped observation in fission or in γ spectroscopy, however, their long lifetime makes them ideally suited for an observation with Penning traps.
A good test case could be ^{239}U, where the 195 ns fission isomer in the neighbouring ^{238}U is well-known and so far experimental studies only resulted in a lower lifetime limit of $t_{1/2} > 250$ ns [Thi02], while from systematics lifetimes up to 20 ms can be anticipated.

6.3.2. In-trap and out-of-trap spectroscopy with Penning traps

6.3.2.1. Electron spectroscopy

Presently the main limitation of high-resolution electron spectroscopy is given by the thickness of radioactive sources due to scattering and energy loss in the source material. This problem can be avoided by considering radioactive ions localised in a Penning trap as an ideal carrier-free source where energy loss or scattering do not influence the line shape. Therefore it is planned to perform e.g. high-resolution spectroscopy of heavy elements in the Penning-trap system with high efficiency, focussing on α and electron spectroscopy. Utilising the isobaric suppression capability of the purification trap as first stage of the trap system very pure sources can be obtained.

At the REXTRAP Penning-trap system at ISOLDE/CERN the feasibility of in-trap conversion electron spectroscopy has already been successfully demonstrated [Wei02]. The conversion electrons emitted by the trapped ions within a confined cylindrical volume are transported by the strong magnetic field of the trap through an ejection diaphragm to a detector placed behind the trap exit.

6.3.2.2. Lifetime of 2^+ states in heavy nuclei

In addition to the electron spectroscopy the 'shake-off' process of electrons can be investigated, since many electrons are emitted via this atomic process that occurs with high efficiency for outer electrons. The physics goal of such measurements is given by the determination of lifetimes of 2^+ states in order to derive the quadrupole moments of nuclei in a situation where actually no other experimental access exists. Key ingredients for the theoretical description of heavy nuclei are the knowledge on the deformation parameter β_2 or the knowledge on the quadrupole momentum, respectively. The correlation between quadrupole moment and lifetime is given by the Grodzins systematics in an extended version, correlating the quadrupole moment Q_0 and the energy of the first excited 2^+ state [Thi02], which can be inferred from its lifetime. Theoretical predictions for the behaviour of the quadrupole deformation β_2 and of the excitation energy of the first excited 2^+ states for the region of deformed superheavy elements ($100 < Z < 120$) were given by Sobiczewski et al. [Sob01]. It turns out that for a similar energy of the 2^+ state a variation of the quadrupole deformation of about 10 – 20 % can occur as a function of N and Z. Therefore an experimental verification of these predictions would be of great importance for the understanding of the structure of heavy and superheavy nuclei.

Typically the α decay of a heavy even-even nucleus in about 10 – 20 % leads to the first excited 2^+ state of the daughter nucleus [Sob01]. The populating α decay leads to the emission of low-energy 'shake-off' electrons, which allow for a localisation of the decay position. The determination of the direction of the α particles yields the velocity and the direction of the heavy recoil nucleus. The recoil nucleus decays after the lifetime of the 2^+ state, which is typically in the order of 100 ps, via L conversion, again inducing the emission of several shake-off electrons.

In the Penning trap a cold ion ensemble localised in the centre can be obtained e.g. by side-band cooling with a corresponding cyclotron radius in the order of 50 μm. The low-energetic atomic electrons will be confined to the magnetic field lines of the strong field of the Penning trap (~7 T) with very small gyration radii (~15 μm at 1 keV electron energy). They can be guided efficiently to segmented electron detectors at both sides of the trap which allows for a measurement of electron-electron coincidences resulting in a precise localisation of the ions.

The recoil nucleus typically travels a distance of around 50 μm during the lifetime of the 2^+ state. Therefore the origin of the shake-off electrons at the position of the subsequent conversion transition will be displaced by this distance compared to the position of the α decay. This decay length can be determined via a position measurement of the two components of the shake-off electrons. This allows for a measurement of the lifetime of the 2^+ state according to the 'recoil distance' method.

The magnetic field of the trap can be adiabatically widened on the axis behind the trap magnet, thus achieving e.g. a magnification of the decay region in the trap centre by about a factor of 100. This allows for a significant improvement of the spatial resolution for the decays in the centre of the trap.

The shake-off process itself can be investigated for K, L, M and N shell electrons from the α spectra coincident with the electrons. The theory of K-shell ionisation predicts an increase of the ionisation probability of about an order of magnitude for a doubled α energy [Gra75]. A better understanding of shake-off processes can be achieved by exploiting the coincidence condition between the α particle and the carrier-free source.

The position-resolved electron spectroscopy as well as the position-resolved α-recoil coincidence spectroscopy at the same time enable the diagnostics of the size and the shape of the ion cloud in the trap. An explicit *Z* identification is provided by the L, M and N conversion lines.

The rotational energy and therefore the spin can be determined from the measured energy of the K and L lines, since the converted transitions are rotational states. Thus with such a technique significantly more conclusive assignments during the construction of level schemes are achievable, especially in odd nuclei compared to the actually used α-spectroscopic methods.

6.3.2.3. Rare ground-state α decays

The new experimental set-up will also allow for studies of rare α decays where the detection and discrimination from the background using other spectroscopic methods is hardly or not at all possible due to the low branching ratios, in particular relative to the faster and dominant β decays. The systematics of the α-decay ground-state energies Q_α in the region of $N = 62 - 85$ given by the AME2003 [Wap03], shows that in the mass region of the light neutron-deficient rare earth elements around $A = 150$ the values of Q_α are often based on systematic extrapolations rather than on measurements. Thus shell structure effects may be washed out by the systematics. These uncertainties could be avoided by the measurement of Q_α values of rare α ground-state decays.

The reduction of the background is done in a first stage by the 90° dipole magnet, where the primary beam is separated from the reaction products. With regard to weak α-decay branches with branching ratios of $\Gamma_\alpha/\Gamma_\beta \leq 10^{-2}$ this reduction has to be improved by using the buffer-gas cell and the extraction RFQ and the subsequent Penning-trap system, since a purification level of 10^{-5} is necessary to remove the isobaric background.

6.3.3. High-precision *Q* value measurements related to fundamental interactions

If technical improvements on Penning traps indeed succeed to reach the goal of sub-eV mass resolution, new and unprecedented opportunities will arise for contributions in the field of fundamental interactions.

If the *Q* value for ^{3}H and ^{3}He in β decay can be measured to a precision of ~100 meV this will have direct impact on the current experimental efforts to fix the absolute mass of the antineutrino. In the KATRIN (**KA**rlsruhe **TRI**tium **N**eutrino) experiment, a next-generation tritium β-decay experiment, it is foreseen to measure the mass of the electron antineutrino to a precision of 0.2 eV [Tit03]. With the availability of a much more precise *Q* value a smaller region in the Curie plot would have to be investigated, since the end point of the β spectrum would be fixed.

Another application of precise *Q* values would be the situation of double β decays and super-allowed β decays.
So for the search for a neutrinoless double β decay in ^{76}Ge decaying to ^{76}Se the precise knowledge of the *Q* value would limit the region in the β-sum energy spectrum to be investigated for the appearance of a peak structure. Alternative candidates for a 0νββ decay are for example ^{100}Mo and ^{150}Nd, where the disadvantage of a separation between the source and detector functionality, which is simultaneously given for ^{76}Ge, can be over-compensated by their shorter half-life. Thus background contributions would become negligible and the quest for distinguishing between a Majorana or a Dirac character of the neutrino could be pursued with much higher sensitivity.
Superallowed $0^+ \rightarrow 0^+$ nuclear β decay is a sensitive probe of the vector part of the weak interaction. A measurement of the ft value for such a transition yields a direct determination of the vector coupling constant G_V, provided that small isospin symmetry-breaking and radiative corrections are properly accounted for [Har03].
Until now, the ft values of nine $0^+ \rightarrow 0^+$ transitions (from ^{10}C to ^{54}Co) have been measured with ~0.1 % precision or better, resulting in fully consistent values of G_V. Contributing to the high-precision measurement of superallowed $0^+ \rightarrow 0^+$ β decay in heavy $N = Z$ nuclei by determining the *Q* value with a high-precision mass measurement will help to establish an even more precise value for V_{ud}, the up-down element of the Cabibbo-Kobayashi-Maskawa (CKM) quark mixing matrix.

Appendix

In the Appendix all relevant descriptions for the operation of the gas-cell/extraction-RFQ set-up and the test facilities at the MLL are given.

1. The control system for gas cell and extraction RFQ

The present control system is based on LabVIEW and communicates with the front-end modules via interfaces using PROFIBUS, CAN-bus and GPIB. The test programs at the MLL use in addition different PC-based data acquisition hardware.

1.1. The control of the iseg HV modules

Two high voltage modules (model iseg EHQ F005p ($U_{max} = +500$ V, $I_{max} = 100$ µA) for the RFQ and model iseg EHQ F025p ($U_{max} = +2500$ V, $I_{max} = 50$ µA) for the extraction nozzle and DC electrodes inside the cell), both with 16 channels and placed in an iseg rack (model ECH 228L-F), are actually used for the gas-cell/RFQ system. The connection to LabVIEW is done via a CAN-Bus interface.

The control panel used for both modules is shown in Figure A.1. The graphical user interface allows to toggle (1) between the (nominal) 16 HV-channels of the EHQ F005p-module used for the 12 channels of the RFQ and for the lens following the RFQ and the EHQ F025p-module used for the extraction nozzle and the DC-electrode system. Thereby the panel allows not only for the individual setting of the voltages (2), but also for monitoring the actual voltages (3) and currents (4) of all channels. Within the running LabVIEW application the voltages applied by the modules can be switched on and off without a complete stop (5). In order to stop the complete application the 'STOP' (6) has to be pressed. In this case the voltages applied by the iseg modules keep their last value. For a change of the values the application has to be restarted. In addition to the individual setting of the voltages there are three functions for an associated voltage setting. For the channels 0 – 11 (7) and 12 – 15 (8) an offset can be applied which is added to the set values. The ramp function can be applied to the channels 0 – 11 (9), which is a feature used for the power supply of the 12 RFQ segments. Besides the maximum voltages (in the example 5.5 V) the channel where this maximum of the ramp should be reached (channel 1 in the example) can be chosen. It should be noted that channel 0 is not included in the ramp function due to software problems. Therefore the voltage value for channel 0 has to be adapted to the wanted ramp and then be applied manually in (2). In the channels before the maximum the DC increases linearly starting at 0 V, while in the channels after the maximum the voltages decreases linearly down to 0 V. The ramp can also be applied in combination with the offset.

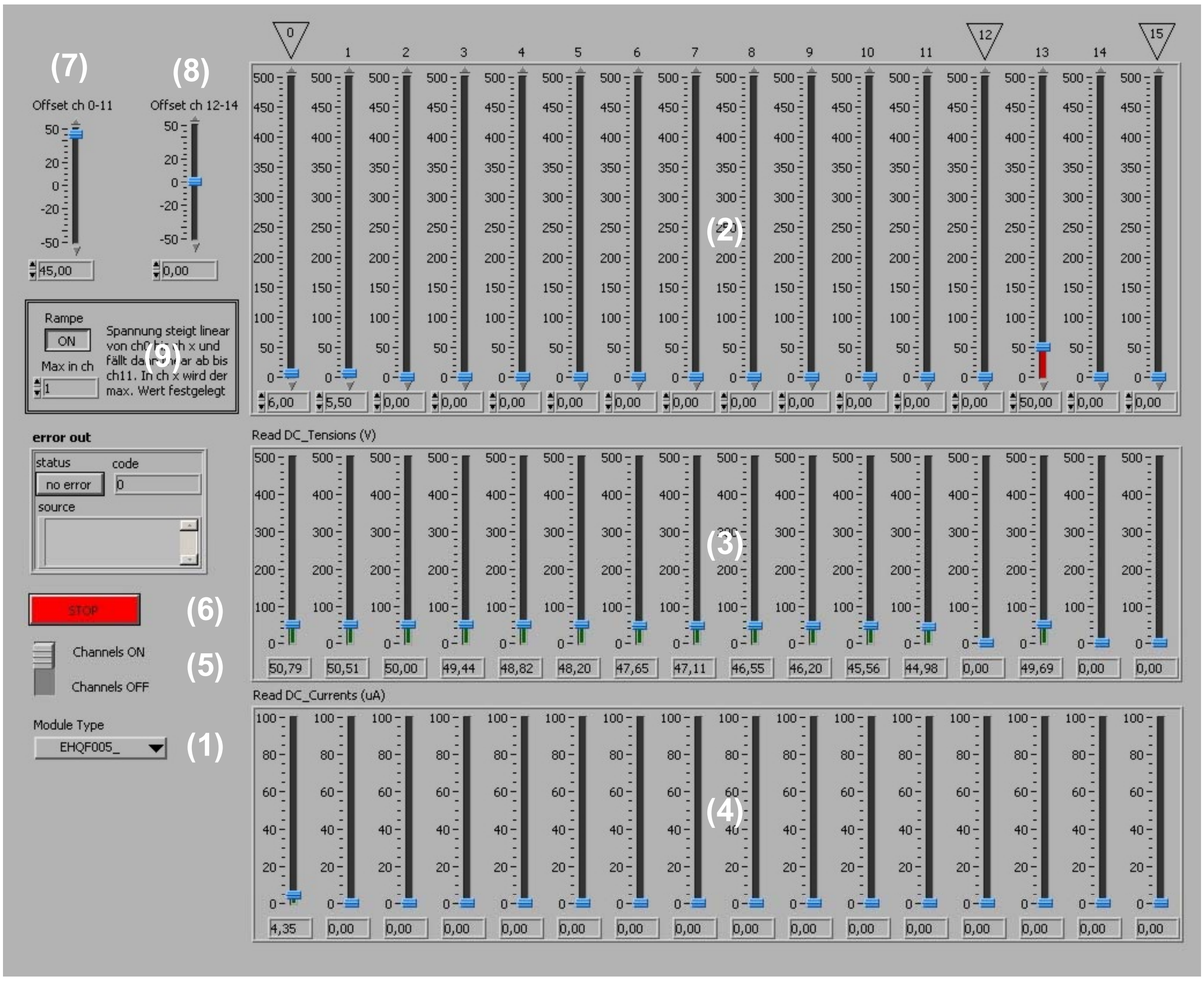

Offset ch 0-11: 45,00

Offset ch 12-14: 0,00

Rampe: ON

Max in ch: 1

Spannung steigt linear von ch0 bis ch x und fällt dann linear ab bis ch11. In ch x wird der max. Wert festgelegt

error out: status: no error; code: 0; source:

Module Type: EHQF005_

	0	1	2	3	4	5	6	7	8	9	10	11	12	13	14	15
	6,00	5,50	0,00	0,00	0,00	0,00	0,00	0,00	0,00	0,00	0,00	0,00	0,00	50,00	0,00	0,00
Read DC_Tensions (V)	50,79	50,51	50,00	49,44	48,82	48,20	47,65	47,11	46,55	46,20	45,56	44,98	0,00	49,69	0,00	0,00
Read DC_Currents (uA)	4,35	0,00	0,00	0,00	0,00	0,00	0,00	0,00	0,00	0,00	0,00	0,00	0,00	0,00	0,00	0,00

Figure A.1
The control panel for the iseg HV modules used for the extraction RFQ, the extraction nozzle and the DC electrodes inside the gas cell.

In the present panel shown in Fig. A.1 the set voltage values for the ramp and the value for the channel where the ramp maximum is, are not displayed in (2).
The nominal voltage values displayed in (3) can in some cases differ by some percent compared to the set values.
If the panels for both iseg modules are used, special care has to be taken that only one panel is running at any given time, otherwise the LabVIEW application will crash and has to be restarted followed by a resetting of the values.

1.2. The DS345 function generator control

The function generators DS345 are presently used for the RF funnel and the extraction RFQ. The communication between LabVIEW and the generators is done via GPIB. Figure A.2 shows the standard control panel for the DS345 available from National Instruments. Since during present experimental operations only RF amplitude and RF frequency of the sine function are changed, only the GPIB address of the DS345 (1) (can be changed manually at the generator) and the control for frequency and amplitude (2) are of importance. The control program behind this panel is also included into the data acquisition shown in section 3.2.

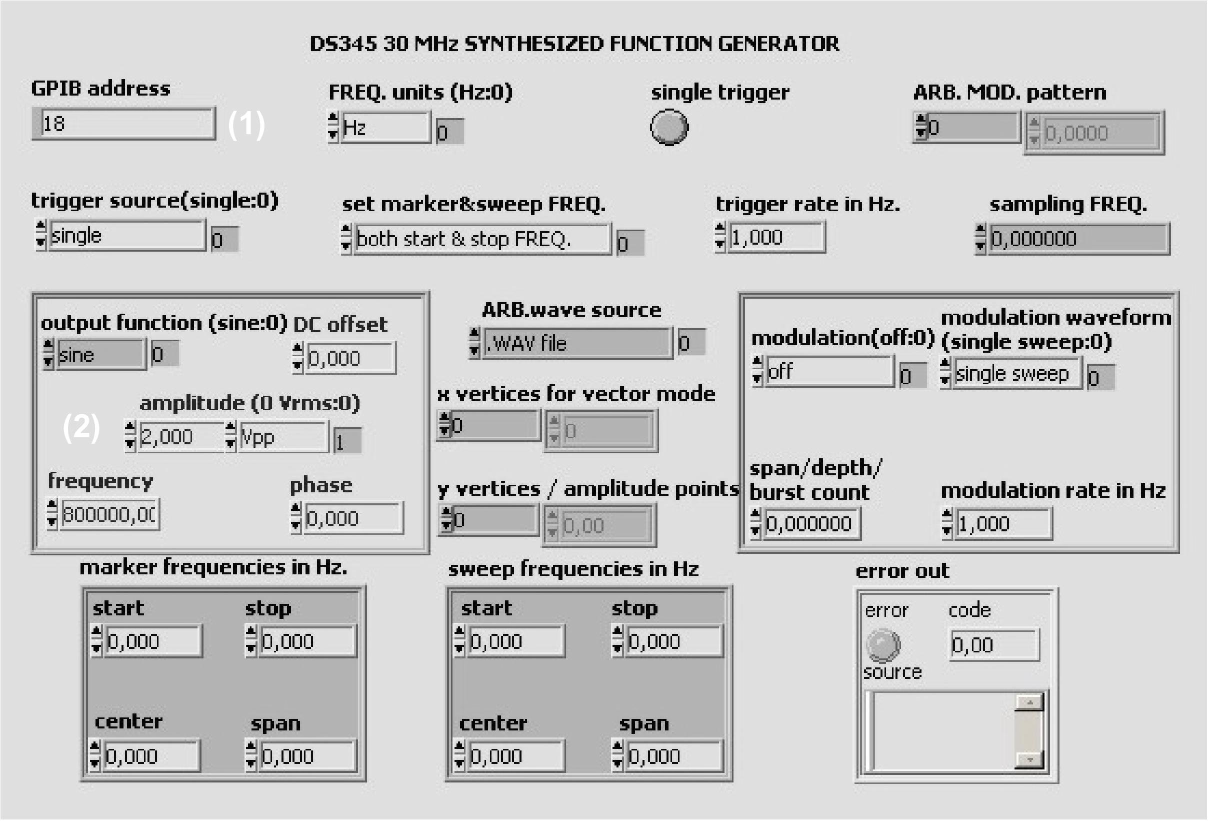

DS345 30 MHz SYNTHESIZED FUNCTION GENERATOR

GPIB address: 18
FREQ. units (Hz:0): Hz 0
ARB. MOD. pattern: 0 0,0000
trigger source(single:0): single 0
set marker&sweep FREQ.: both start & stop FREQ. 0
trigger rate in Hz.: 1,000
sampling FREQ.: 0,000000
output function (sine:0): sine 0
DC offset: 0,000
amplitude (0 Vrms:0): 2,000 Vpp 1
frequency: 800000,0(
phase: 0,000
ARB.wave source: .WAV file 0
x vertices for vector mode: 0 0
y vertices / amplitude points: 0 0,00
modulation(off:0): off 0
modulation waveform (single sweep:0): single sweep 0
span/depth/ burst count: 0,000000
modulation rate in Hz: 1,000
marker frequencies in Hz.: start 0,000 stop 0,000 center 0,000 span 0,000
sweep frequencies in Hz: start 0,000 stop 0,000 center 0,000 span 0,000
error out: error code 0,00 source

Figure A.2
The control panel for the DS345 function generator used for the extraction RFQ and the RF funnel inside the gas cell.

1.3. The control of the baking system

In order to assure a homogeneous heating procedure together with the capability to introduce temperature gradients in the system that take into account the different temperature sensitivities of critical components like the metallic window foil, the full-metal gate valve and the mass-flow control valve, a control system [Voi03] for altogether 30 channels has been installed. The system enables measuring the surface temperature of each heated segment separately via NiCr-Ni temperature sensors for the closed-loop control of the respective heating element. The acquisition of the temperatures and the power supply for the heating jackets are done by two programmable modules (Sigmann-Elektronik), connected amongst each other and with the control PC via PROFIBUS and shown in Fig. A3. Since the heating segments for the SHIPTRAP gas-cell/extraction-RFQ set-up have different, non-standard power requirements (54 V/15 W – 235 V/230 W) and as the control system was designed to be based on PROFIBUS, the modules were developed for the SHIPTRAP project.

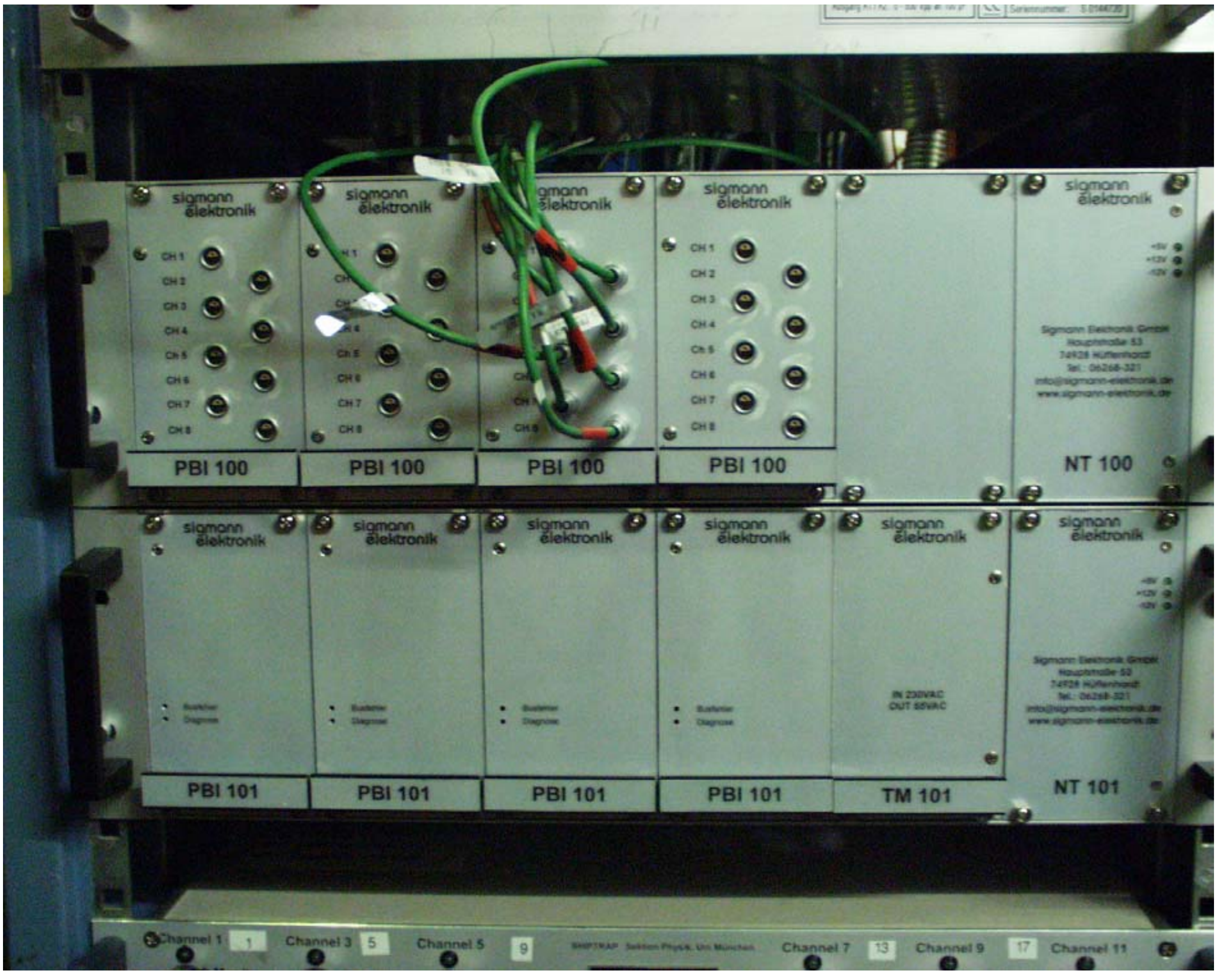
sigmann elektronik
CH 1
CH 2
CH 3
CH 4
CH 5
CH 6
CH 7
CH 8
PBI 100
PBI 100
PBI 100
PBI 100
NT 100
PBI 101
PBI 101
PBI 101
PBI 101
IN 230VAC OUT 65VAC
TM 101
NT 101
Channel 1
1
Channel 3
5
Channel 5
9
Channel 7
13
Channel 9
17
Channel 11

Figure A.3
The modules of the vacuum-chamber baking system. The sensor module (top) is connected to the NiCr-Ni-temperature sensors (green cables). The temperature data is transmitted via PROFIBUS to the LabVIEW-based control system. The On/Off-signals from LabVIEW are then transmitted to the power module (bottom), where the heaters are electrically connected. The system is designed to control up to 32 individual channels with different power consumptions, ranging from 15 W up to 230 W, according to the respective mechanical component to be baked. The different sub-modules are described in the text.

As shown in Figure A.3 the sub-module PBI 100 (8 channels) is used for the temperature acquisition of all channels. In total four PBI 100 sub-modules are connected to PROFIBUS via the sub-module NT 100. Since, as mentioned before, different voltages were applied at the heating elements, two types of power-supply sub-modules are used. Three sub-modules PBI 101 (starting from the left hand side in Fig. A.3) with altogether 24 channels supply a voltage of 235 V AC and are fused by 6.7 A, resulting in a maximum power of around 1575 W per module. For the heating jackets of the DN16 and DN35 flanges the sub-module TM 101 supplies 54 V AC to the PBI 101 at its left hand side. As this PBI 101 is also fused by 6.7 A, the 8 output channels altogether supply around 360 W. All four power sub-modules are connected via the NT101 to PROFIBUS.

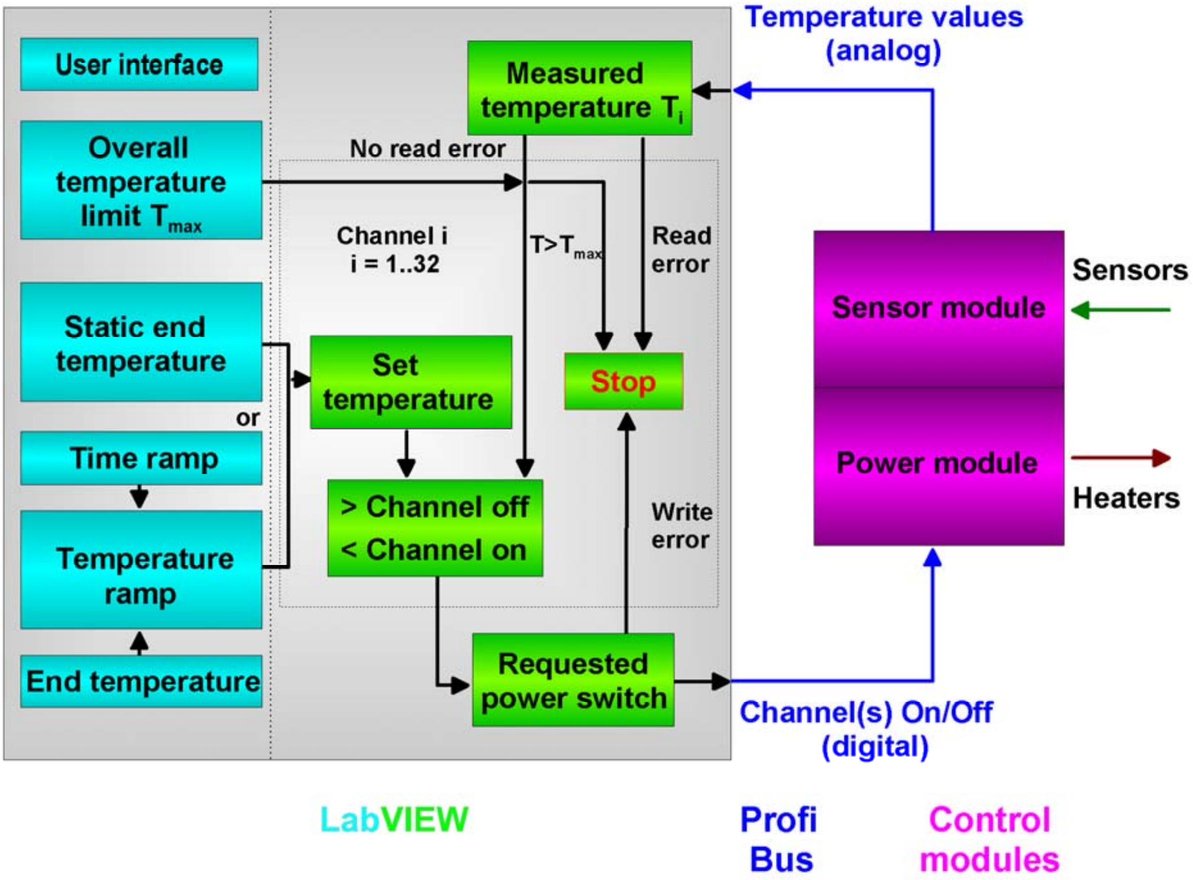
Temperature values (analog)
User interface
Measured temperature T_i
No read error
Overall temperature limit T_{max}
Channel i
i = 1..32
$T>T_{max}$
Read error
Sensors
Sensor module
Static end temperature
Set temperature
Stop
or
Time ramp
Power module
Heaters
> Channel off
< Channel on
Write error
Temperature ramp
End temperature
Requested power switch
Channel(s) On/Off (digital)
LabVIEW
Profi Bus
Control modules

Figure A.4
Flow chart of the control system for the baking system. The LabVIEW area communicates with the modules via PROFIBUS.

Figure A.4 shows a flow-chart of the heating procedure. The program allows to choose between two options, a time ramp to reach a homogeneous heating and a control of all individual channels with static temperature values. For each channel i the measured temperature T_i is continuously compared to the preset temperature and with an overall temperature limit T_{max}. If the measured temperature of one channel exceeds the temperature limit, the heating procedure ends with an overall stop. There is also an overall stop if read or write errors in the PROFIBUS communication occur. During operating conditions the channels of the power module are switched depending on the relation of measured and preset temperatures.

In Fig. A.5 the panel of the baking control system is shown. Altogether 30 channels can be addressed, subdivided in two rows of 15 channels each. With (1) the overall temperature limit is set. The values for the limit, the measured and the set temperature for each channel are numerically displayed in (2) and graphically in (3). For the case that the channels are set individually and not via a time ramp, as shown in the lower row, the different temperatures are written in (4). The coloured rectangles at (5) appear if the corresponding channel is heating (heating element switched on) (blue + 'low') or if the temperature in this channel exceeds the limit (red + 'high'). If the channel is not heating (heating element switched off) and the measured temperature is lower than the limit no rectangles are displayed. The same is shown in (6), in this case not for the individual channels but for the complete module.
The values for the time ramp, like the initial temperature, the final temperature and the rising speed for the temperature have to be written to (7). The ramp is set for each row by pressing the ramp button and displayed by the button colour. In the top row the time ramp is switched on, indicated by the red light. Several channels are bundled in order to be able to set different values for the ramp. This could be important if one part of the set-up should not be heated up as high as the other parts. The ramp itself can be used for a controlled heating as well as for a controlled cooling down of the set-up.
Since no hardware reset at the heating modules is implemented in the case that the LabVIEW control application is stopped (or crashes unexpectedly), the channels have to be switched off by pressing one of the buttons at (8). The left hand button is for the case of the individual temperature set, the other one for stopping the time ramp configuration. In (9) error messages of the PROFIBUS will be displayed, leading in most cases to a stop of the control application. In this case all channels which were switched on just before are still running. In order to avoid damages, LabVIEW has to be restarted quickly or the modules have to be switched off. In a future revision of this heating system, hardware provisions have to be implemented covering the scenario of a LabVIEW crash during the heating procedure, leading to a safe stop of all heating operations.
The possibility to apply a local temperature ramp (10) is actually not used for the set-up and is described in more detail in [Voi03].

The exemplarily displayed temperature values in Fig. A.5 show in some cases measured temperatures higher than the set ones. This can occur at temperatures below 100 °C, as the high heating power of several heating jackets (in particular at the shutter valve of the gas cell) leads to a further increase of the temperature after the stop of the electrical power supply.

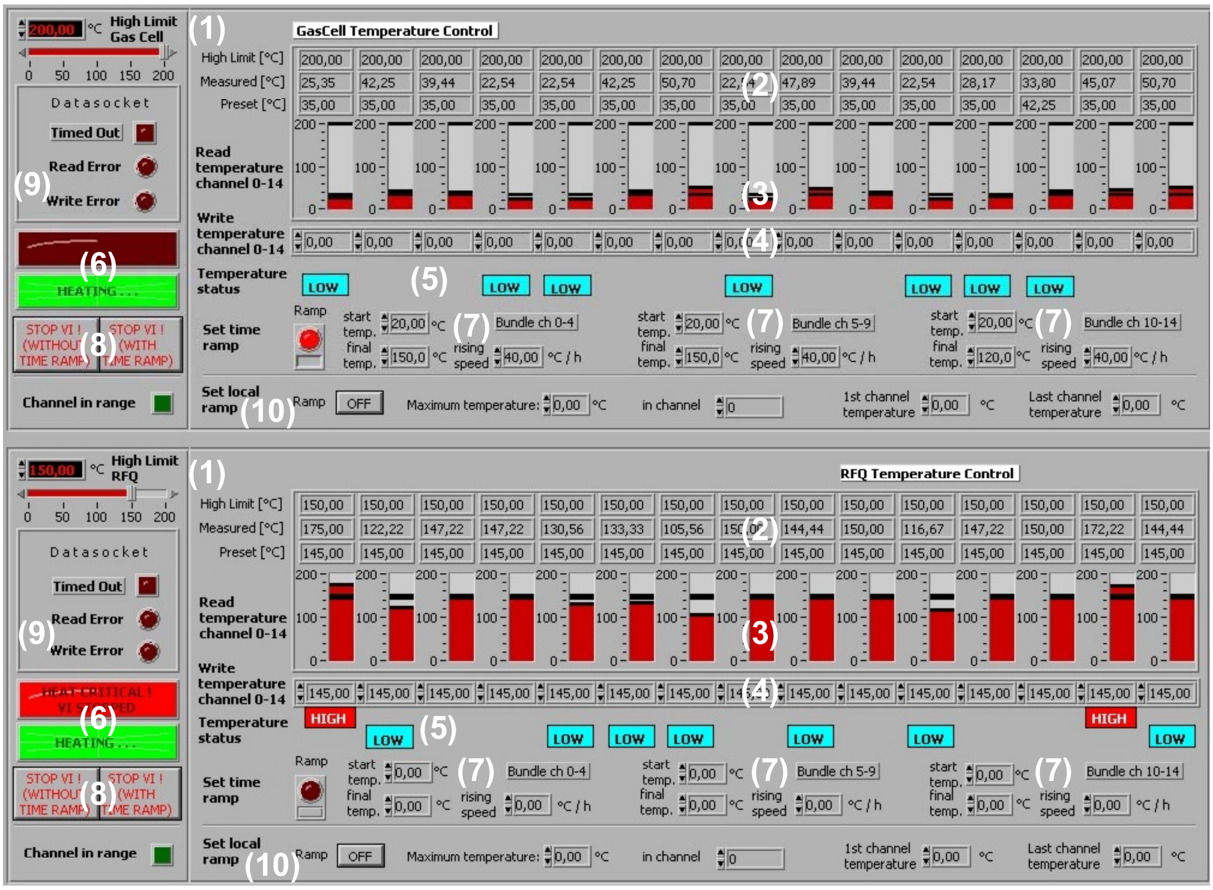

GasCell Temperature Control

High Limit Gas Cell 200,00 °C

High Limit [°C]	200,00	200,00	200,00	200,00	200,00	200,00	200,00	200,00	200,00	200,00	200,00	200,00	200,00	200,00	200,00
Measured [°C]	25,35	42,25	39,44	22,54	22,54	42,25	50,70	22,54	47,89	39,44	22,54	28,17	33,80	45,07	50,70
Preset [°C]	35,00	35,00	35,00	35,00	35,00	35,00	35,00	35,00	35,00	35,00	35,00	35,00	42,25	35,00	35,00
Write temperature channel 0-14	0,00	0,00	0,00	0,00	0,00	0,00	0,00	0,00	0,00	0,00	0,00	0,00	0,00	0,00	0,00
Temperature status	LOW			LOW	LOW			LOW			LOW	LOW	LOW		

Set time ramp: Ramp ●

Bundle ch 0-4: start temp. 20,00 °C; final temp. 150,0 °C; rising speed 40,00 °C / h

Bundle ch 5-9: start temp. 20,00 °C; final temp. 150,0 °C; rising speed 40,00 °C / h

Bundle ch 10-14: start temp. 20,00 °C; final temp. 120,0 °C; rising speed 40,00 °C / h

Set local ramp: Ramp OFF; Maximum temperature: 0,00 °C in channel 0; 1st channel temperature 0,00 °C; Last channel temperature 0,00 °C

RFQ Temperature Control

High Limit RFQ 150,00 °C

High Limit [°C]	150,00	150,00	150,00	150,00	150,00	150,00	150,00	150,00	150,00	150,00	150,00	150,00	150,00	150,00	150,00
Measured [°C]	175,00	122,22	147,22	147,22	130,56	133,33	105,56	150,00	144,44	150,00	116,67	147,22	150,00	172,22	144,44
Preset [°C]	145,00	145,00	145,00	145,00	145,00	145,00	145,00	145,00	145,00	145,00	145,00	145,00	145,00	145,00	145,00
Write temperature channel 0-14	145,00	145,00	145,00	145,00	145,00	145,00	145,00	145,00	145,00	145,00	145,00	145,00	145,00	145,00	145,00
Temperature status	HIGH	LOW			LOW	LOW	LOW		LOW		LOW			HIGH	LOW

Set time ramp: Ramp ●

Bundle ch 0-4: start temp. 0,00 °C; final temp. 0,00 °C; rising speed 0,00 °C / h

Bundle ch 5-9: start temp. 0,00 °C; final temp. 0,00 °C; rising speed 0,00 °C / h

Bundle ch 10-14: start temp. 0,00 °C; final temp. 0,00 °C; rising speed 0,00 °C / h

Set local ramp: Ramp OFF; Maximum temperature: 0,00 °C in channel 0; 1st channel temperature 0,00 °C; Last channel temperature 0,00 °C

Figure A.5
The panel for the control of the baking system. Its function is described in the text.

1.4. The control of the vacuum and gas-supply system

The vacuum and the gas-supply system which are presently still under manual operation will be controlled in the new Munich set-up via PROFIBUS and SIMATIC modules. Figure A.6 schematically shows the planned layout of the control system. The turbomolecular pumps connected to the gas cell (TMU 400) and the extraction chamber (TMU 1600) will be coupled via their controls (TCM 1601) and so called gateways to the PROFIBUS and subsequently the LabVIEW control. In the case of the turbomolecular pumps the actual rotational frequency will be monitored. In addition the control panel will display appearing alarm messages and other operational values like the actual power consumption or the operational time of the pumps.
Other parts of the vacuum system will be connected to SIMATIC modules, which are themselves connected via PROFIBUS to LabVIEW. The analog voltage output signal of the different vacuum gauges being proportional to the measured residual and buffer-gas pressure will be read by AI (analog input) channels of the SIMATIC.

Another AI channel will read the output voltage of the FC-780CHT flow-control valve, which returns the measured buffer-gas flow rate. The set flow rate on the other hand is transferred via an analog voltage output (AO) signal of the SIMATIC to the flow-control valve.
With digital output signals (DO) all valves will be controlled, which are capable of remote operation, i.e. the shutter valve between stopping chamber and pump.

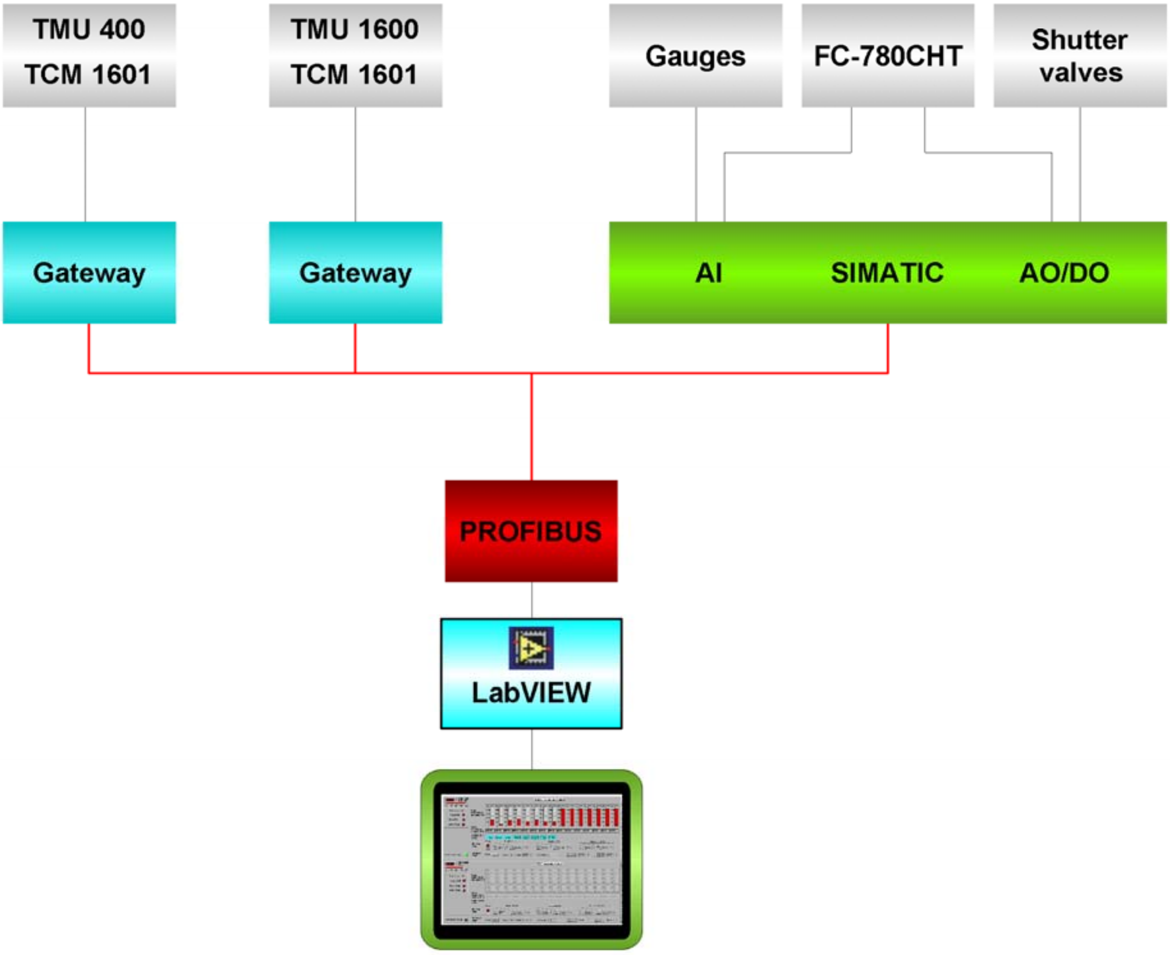

Figure A.6
Schematic view of the control system planned for the vacuum and buffer-gas supply system. The LabVIEW control application will be connected via PROFIBUS to the pumps and to SIMATIC modules containing the analog and digital channels for the control of the gauges, the gas flow control and the shutter valves.

Two crucial parts are actually not planned to be included into the remote control. These parts are the pre-pump and the gas-purification system, as in both cases only manual valves are connected. Therefore the pre-pump will have to be started and stopped manually in order to avoid damages at the entrance window (see Sect. 3.3.2

and 3.6.1). Since the gas-purification system will be damaged if it is vented during operation or heated up under bad vacuum conditions in this case a manual control also seems to be safer than a remote control without knowledge about the status of the connected valves.

2. The electrical connectors of the gas cell and the extraction RFQ

In order to connect the electrical feedthroughs of the gas cell and the extraction RFQ in the correct way without having a look inside the chambers, the allocations for the plugs is given in Fig. A.7 for the cell and in Fig. A.8 for the extraction chamber. On the left hand side of Fig. A.7 the backside flange (DN250) of the gas cell is shown. The connectors (SHV) for the five segments of the DC electrode are shown, starting with DC 1 as the first segment near the flange, while DC 5 is the segment in front of the funnel. On the right hand side of Fig. A.7 the connectors for the nozzle (SHV) and for the two phases of the funnel (SUB-D) are shown. With Funnel 1 the first ring electrode in front of the nozzle is meant, while Funnel 40 is the electrode close to the DC electrode.

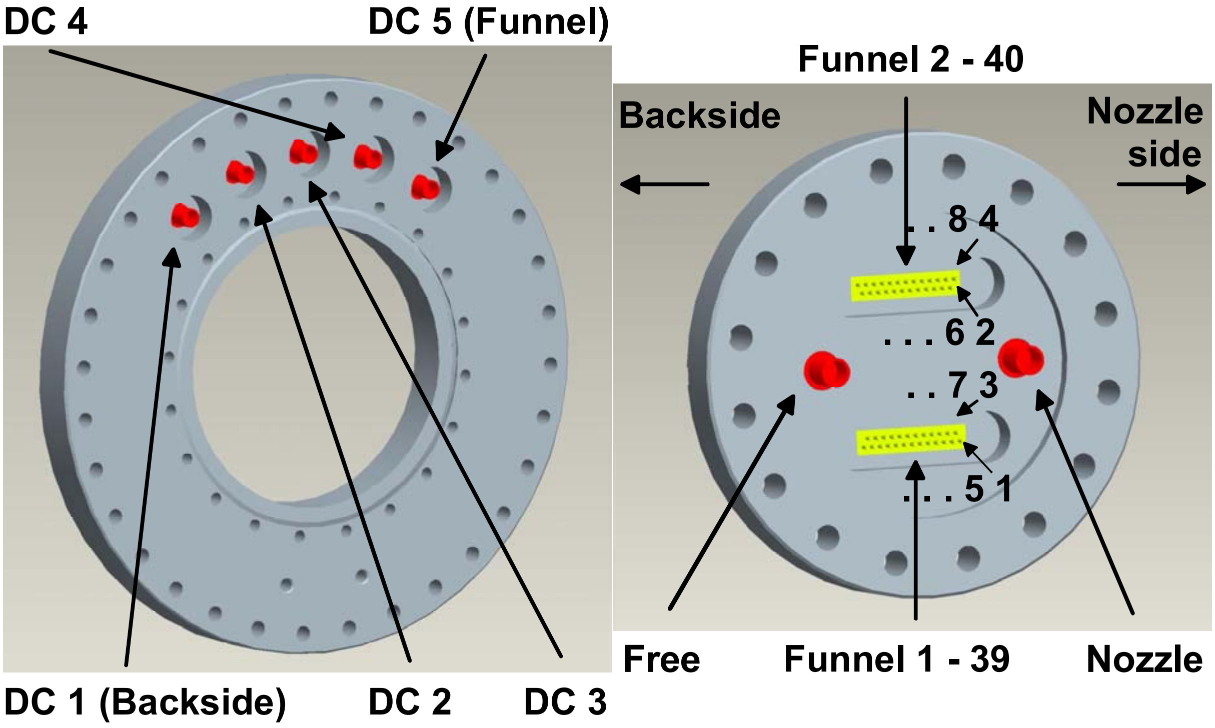

Figure A.7
The allocation of the electrical feedthroughs for the gas cell. On the left hand side the backside flange (DN250) of the gas cell is shown. The connectors (SHV) for the five segments of the DC electrode are shown, starting with DC 1 as the first segment nearby the flange, while DC 5 is the segment in front of the funnel. On the right hand side the flange with the connectors for the nozzle (SHV) and for the two phases of the funnel (SUB-D) is shown. With Funnel 1 the first ring electrode in front of the nozzle is meant, while Funnel 40 is the electrode close to the DC electrode. The connection at the two SUB-D plugs is done crosswise, as indicated by the channel numbers.

In Fig. A.8 the flange with the connectors for the electrodes inside the extraction chamber is shown. Extraction plate and lens are connected via SHV, while the two RF phases of the RFQ are connected via SUB-D connectors. Since the DC gradient is applied along the longitudinal axis of the RFQ, there is no distinction in the numbering.

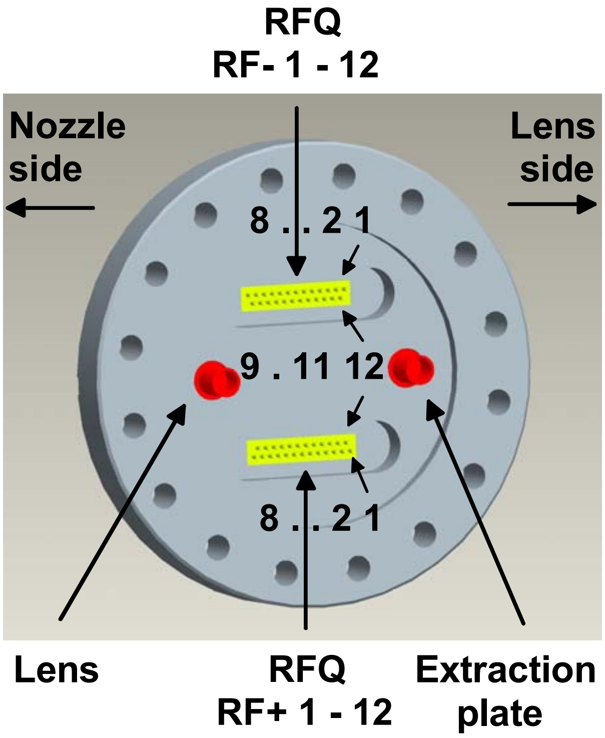

Figure A.8
The flange with the connectors for the electrodes inside the extraction chamber. Extraction plate and lens are connected via SHV, while the two RF phases of the RFQ are connected via SUB-D connectors. As the DC gradient is applied along the longitudinal axis of the RFQ there is no distinction in the numbering. The connection at the two SUB-D plugs is done in turn, as indicated by the channel numbers.

3. The MLL test equipment

The test equipment at the MLL consists in the broadest sense of the beam line, the detectors, the QMS spectrometer and the data acquisition.

3.1. The beam-line settings

As the set-up is positioned under 0° relative to the accelerator only a Wien-filter is available for the selection of the proper beam energy instead of the commonly used 90° analysing dipole magnet. This requires extreme care of selecting the correct charge state from a narrow distribution, in particular with the subsequent tuning onto the ^{121}Sb target requiring an adaptation of the Wien-filter settings.

In Table A.1 the commonly used parameters for the $^{35}Cl^{11+}$ beam at 150 MeV, including the setting of the Wien-filter, are given. After the C-foil in front of the cell a charge distribution is given, where the setting of the dipole magnet is given for three charge states in order to check the right beam energy.

Charge state	Wien filter [A]	Wien filter [mT]	Relative intensity	Flux density [mT]	Current [A]
14^+	61.40	37.00	2.1	1065	240.5
15^+	61.40	37.00	3.3	994	222.5
16^+	61.40	37.00	1.0	931	207.5

Table A.1
Commonly used settings for $^{35}Cl^{11+}$ at 150 MeV for the Wien filter and the 90° dipole magnet in the 0° beam line of the MLL. Displayed are in addition the relative intensities of the three exemplary charge states.

In Figure A.9 the calibration of the 90° dipole magnet used at the MLL 0°-beam line is given. The calibration of the magnetic flux density is given as a function of the current applied at the magnet, since there is no fixed and calibrated Hall sensor for the field measurement.

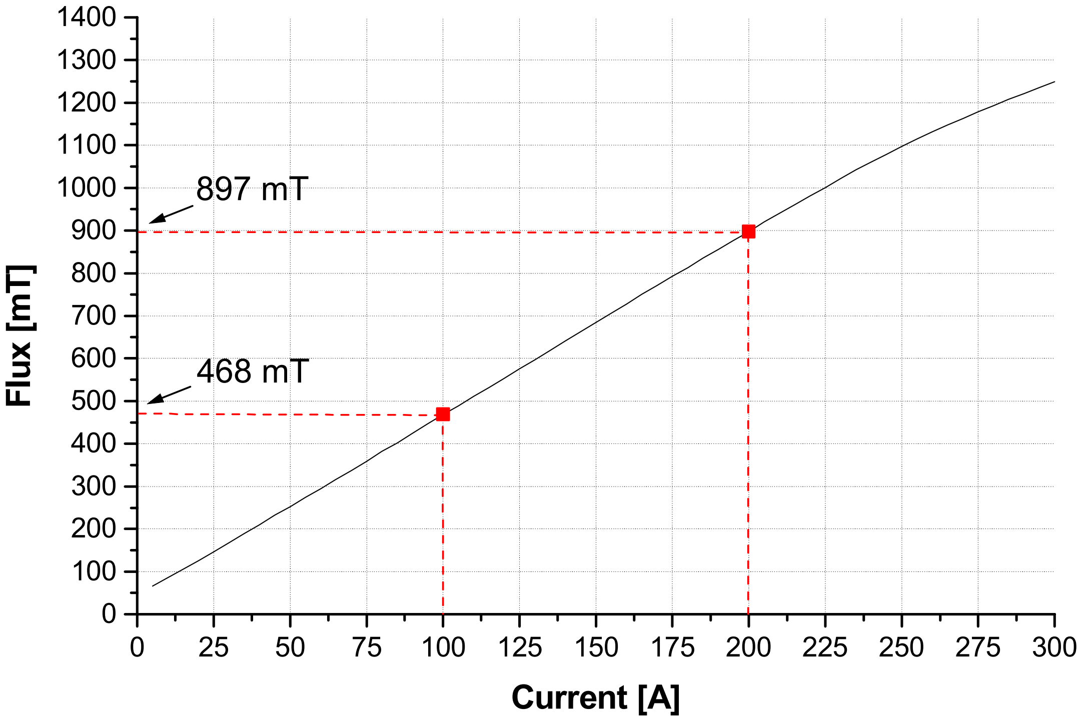

Figure A.9
Calibration for the 90° dipole used for the MLL test set-up. The magnetic flux density is given as a function of the current applied to the magnet.

3.2. The data-acquisition system

The present data-acquisition system used for off-line measurements controls the function generators for the RFQ and the RF funnel and the QMS mass spectrometer. The SRS DS345 function generators are controlled via GPIB. Since only sinusoidal functions were used for the RFQ and RF funnel, only two parameters, the RF frequency and the RF amplitude, are controlled. Figure A.10 shows the control panel of the program used for measurements. For the remote control of the QMS an analog output (AO) channel of a NI 6035E multifunction DAQ PCI card from National Instruments is used. The same device is used in order to count the discriminated signals from the different ion detectors (4).

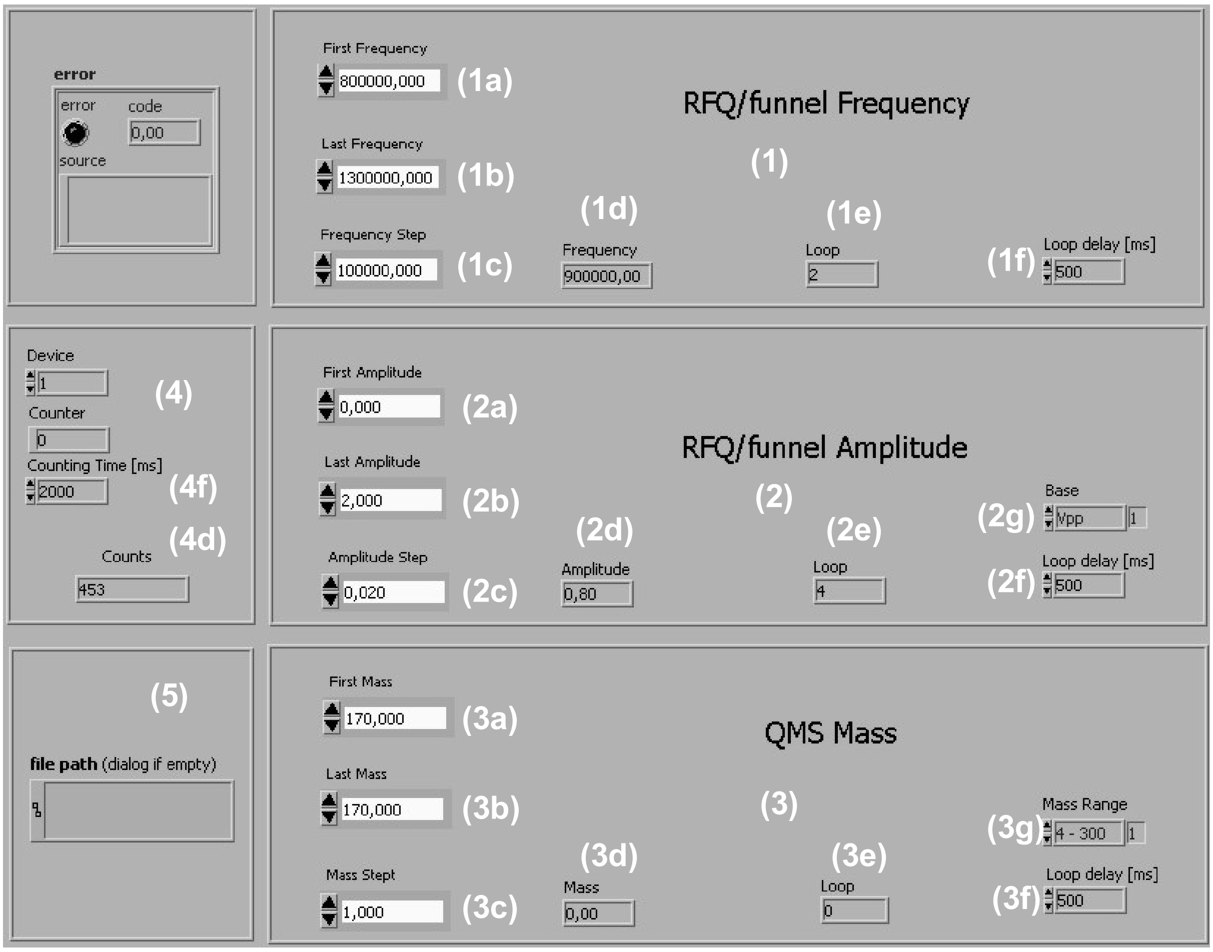

error code: 0,00

First Frequency: 800000,000
Last Frequency: 1300000,000
Frequency Step: 100000,000
Frequency: 900000,00
Loop: 2
Loop delay [ms]: 500

Device: 1
Counter: 0
Counting Time [ms]: 2000
Counts: 453

First Amplitude: 0,000
Last Amplitude: 2,000
Amplitude Step: 0,020
Amplitude: 0,80
Loop: 4
Base: Vpp 1
Loop delay [ms]: 500

file path (dialog if empty)

First Mass: 170,000
Last Mass: 170,000
Mass Stept: 1,000
Mass: 0,00
Loop: 0
Mass Range: 4 - 300 1
Loop delay [ms]: 500

Figure A.10
Control panel for the data acquisition used for off-line measurements. Its function is described in the text.

Three parameters can be scanned with the actual program, the RF frequency (1), the RF amplitude (2) and, if used, the ion mass at the QMS (3). The parameters are changed hierarchically in the order as they are displayed, i.e. for every RF amplitude first the mass will be scanned before the amplitude is changed. In an analogous way first the RF amplitude is changed for a fixed RF frequency before this one will be varied.

For all three parameters a start value (a), a stop value (b) and the corresponding step width (c) have to be given. For the case that one parameter should be kept fixed the start and stop values are equal. The actual values for the set parameters are shown in (d), while (e) displays the number of the actual loop. At (2g) the bases for the RF amplitude of the DS345 (V_{pp}, V_{rms}, -dBm) and at (3g) the mass range of the QMS (1 – 100, 4 – 300) can be chosen.

As several parts may have a delay time, the waiting time of the different loops can be chosen in (f). The number of detected ions within the time period chosen in (4) are then displayed in (4d). For every setting the values for the RF frequency, the RF amplitude, the mass and the number of counts are saved. In (5) the file path for the data file can be chosen. If no file path is included, the user is asked before starting the scan for the name of the following data file.

4. Compilation of design and operational parameters

In this section the main parameters concerning the design of the SHIPTRAP gas-cell/extraction-RFQ set-up (Table A.2) and the optimum set of operation parameters (Table A.3) for a He buffer-gas pressure of around 50 mbar are displayed.

Stopping chamber	
Length	330 mm
Diameter	250 mm
Entrance window diameter	60 mm
Effective mean stopping length	130 mm ± 90 mm + funnel (longitudinal) 195 mm ± 85 mm (transversal)
DC electrode	
Length	180 mm, 35 mm per segment
Outer diameter	180 mm
Inner diameter (support structure)	160 mm
Number of segments	5
RF funnel	
Entrance inner diameter	130.0 mm
Exit inner diameter	5.0 mm
Number of ring electrodes	40
Ring thickness	1.0 mm
Gap between two rings	1.0 mm
Extraction nozzle	
Half-angle subsonic part	45.0°
Half-angle supersonic part	19.0°
Entrance diameter	2.0 mm

Nozzle throat diameter	0.6 mm
Exit diameter	6.0 mm
Extraction RFQ	
Length	180 mm, 15 mm per segment
Rod diameter	11 mm
Aperture diameter	10 mm
Number of segments	12
Extraction plate	
Hole diameter	5.0 mm
Plate thickness	1.0 mm
Lens	
Inner diameter	10.0 mm
Length	10.0 mm

Table A.2
Main design parameter of the present set-up.

Buffer-gas cell		
DC electrode	DC 1:	280 V +
	DC 2:	280 V +
	DC 3:	280 V +
	DC 4:	255 V
	DC 5:	235 V
RF funnel	800 kHz, 190 – 200 V_{pp},	
	ΔE_{DC}:	0.5 V/cm
	DC funnel entrance:	100 V
	DC funnel exit:	60 V
Nozzle		62.0 – 62.5 V
Extraction chamber		
Extraction RFQ	1100 kHz, 275 V_{pp} (q = 0.6 for ^{152}Er)	
	DC first segment:	51 V
	DC last segment:	45 – 51 V
Extraction plate		Grounded
Lens		30 – 50 V

Table A.3
Optimum set of operational parameters for a He buffer-gas pressure of around 50 mbar as obtained for the extraction of ^{152}Er ions, injected perpendicular to the extraction axis (SHIPTRAP case).

5. Possible candidates for mass measurements at the MLL

In Table A.4 the candidates from Sect. 6.2.4.2 are displayed with possible projectile/target combinations. The reaction cross sections are calculated using PACE4 taking into account the maximum beam energies available from the MLL Tandem accelerator.

Mass	Element	Mass uncertainty [keV]	Half life	Projectile/ Target	Cross section [mb]
62	Ge	150			
63	Ge	210	95 ms	^{32}S/^{40}Ca	1
65	As	320	190 ms	^{35}Cl/^{32}S	1
66	As	730	96 ms	^{35}Cl/^{40}Ca	3
67	Se	210	107 ms		
70	Br	330	80 ms	^{35}Cl/^{40}Ca	4
71	Br	610	21 s	^{16}O/^{58}Ni	25
	Kr	700	97 ms		
78	Y	430	440 ms	^{32}S/^{50}Cr	1
79	Y	480	15 s	^{32}S/^{54}Fe	14
	Zr	430			
80	Y	190	35 s	^{32}S/^{54}Fe	52
	Zr	1600	44 s	^{32}S/^{54}Fe	3
81	Zr	180	15 s	^{35}Cl/^{50}Cr	10
82	Zr	240	32 s	^{32}S/^{54}Fe	30
83	Nb	340	4.1 s	^{32}S/^{54}Fe	10
84	Zr	210	26 min	^{35}Cl/^{54}Fe	97
	Nb	320	12 s	^{35}Cl/^{54}Fe	12
85	Nb	240	21 s	^{35}Cl/^{54}Fe	59
	Mo	300	6 s	^{35}Cl/^{54}Fe	5
86	Mo	470	17 s	^{32}S/^{58}Ni	25
87	Mo	240	13.4 s	^{37}Cl/^{54}Fe	13
	Tc	320		^{32}S/^{58}Ni	5
88	Tc	220	3.5 s	^{35}Cl/^{58}Ni	8
89	Tc	220	13 s	^{35}Cl/^{58}Ni	28
	Ru	540		^{35}Cl/^{58}Ni	2
90	Tc	260	8.7 s	^{37}Cl/^{58}Ni	41
	Ru	320	13 s	^{32}S/^{64}Zn	1
91	Tc	220	3 min	^{32}S/^{64}Zn	122
	Ru	630	8 s	^{32}S/^{64}Zn	17
92	Ru	320	3.7 min	^{32}S/^{64}Zn	149
	Rh	430		^{32}S/^{64}Zn	1
93	Rh	430		^{32}S/^{64}Zn	3
	Pd	430			
94	Rh	480	25.8 s	^{35}Cl/^{64}Zn	41
	Pd	430	8.9 s		
95	Rh	160	2 min	^{35}Cl/^{64}Zn	175

Mass	Element	Mass uncertainty [keV]	Half life	Projectile/ Target	Cross section [mb]
95	Pd	430	13 s	$^{35}Cl/^{64}Zn$	6
	Ag	430	2 s	$^{35}Cl/^{64}Zn$	1
96	Pd	160	2 min	$^{35}Cl/^{64}Zn$	39
	Ag	430	5.1 s	$^{35}Cl/^{64}Zn$	1
97	Pd	320	3 min	$^{35}Cl/^{70}Ge$	75
	Ag	350	19 s	$^{35}Cl/^{70}Ge$	10
	Cd	430	3 s		
99	Ag	160	10.5 s	$^{35}Cl/^{70}Ge$	65
	Cd	220	16 s	$^{35}Cl/^{70}Ge$	2
	In	430			
100	In	270	3.5 s	$^{32}S/^{74}Se$	1
101	Cd	160	1.2 min	$^{32}S/^{74}Se$	30
	In	320	16 s	$^{32}S/^{74}Se$	6
103	Sn	320	7 s		
106	Sb	340	600 ms		
107	Sb	320	3.7 s		
108	Sb	220	7 s	$^{32}S/^{84}Sr$	12
110	Sb	220	23.5 s	$^{32}S/^{92}Mo$	15
	I	330	650 ms		
111	I	320	2.5 s	$^{32}S/^{84}Sr$	2
112	Te	180	2 min	$^{35}Cl/^{84}Sr$	9
	I	230	3.4 s	$^{32}S/^{84}Sr$	1
114	I	320	2.1 s	$^{32}S/^{92}Mo$	53
	Cs	330	570 ms		
115	Cs	320	1.4 s		
116	Cs	110	700 ms	$^{35}Cl/^{84}Sr$	2
117	Ba	320	1.8 s		
118	Ba	210	5.2 s		
119	Ba	210	5.3 s	$^{32}S/^{92}Mo$	6
	La	430			
120	Ba	320	32 s	$^{32}S/^{92}Mo$	37
	La	540	2.8 s	$^{32}S/^{92}Mo$	6
121	Ba	150	29.7 s	$^{32}S/^{92}Mo$	71
	La	540	5.3 s	$^{32}S/^{92}Mo$	20
	Ce	540			
122	La	320	8.6 s	$^{35}Cl/^{92}Mo$	6
	Ce	430			
123	La	210	16 s	$^{35}Cl/^{92}Mo$	91
	Ce	320	3.8 s	$^{35}Cl/^{92}Mo$	6
124	Ce	320	6 s	$^{32}S/^{96}Ru$	37
	Pr	640	1 s	$^{32}S/^{96}Ru$	3
125	Ce	210	10.2 s	$^{32}S/^{96}Ru$	55
	Pr	430	3.3 s		
126	Pr	210	3.1 s	$^{35}Cl/^{96}Ru$	3

Mass	Element	Mass uncertainty [keV]	Half life	Projectile/ Target	Cross section [mb]
126	Nd	430	3.4 s		
127	Pr	210	4.2 s	^{35}Cl/^{96}Ru	48
127	Nd	430	1.8 s	^{35}Cl/^{96}Ru	5
128	Nd	210		^{35}Cl/^{96}Ru	15
	Pm	430			
129	Nd	220	5 s	^{32}S/^{102}Pd	12
	Pm	430			
130	Pm	320	2.2 s	^{32}S/^{102}Pd	7
	Sm	430			
131	Pm	210		^{32}S/^{102}Pd	17
	Sm	320	1.2 s	^{32}S/^{102}Pd	1
132	Pm	210	6.4 s	^{32}S/^{106}Cd	23
	Sm	320	4 s	^{32}S/^{106}Cd	1
133	Sm	210	2.9 s	^{35}Cl/^{102}Pd	12
134	Sm	210	10.1 s	^{32}S/^{106}Cd	47
	Eu	210	500 ms	^{32}S/^{106}Cd	1
135	Sm	170	10.3 s	^{32}S/^{107}Ag	49
	Eu	320	1.5 s	^{32}S/^{106}Cd	4
136	Eu	210	3 s	^{32}S/^{109}Ag	8
	Gd	430			
137	Eu	210	11 s	^{35}Cl/^{106}Cd	30
	Gd	430	7 s	^{35}Cl/^{106}Cd	5
138	Gd	210		^{35}Cl/^{106}Cd	10
139	Gd	210	4.9 s	^{32}S/^{116}Sn	8
140	Tb	860	2.4 s	^{32}S/^{116}Sn	3
	Dy	540		^{32}S/^{116}Sn	1
141	Dy	320	1 s		
142	Tb	320	300 ms	^{32}S/^{116}Sn	18
	Dy	390	2.3 s	^{35}Cl/^{112}Sn	3
143	Dy	210	3.9 s	^{35}Cl/^{112}Sn	12
144	Ho	320	700 ms		
145	Ho	320	2.4 s		
	Er	430	900 ms		
146	Ho	210	3.5 s	^{32}S/^{120}Te	14
	Er	320	1.7 s		
147	Er	320	2.5 s	^{32}S/^{120}Te	7
	Tm	320	360 ms		
148	Ho	140	2 s	^{32}S/^{122}Te	93
	Er	210	4.6 s	^{32}S/^{122}Te	10
	Tm	430	700 ms		
149	Tm	320	900 ms		
150	Tm	210	2.3 s	^{35}Cl/^{120}Te	1
	Yb	430			
151	Yb	320	1.6 s		

Mass	Element	Mass uncertainty [keV]	Half life	Projectile/ Target	Cross section [mb]
151	Lu	430	85 ms		
152	Yb	220	3.1 s		
153	Yb	210	4.1 s		
153	Lu	220	900 ms		
	Hf	540			
154	Lu	220	1.2 s		
	Hf	540	2 s		
155	Hf	430	890 ms		
156	Ta	430	165 ms		
157	Hf	210	110 ms	^{32}S/^{130}Ba	32
160	W	220	81 ms		
161	W	210	410 ms		
162	Re	220	100 ms		
164	Re	170	380 ms		
166	Re	90	2.2 s	^{35}Cl/^{136}Ce	2
168	Ir	160	160 ms		
170	Ir	110	1.1 s		
172	Ir	110	2.1 s	^{32}S/^{144}Sm	25
174	Au	110	120 ms		
176	Au	110	1.3 s	^{35}Cl/^{144}Sm	2
178	Tl	120			
180	Tl	130	1.9 s		
186	Tl	200	2.9 s	^{35}Cl/^{158}Dy	29
190	Bi	200	5 s	^{35}Cl/^{160}Dy	14
194	Tl	150	33 min	^{35}Cl/^{164}Dy	3
	At	200	180 ms		

Table A.4
Possible candidates for mass measurements at the MLL. The isotopes are displayed with possible projectile/target combinations and with the reaction cross sections calculated with PACE4.

Bibliography

[Ärj87] J. Ärje et al., *Ion Guide Method for On-Line Isotope Separation*, Nucl. Instr. Meth. **B26**, 384 (1987)

[Äys98] J. Äystö et al., *Proposal for SHIPTRAP*, (1998)

[Ber01] M. Berz and K. Makino, *COSY INFINITY Version 8.1 User's Guide and Reference Manual*, MSU (2001)

[Bes02] I. Bergström et al., *SMILETRAP – A Penning trap facility for precision mass measurements using highly-charged ions*, Nucl. Instr. Meth. **A487**, 618 (2002)

[Bet32] H. A. Bethe, *Bremsformel für Elektronen relativistischer Geschwindigkeit*, Z. f. Physik **76**, 293 (1932)

[Bla02] K. Blaum et al., *Carbon clusters for absolute mass measurements at ISOLTRAP,* Eur. Phys. J. **A15**, 245 (2002)

[Bla04] K. Blaum, *Accurate Atomic Masses: Status and Perspectives of Penning Trap Spectrometry*, DGMS 2004 Leipzig, oral presentation

[Boh41] N. Bohr, *Velocity-range relation for fission fragments*, Phys. Rev. **59**, 270 (1941)

[Blo33] F. Bloch, *Bremsvermögen von Atomen mit mehreren Elektronen*, Z. f. Physik **81**, 363 (1933)

[Boh48] N. Bohr, *The penetration of atomic particles through matter*, Mat. Fys. Medd. **18**(8) (1948)

[Bol96] G.Bollen et al., *ISOLTRAP: a tandem Penning trap system for accurate on-line mass determination of short-lived isotopes*, Nucl. Instr. Meth. **A368** , 675 (1996)

[Bri71] H. C. Britt et al., *Systematics of Spontaneously Fissioning Isomers*, Phys. Rev. **C4**, 1444 (1971)

[Bro02] B. A. Brown et al., *Proton drip-line calculations and the rp process*, Phys. Rev. **C65** (2002)

[Cla03] J. Clark et al., *Improvements in the injection system of the Canadian Penning trap mass spectrometer*, Nucl. Instr. Meth. **B204** , 487 (2003)

[Cob58] J. D. Cobine, *Gaseous Conductors*, Dover Publications Inc., New York (1958)

[Dah00] D. A. Dahl, *SIMION 3D 7.0*, Idaho National Engineering and Environmental Laboratory Idaho Falls, ID 83415 (2000)

[Daw76] P. H. Dawson, *Quadrupole mass spectrometry and its applications*, Elsevier Scientific Publishing Company, Amsterdam (1976)

[Dil99] J. Dilling et al., *The SHIPTRAP project: A capture and storage facility at GSI for heavy radionuclides from SHIP*, Hyp. Int. **127**, 491 (1999)

[Dil01] J. Dilling et al., *A Physics Case for SHIPTRAP: Measuring the Masses of Transuranium Elements*, Hyp. Int. **132**, 495 (2001)

[Dil03] J. Dilling et al., *The proposed TITAN facility at ISAC for very precise mass measurements on highly charged short-lived isotopes*, Nucl. Instr. Meth. **B204**, 492 (2003)

[Eli04] S. Eliseev, Dissertation Universität Gießen, in preparation

[Eng01] O. Engels et al., *First Measurements with the Gas Cell for SHIPTRAP*, Hyp. Int. **132**, 505 (2001)

[Fir96] R. B. Firestone, ed. by V. S. Shirley, 8th ed., John Wiley & Sons, New York (1996)

[Gab88] G. Gabrielse and J. Tan, *Self-shielding superconducting solenoid systems*, J. Appl. Phys. **63**, 5143 (1988)

[Gau74] H. Gauvin and Y. le Beyec, *Nuclear reactions of 118Sn, 121Sb and 127I with argon ions*, Nucl. Phys. **A223**, 103 (1974)

[Gav02] A. Gavron, *PACE4 Version 4.5 (2002)*, www.nscl.msu.edu/lise

[Ger95] H. Vogel, *Gerthsen Physik*, 18. Aufl., Springer-Verlag Berlin Heidelberg (1995)

[Gra75] B. Grasemann, *Atomic Inner Shell Processes*, Academic Press (1975)

[Hab03] D. Habs et al., *The Munich accelerator for fission fragments MAFF*, Nucl. Instr. Meth. **B204**, 739 (2003)

[Har03] J. C. Hardy et al., *High Precision Measurement of the Superallowed $0^+ \rightarrow 0^+$ β decay of ^{22}Mg*, Phys. Rev. Lett. **91**, 082501 (2003)

[Hei03] S. Heinz et al., *A new concept for cooling low-energy ion beams*, J. Phys. **B36**, 971 (2003)

[Her02] F. Herfurth et al., *Accurate mass measurements of very short-lived nuclei: prerequisites for high-accuracy investigations of superallowed β-decays*, Eur. Phys. J. **A15** 17 (2002)

[Heß04] F. P. Heßberger, private communication (2004)

[Hof00] S. Hofmann and G. Münzenberg, *The discovery of the heaviest elements*, Rev. Mod. Phys. **72**, 733 (2000)

[Hof79] S. Hofmann et al., Z. Phys **A291**, 53 (1979)

[Hof89] S. Hofmann et al., Z. Phys **A333**, 107 (1989)

[Huy02] M. Huyse et al., *Intensity limitations of a gas cell for stopping, storing and guiding of radioactive ions*, Nucl. Instr. Meth. **B187**, 535 (2002)

[Kap85] I. M. Kapchinskij, *Theory of Resonance Linear Accelerators*, Harwood Publ., Chur (1985)

[Kel02] A. Kellerbauer, *A Study of the Accuracy of the Penning Trap Mass Spectrometer ISOLTRAP and Standard Model Tests with Superallowed Beta Decays*, PHD Thesis, University of Heidelberg, Germany (2002)

[Kud96] Y. Kudryavtsev et al., *Beams of short lived nuclei produced by selective laser ionization in a gas cell*, Nucl. Instr. Meth. **B114**, 350 (1996)

[Kud01] Yu. Kudryavtsev et al., *A gas cell for thermalizing, storing and transporting radioactive ions and atoms. Part I: Off-line studies with a laser ion source*, Nucl. Instr. Meth. **B179**, 412 (2001)

[Lad79] J. Ladislas Wiza, *Microchannel Plate Detectors*, Nucl. Instr. Meth. **162**, 587 (1979)

[Lab98] *User Manual for LabVIEW*, National Instruments (1998)

[Len32] W. Lenz, *Über die Anwendbarkeit der statistischen Methode auf Ionengitter*, Z. f. Physik **77**, 713 (1932)

[Lin54] J. Lindhard, *On the properties of a gas of charged particles*, Mat. Fys. Medd. **28(8)** (1954)

[Lun99] M. D. Lunney and R. B. Moore, *Cooling of mass-separated beams using a Radiofrequency quadrupole ion guide*, Int. J. Mass Spectrom. **190/191**, 153 (1999)

[Mai00] M. Maier, *Abbremsen, Einfangen und Kühlen von radioaktiven Spaltfragmenten in einer Ionenfallenanlage*, Diplomarbeit Universität Heidelberg (2000)

[Mol47] G. Molière, *Theorie der Streuung schneller geladener Teilchen I.*, Z. f. Physik **2a**, 133 (1947)

[Mun95] F. Muntean, *Transmission study for r.f.-only quadrupoles by computer simulation*, Int. J. Mass Spectrom. **151**, 197 (1995)

[Mün79] G. Münzenberg et al., *The velocity filter SHIP, a separator of unslowed heavy ion fusion products*, Nucl. Instr. Meth. **161**, 65 (1979)

[Naa96] R. Naaman et al., Rev. Sci. Instr. **67**, 3332 (1996)

[Nol02] J. A. Nolen, *The U.S. Rare Isotope Accelerator Project*, XXI International LINAC Conference, Gyeongju, Korea (2002), oral presentation

[Nor70] L. C. Northcliffe and R. F. Schilling, *Range and stopping-power tables for heavy ions*, Nuclear Data Tables **A7**, 223 (1970)

[Nuc96] Nuclear Data Sheets **79(1)** (1996)

[Pau53] W. Paul and H. Steinwedel, Z. Naturforsch. **A8**, 448 (1953)

[Pas89] F. Paschen, Wied. Ann. **37**, 69 (1889)

[Pen36] F. M. Penning, Physica **3**, 873 (1936)

[Pla03] W. Plaß, private communication (2003)

[Pro81] *Proc. 10th Int. Conf. on Electromagnetic Isotope Separators and Techniques Related to Their Applications*, Nucl. Instr. Meth. **186**, (1, 2) (1979)

[Rei92] W. Reisdorf and M. Schädel, Z. Phys. **A343**, 47 (1992)

[Rod03] D. Rodríguez Rubiales, *An RFQ for accumulation and cooling of heavy radionuclides at SHIPTRAP and high precision mass measurements on unstable Kr isotopes at ISOLTRAP*, Dissertation University of Valéncia, Spain (2003)

[Sav00] G. Savard et al., *Experiments on the conceptual design of a gas-catcher system for in-flight-separated exotic nuclear beams as a part of a next-generation facility*, GSI proposal S258 (2000)

[Sav01] G. Savard et al., *The Canadian Penning Trap Spectrometer at Argonne*, Hyp. Int. **132**, 223 (2001)

[Sav01a] G. Savard, *The U.S. Rare Isotope Accelerator Project*, PAC 2001, Chicago USA, oral presentation

[Sav02] G. Savard, private communication

[Sav03] G. Savard et al., *Mass Measurements Along the rp-Process Using the Canadian Penning Trap Mass Spectrometer*, Physics Division Annual Report 2002 ANL-03/23, 16 (2003)

[Sav03a] G. Savard et al., *Precise Mass Measurements of Neutron-Rich Nuclei from Fission Fragments of ^{252}Cf*, Physics Division Annual Report 2002 ANL-03/23, 44 (2003)

[Sav03b] G. Savard, *Ion Catcher Network, Working group meeting on gas cells*, IKS Leuven (2003), oral presentation

[Sch03] S. Schwarz et al., *The low-energy-beam and ion-trap facility at NSCL/MSU*, Nucl. Instr. Meth. **B204**, 507 (2003)

[Sew99] M. Sewtz, *International Workshop on Ion Chemical Aspects in Ion Guide Systems*, Mainz Germany (1999), oral presentation

[Sha98] S. A. Shaffer et al., *An Ion Funnel Interface for Improved Ion Focusing and Sensitivity Using Electrospray Ionisazion Mass Spectrometry*, Anal. Chem. **70**, 4111 (1998)

[Shi92] K. Shima et al., *Equilibrium Charge Fractions of Ions of Z = 4-92 emerging from a Carbon Foil*, Atomic Data and Nuclear Data Tables **51**, 173 (1992)

[Sik03] G. Sikler, *Massenspektrometrie kurzlebiger Sr- und Sn-Isotope und Aufbau der SHIPTRAP-Penningfallen*, Dissertation Universität Heidelberg (2003)

[Sob01] A. Sobiczewski et al., *Problem of “deformed” superheavy nuclei*, Phys. Rev. **C63**, 034306 (2001)

[Som32] A. Sommerfeld, *Asymptotische Integration der Differentialgleichung des Thomas-Fermischen Atoms*, Z. f. Physik **78**, 238 (1932)

[Sze03] J. Szerypo et al., *MAFFTRAP: Ion Trap System for MAFF*, Nucl. Instr. Meth. **B204**, 512 (2003)

[Tas89] P. Taskinen et al., *Efficiency and delay of the fission ion guide for on-line mass separation*, Nucl. Instr. Meth. **A281**, 539 (1989)

[Thi02] P. G. Thirolf and D. Habs, *Spectroscopy in the Second and Third Minimum of Actinide Nuclei*, Progr. Part. Nucl. Phys. **49**, 325 (2002)

[Tit03] N. A. Titov for the KATRIN Collaboration, *KATRIN PROPOSAL: SENSITIVITY AND SYSTEMATICS*, written version of the talk presented at NANP-2003, Dubna (2003)

[Var98] V. L. Varentsov et al., *Numerical investigations of internal supersonic jet targets formation for storage rings*, Nucl. Instr. Meth. **A413**, 447 (1998)

[Var02] V. L. Varentsov, *A new ion guiding and extraction system for SHIPTRAP*, IONCATCHER simulation working group meeting, Munich Germany (2002), oral presentation

[Var03] V. L. Varentsov and D. Habs, *The 'fair-wind' gas cell – a new concept of a buffer gas cell design*, Nucl. Instr. Meth. **A496**, 286 (2003)

[Ver94] L. Vermeeren et al., *An On-Line Laser Ion Source Based on Resonance Photoionization in a Gas Cell*, Phys. Rev. Lett. Vol **73(14)**, 1935 (1994)

[dVo83] M. J. A. de Voigt et al., *High-spin phenomena in atomic nuclei*, Rev. Mod. Phys. **55**, 949 (1983)

[Voi03] F. Voit, *Aufbau und Testmessungen an einer Gaszelle zum Stoppen und Kühlen schwerer Ionen*, Diplomarbeit Universität München (2003)

[Wad02] M. Wada et al., *Slow and trapped RI-beams from projectile fragment separator,* EMIS-14, Victoria Canada (2002), oral presentation
http://www-ap.riken.go.jp/rf/

[Wad03] M. Wada et al., *Slow RI-beams from projectile fragment separators*, Nucl. Instr. Meth. **B204**, 507 (2003)

[Wad03a] M. Wada et al., *Status of SlowRi Developments*,
http://www-ap.riken.go.jp/rf/

[Wap03] A. H. Wapstra et al., *The AME2003 atomic mass evaluation*, Nucl. Phys. **A729**, 129 (2003)

[Web82] J. Weber et al., Jahresbericht Beschleunigerlabor Garching, 16 (1982)

[Wei02] L. Weissman et al., *In-trap conversion electron spectroscopy*, Nucl. Instr. Meth. (2002)

[Zie85] J. F. Ziegler et al., *The Stopping and Range of Ions in Solids*, Pergamon Press (1985)

[Zie03] J. F. Ziegler et al., *SRIM, The Stopping and Range of Ions in Matter*, http://www.srim.org/ (2003)

[Zho00] Z. Zhou, *Ein hochauflösendes Flugzeitmassenspektrometer mit Orthogonal-Extraktion und Gasgefülltem Radio Frequenz Quadrupol Interface*, Dissertation, Universität Gießen (2000)

Acknowledgement – Danksagung

At the end I want to thank all who have helped to make the successful completion of my work possible. Therefore thanks to …

Zu guter Letzt möchte ich mich bei allen bedanken, die den erfolgreichen Abschluß meiner Arbeit ermöglicht haben. Daher danke ich ...

- Prof. Dietrich Habs dafür, daß er diese Arbeit ermöglicht hat und für sein massives Interesse an deren Fortgang.
- Dr. Oliver Engels dafür, daß er mich für das Projekt „getrapt“ hat.
- Dr. Peter Thirolf in besonderem Maße. Die Zusammenarbeit mit ihm war sehr lehrreich und hat viel Spaß gemacht.
- Dr. Sophie Heinz für eine gute Zusammenarbeit. Vielleicht trinkt sie ja irgendwann doch noch ein Bierchen mit mir.
- Victor Varentsov for a fruitful work. His insistence with regard to the RF funnel was decisive.
- all members of the SHIPTRAP collaboration for a good teamwork.
- der SHIP Gruppe an der GSI für ihre Hilfsbereitschaft und die gute Zusammenarbeit.
- allen Mitarbeitern am Beschleunigerlabor, die stets hilfsbereit und um eine erfolgreiche Strahlzeit bemüht waren.
- allen Mitarbeitern der Werkstätten an der Sektion und am BL und des Technologischen Labors für ihre ausgezeichnete Arbeit und ihre Hilfsbereitschaft.
- Rainhardt Satzkowski für seine Hilfe und Zuverlässigkeit bei den Transporten von und zur GSI.
- den Konstrukteuren Peter Hartung und Michael Schumann für die gute Umsetzung meiner Vorstellungen.
- der Rechnerbetriebsgruppe für ihre Hilfsbereitschaft und für die prompten Lösungen meiner datentechnischen Probleme.
- allen Kollegen am Lehrstuhl Habs, die ich bislang noch nicht erwähnt habe, für die gute Zusammenarbeit und das gute Arbeitsklima.
- den Freunden im dritten Stockwerk für unvergeßliche Kaffeerunden.
- allen PraktikantInnen, deren Betreuung mir sehr viel Spaß gemacht hat.
- meinen Lieben daheim, die mich immer unterstützt haben, auch wenn sie so manches Mal auf mich verzichten mußten.

Lebenslauf

Persönliche Daten

Name	Jürgen Benno Neumayr
Geburtsdatum/-ort	17.08.1972 in Wasserburg am Inn
Wohnort	Alpenstraße 3 83527 Haag in OB
Familienstand	ledig
Staatsangehörigkeit	deutsch

Schulbildung

Sept. 1978 – Juli 1982	Grundschule in Reitmehring
Sept. 1982 – Juni 1991	Luitpold-Gymnasium in Wasserburg am Inn, Abitur

Grundwehrdienst

Okt. 1991 – Sept. 1992	PzGrenBtl 222 in Murnau

Studium

Okt. 1992 – Sept. 1999	Physikstudium an der LMU München, Diplom
Sept. 1998 – Sept. 1999	Diplomarbeit in der Arbeitsgruppe Faessler: *Untersuchung von Driftrohr-Detektoren mit Protonen am Münchener Tandem-Beschleuniger*

Promotion

Okt. 1999 –	LMU München, Lehrstuhl Habs